CONDUCTION MECHANISMS IN THICK FILM MICROCIRCUITS
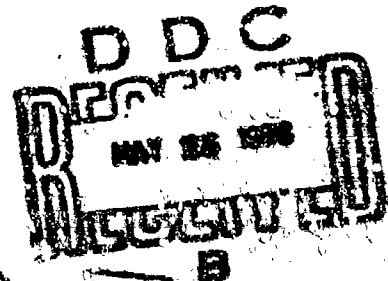
Final Technical Report

R. W. Vest

Purdue University

West Lafayette, Indiana

December 1975

Final Technical Report

CONDUCTION MECHANISMS IN THICK FILM MICROCIRCUITS

Grant Numbers: DAHC-15-70-G7

DAHC-15-73-G8

ARPA Order Number —1642

Grantee: Purdue Research Foundation

Principal Investigator: R. W. Vest (317) 749-2601

Effective Date of Grant: 7/1/70

Grant Expiration Date: 6/30/75

Amount of Grants: $259,183

December 1975

Forward

ABSTRACT

This report describes a wide range of experimental studies which led to the development of models relating the sheet resistance and temperature coefficient of resistance (TCR) of thick film resistors to physical properties of the ingredient materials. The system studied was ruthenium dioxide conductive (RuO_2), lead-borosilicate glass (63% PbO-25% B_2O_3-12% SiO_2) and alumina substrate (96% Al_2O_3-AlSiMag 614). The pertinent physical properties of these ingredient materials were measured when these data were not available from previous work. The resistor properties and materials properties were related through studies of microstructure development. The processes involved in microstructure development include: glass sintering, glass spreading, microrearrangement, glass densification, conductive sintering, and conductive ripening. The kinetics of these processes depend on surface tension of the glass, viscosity of the glass, density of the glass, particle size of the glass, particle size of the conductive, surface energy of the conductive, interfacial energy between the conductive and the glass, and solubility of the conductive in the glass. The sheet resistance and TCR depend on all these materials properties in addition to resistivity and TCR of the conductive. A model is developed which reproduces the experimental blending curve over six orders of magnitude in sheet resistance, and can account for any observed TCR in thick film resistors.

Table of Contents

LIST OF FIGURES

LIST OF TABLES

SECTION I

Introduction

1.1   General

Many of the needs for lightweight and compact electronic circuits that
are beyond the range of monolithic technology can be satisfied by combining
monolithic and thick film technologies. Design functions such as flexibility
in component use, tight electrical tolerances, high voltage requirements,
and power dissipation that are difficult in monolithic design are easily
obtainable in these "hybrid" devices while still maintaining the high degree
of stability and reliability required for computer and military applications.
However, when one considers the amount of research and engineering which
has been devoted to each of the partners in this marriage of convenience,
thick film technology suffers greatly by comparison. Both partners must
continue to develop if the marriage is to prosper.

It is often stated that thick film microelectronics is a "materials
limited" technology. In certain respects this is an unfair indictment of
the material scientists because desired materials specifications are lacking
in many areas; optimum properties must be defined before optimum materials
can be developed. It is easy to specify the desired system performance,
but this is often insufficient to determine the desired properties of the
constituents of the system. The purpose of this project was to develop
relationships between the physical properties of the constituent materials
and the electrical properties of thick film resistors.

A better understanding of conduction mechanisms in thick film resistors
is necessary before scientifically sound programs can be initiated to either
develop new materials or improve existing systems so as to:

1. Increase the performance range (e.g. higher and lower values of
    sheet resistance, lower temperature and voltage coefficients of
    resistivity, higher stability, etc.).

2. Extend the operating range (temperature, pressure, humidity, etc.).

3. Reduce processing costs (e.g. improve yield and eliminate resistor
    adjustment).

4. Reduce materials costs (e.g. eliminate noble metal constituents).

5. Reduce size

Thick film resistors are composite systems consisting of two or more phases. The electrically conducting phase (or phases) is present in the formulation as discrete particles (or as a homogeneous solution in the case of resinate systems), but a physically continuous electrically conducting network must develop along the length of the resistor during the firing operation. One of the primary goals of this project was to relate the final microstructure and the kinetics of its formation to the physical properties of the ingredient materials. For a resistor formulation consisting of discrete particles of an insulating glass and a crystalline conducting phase, the following experimental observations must be predicted by any viable model of conduction mechanism:

a. The conducting phase must include an oxide or an oxidizable metal for the resistance to vary continuously over a wide composition range (volume fraction of glass to conductive).

b. Good resistors can be made with volume fractions of conductive far less than that required for a continuous conductive phase assuming random distribution.

c. Resistor properties are different for different glasses with the same conductive.

d. The changes in resistor properties for different conductives and the same glass are not simply related to the different electrical properties of the conductives.

e. Resistor properties vary with the particle size of the conductive.

f. The temperature coefficient of resistance (TCR) of the resistor is much less than the TCR of the conductive.

1.2   Review of Previous Work

The observation that the electrical properties of thick film resistors are not simply related to the electrical properties of ingredient materials has led to numerous models of conduction mechanisms. Some of the earlier models considered the influence thermal stresses based on the idea that since the glass is an insulator and the resistor conducts, the particles of the conductive ingredient must be in contact with each other. If the contact resistance is significant, then any pressure forcing the particles

together should be important. For example, the large positive TCR of crystalline RuO_2 could be offset in RuO_2 resistors by a changing contact resistance. As the temperature increases, the bulk resistance of the RuO_2 increases, but the differences in thermal expansion could cause the particles of RuO_2 to be pushed together more tightly thereby decreasing the contact resistance. If the expansion coefficients are chosen correctly it should be possible to have a nearly zero TCR.

This pressure dependent particle contact resistance concept has been pursued by several workers [1,2]. Brady [2] assumed that the conductance of the resistor was due to a network of conductors in the form of overlapping cylinder or needle shaped elements arranged in a "jack-straw" fashion. The approach then concentrates on the resistance that might be formed at the interface between two contacting cylinders, although the derivation is equally valid for spherical particles. The change in this constriction resistance with pressure (temperature) must be a significant factor in the observed resistor TCR. This basic approach has been applied [3] to correlate data obtained from both thick film resistors prepared on a substrate and parallelopiped sintered samples made with iridium dioxide powder and glass. The monotonic relationship observed between the TCR and the differences in linear coefficients of thermal expansion of the different materials was interpreted utilizing the particle contact resistance concept. A transmission electron micrograph of what was felt to be a typical thick film resistor showed clusters of particles ($\sim 1\mu m$) forming a semicontinuous network with some evidence of dissolved material close to the particles. This micrograph was used as additional evidence to support the hypothesis of contacting particles.

The particle-to-particle contact resistance concept has been criticized by Collins [4] who proposed that structural models of resistive glazes based on a distribution of physically discrete conductor particles within a glass cannot account for the most important characteristics of real composite resistive systems (such as resistance range, TCR, linearity, noise, etc.) due to the unstable nature of the contact resistance between individual particles. An alternate microstructure was proposed by Collins [4] consisting of continuous conductive paths meandering through the glass matrix. In this case the resistor would have the properties of the material

in the conductive path, but no suggestions were offered as to nature of this material.

Van Loan [5] has supported Collins' model with microstructural investigations. He found that sub-micron sized RuO_2 particles in thick film resistors had a strong tendency to agglomerate into thick, short, multi-stranded chains. During firing a filamentary three dimensional network of extended RuO_2 chains was formed, but he concluded that complete sintering of the RuO_2 did not occur. Van Loan further postulated that certain constituents of the glass may diffuse into the RuO_2 during firing thereby altering its electrical properties, and that interparticle boundary phases are possibly formed; but he concluded that the principal way in which the glass controls the electrical properties of the system is in the extent to which it facilitates formation of the conductive filamentary microstructure.

A model proposed for palladium-silver resistors [6, 7] requires a microstructure of PdO surrounded by Pd-Ag solid solution with the negative TCR of the semiconducting PdO compensating for the positive TCR of the metal phase. Kahan [8] also studied the PdO/Ag-Pd resistor, and developed some support for Brady's contact resistance model, but concluded that a better correlation of the experimental observations could be obtained with a equivalent circuit model consisting of a metallic conducting contact in parallel with a semi-conducting contact. A parallel contact model was also proposed by Usowski and Van Zeeland [9] to correlate observations between sheet resistance and voltage coefficient of resistance. This model had a purely resistive contact in parallel with a field dependent contact.

Additions of Nb_2O_5 to thick film formulations with a conductive consisting of RuO_2 are reported [10] to cause large changes in resistor parameters. For example, in one case a reduction in TCR by a factor of ten was accomplished with a niobium content of 5 atomic percent. It was proposed that the change in the intrinsic properties of the conductive during processing was due to the fact (assumed) that RuO_2 is usually defective in oxygen, probably with a corresponding amount of Ru^{3+} in place of the Ru^{4+} in the crystal lattice. These oxygen vacancies were proposed as the cause of variations in resistor performance, and addition of a pentavelent oxide, Nb_2O_5, was the method chosen to balance the vacancies. It was also

proposed that since the TCR of ruthenium dioxide is very positive, the addition of a compensating oxide might be expected to lower the TCR and thereby be a TCR control for the resistors.

The formation of new phases which contribute to the conduction is the basis of a model proposed by Sartain [11]. His argument is based on the observation that curves of the resistance vs. temperature of thick film resistors made with IrO_2 or RuO_2, and the resistance vs. temperature of a glass are similar to the corresponding curves of heavily doped and intrinsic silicon, respectively. Sartain's conclusion was that IrO_2 or RuO_2 dissolved and produced a semiconducting glass that is degenerate at high levels of doping. A similar model has been proposed [12] for conduction in three commercial thick film systems, DuPont 1100, Alloys B, and Electroscience 2800. The model postulates localized conduction in a narrow band of states formed by the transition metal oxide doping of the glassy matrix.

Studies [13] of conduction processes in an Au-Rh-glass thick film system led to the conclusion that the glass influences the structure of the conducting part of the film, but not the composition of its components. Biesterbos [13] also concluded that over a certain range of compositions the dominant charge transport mechanism involved a tunneling process through very thin barriers between conductive particles. Studies by Seager and Pike [14] of DuPont 1200 Series and Cermalloy 500 Series resistors led to a similar conclusion that conduction occurs via chains of conducting particles with interparticle potential barriers which form tunnel junctions.

There are no known studies of the variation of intrinsic properties of thick film resistors with particle size, but results showing the effect of RuO_2 particle sizes and shapes on resistor TCR have been reported [15]. It was observed that the TCR tended to increase with increasing particle size of RuO_2, but no quantitative conclusions could be drawn.

In summary, none of the conduction mechanism models which have been proposed will correlate all of the observed results, several of the models contradict one another, and not all possibilities have been considered.

1.3   Project Goals and Plan

The primary problem in reaching an understanding of typical industrially

processed thick film resistor and conductor systems is the complexity of
the total manufacturing operation. The large number of variables which
influence the value of the resistor make it extremely difficult to purposely
change one variable and be certain that some other variable is not changing
unexpectedly and completely distorting the meaning of the experimental data.
In particular, many resistor systems have small amounts of ingredients added
because experience has shown that they improve TCR, stability, etc. From
the standpoint of scientific understanding, however, they only cause confusion.

It was felt that the only way to reach an understanding of thick film
resistors was to first perform experiments with the basic ingredient
materials and to limit the variety of experimental samples to those that
were as conceptually simple and easy to define as possible. This was the
procedure followed in the initial phase of this project in an attempt to
identify the important material properties and processing variables, and to
determine their influence individually on system performance.

The primary thrust of the second phase of the experimental program
was to relate the electrical properties of the thick films to the material
properties and processing conditions through microstructure. The materials
properties considered were: resistivity; temperature coefficient of
resistivity, coefficient of thermal expansion; interfacial energy; particle
size; viscosity; solubility; and chemical reactivity with other constituents.
The processing conditions considered were: time; temperature; and atmosphere
during firing. The microstructure studies included: sintering kinetics
of glass and conductive; spreading rates of the glass on the conductive;
rearrangement of the conductive network; and ripening of the conductive.
The basic test system for all studies of material properties, microstructure,
and system performance was RuO_2 conductive, $PbO-B_2O_3-SiO_2$ glass, and 96%
Al_2O_3 substrate.

The specific objectives of the program were:

1. Determine the dominant mechanisms responsible for microstructure
   development, and establish the relative importance of the various
   properties of the ingredient materials.
2. Determine the dominant mechanisms limiting electrical charge
   transport, and establish the relative importance of the various
   properties of the ingredient materials.

3. Develop phenomological models to inter-relate the various material
    properties with system performance.

SECTION 2
Theoretical Considerations

2.1   Sintering and Ripening

2.1.1   Driving Forces

If a system consisting of two particles in mutual contact with each
other is left for a certain period of time, bonding between them will take
place even though the temperature is lower than the melting point. The
driving force for such a reaction, commonly called sintering, is the
decrease in the surface area and hence the lowering of the surface energy
of the system. The capillary forces responsible for sintering can be
developed utilizing surface thermodynamics.

In a heterogeneous system, if the interface between the two phases
under equilibrium is planer, the pressure P_o is the same in both phases,
but the existence of a curved surface of separation gives rise to a
pressure difference between the two phases. Consider two phases having
pressures and volumes P_1, V_1 and P_2, V_2 respectively. Laplace's equation
[16] for the differential pressure on both sides of the curved interface
can be written as,

$$P_1 - P_2 = \gamma_{sv} \left[\frac{1}{r_1} + \frac{1}{r_2} \right] \tag{2.1}$$

In this equation, r_1 and r_2 are the principal radii of curvature at a given
point and are taken as positive when directed in the interior of the first
phase; γ_{sv} is the solid-vapor interfacial energy and is assumed to be
isotropic in the discussion that follows. Considering the second phase to
be a vapor which obeys the ideal gas law, the surface pressures
$(\Delta P_i = P_i - P_o)$ acting in the two phases can be determined from Eq. 2.1
and they are,

$$\Delta P_1 = \gamma_{sv} \left[\frac{1}{r_1} + \frac{1}{r_2} \right] \tag{2.2}$$

$$\Delta P_2 = \frac{\gamma_{sv} V_1}{RT} \left[\frac{1}{r_1} + \frac{1}{r_2} \right] \tag{2.3}$$

Where R is the universal gas constant and T is the absolute temperature.

Since the system under consideration involves a solid phase (RuO_2) and a liquid phase (glass) any interaction between them requires some degree of wetting of RuO_2 by the glass. Wetting can be described in terms of a contact angle Θ and the interfacial energies γ_{1v}, γ_{sl} and γ_{sv} between the liquid/vapor, solid/liquid and solid/vapor phases respectively. The relationship among these is shown in Fig. 2.1 and can be described by the equation,

$$\gamma_{sv} = \gamma_{sl} + \gamma_{1v} \cos \iota \tag{2.4}$$

For complete wetting, Θ is zero and $\gamma_{sv} \geq \gamma_{sl} + \gamma_{1v}$. In such a case complete penetration of the liquid between the solid grains take place. For partial wetting,

$$\Theta < 90° \text{ and } 1 > \frac{\gamma_{sv} - \gamma_{sl}}{\gamma_{1v}} > 0.$$

For the case of two solid phase particles wet by a glass, a thin liquid film forms between the particles during the initial stages of wetting; the geometry corresponding to this situation can be represented by Fig. 2.2. The pressure in the liquid film follows from Eq. 2.2 to be,

$$\Delta P_L = \gamma_{1v} \left[\frac{1}{\rho_1} - \frac{1}{\rho_2} \right] \tag{2.5}$$

This pressure inside the liquid film between the particles is less than the ambient pressure provided $\rho_2 < \rho_1$, and these capillary forces pull the particles together. In addition there is a pressure arising from the surface tension term acting at the wetting perimeter and given by:

$$\Delta P_\gamma = \frac{2\gamma_{1v} \cos \Theta}{r \sin \chi} \tag{2.6}$$
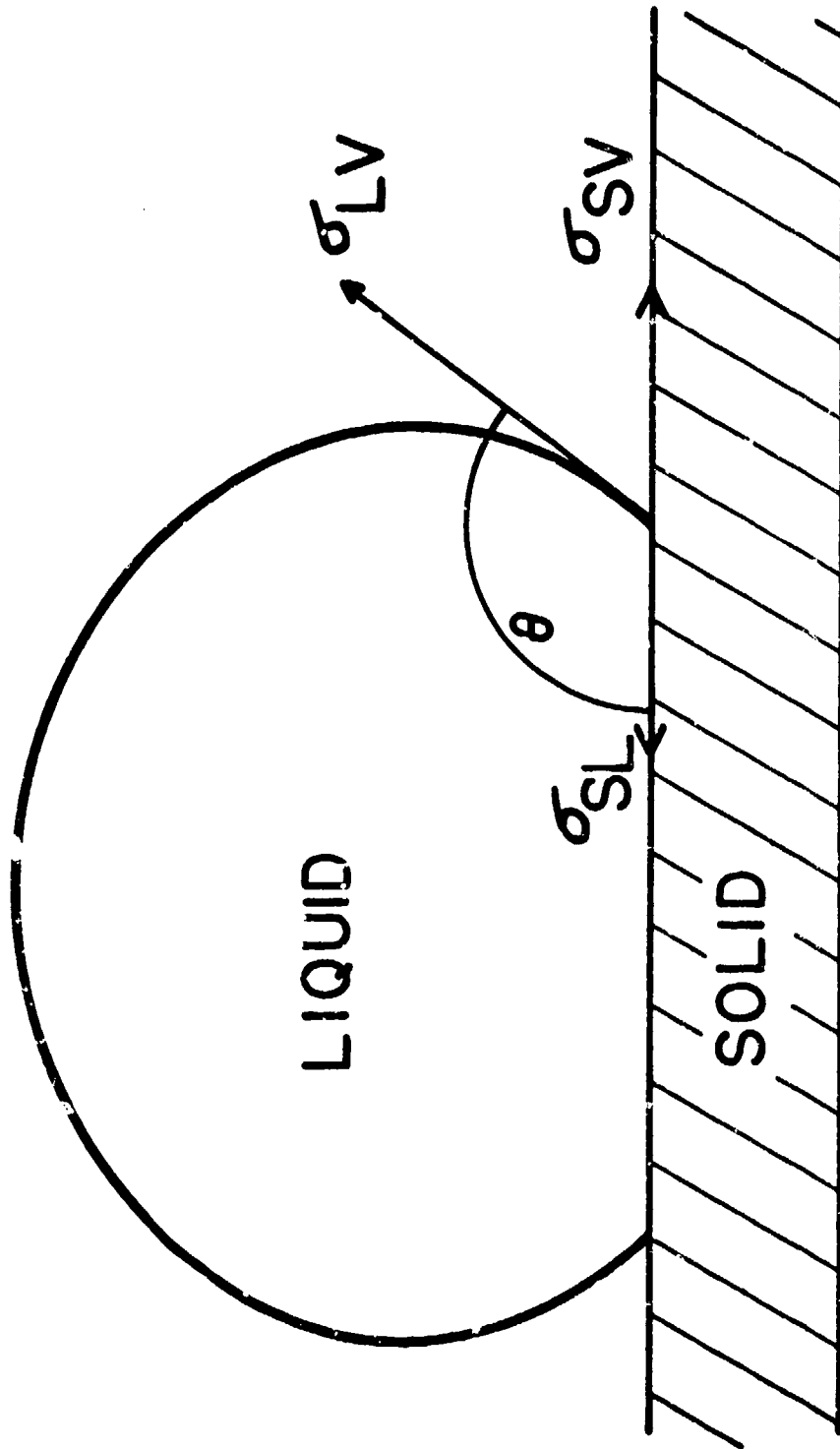
Figure 2.1   Solid-Liquid-Vapor interface
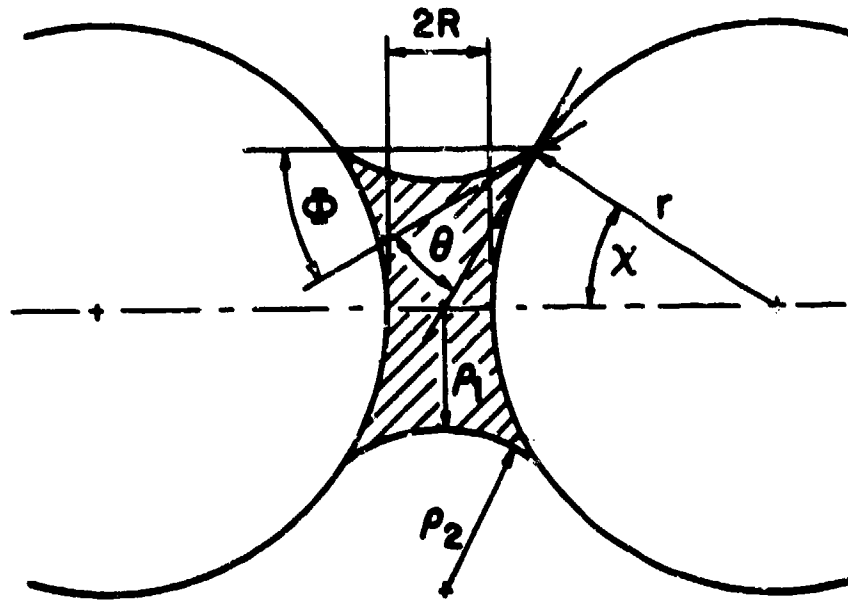
Figure 2.2   Liquid Bridge Between Solid Particles

The particles are thus subjected to a net force,

$$F = [\Delta P_\gamma + \Delta P_L] \ S \tag{2.7}$$

Where S is the area of projection of the liquid-solid interface onto a plane perpendicular to the direction of the force. Equation 2.7 has been solved [17] for F as a function of the interparticle distance (2R) with the volume of the liquid bridge (V) kept constant to give:

$$F = 2 \pi \gamma_{1v} \ r \ \sin \chi \ \sin [\chi+\Theta] + \pi \gamma_{1v} r^2 \sin^2\chi \ [\frac{1}{\rho_1} - \frac{1}{\rho_2}] \tag{2.8}$$

where

$$\rho_1 = r \ \sin \chi - [r \ (1-\cos\chi) + R] \ \frac{1-\sin \ (\chi+\Theta)}{\cos \ (\chi+\Theta)}$$

$$\rho_2 = \frac{r \ (1-\cos\chi) + R}{\cos \ (\chi+\Theta)}$$

$$V = 2\pi \ [\cos \ (\chi+\Theta) - \left(\frac{\pi}{2} - (\chi+\Theta)\right)][\rho_2^3 + \rho_1\rho_2^2] + \pi \ \rho_1^2\rho_2\cos(\chi+\Theta)$$

Equation 2.8 has been solved for $F = F(R)$ at various values of V/Vo where $V_o = 4/3 \ \pi r^3$ is the volume of the solid particles. The attractive force is highest for small contact angles and decreases as the contact angle increases, but is still attractive until the contact angle approaches 90°.

The compressive force given by Eq. 2.8 exists only during initial stages of wetting of RuO_2 particles by the glass, and decreases as the amount of liquid content in the film increases. This force becomes zero when the particles are completely immersed in the glass. At this stage, driving forces for further densification arise due to the decrease in the liquid-vapor surface area of the pores formed inside the glass. The pressure inside the pores is less than the ambient pressure and can be computed to be [18]:

$$\Delta P_P = \frac{-2\gamma_{1v}}{r_p} \tag{2.9}$$

where r_p is the pore radius. The negative pressure inside the closed pores is equivalent to placing the entire system under an equal hydrostatic pressure. Equation 2.9 applies only for the case where any gas trapped in the pore is soluble in the liquid; an additional term must be included to account for the increasing pressure of an insoluble gas with decreasing pore radius.

It follows from the above considerations that there are two types of driving forces responsible for the rearrangement process that occurs in a system consisting of solid, liquid, and vapor phases. In the initial stages of wetting, the liquid film formed between the particles pulls them and holds them together. In the latter stages, there is an overall compressive force acting on the compact leading to extensive movement of the conductive particles. This regrouping due to capillary forces occurs by means of the particles sliding with respect to each other which in general corresponds to viscous flow of the materials. Kingery [19] assumed that densification due to the rearrangement process depends entirely on viscous flow and gave the following equation for the time dependence of shrinkage.

$$\frac{\Delta L}{L_o} \sim t^{\,1+y} \tag{2.10}$$

where L_o is the original length and ΔL is the change in length of the compact. The exponent in Eq. 2.10 is greater than unity because as the pore size in the liquid decreases, the capillary pressure inside them becomes more negative thus increasing the effective compressive force on the compact. Although the various interfacial energies control the driving forces for the regrouping of RuO_2 particles in the glass, it is the viscosity of the glass and particle size of the conductive particles that control the rate at which the process occurs.

2.1.2   Kinetic Relationships for Sintering

Frenkel [20] treated the problem of coalescence of spheres assuming that the neck between the spheres is filled by Newtonian viscous flow under the action of the capillary forces. For initial stage sintering of two spherical particles, the geometrical relationships shown in Fig. 2.3
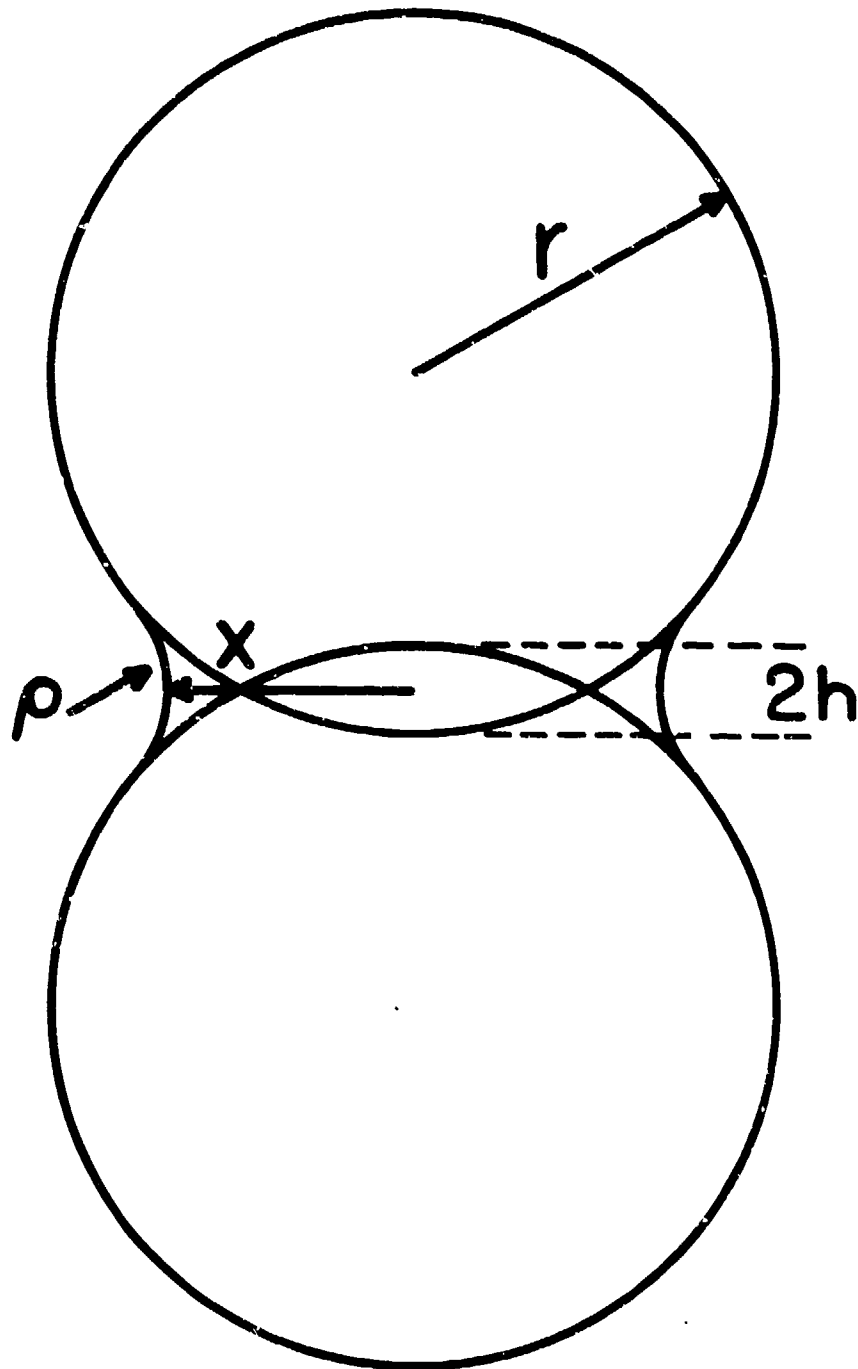
Figure 2.3   Initial Stage of Viscous Flow Sintering

apply for viscous flow. Here ρ and x are the principal radii of curvature of interest. Since the radius of curvature of the neck (ρ) is much less than the radius of the contact area between the particles (x), the pressure in the neck region follows from Eq. 2.2 to be,

$$\Delta P_1 = \frac{-\gamma_{sv}}{\rho} \tag{2.11}$$

The minus sign arises from the fact that ρ is directed in the interior of the second phase. Equation 2.11 describes the negative pressure or the tensile stress acting in the neck region and this provides the driving force for the sintering process. If the material in the neck region behaves as a Newtonian viscous fluid, neck growth between the two spheres should be related to time according to the following relationship derived by Frenkel [20].

$$[\frac{x}{r}]^2 = [\frac{3}{2}\frac{\gamma_{sv}}{\eta}]\, r^{-1}\, t \quad \text{for } \frac{x}{r} \leq 0.3 \tag{2.12}$$

In this equation, η is the viscosity of the material undergoing sintering. The generalized solution for non-Newtonian fluids has been reported by Kuczynski et. al. [21]. The experimental observations indicated that neck growth of glass spheres in fact follows Eq. 2.12 [22].

Considering Fig. 2.3 the shrinkage per sphere is h and h is approximately equal to ρ. For $\frac{x}{r} \leq 0.3$, it can be shown that $\rho \simeq \frac{x^2}{4r}$ and the decrease in the center to center distance between the two spheres, or the relative change in the length of a powder compact, can be computed to be [23]

$$\frac{\Delta L}{L_o} = [\frac{3}{4}\frac{\gamma_{sv}}{\eta}]\, r^{-1}\, t. \tag{2.13}$$

Equations 2.12 and 2.13 describe the initial stage sintering kinetics of glass particles considering that Newtonian viscous flow is the predominant mechanism. The significant material properties involved are solid-vapor interfacial energy, viscosity and particle size of the glass.

Once a liquid film is formed between the solid conductive particles, they are pulled together because of the negative pressure existing in the film. Since the glass behaves as a viscous fluid, it will be squeezed out

of the neck area until the particles are very close to each other. The
glass may not be squeezed out completely and a very thin layer might exist
separating the particles [18]. The geometry shown in Fig. 2.4 represents
such a situation. The major part of the compressive force given by
Eq. 2.8 is carried by the particles at the contact point. This force
decreases as the particles get closer together or as the amount of liquid
increases, and becomes zero when the particles are completely immersed in
the liquid phase. At this stage the closed pores give rise to an effective
compressive force on the compact and the major fraction of this force is
also carried by the contact area between the particles. The compressive
forces at the contact area resulting from the two factors mentioned above
exist irrespective of whether the glass between the particles is completely
squeezed out during the rearrangement process or a very thin layer of glass
is left in between them.

Kingery [19] has proposed a liquid phase sintering model assuming that
a very thin layer of the liquid exists between the solid phase particles.
Referring to Fig. 2.4, the compressive stress at the contact area causes
an increase in the chemical potential or activity of the solid phase in that
area. The increase in the vapor pressure due to an applied pressure ΔP_1
is given by,

$$V_o \ \Delta P_1 = RT \ \ln \frac{P_1}{P_o}$$

(2.14)

Combining Eqs. 2.2 and 2.14 gives,

$$\ln \frac{P_1}{P_o} = \frac{V_o \ \gamma_{sv}}{RT} \ [\frac{1}{r_1} + \frac{1}{r_2}]$$

(2.15)

or in more general terms,

$$\ln \frac{a_1}{a_o} = \frac{V_o \ \gamma_{sv}}{RT} \ [\frac{1}{r_1} + \frac{1}{r_2}]$$

(2.16)

where a is the activity of the conductive and V_o is the molar volume.

Referring to Fig. 2.4, the increase in the activity at the contact
points is given by,
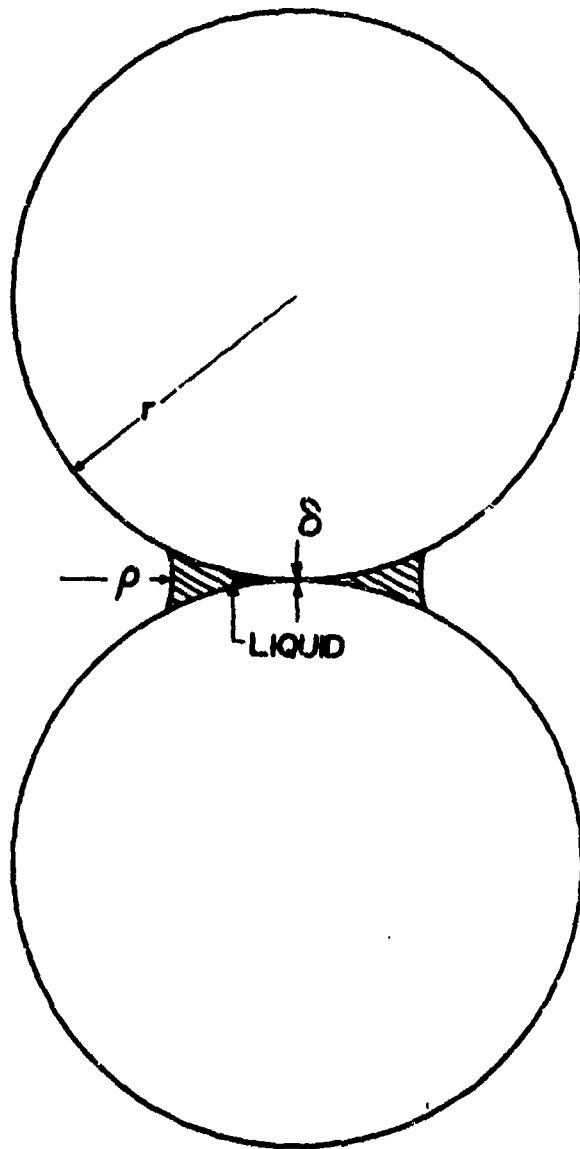
Figure 2.4   Initial Arrangement of Particles Undergoing Liquid
Phase Sintering

$$\ln \frac{a_1}{a_o} = \frac{\gamma_{1v} V_o}{\rho RT} \qquad (2.17)$$

whereas the increase in the activity due to the compressive force arising from the presence of closed pores is,

$$\ln \frac{a_1}{a_o} = \frac{2\gamma_{1v} V_o}{r_p RT} \qquad (2.18)$$

The increase in the activity provides the driving force for transferring the material away from the contact points. There is an increased rate of dissolution of species at the junction and transfer of the material away from the contact points and deposition at the free surface* allowing the center-to-center distance between the particles to be decreased and hence densification takes place. This process by which the material dissolves at one place and deposits at the other is known as solution-precipitation. When the rate determining step is that of diffusion of the dissolved species through the liquid phase, the process is diffusion controlled. If the dissolution or redeposition of the species is slower than their diffusion through the liquid phase, the process is phase boundary reaction controlled.

From the above assumptions, Kingery [20] developed the following equations relating neck growth of the spheres $(\frac{x}{r})$ and the relative shrinkage of compacts $(\frac{\Delta L}{L_o})$ containing spherical particles to time of sintering using the same geometrical configuration for the approach of particles as shown in Fig. 2.3. If the process is diffusion controlled,

$$[\frac{x}{r}]^6 = [\frac{48 K_1 \delta C_o \gamma_{1v} V_o D}{K_2 RT}] r^{-4} t \qquad (2.19)$$

$$[\frac{\Delta L}{L_o}] = [\frac{6 K_1 \delta C_o \gamma_{1v} V_o D}{K_2 RT}]^{\frac{1}{3}} r^{-\frac{4}{3}} t^{\frac{1}{3}} \qquad (2.20)$$

where K_1 is a constant of proportionality relating the ratio of the contact area to the projected particle area, δ is the thickness of the liquid film separating the particles, C_o is the equilibrium solubility

---

*In the discussion reported here, the term "free surface" is used for the surface of the particles substantially away from the neck area.

of the solid in the liquid, D is the diffusion coefficient of the slowest moving species and K_2 is the ratio of pore to particle radius. For the phase boundary reaction controlled process, the corresponding equations are,

$$[\frac{x}{r}]^4 = [\frac{8 \, K_1 \, C_o \, \gamma_{lv} \, V_o \, K_T}{K_2 \, RT}] \, r^{-2} \, t \qquad (2.21)$$

$$[\frac{\Delta L}{L_o}] = [\frac{2 \, K_1 \, C_o \, \gamma_{lv} \, V_o \, K_T}{K_2 \, RT}]^{\frac{1}{2}} \, r^{-1} \, t^{\frac{1}{2}} \qquad (2.22)$$

where (K_T) is a rate constant for the phase boundary reaction.

Whenever Eqs. 2.19 – 2.22 are to be applied to any system undergoing liquid phase sintering, the assumptions made must be properly taken into consideration. The assumption that the average particle size remains the same throughout the initial stage sintering period may not always hold good because of the grain growth immediately after the formation of the liquid phase. The model assumes complete wetting of the solid by the liquid and the penetration of the grains by the liquid phase. If there is no penetration of the grains by the liquid, the grains will be joined only at the contact points. This can also occur even in the case of perfect wetting if the liquid between the particles is squeezed out completely during the process of drawing them together. Another factor to be considered is the increased solubility of the components at the free surface because of the curvature associated with it. The increase in activity at the free surface is given by,

$$\ln \frac{a_2}{a_o} = \frac{V_o}{RT} \, \frac{2\gamma_{sl}}{r} \qquad (2.23)$$

where a_2 is the activity at the free surface. Kingery's model assumes that this increase in solubility at the free surface predicted by Eq. 2.23 is much smaller as compared to the increase in solubility at the contact area given by Eqs. 2.17 and 2.18.

A completely different situation arises when the two particles are touching each other with no liquid film between them and there are no compressive stresses acting at the contact area. Such a condition can

exist in the systems where the liquid phase completely wets the solid
phase only if: (1) the particles were initially touching and the liquid
does not penetrate between them; (2) the liquid is completely squeezed
out of the contact area during rearrangement; (3) the solid particles are
completely immersed in the liquid and hence there are no compressive
forces due to the liquid film; and (4) complete pore elimination has taken
place thus eliminating the compressive forces due to negative pressure
inside the pores. In the case of the systems where the liquid does not
completely wet the solid particles, the liquid may not penetrate between
the particles. In fact, if the contact angle is greater than 90°C, the
liquid stays in the form of discrete pockets. Under these conditions the
solid particles stay touching each other and the closed pores may not
exist in the compact.

Consider a system of two particles that are touching each other and
completely immersed in the liquid phase. It is also assumed that the
compressive stresses at the contact points due to closed pores are
negligible. Referring to the geometry shown in Fig. 2.5, it can be shown
that the capillary forces due to the curvature of the neck create a tensile
stress at the neck region given by,

$$\Delta P_1 = - \frac{\gamma_{sl}}{\rho} \tag{2.24}$$

At the same time there is a compressive stress at the free surface given
by the relationship,

$$\Delta P_2 = \frac{2\gamma_{sl}}{r} \tag{2.25}$$

The tensile stress at the neck results in a decrease in the activity
of the components. This decrease can be computed to be,

$$\ln \frac{a_1}{a_o} = \frac{V_o}{RT} \frac{\gamma_{sl}}{\rho} \tag{2.26}$$

where a_1 is the activity at the neck and a_o is the activity in the absence
of the curvature. Similarly, at the free surface the activity of the
components increases according to Eq. 2.23.

Equarions 2.23 and 2.26 predict that the solid phase should dissolve
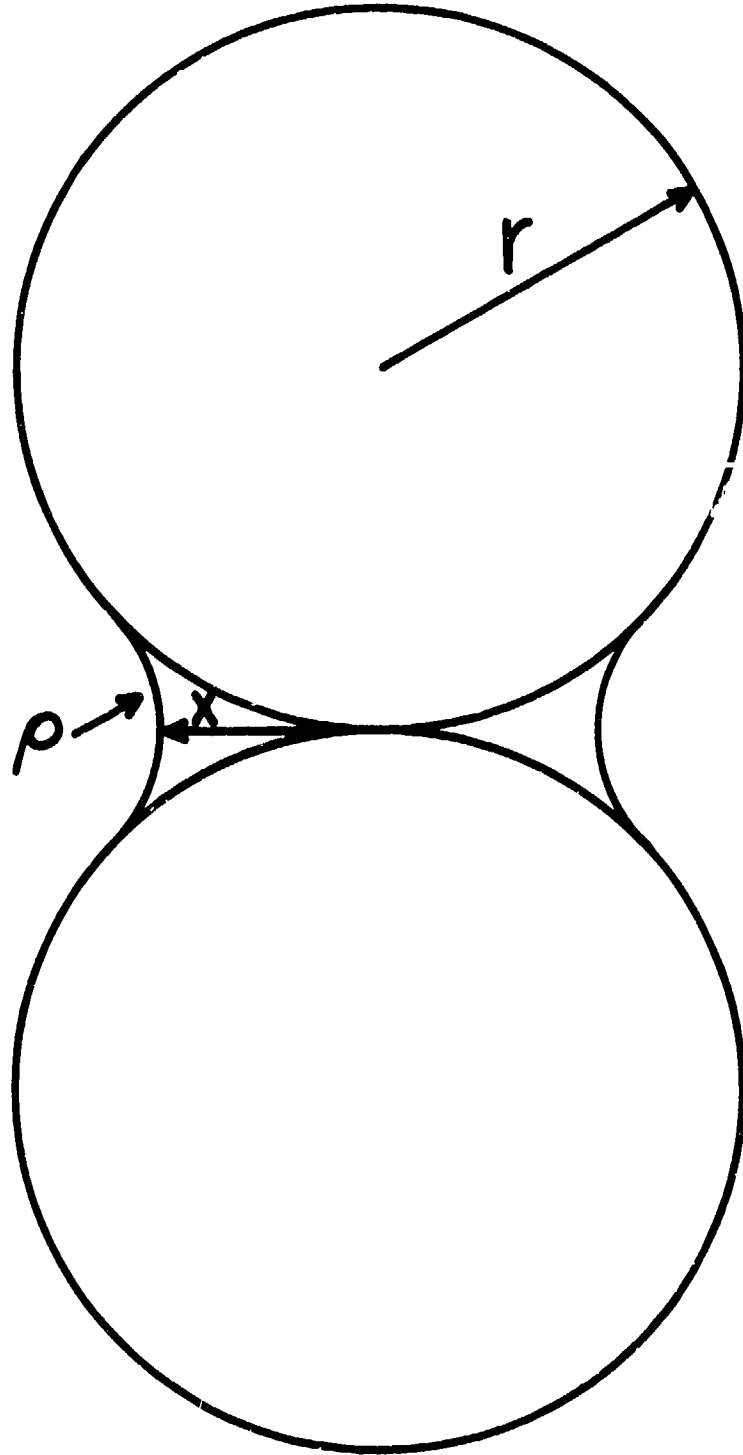
Figure 2.5   Initial Arrangement of Particles Undergoing Sintering

more at the free surface and deposit at the neck thus increasing the neck radius, but no decrease in the center to center distance can be expected. The time dependence of neck growth by this mechanism can be computed to be [23].

$$\left[\frac{x}{r}\right]^3 = \left[\frac{3\pi M \, \alpha_1 \, C_o \, \gamma_{s1} \, (M/2\pi RT)^{\frac{1}{2}}}{d_1^2 \, RT}\right] \, r^{-2} \, t \qquad (2.27)$$

where M is the molecular weight, α_1 is the sticking coefficient of the surface and d_1 is the density of the solid phase. It has been assumed that diffusion through the glass to the neck region is rapid and hence is not the rate determining factor.

The tensile stress at the neck increases the vacancy concentration according to,

$$\ln \frac{c_1}{c_o} = \frac{\delta_o}{KT} \, \frac{\gamma_{s1}}{\rho} \qquad (2.28)$$

where c_1 is the vacancy concentration at the neck, c_o is the vacancy concentration in the absence of the curvature, δ_o is the vacancy volume and K is Boltzmann's constant. Similarly, the vacancy concentration c_2 at the free surface decreases according to,

$$\ln \frac{c_2}{c_o} = \frac{\delta_o}{KT} \, \frac{2\gamma_{s1}}{r} \qquad (2.29)$$

The vacancies diffuse away from the interface under tension and are replaced by the atoms thus increasing the neck radius. The diffusional process requires a vacancy sink which can be either an external surface or an internal grain boundary. In the case where the external surface is a vacancy sink, diffusion can occur on the surface or through the volume of the grains. The former process is called surface diffusion and the latter, volume diffusion. If the internal grain boundary acts as a vacancy sink, the process is said to be occurring by grain boundary diffusion. There is no center to center distance decrease when the particles undergo sintering by surface diffusion, whereas, volume diffusion and grain boundary diffusion do give rise to shrinkage.

The time dependence of the neck growth and relative shrinkage for the above processes is given by the following relationships.

Surface diffusion [24]:

$$[\frac{x}{r}]^7 = [\frac{56\gamma_{s1}\,\delta_1^{\,4}\,D_s}{KT}]\;r^{-4}\,t \tag{2.30}$$

Volume diffusion [24]:

$$[\frac{x}{r}]^5 = [\frac{40\gamma_{s1}\,\delta_1^{\,3}D_v}{KT}]\;r^{-3}\,t \tag{2.31}$$

$$[\frac{\Delta L}{L_o}] = [\frac{40\gamma_{s1}\,\delta_1^{\,3}D_v}{KT}]\;r^{-\frac{6}{5}}\,t^{\frac{2}{5}} \tag{2.32}$$

Grain boundary diffusion [25]:

$$[\frac{x}{r}]^6 = [\frac{96\gamma_{s1}\,\delta_o\,b\,D_g}{KT}]\;r^{-4}\,t \tag{2.33}$$

$$[\frac{\Delta L}{L_o}] = [\frac{12\gamma_{s1}\,\delta_o\,b\,D_g}{KT}]^{\frac{1}{3}}\;r^{-\frac{4}{3}}\,t^{\frac{1}{3}} \tag{2.34}$$

In Eqr. 2.30 - 2.34, δ_1 is the interatomic distance, D_s, D_v and D_g are surface, volume and grain boundary diffusion coefficients respectively and b is the grain boundary thickness.

The concave radius of curvature of the neck results in a decrease of the partial pressure of the species at the neck, whereas, the partial pressure of the species at the free surface is increased because of the convex radius of curvature. The transport of the vapor species from the free surface to the neck can lead to the welding of the particles together. Such a process is called evaporation-condensation. The growth of neck radius with time for such a process follows the following relationship [23],

$$[\frac{x}{r}]^3 = [\frac{3\pi M\,\alpha_1\,P_o\gamma_{s1}\,(M/2\pi RT)^{\frac{1}{2}}}{d_1^2\,RT}]\;r^{-2}\,t \tag{2.35}$$

In this equation, P_o is the equilibrium vapor pressure over a flat surface. There is no shrinkage during initial stage sintering by evaporation-condensation.

Another mechanism by which sintering can take place is plastic flow.
Lenel and coworkers [26] have pointed out that in the neck area or near the
small pores dislocations can be created in small quantities to actuate the
plastic flow. Johnson [27] has reported that in certain cases more than
one mechanism could be operating at the same time and might significantly
affect the neck growth and shrinkage. Particle size distribution effects
in initial stage sintering have been considered by Coble [28]

The general expression for the time dependence of the neck growth for
the initial stage sintering of spherical particles can be written as,

$$[\frac{x}{r}]^n = F\ (T)\ r^{-m}\ t \tag{2.36}$$

where F (T) is a function of temperature and is a characteristic of the
mechanism involved. The corresponding values of F (T), m and n for the
different mechanisms are given in Table 2.1.

Similarly the general expression for the shrinkage relationships can
be written as,

$$[\frac{\Delta L}{L_o}] = G\ (T)^{n'}\ r^{-m'}\ t^{n'} \tag{2.37}$$

The values of G (T), n' and m' for the different sintering mechanisms
leading to shrinkage are given in Table 2.2.

2.1.3   Ripening

The increase in the activity of the components at the surface of the
spherical particles follows the relationship indicated in Eq. 2.23.
According to this equation, the increase in the activity and hence the
increase in the rate of dissolution is inversely proportional to the
radius of the particles. The smaller particles dissolve at a faster rate
thus increasing the concentration of the dissolved species in their immediate
vicinity. Because of the slower dissolution of the bigger particles, the
concentration of the dissolved species in their immediate surroundings is
lower. Thus a concentration gradient is established which provides the
driving force for the material transfer through the liquid. This process,

Table 2.1 Summary of Neck Growth Relationships.

Mechanism	F(T)	n	m
Newtonian Viscous Flow	$\dfrac{3}{2}\dfrac{\gamma_{sv}}{\eta}$	2	1
Volume Diffusion	$\dfrac{40\gamma_{sl}\delta_1{}^3 D_v}{KT}$	5	3
Surface Diffusion	$\dfrac{56\gamma_{sl}\delta_1{}^4 D_s}{KT}$	7	4
Grain Boundary Diffusion	$\dfrac{96\gamma_{sl}\delta_o bD_g}{KT}$	6	4
Evaporation-Condensation	$\dfrac{3\pi M\alpha_1 P_o\gamma_{sl}(M/2\pi RT)^{\frac{1}{2}}}{d_1^2 RT}$	3	2
Solution-Precipitation:			
A. Kingery's Model			
1. Diffusion Controlled Process	$\dfrac{48K_1\delta C_c\gamma_{1v}V_o D}{K_2 RT}$	6	4
2. Reaction Controlled Process	$\dfrac{8K_1 C_o\gamma_{1v}V_o K_T}{K_2 RT}$	4	2
B. Without Shrinkage	$\dfrac{3\pi M\alpha_1 C_o\gamma_{sl}(M/2\pi RT)^{\frac{1}{2}}}{d_1^2 RT}$	3	2

Table 2.2 Summary of Shrinkage Relationships.

Mechanism	G(T)	n´	m´
Newtonian Viscous Flow	$\dfrac{3}{4}\dfrac{\gamma_{sv}}{\eta}$	1	1
Volume Diffusion	$\dfrac{40\,\gamma_{sl}\,\delta_l{}^3\,D_v}{kT}$	$\dfrac{2}{5}$	$\dfrac{6}{5}$
Grain Boundary Diffusion	$\dfrac{12\,\gamma_{sl}\,\delta_o\,b\,D_g}{kT}$	$\dfrac{1}{3}$	$\dfrac{4}{3}$
Solution-Precipitation:			
Kingery's Model			
1. Diffusion Controlled Process	$\dfrac{6\,K_1\,\delta C_o\,\gamma_{lv}\,V_o\,D}{K_2\,RT}$	$\dfrac{1}{3}$	$\dfrac{4}{3}$
2. Reaction Controlled Process	$\dfrac{2\,K_1\,C_o\,\gamma_{lv}\,V_o\,K_T}{K_2\,RT}$	$\dfrac{1}{2}$	1

by which the bigger particles grow at the expense of the smaller ones in
metallic systems was originally advanced by Price, Smithells and Williams
[29] and is essentially the Ostwald ripening process. Greenwood [30]
treated the ripening process quantitatively and arrived at an expression
for the time dependence of the average particle size. The kinetic equations
reported below have been taken from a recent review article by
Fischmaister et. al. [31] which is based upon the theories developed by
Lifshitz and Slyosov [32] and Wagner [33].

If one assumes that diffusion controlled solution-precipitation is the
rate determining process for the particle growth, the average particle
radius obeys the following time dependence.

$$[\bar{r}(t)]^3 - [\bar{r}(0)]^3 = [\frac{8}{9} \frac{C_o \gamma_{al} V_o^2 D}{RT}] t \qquad (2.38)$$

In this equation $\bar{r}(t)$ is the average particle radius at time t and $\bar{r}(0)$
is the average particle radius at time zero. If the growth occurs by a
phase boundary reaction controlled solution-precipitation process, the
average particle radius increases according to,

$$[\bar{r}(t)]^2 - [\bar{r}(0)]^2 = [\frac{8}{9} \frac{2 C_o \gamma_{al} V_o^2 K_T}{RT}] t \qquad (2.39)$$

where (K_T) is the transfer coefficient.

2.1.4   Parameters Affecting Kinetics

Let us summarize the different parameters that could affect the kinetics
of the different stages of microstructure development during firing of RuO_2-
glass thick film resistors.

Wettability. Very low contact angles are necessary for the glass to form
a liquid film between the conductive particles as shown in Fig. 2.2. The
effect of wettability on the microstructure has been described in the
previous section. Pask and coworkers [34] have pointed out that contact
angles under chemical equilibrium conditions could be different from those
under nonequilibrium conditions. Any wetting of the solid by the liquid can

give rise to some interaction at the solid-liquid interface. This can
change the chemical composition of the liquid either due to the solution of
the solid phase or a chemical reaction with the solid phase. The mass
transfer across the interface might result in a decrease in the corresponding
specific interfacial energy causing the liquid drop to spread on the solid
surface if the reduction in interfacial energy is large and diffusion rate
of the reaction products are slow compared to the flow rate of the liquid.
After completion of the reaction at the interface and after the liquid is
saturated with the reaction product, the specific interfacial energy
gradually increases towards the static value thus giving the equilibrium
contact angle. This effect calls for certain precautionary measures during
contact angle measurements in order to make sure that the contact angle
obtained is the equilibrium contact angle. The other possibility that has
to be considered for the system under study in this investigation is the
interaction between the substrate (96 v/o alumina) and the glass which
might change the composition of the glass and hence the wetting characteristics.
Surface tension of the glass. The driving forces for all the different
stages of liquid phase sintering depend upon the surface tension of the liquid.
The RuO_2-glass and glass-substrate interactions can change the surface tension
of the glass.

Viscosity of the glass. Viscosity of the glass is an important parameter
controlling the sintering kinetics. The more viscous the glass, the slower
the rate of sintering of the glass and the rate of the rearrangement process.
Viscosity also affects the conductive sintering and ripening kinetics if the
mechanism is diffusion controlled solution-precipitation process. Assuming
that the Stokes-Einstein relationship [30] is valid, the diffusion coefficient
can be related to the viscosity of the liquid by the following relationship.

$$D = \frac{RT}{N} \; \frac{1}{6\pi \eta r} \tag{2.40}$$

In this equation, r is the radius of the diffusing species and N is
Avogadro's number. Any increase in viscosity will decrease the rate of
diffusion through the glass. The glass viscosity might be altered by the
interactions between the substrate and the glass.

Solubility of RuO_2 in the glass. The equilibrium solubility of RuO_2

in the glass directly affects the conductive sintering and ripening
processes when the dominant mechanism is one of solution-precipitation.
The rate of sintering is enhanced for smaller particles due to the faster
rate of dissolution predicted by Eq. 2.23.

Chemical reactions between the ingredient materials. The three main
ingredient materials involved in this study are RuO_2, glass and the
substrate. The possible interactions are the reactions between RuO_2-
substrate and RuO_2-glass giving new phases, and reactions between glass
and substrate, leading to changes in the properties of the glass such as
surface tension, viscosity, wettability and solubility of RuO_2 in the
glass.

Oxidation and Reduction of the phases undergoing sintering. The thermo-
dynamic stability of the phases are of prime importance for the sintering
study. Any reduction or oxidation of RuO_2 or the glass will alter the
sintering kinetics. Some of the features regarding the thermodynamic
stability of RuO_2 and the kinetics of oxidation and reduction of RuO_2 are
discussed in Section 4.1.4.3.

Sintering medium. Liquid phase sintering studies have been conducted in
air, inert atmosphere or vacuum depending upon the thermodynamic stability
of the phases under consideration. For this particular system containing
RuO_2 and glass, sintering studies were conducted in air as both of these
materials are stable in air at the sintering temperatures.

Particle size. The sintering kinetics are drastically affected by the
particle size as indicated by Eq. 2.36. As the particle size increases,
the rate of sintering decreases, the rate of decrease depending upon the
particular mechanism operating. From Eq. 2.36, the times required for the
initial stage sintering of the particles of different sizes for any
particular mechanism under similar conditions can be written as,

$$[\frac{t_x}{t_y}] = [\frac{r_x}{r_y}]^m \qquad (2.41)$$

This relationship is known as Herring's scaling laws [35] and can be used
to extrapolate the results from the data obtained on a particular particle
size to any different size.

Effect of compacting pressure. The compacting pressure has a positive

effect on sintering as it promotes intimate contacts of the particles,
but it can also form closed pores in the compacts. If the capillary
pressure is lower than the gas pressure in the pores, the porosity will
remain even after long hours of heating. In certain cases the sample
may expand due to the expansion of the gas inside the pores increasing
the pore size. This indicates that increasing the compacting pressure
may not always help densification.

Effect of the amount of the liquid. Kingery [19] noted that if the amount
of the liquid is greater than 35 v/o, complete densification is possible
by a regrouping process alone. In systems where a solution-precipitation
process is dominant, the amount of liquid phase also affects the grain
growth. In general, the rate and degree of densification increase with
the amount of the liquid phase. If the amount of liquid is too small,
there is considerable contiguity of the solid grains and solid state
sintering is possible.

Uniformity of mixing. Homogeneity of the mixture containing the solid
phase and the binder phase (the phase that will become liquid) particles
is necessary in all liquid phase sintering systems, particularly in those
with a small amount of the binder phase.

Non-isothermal Conditions. All of the kinetic equations developed hold
only for isothermal sintering, whereas thick film processing involves
various heating and cooling rates with short (if any) constant temperature
zones. Several authors [36-39] have considered sintering at constant
heating rate. It is first necessary to determine the activation energy
(Q) for sintering from a series of isothermal experiments and use of the
equation

$$\frac{\Delta L}{L} = K_o \exp\left(\frac{-Q}{RT}\right).$$ (2.42)

Then any of the equations for neck growth or shrinkage can be written in
terms of the heating rate y. For example, Eq. 2.13 for shrinkage by
viscous flow becomes [40]

$$\frac{\Delta L}{L} = \frac{4064^{\gamma}sv\ R}{y r \eta Q} \exp\left(\frac{-Q + 5800}{RT}\right)$$ (2.43)

2.2   Resistor Geometry Effects

Several aspects of thick film processing technology can lead to non-uniform geometries of the fired resistor. When the ink is initially transfered from the screen to the substrate it is present as a series of isolated right cyclinders corresponding to the screen mesh. During the leveling process these cylinders merge to form a uniform film. If the leveling process does not proceed to a sufficient extent a waviness with the periodicity of the screen mesh will remain on the resistor surface, while "bleedout" will result if the leveling proceeds too far. "Bleedout" can also occur during firing if the time-temperature product is too high. Improper set-up of the screening machine can lead to varying film thickness along the length or width of the resistor; this thickness variation can be either monotonic or periodic with a period long compared to the screen mesh period.

Thickness variations across the width of a resistor do not cause resistance variations because the cross sectional area along the current path remains constant for a given volume of resistor material deposited. Thickness variations along the length of a resistor do lead to resistance variations for a given volume of resistor material deposited and these will be considered. For modeling purposes the square wave and saw tooth geometries shown in Fig. 2.6 will be considered. These represent the two limiting cases for thickness variations due to the screen mesh pattern on the resistor surface, and the saw tooth is a good approximation for the monotonic or long period variations. Both geometries are depicted in Fig. 2.6 for one cycle but the results will be applicable to any number of cycles because the electrodes at either end are equi-potential surfaces; the waves had to be drawn twice the normal cycle in order to achieve this result.

The resistance of a resistor having the square wave shape shown in Fig. 2.6 (a) and width ω can best be determined by conformal mapping techniques. Using suitable coordinate transformations it can be shown [41] that for values of $t_2/t_1 < 1.5$ the number of squares (n) is given by

$$n = \frac{2\ell}{t_1} + \frac{2\ell}{t_2} + \frac{2}{\pi} \; [\frac{(S^2+1)}{S} \; \ln \; (\frac{S+1}{s}) \; -2 \; \ln \; (\frac{4S}{S^2-1}) \;] \quad (2.44)$$
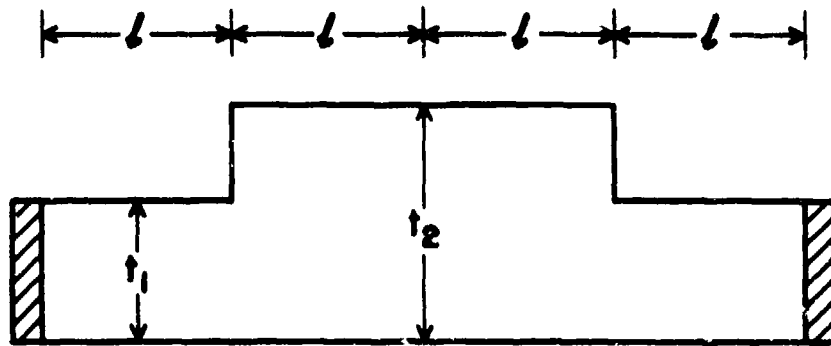
(a) SQUARE WAVE
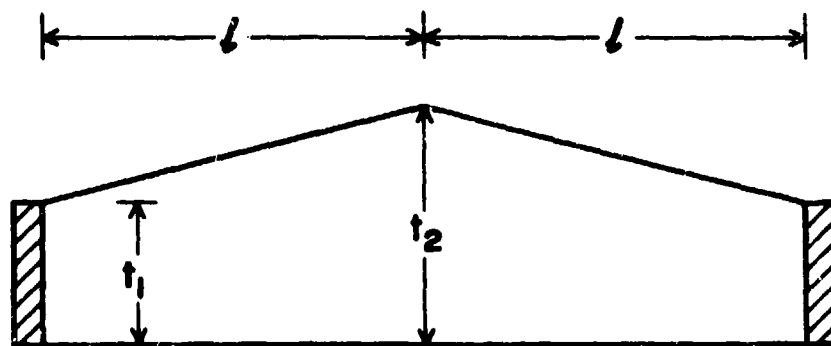
(b) SAW TOOTH

Figure 2.6   Resistor Geometry Models

where $S = t_2/t_1$. The resistance (R) of the film is then

$$R = \frac{n}{\omega} ,$$ (2.45)

where ρ is the resistivity. The resistance of a resistor with the same volume of resistor material but with a flat surface is given by

$$R_o = \frac{4\ell\rho}{\omega t} = \frac{8\ell\rho}{\omega(t_1 + t_2)}$$ (2.46)

where

$$t = (t_1 + t_2)/2.$$

Therefore

$$\frac{R}{R_o} = \frac{n(t_1 + t_2)}{8\ell}$$ (2.47)

Substituting the value of n from Eq. 2.44 and simplifying gives

$$\frac{R}{R_o} = \frac{1}{2} + \frac{S^2 + 1}{S} [\frac{1}{4} + \frac{t}{2\pi\ell} \ln(\frac{S+1}{S-1})] - \frac{t}{\pi\ell} \ln(\frac{4S}{S^2-1})$$ (2.48)

Equation 2.48 can be solved for various values of the parameter t/ℓ. For the problem of the screen pattern surface variation, the value of ℓ can be approximated as the average of the wire diameter and mesh opening. Taking a nominal film thickness (t) of 1 mil (0.001") the dependence of R/R_o on S is plotted in Fig. 2.7 for four different screen mesh sizes. The deviation of R from R_o is seen to increase rapidly as the amplitude of the surface irregularily increases and reaches 29% at t_2/t_1 equal to 2 for the 325 mesh screen.

The saw tooth geometry of Fig. 2.6 (b) does not lend itself as easily to conformal mapping techniques, but the problem can be solved by using the flux tube approximation. If N_p is the number of flux tubes in parallel along the length of the resistor, and N_s is the number of squares in series in each flux tube then

$$R = \frac{N_s \rho}{N_p \omega}$$ (2.49)

where ρ and ω are the resistivity and width of the resistor as before.
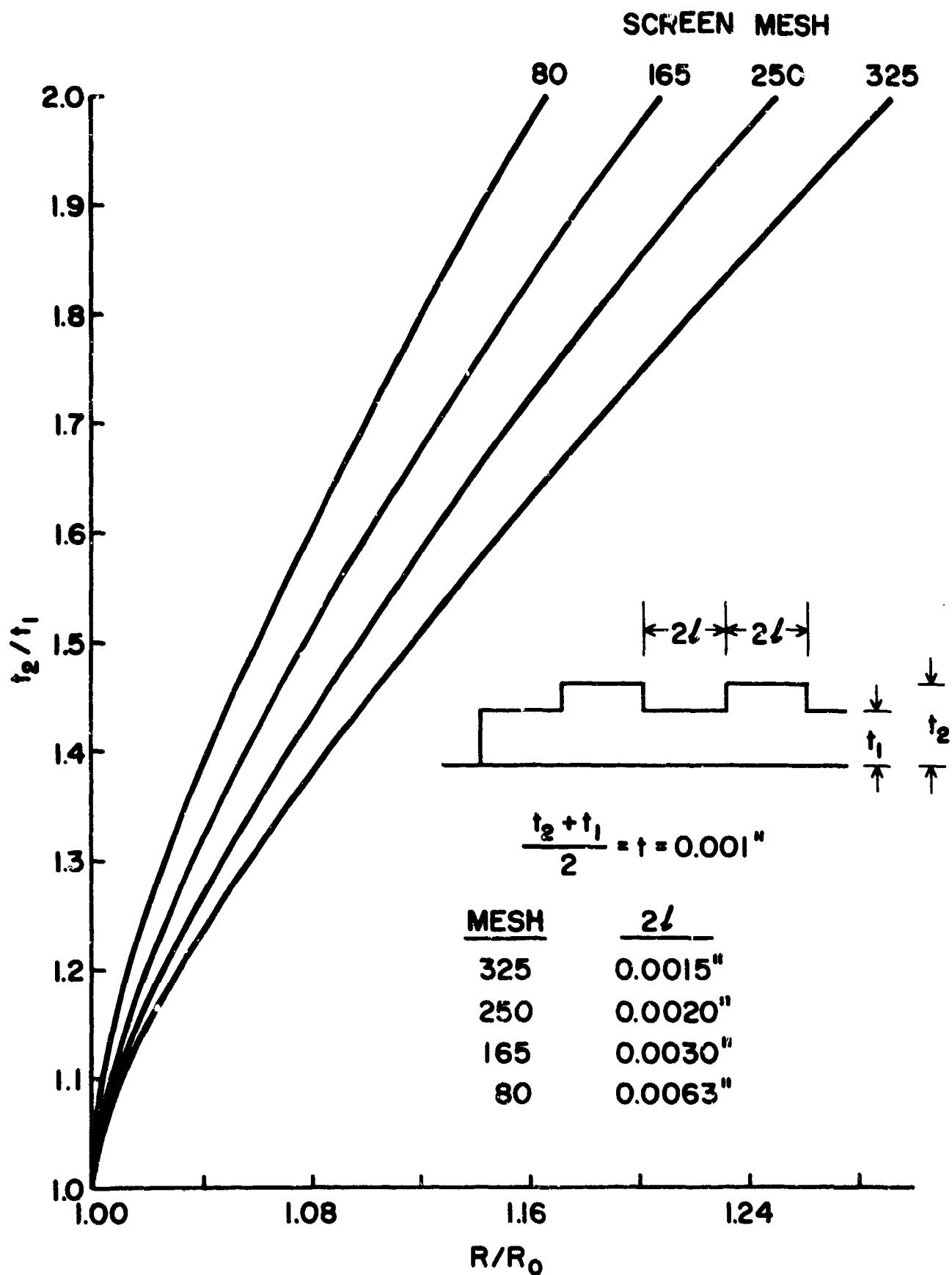
Figure 2.7   Variation in Resistance with Square Wave
              Surface Roughness

N_s can be approximated as the ratio of the average length of a flux tube to the average length of a square to give

$$N_s = \frac{2\ell + 2[\ell^2 + (t_2-t_1)^2]^{1/2}}{2} \Bigg/ \frac{\frac{t_2}{N_p} + \frac{t_1}{N_p}}{2} \qquad (2.50)$$

Combining Eqs. 2.49 and 2.50 gives

$$R = \frac{2\ell + 2[\ell^2 + (t_2-t_1)^2]^{1/2}}{t_2 + t_1} \frac{\rho}{\omega} \qquad (2.51)$$

The resistance of a resistor with the same length and width and containing the same volume of resistor material but with a flat surface is given by

$$R_o = \frac{2\ell\rho}{\omega t} \qquad (2.52)$$

where $t = (t_1 + t_2)/2$ as before. Therefore

$$\frac{R}{R_o} = \frac{\ell + [\ell^2 + (t_2-t_1)^2]^{1/2}}{2\ell} \qquad (2.53)$$

Rearranging Eq. 2.53 to contain the same variables as Eq. 2.48 gives

$$\frac{R}{R_o} = \frac{1}{2} + \frac{1}{2} [1 + 4 (\frac{t}{\ell})^2 (\frac{S-1}{S+1})^2]^{1/2} \qquad (2.54)$$

where $S = t_2/t_1$ as before. Calculating ℓ values from the wire diameter and mesh opening, and taking a nominal thickness of 1 mil (0.001") the dependence of R/R_o on S shown in Fig. 2.8 is obtained. A comparison of Fig. 2.7 and 2.8 shows that the square wave model predicts variations three times as great as the saw tooth. The actual case will lie somewhere between these two extremes, and probably closer to the saw tooth. These figures combined with a measurement of the surface roughness due to the screen pattern can establish limits on the measured resistance variation due to this effect.

Equation 2.54 can also be used to calculate the deviation in resistance value due to monotonic or long period thickness variations

SCREEN MESH

$$t = \frac{t_1 + t_2}{2} = 0.001"$$

MESH	ℓ
325	0.0015"
250	0.0020"
165	0.0030"
80	0.0063"
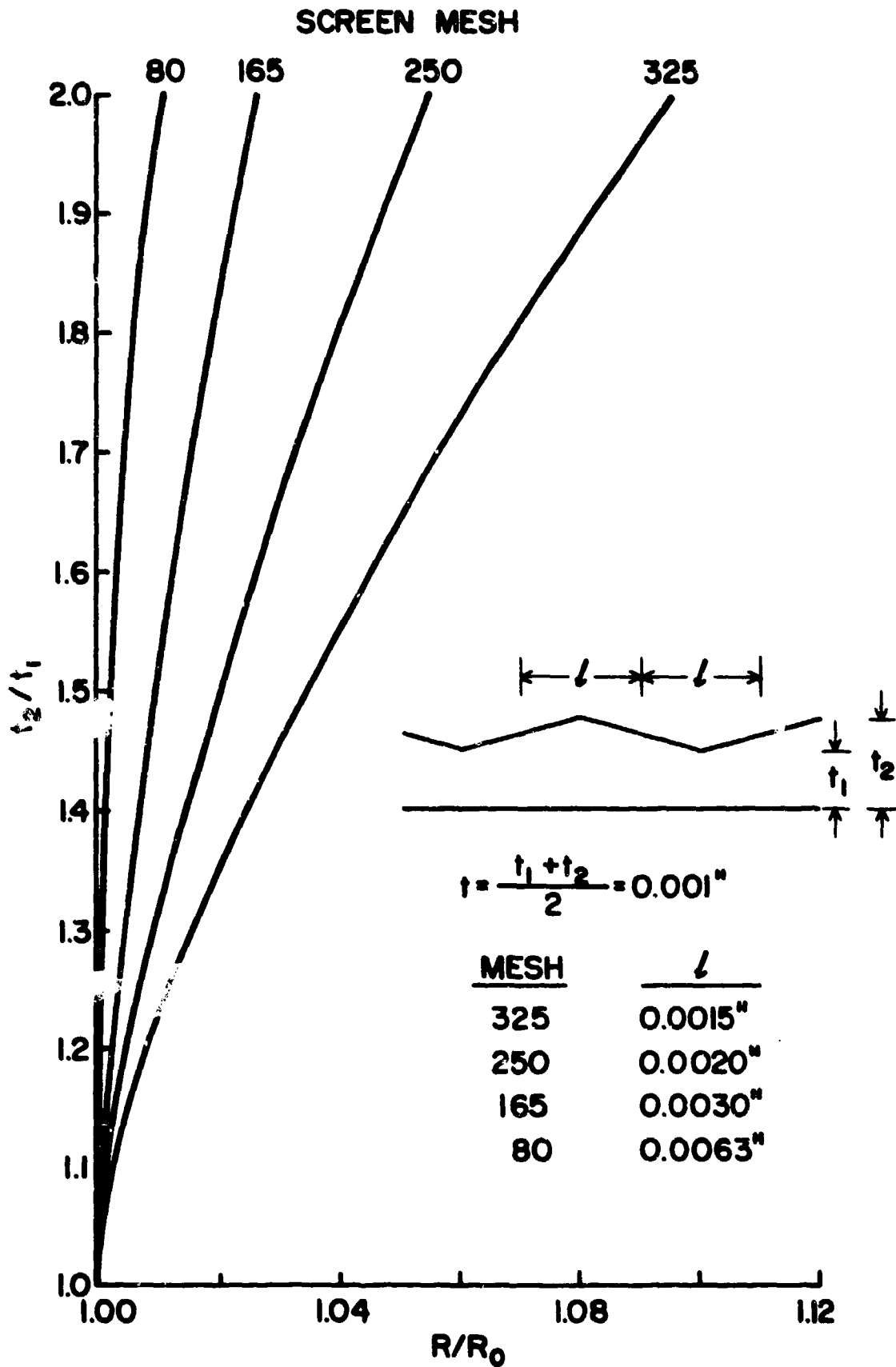
Figure 2.8   Variation in Resistance with Sawtooth Surface Roughness

resulting from improper printer set up, but the effect is seen to be small. For example, a 20 mil long resistor 1 mil thick with S = 2 (a more severe case than ever expected in practice) would give R/R_o = 1.001, a deviation of only 0.1%.

SECTION 3
Special Apparatus Development

3.1   Experimental Firing Facility

The standard method of processing thick film resistors and conductors is to use a tunnel kiln, but for many research applications kilns have the disadvantages of limitations in profile versatility and long times to reach equilibrium if the profile is changed. To overcome these shortcomings, a furnace system was designed and constructed so as to duplicate the profile of any tunnel kiln (within its maximum temperature limit), while allowing rapid changes in profile. The basic system shown in Fig. 3.1 consisted of a tube furnace with a nearly linear temperature profile varying from approximately room temperature at one end to about 1200°C near the center. A sample to be heated was moved back and forth in the tube furnace by a servo driven push rod controlled by a program cam wheel. Provision was made to record both temperature and resistance during the firing cycle.

The tube furnace was a three zone, multiple-tap furnace with independent temperature control for all three zones. The center zone was 8.5 cm long, wound with Pt-Rh wires, and was capable of 1500°C. The other two zones were 30 cm long and were wound with Kanthal A-1 alloy. One of the Kanthal zones was part of the linear profile while the other was used for preheating any flowing gas. The furnace tube (2.5 cm I.D.) had gas seals at both ends so that a wide range of atmospheres could be introduced into the furnace.

The part to be fired was placed on an alumina Dee tube that was fastened to a four hole alumina push rod as shown in Fig. 3.2. Outside the furnace, the other end of the push rod was clamped to a gear rack which meshed with a pinion gear driven by a servomechanism. The shaft for the drive pinion was connected to a ten turn potentiometer which furnished a feedback voltage proportional to the position of the Dee tube in the furnace.
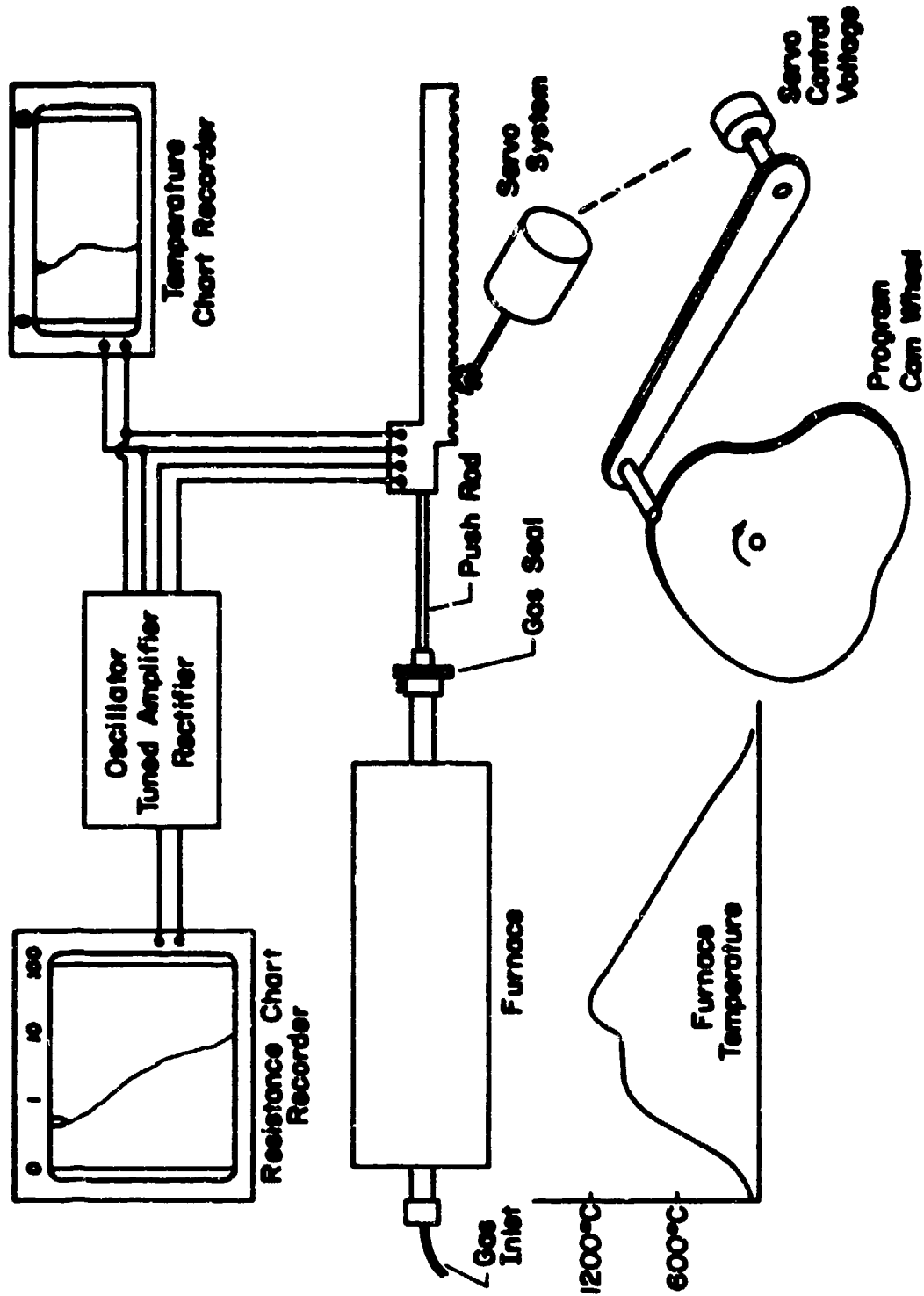
Figure 3.1   Diagram of Furnace and Resistance Measuring System
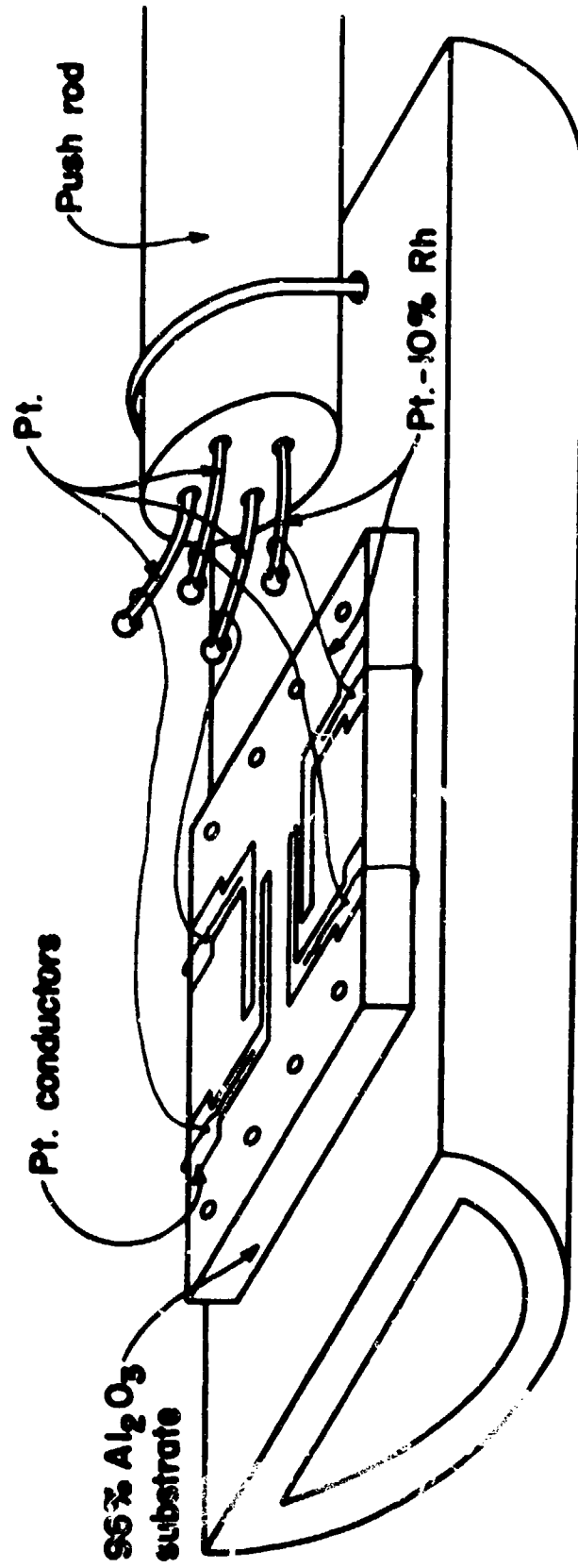
Figure 3.2   Sample Holder Assembly

This voltage, minus an imput voltage, was the error voltage to the servo amplifier.

The input voltage was usually furnished by either a manually adjusted ten turn potentiometer or by a single turn potentiometer rotated by a lever following the shape of a program cam wheel. An increasing radius of the cam increased the input voltage and caused the sample to be moved to a region of higher temperature. Because the time-temperature relationship was determined by a cam wheel the only delay in changing profiles was the time required to change program cam wheels. The versatility of the time-temperature relationships obtainable with the furnace was limited only by the angular speed of the cam wheel, the maximum speed of motion of the sample in the furnace, and the rate at which the sample could change temperature. Cam wheels were made with the aid of a computer program which took into account the temperature vs. distance of the furnace and the geometry of the cam shaft and lever. The input to the program was the desired temperature versus time and the output was angle-radius points that determined the shape of the cam.

The program cam wheel was rotated by a stepping motor driven by a square wave voltage; the angular rate of rotation was determined by the frequency of this voltage. A block diagram of the cam drive system is shown in Fig. 3.3. The maximum rate of rotation was one revolution in two minutes and corresponded to 60 Hz. An electronic drive circuit provided 12 additional lower frequency square wave voltages, decreasing in binary steps. The lowest frequency corresponded to 8192 minutes (1 1/2 weeks) rotation time. The twelve lowest frequencies were connected to three twelve position selector switches, wired in parallel so that any of the twelve frequencies was available at each wiper terminal. The angular rate of rotation of the cam wheel was determined by which of the three selector switches was connected to the motor drive circuit.

The shaft for the cam wheel also drove a programmable switch assembly consisting of six SPDT microswitches operated by adjustable cams. The cams were easily adjusted to permit closures of from zero to 360° of shaft rotation. This switch assembly selected which of the three frequencies, determined by the selector switches, controlled motor speed and permitted
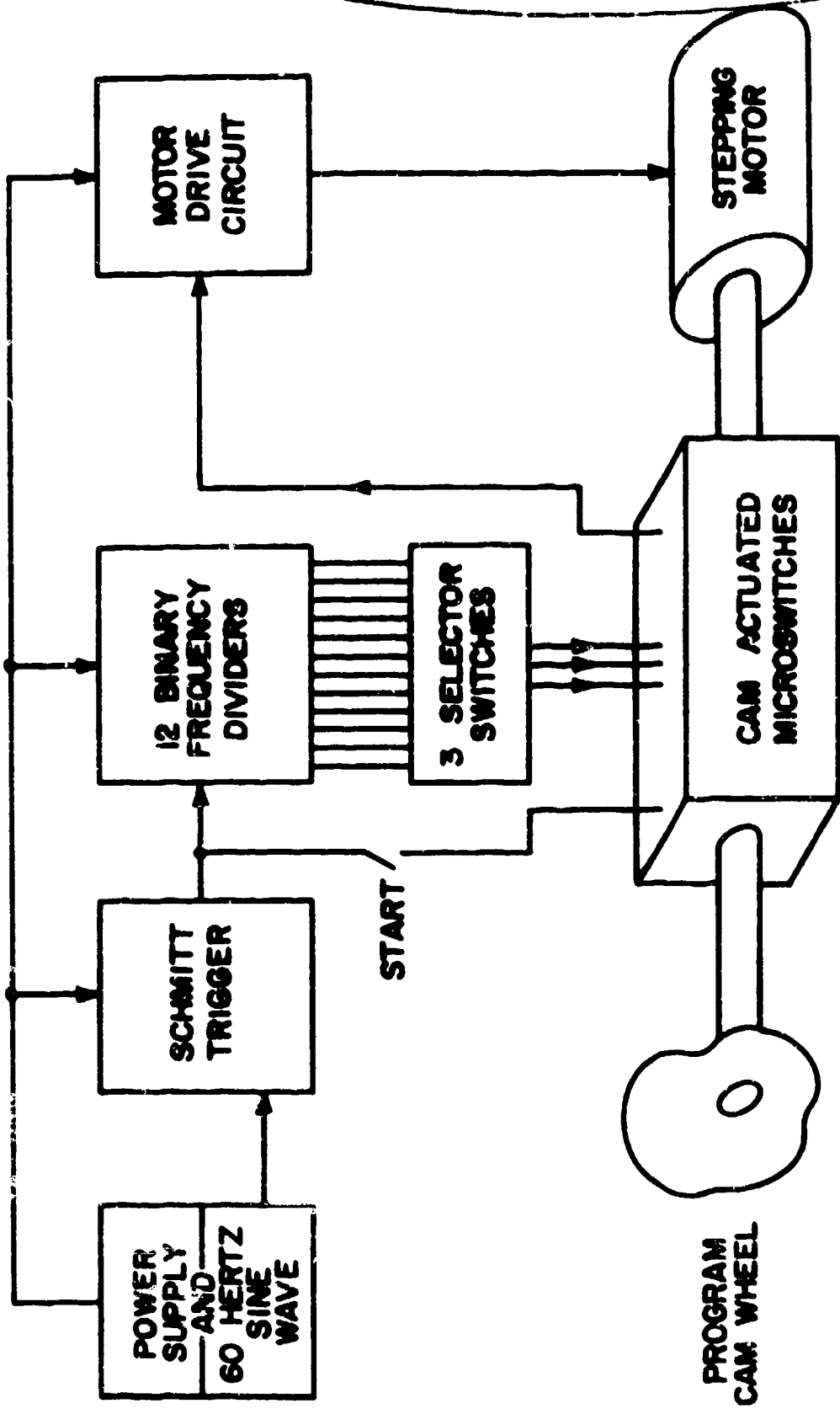
Figure 3.3   Block Diagram of Cam Drive System

the rate of rotation to change anywhere in the program. This feature permitted, for example, one time-temperature profile to contain rapid rates of temperature change lasting a few minutes as well as constant or slowly varying temperatures lasting several days.

3.2   Resistance and Temperature Measuring System

A simplified schematic of the resistance and temperature measuring system is shown in Fig. 3.4. The oscillator, V_s was set to 1000 Hz, R_s was a variable series resistor to limit the current in the sample, and R_{C1} and R_{C2} represent lead wire resistance plus any resistance of the sample up to the potential leads. A frequency of 1000 Hz was chosen because reactive effects are negligible for sample resistances encountered, and 1/f noise and 60 Hz interference are minimized. One of the two preamplifiers and the tuned amplifier were used to sense the voltage across the potential terminals of the sample, and the rectified, quasi-dc, output voltage drove a three decade chart recorder. In four terminal measurements the lead wire resistances do not influence the determination of the resistance between the potential terminals, R, and for large resistance samples where R_{C1} and R_{C2} were negligible, two terminal measurements could be used. Sample temperature was determined with a platinum - platinum + 10% rhodium thermocouple that was part of the four leads to the resistor. The dc thermal emf and the ac resistance measuring voltage were easily separated and did not influence one another.

The sense amplifier for resistance measurements is shown in greater detail in Fig. 3.5. The low impedance preamplifier consisted of operational amplifiers Al, A4, A5 and A6 and associated components. The high impedance preamplifier, using A2 and A3 with junction field effect transistor input stages and the 10 megohm feedback and input resistors of the standard differential amplifier configuration in place of Al, had a 20 megohm input impedance at the plus terminal and a voltage gain of 1. The circuit consisting of A3, the 1100 pf capacitor, and two fixed resistors plus one potentiometer is a standard variable negative capacitance circuit. Its purpose was to cancel the circuit capacitance which
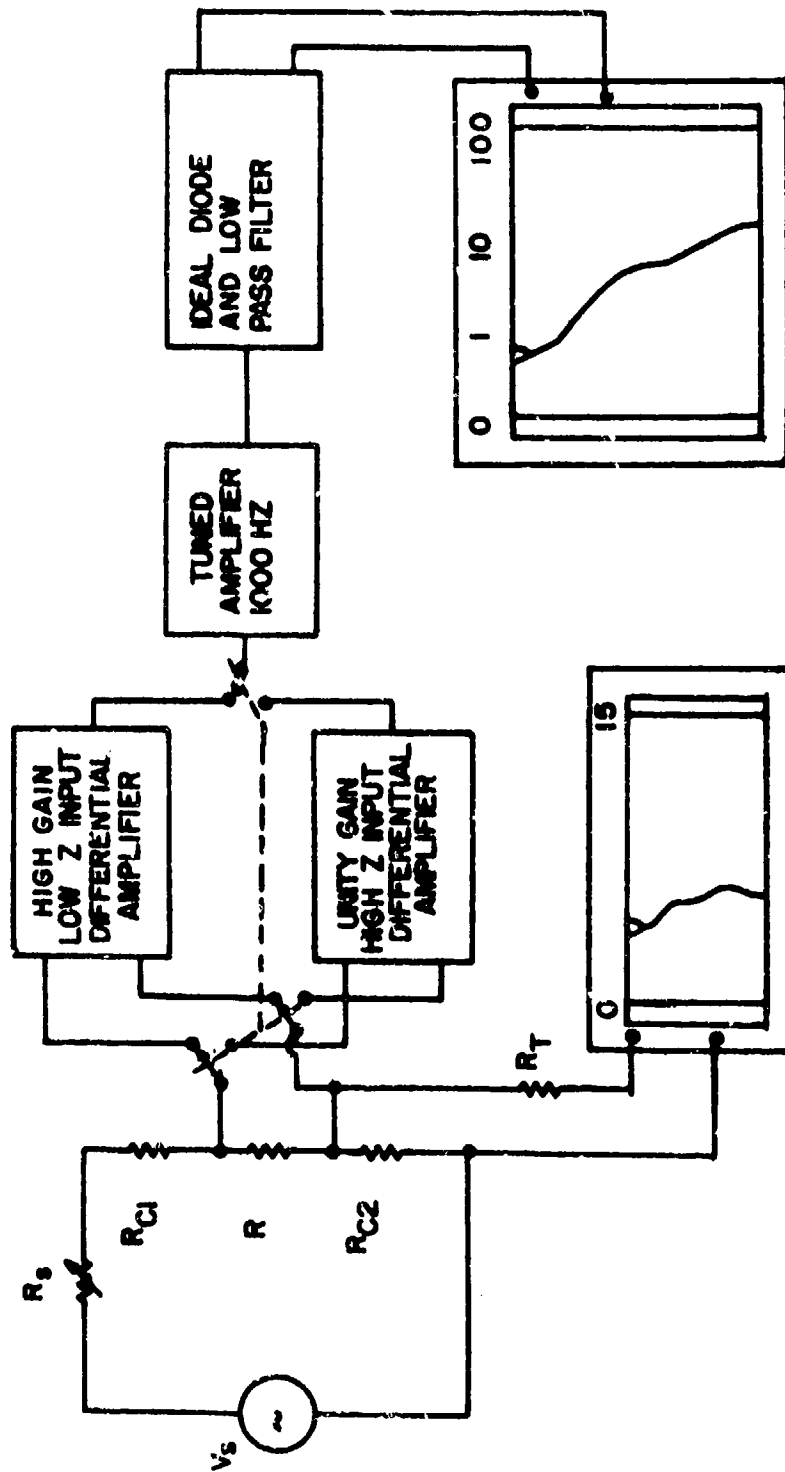
Figure 3.4   Resistance and Temperature Measuring System

43
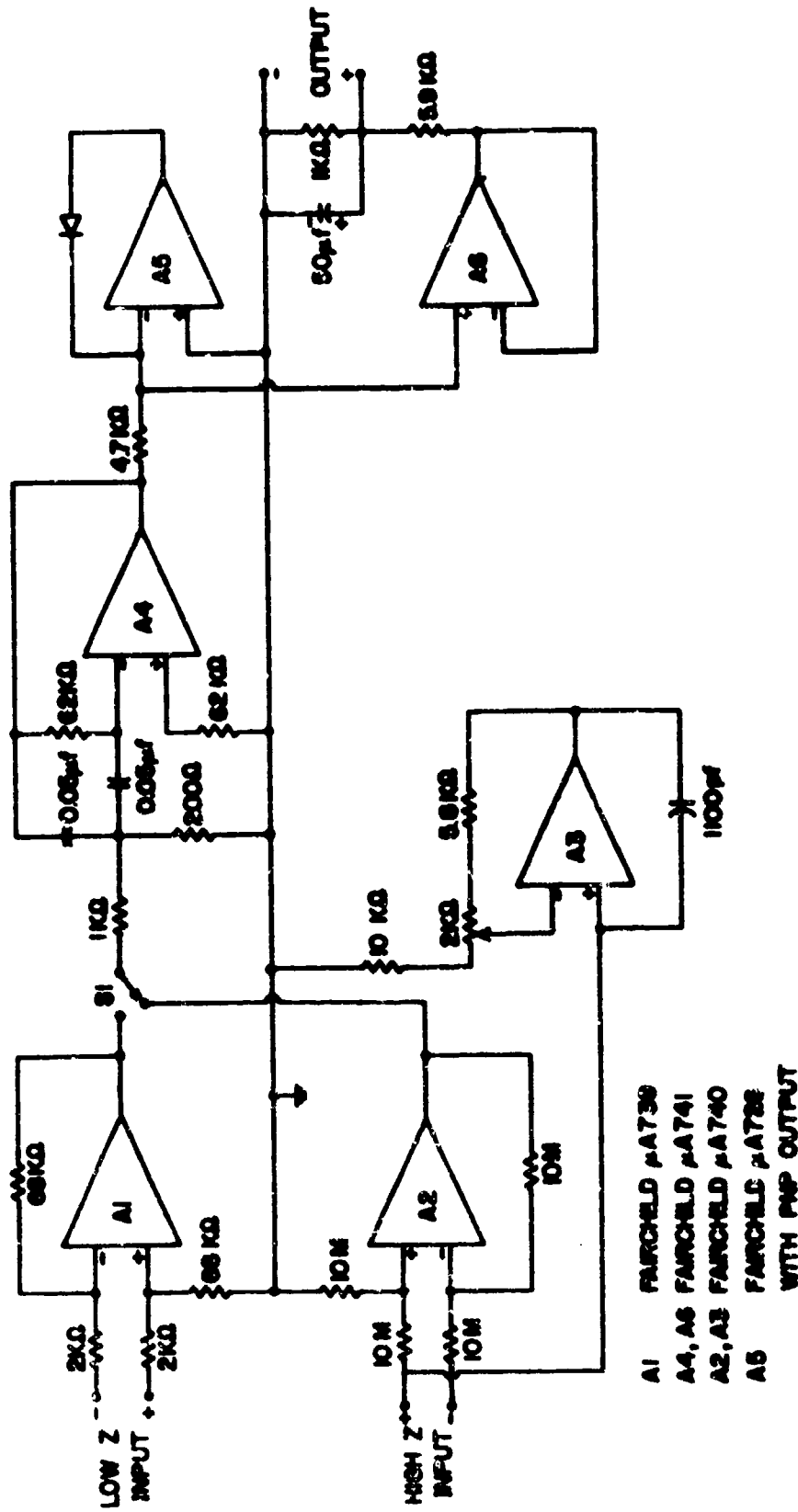
Figure 3.5   Resistance Sense Amplifier

consisted mostly of cable capacitance from the sample to the amplifier input. If the total capacitance became negative the preamplifier circuit would oscillate so the net capacitance was adjusted to + 15 pf. The reactance of 15 pf at 1000 Hz is about 10 megohms, and as long as R_S in Fig. 3.4 was less than or equal to 1 megohm this reactance caused negligible error. By considering the noninfinite impedance of the measuring circuit it was possible to make resistance measurements in excess of 20 megohms.

The value of R_S and the magnitude of V_S of Fig. 3.4 were changed depending on the sample resistance. For low resistance samples V_S and R_S were made large so that they approximated a constant current source. Under these conditions the deflection of the chart pen was directly related (proportional within each decade) to the sample resistance. When sample resistances were very large during some portion of the experiment the oscillator voltage was decreased so that the pen was on-scale for an infinite sample resistance and R_S was then selected for the best sensitivity over some range of resistance. Sample resistances were always determined by comparing them to standard resistors rather than by determining V_S and the gain of the amplifier.

3.3   Video Hot Stage Microscope

The neck growth between adjacent spherical particles during sintering and microstructure development during resistor firing were followed utilizing the modified metallograph shown in Fig. 3.6. The entire optical portion of the metallograph was inverted on the floating mounts so that the sample could be heated in an upright position and viewed from the top. The regular camera system was removed and replaced by a Sony AUC-3200 black and white video camera. A second video camera was used to monitor a digital voltmeter that measured the sample thermocouple emf and a digital clock. A Sony special effects unit was then used to mix the two video signals so that the emf and time were positioned in a corner or a side of the viewing area. All information thus obtained was recorded
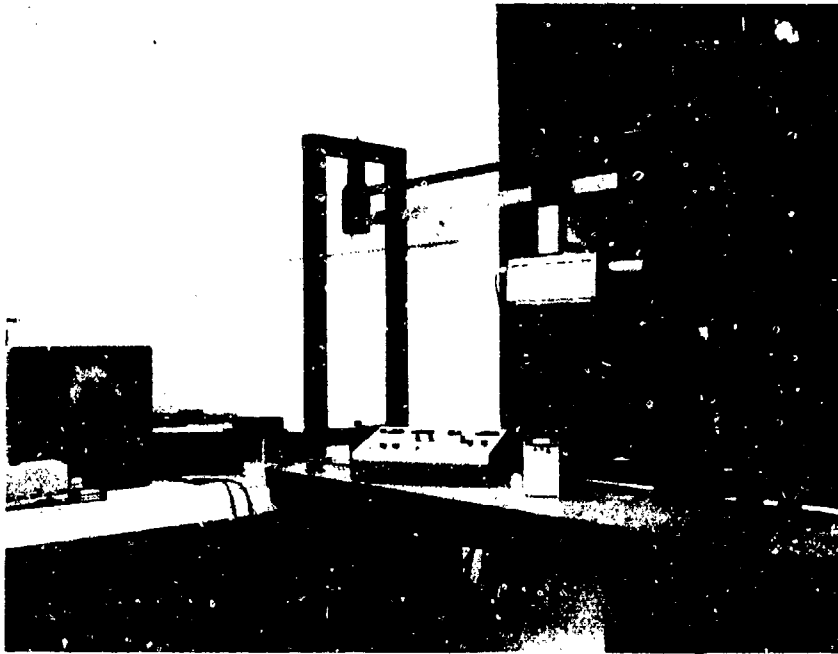
Figure 3.6   Metallograph with Video Cameras

on a Sony AV-3600 video recorder with stop frame capability, and observed on a Conrac SNA television monitor.

The hot stage unit on which the samples were heated was a Unitron MMS vacuum heating stage modified slightly as shown in Fig. 3.7. It consisted of water cooled upper and lower portions constructed of stainless steel which were bolted together and sealed with a thick rubber gasket that slightly separated the two portions; small holes in the gasket provided feed-throughs for thermocouples. The tungsten ribbon electric heater normally used in this unit was replaced by a cylindrical heater consisting of 10 mil platinum + 30% rhodium wire wound on a boron nitride core, 3/8" in diameter. This heater was positioned in the lower portion of the hot stage on a refactory base and was insulated with Fiberfrax contained in a larger refractory tube. The sample holder was a small platinum pan located on top of the boron nitride core, and platinel thermocouple leads were used to record the sample temperature. Another platinel thermocouple was positioned in the center of the boron nitride core and used to control the temperature of the furnace.

Because of the high temperatures in the hot stage, a 5 mil thick platinum foil heat shield with a 0.5 cm hole was used to cover the quartz viewing window, 16 mm in diameter and 1 mm in thickness as shown in Fig. 3.7. The shutter between the quartz window and the specimen prevented any organic material or water vapor from condensing on the quartz window during the initial heating. The shutter mechanism was a quartz plate with a 0.5 cm viewing hole that could be adjusted from outside the hot stage. The heat shield, shutter, and distance to the sample holder required a total distance of more than 5.8 mm between the sample and the objective. A special focal length lens (Vickers M-028041) with a working distance of 14 mm at 20x was used, and a Corning water cooled infrared filter was installed between the quartz viewing window and the objective.

The system was used with either reflected light or transmitted light.
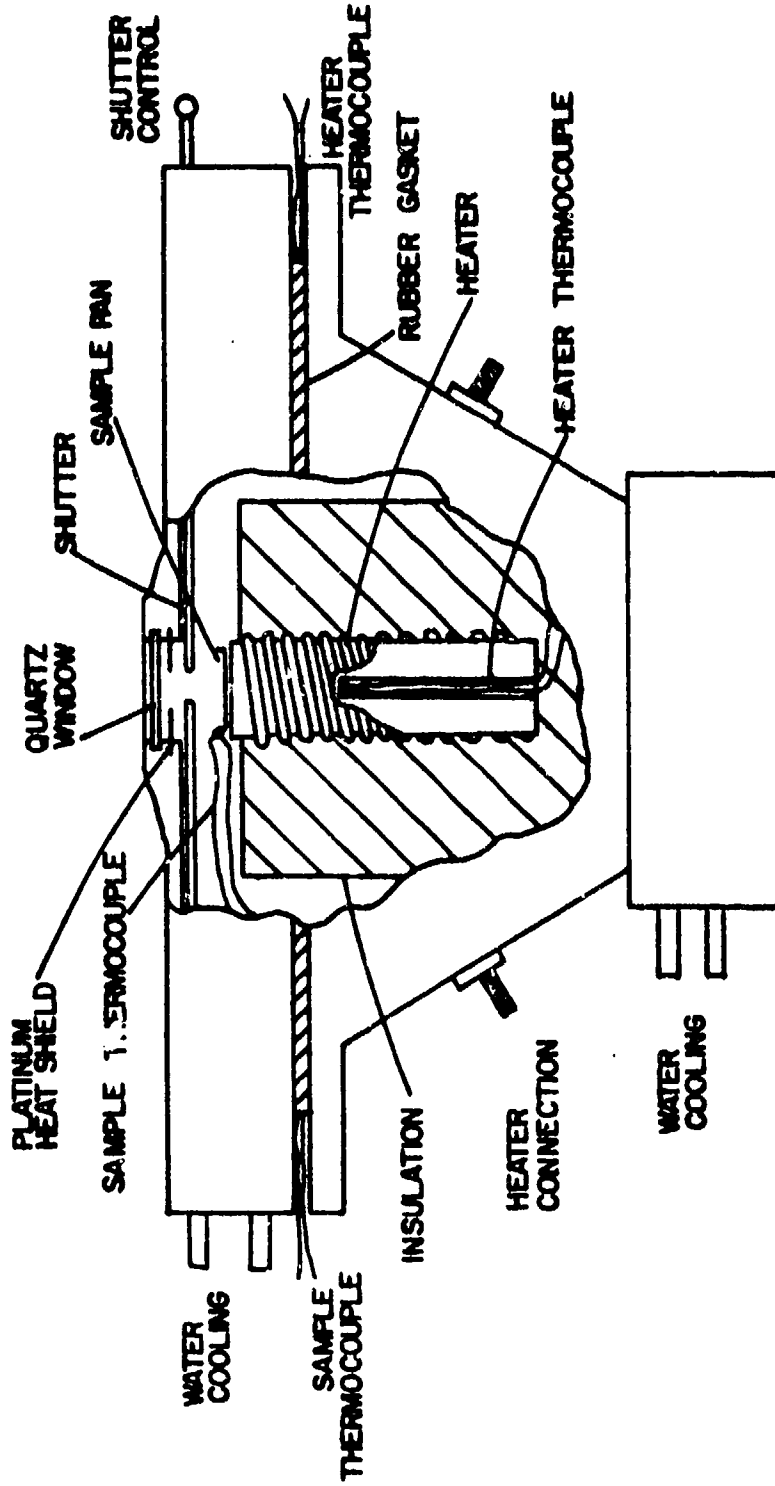
Figure 3.7   Metallograph Hot Stage

The sample was placed directly on a fused quartz tube which ran through
the hollow heater core for studies in transmitted light. The light,
focussed on the bottom end of the fused quartz tube by a system of fiber
optics from a high intensity projector lamp, was carried all the way to
the sample with little loss of intensity.

3.4   Roller Mill

An important aspect of maintaining uniformity in thick-film inks is
the uniform dispersion of the inorganic powders in the screening agent.
Although paddle wheel types of blenders are often adequate for macro
dispersion and for redispersing after settling, experience has shown that
they are usually not sufficient for microdispersion (breaking up small
agglomerations of powder held together by surface forces). To accomplish
a thorough and presumably uniform dispersion, the thick film industry has
for many years used a three-roll mill (shown schematically in Fig. 3.8).

Two of the rolls are for mixing; they rotate in opposite directions,
and are either positioned to maintain a very small spacing or are held
together under spring tension. The surfaces of the two mixing rolls move
downward at their point of contact in order to contain the volume of
material being mixed. The second roll rotates faster than the first so
that there is a shear force between the rolls that improves dispersion
over what it would be if both rolls rotated at the same rate; the greater
the shear, the better the dispersion. The third roll is called the take-
off or transfer roll. It accomplishes the removal of the mixed material
from the mill by removing it from the second roll and transferring it to
the take off blade that scrapes the ink off the roll. The third roll
rotates faster than the second roll to avoid any accumulation of material.

Commercially available three-roll mills which have the features
described above are quite expensive, and in addition, require a minimum
of several hundred ml of formulation for proper operation. To overcome
these difficulties, the three-roll mill, shown in Fig. 3.9, was designed
and constructed for laboratory formulation of research inks. Figure 3.9a
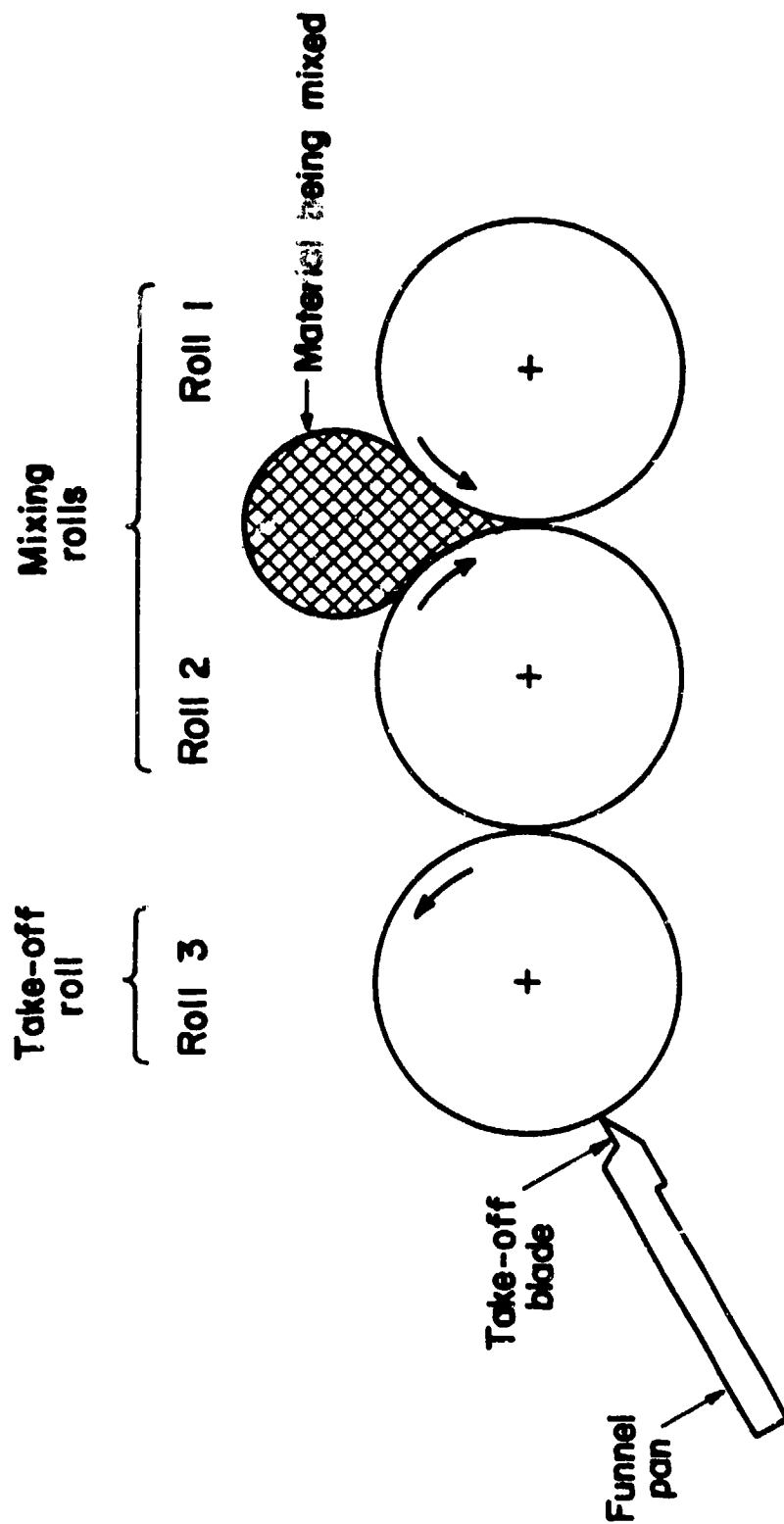
Figure 3.8   Three Roll Dispersing Mill Schematic

a. Dispersing Cycle
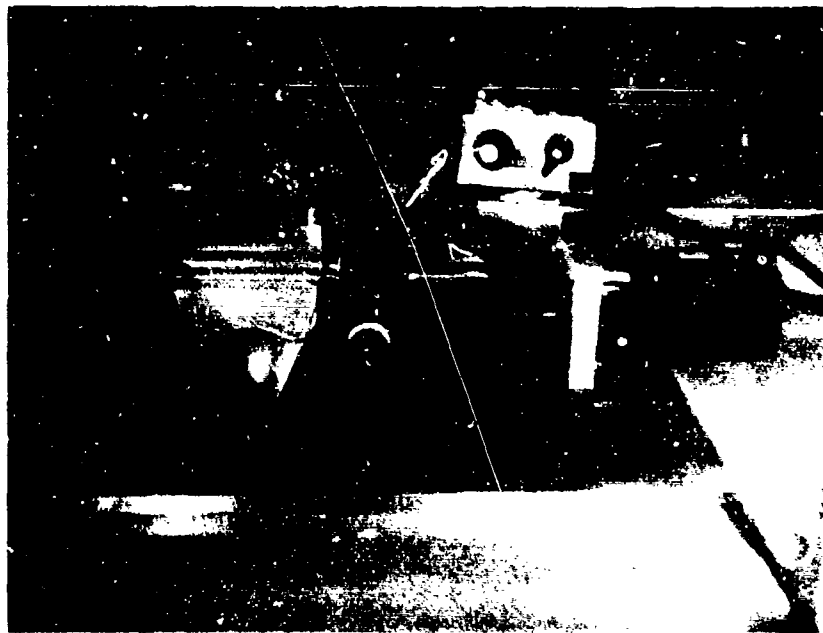
b. Take-off Cycle

Figure 3.9   Laboratory Three Roll Mill

shows a dispersing cycle using a silver-palladium conductive formulation, and the take-off cycle is shown in Fig. 3.9b. The small rolls, 1-1/4 inch diameter x 4 inch long, permitted the blending of quantities as small as 5-10 ml and up to about 50 ml. The rolls were made of type 303 stainless steel, and fitted with fused quartz sleeves so that SiO_2 was the only contaminant introduced through wear of the rolls. The spindles were mounted on modified gimble sleeve bearings that provided desirable run-out while permitting small mis-alignments during adjustment and cleaning. The two outer rolls were mounted in slide blocks that were individually adjusted as shown. The adjustment mechanism used 1/4-40 threads for micrometer adjustment and incorporated a spring drive that reduced the possibility of damage to the rolls. The gear train consisted of spindle, idler and drive gears, as shown. This design permitted the rolls to operate with any spacing from 0 to 0.25 inch (convenient for cleaning), and provided for a ratio of roll rotation of 50:150:300. This combination represented a compromise such that the first roll rotated fast enough to keep a large amount of ink on the mill, the third roll rotated slow enough that the ink would not come off due to centrifugal force, and the shear rate between the mixing rolls was sufficiently large. The drive motor was a 5-221 rpm gear motor with electronic speed control that normally operated at 200 rpm. The take-off blade and funnel pan unit and the retainer blocks between the first and second rolls were made of brass, were free to align to the rolls, and were held in place with spring mechanisms. All spindles and rolls were hollow so that rotating water couplings could be connected to permit variations in the temperature of the rolls, either hotter or colder than ambient.

3.5   Screen Printing

3.5.1   General

The purpose of this project was to study microstructure development and charge transport mechanisms in thick-film resistors; however, the printing process had to be studied to an extent sufficient to define its contribution to any observed variation in the final value of resistance.

Numerous articles [42-45] have been written concerning the parameters that influence screen printing and some have discussed specific recommendations to improve the uniformity of deposition. However, screen printing is still more art than science and the results obtained from these studies do not provide specific instructions for setting up an arbitrary printing machine so that the printing uniformity will be optimized, nor do they enable the prediction of the degree of uniformity in resistance value obtainable with optimism adjustment. Therefore, an evaluation program was undertaken to determine these two factors for the laboratory printer. The procedure was to vary one adjustment parameter at a time while all others were held as constant as possible in order tc look for minima in the standard deviation of printing performance. This is discussed in greater detail after the materials and machine are described.

3.5.2   Screening Material and Apparatus

The printing ink used for the evaluation will be described in Section 4.1.5. The viscosity at a shear rate of 1 sec $^{-1}$ was 140 Kcps and the viscosity was 17 Kcps at 150 sec $^{-1}$. These two shear rates were chosen as standardization points to maintain the viscosity of all printing inks as uniform as possible since viscosity is a source of printing variation. A nominal formulation consisted of 40 volume percent inorganic powder and 60 volume percent screening agent made with 5 weight percent N-300 ethyl cellulose dissolved in butyl carbitol (diethylene glycol monobutyl ether) solvent. Final viscosity adjustment was done with solvent content. The printer evaluation was carried out with a glass formulation screened in a square pattern, 0.435" x 0.435", onto a 0.50" x 0.50" x 0.020", 96% alumina substrate. The average thickness of the dried film was 0.00135 inch.

The screen printing machine obtained for this project was a manual version of the Aremco 3100 shown in Fig. 3.10. All motions were controlled by air actuated hydraulic cylinders, and the overall mechanical construction was adequately rigid and repeatable. The machine was adjustable with squeegee speeds of 1-10 ips, squeegee overtravel of 0-0.10 inches, and screen-to-substrate spacing of 0 (contact printing) to 0.10 inches. The machine as installed in the laboratory (Fig. 3.10b) was operated with compressed nitrogen tanks because gas pressure influences the squeegee speed. The
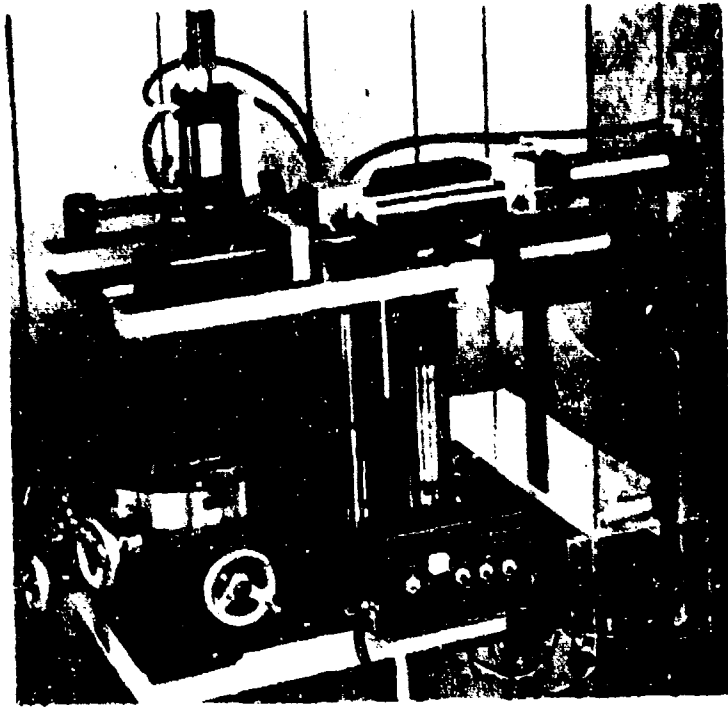
a. As Recieved
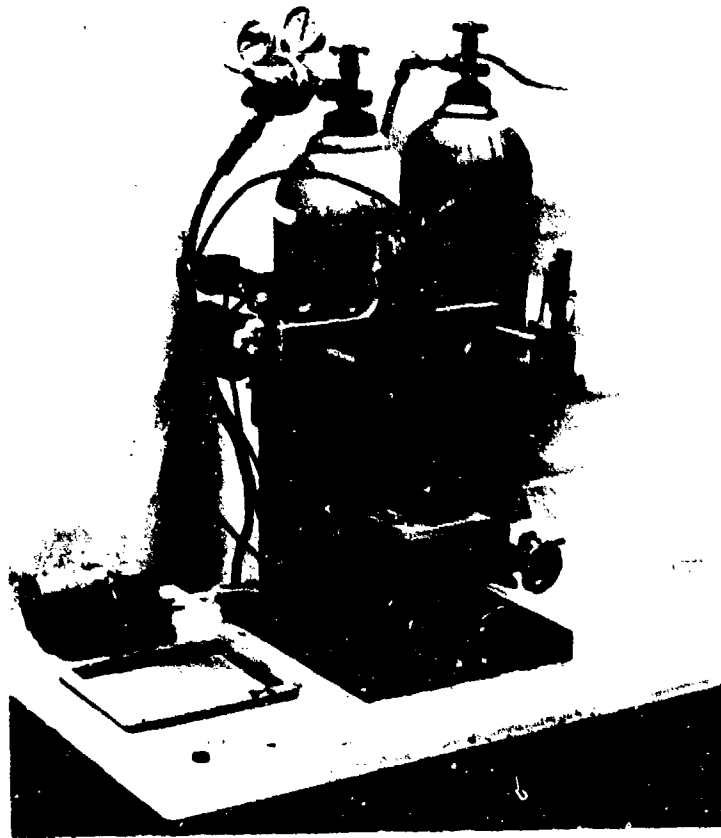
b. Installed in the Laboratory

Figure 3.10   AREMCO 3100 Screen Printing Machine

pressure was kept constant at 100 psi with a two stage regulator,
and was flow stabilized with a second gas cylinder that acted as a ballast
tank. Several minor modifications were made to the machine such as
calibrated control for the squeegee speed adjustment, microswitches for
automatic printing cycles, substrate holder, etc.

A significant modification was made in the squeegee shape. Probably
the most common squeegee shape includes a sharp printing edge and an
inclined leading surface although these two characteristics have been
obtained by a variety of different methods. Figure 3.11a shows the shape
initially selected for this project. Although the inclined leading edge
was maintained, the sharp printing edge was replaced with a 0.050 inch
flat surface parallel to the top of the substrate (screen) surface. This
feature was incorporated in order to reduce the rate of wear of the squeegee
on the screen surface and thereby produce more uniform printing over a
longer time. The basic features of the squeegee holder are shown in
Fig. 3.11b. The blat blade was held between two parallel plates with
rigid spacers that limited the compression of the squeegee blade. The
mechanism that held this squeegee assembly in the machine allowed limited
rotation on one axis so that the long printing edge was always free to
align with the screen surface.

In addition to the mechanical adjustment of the printer there are
numerous other factors which influence the results associated with the
printing operation. These other factors were held constant at the values
given in Table 3.1, and hence become boundary conditions for all subsequent
critical experiments which involve printing.

3.5.3   Evaluation

The first series of experiments dealt with the repeatability of basic
machine adjustments. It was determined that screen-to-substrate distance
and squeegee overtravel remained constant to better than ± 0.001 inch, that
there was no measurable lack of uniformity of squeegee speed near the
center of the stroke, and that the squeegee speed could be repeatably set
to ± 0.2 ips. These latter tests were performed with an electronic
counter and mechanical contacts. The testing then proceeded to the question
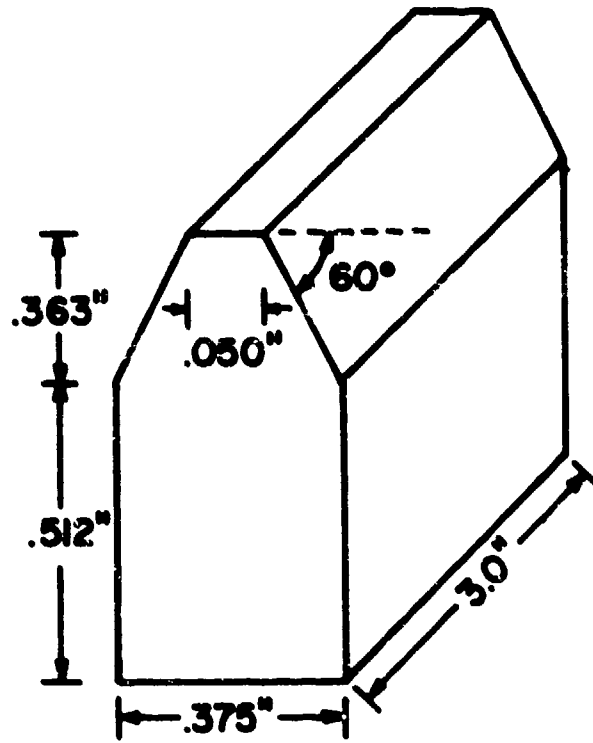
a. Squeegee Shape
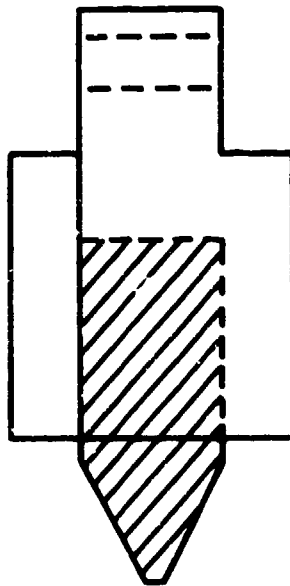
b. Squeegee Holder

Figure 3.11   Squeegee Design

Table 3.1

Boundary Conditions for AREMCO 3100

<table>
<tr><td><u>Screen</u></td><td><u>Squeegee</u></td></tr>
<tr><td>material - 304 stainless stell</td><td>material - polyurethane</td></tr>
<tr><td>mesh - 165</td><td>hardness - 70 durometer</td></tr>
<tr><td>wire diameter - 1.9 mil</td><td>angle of attack - 60°</td></tr>
<tr><td>size - 6 3/4" x 8" I.D.</td><td>print direction - forward</td></tr>
<tr><td>weave - plain</td><td>shape - see Figure 3.11a</td></tr>
<tr><td>tension - 2 to 6 lbs.</td><td>holder design - see Figure 3.11b</td></tr>
<tr><td>emulsion type - polyvinyl alcohol</td><td></td></tr>
<tr><td>emulsion thickness - 0.4 to 0.8 mil</td><td></td></tr>
</table>

of repeatable deposition of ink.

Prior studies [42-45] of the parametric dependencies of thick film screening have used criteria such as ink spread, ink thickness, ink profile, surface smoothness, and line resolution for judging optimum conditions for screening. None of these criteria are directly related to film resistance, our primary concern. The resistance (R) of a thick film resistor or conductor is given by: $R = \rho \, \ell/A$; where ρ is the resistivity of the film, ℓ is the distance between conductive electrodes, and A is the cross sectional area normal to the direction of current flow (thickness times width). The weight (W) of the same film is $W = d \, \ell \, A$, where d is the density of the ink. Combining these equations gives $R = \rho \, \ell^2 d/W$, and if the distance between conductive electrodes (ℓ) is constant, $dR/R = -dW/W$. The relative error in resistance is therefore equal to the relative error in the weight of film deposited, and the weight deposited was selected as the criterion for judging optimum conditions for screening. Errors due to a non-uniform thickness were discussed in Section 2.2, and it was assumed that the resistor was homogeneous through its thickness. To eliminate weight changes due to solvent evaporation the screened substrates were dried at 200°C for 15 minutes to remove all of the butyl carbitol. No additional weight changes to the accuracy of the measurements (0.2 mg) could be detected for drying times up to 30 minutes.

Establishing reasonable uniformity in printing was accomplished by varying the three printing machine variables: squeegee speed, squeegee overtravel, and screen-to-substrate distance. The machine was first adjusted to have a squeegee overtravel of 15 mils and a screen-to-substrate separation of 30 mils, values that preliminary printing showed to be adequate.

The squeegee speed was then varied from 3.0 in/sec to 8.5 in/sec. Table 3.2a shows the average value and the standard deviation (σ) in weight deposited. Figure 3.12a is a graphical display of these results showing percent deviation (100 σ/average weight) plotted versus squeegee speed. The graph shows an obvious (1/3) decrease in percent deviation at the higher speeds. In addition to minimizing percent deviation, it is also important that the weight deposited be independent of squeegee speed.

Table 3.2

Effect of Screen Printer Parameters on Film Weight Deposited

(a) Effect of Squeegee Speed

Squeegee Speed (in/sec)	Average Weight Deposited (mg)	Standard Deviation (σ) (mg)
3.0	10.8	0.29
5.7	11.2	0.16
7.2	11.4	0.15
8.5	11.3	0.12

(b) Effect of Squeegee Overtravel

Squeegee Overtravel (mils)	Average Weight Deposited (mg)	Standard Deviation (σ) (mg)
0	0	--
5	11.9	0.13
10	11.2	0.26
15	11.1	0.14
20	10.2	0.17

(c) Effect of Screen-to-Substrate Distance

S-S Distance (mils)	Average Weight Deposited (mg)	Standard Deviation (σ) (mg)
0	11.5	0.27
10	11.6	0.29
20	11.7	0.20
30	11.6	0.16
40	11.8	0.16
50	11.8	0.18
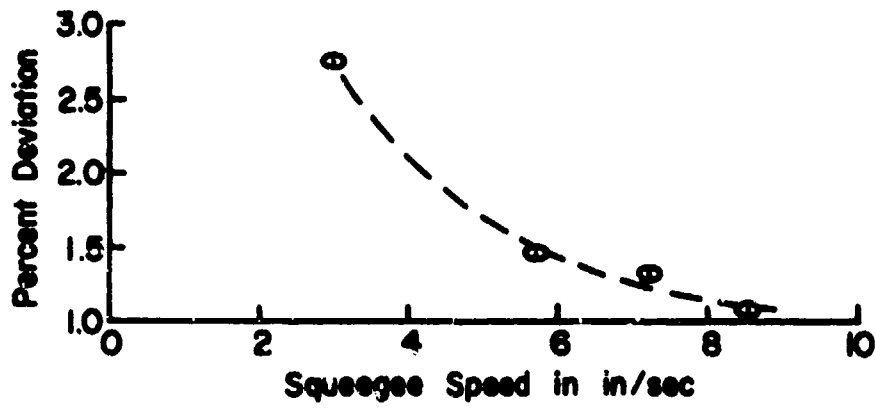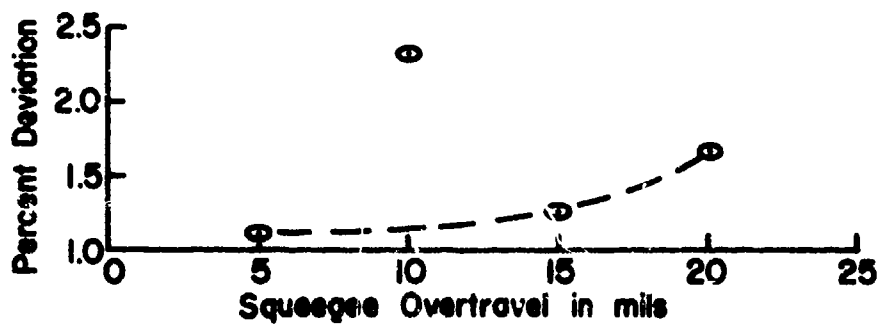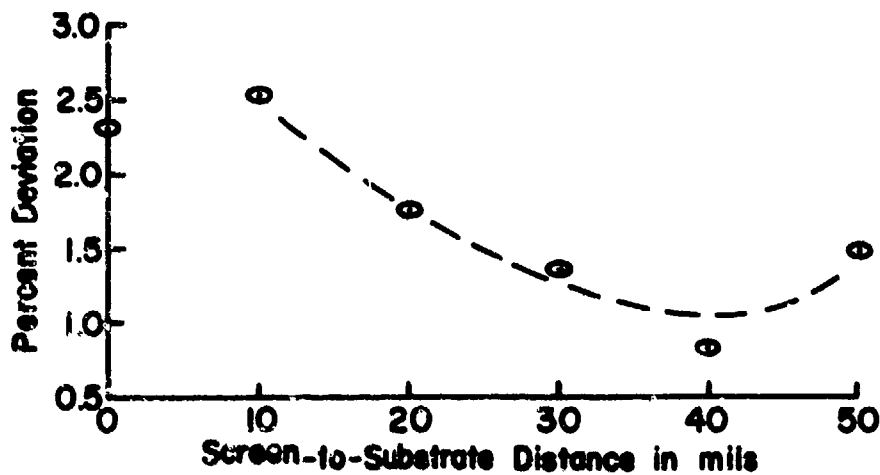
Figure 3.12   Effect of Screen Printer Parameters on
Film Weight Deposited

If this is true then the weight deposited will not vary if the squeegee speed changes slightly. As can be seen from Table 3.2a, the weight deposited was constant above 5.7 ips. Since 5.7 ips was near the center of the linear portion of the speed control adjustment, this value was chosen for further evaluation studies.

The second parameter investigated was the squeegee overtravel. Overtravel is a common industrial parameter used to specify the amount of downward pressure exerted by the squeegee during the printing operation. Zero overtravel is just sufficient to depress the screen down to the substrate and overtravel greater than zero results in the squeegee being compressed as it attempts to push the screen below the top of the substrate. The squeegee speed was set to 5.7 ips, the screen-to-substrate distance set to 30 mils, and the overtravel varied from 0 to 20 mils. Table 3.2b shows that immeasurable material was deposited at zero overtravel and Fig. 3.2b shows that percent deviation decreases with decreasing overtravel but changes very little below 15 mils (the large deviation indicated at 10 mils seems to be due to the fact that there were only six samples, one of which was relatively far from the mean.) Although Fig. 3.12b shows 5 mils overtravel to be optimum, Table 3.2b shows that the weight deposited varied as a function of overtravel at this setting. Therefore, 12 mils overtravel was chosen for further evaluation studies. Table 3.2b shows that the amount deposited was constant in this range while the standard deviation was still small. Also, the deterioration of the screen should not be too rapid at this setting.

The third parameter to be optimized was screen-to-substrate distance. The squeegee speed was set to 5.7 ips, the squeegee overtravel was set to 12 mils, and the screen-to-substrate distance was varied from 0 (contact printing) to 50 mils. Table 3.2c shows that the weight deposited was essentially constant over the range investigated, but Fig. 3.12c shows a minimum in the percent deviation at 40 mils. Thus the optimum settings determined by these experiments were:

> Squeegee Speed: 5.7 ips
> Squeegee Overtravel: 0.012 inches
> Screen-to-substrate Distance: 0.040 inches

These series of evaluation experiments were not carried out with scientific rigor. Only nine samples were used in each sample lot. The parameters could have been varied in smaller steps to obtain more date points, and after finding a tentative minimum in percent deviation the entire experiment could have been repeated, centered about the tentative minimum, as a method of fine tuning. Nevertheless, a useful scientific method has been demonstrated for systematically determining optimum adjustment and the method seems far better than the intuitive approach.

As a final test of the evaluation procedure five groups of fifty samples each were screen printed, dried, and weighed after the machine was randomly misadjusted, cleaned, and readjusted between each group. The results of these five runs were:

Run No.	Average Weight Deposited (mg)	Standard Deviation
1	11.5	0.17
2	11.3	0.22
3	11.6	0.25
4	11.8	0.23
5	11.3	0.20

Figure 3.13 is a histogram showing the compilation of all five runs along with the average and standard deviation.

The conclusions possible from the results of these experiments are that the (2σ) variations in resistance value due to the printing operation will be 4% about the mean for a single printing session and about 5% about the mean over many printing sessions. Actually, the scatter in weight deposited may have been less because the variations in weight were about equal to the accuracy of the balance; if objects of identical mass were weighed the scatter would be about the same ($\pm$ 0.2 mg).

3.6   Tunnel Kiln

The tunnel kiln utilized for thick film firing is shown in Fig. 3.14 and is schematically represented in Fig. 3.15. It was a Lindberg
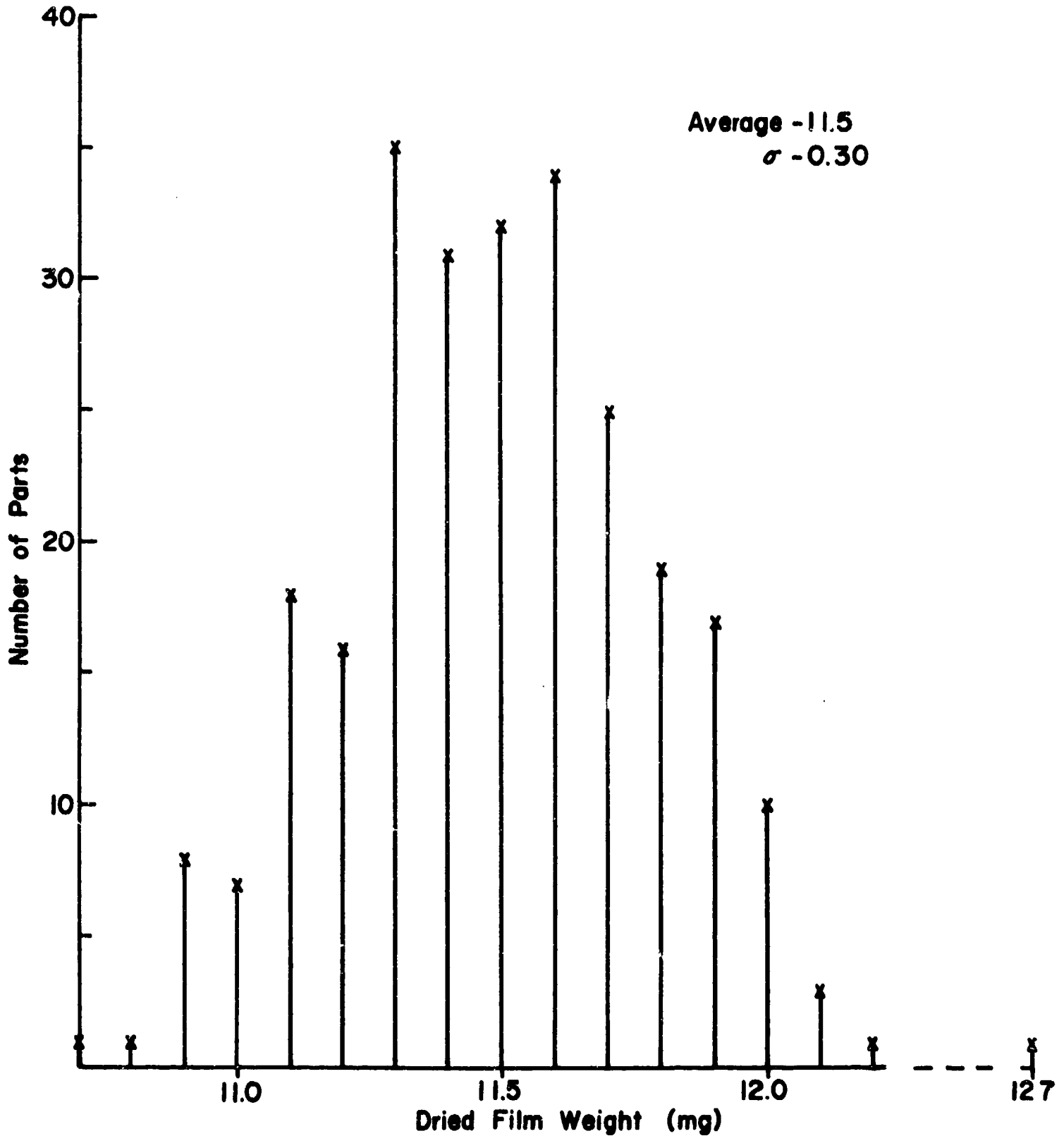
Figure 3.13   Variation of Film Weight Deposited
Over Five Runs
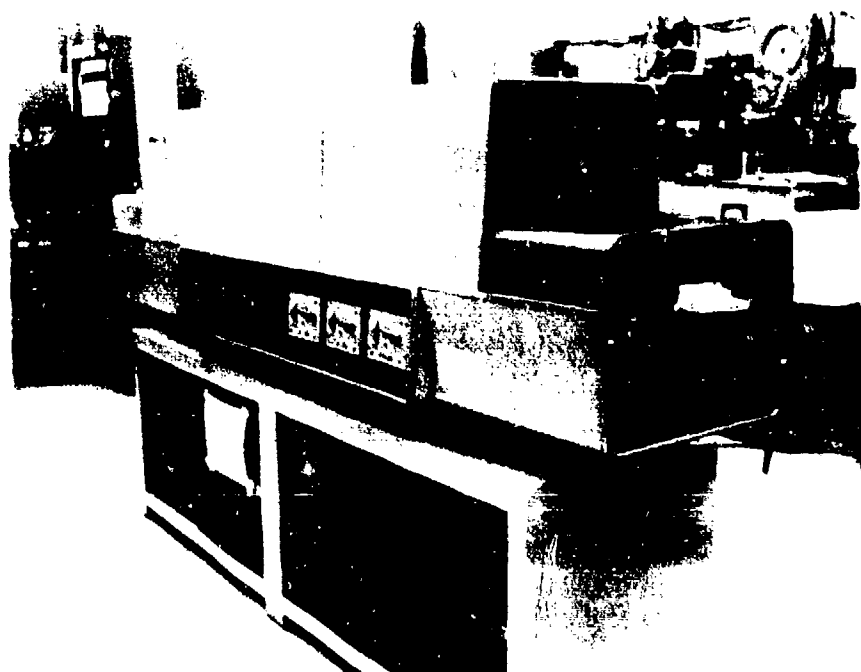
Figure 3.14   Lindberg Tunnel Kiln
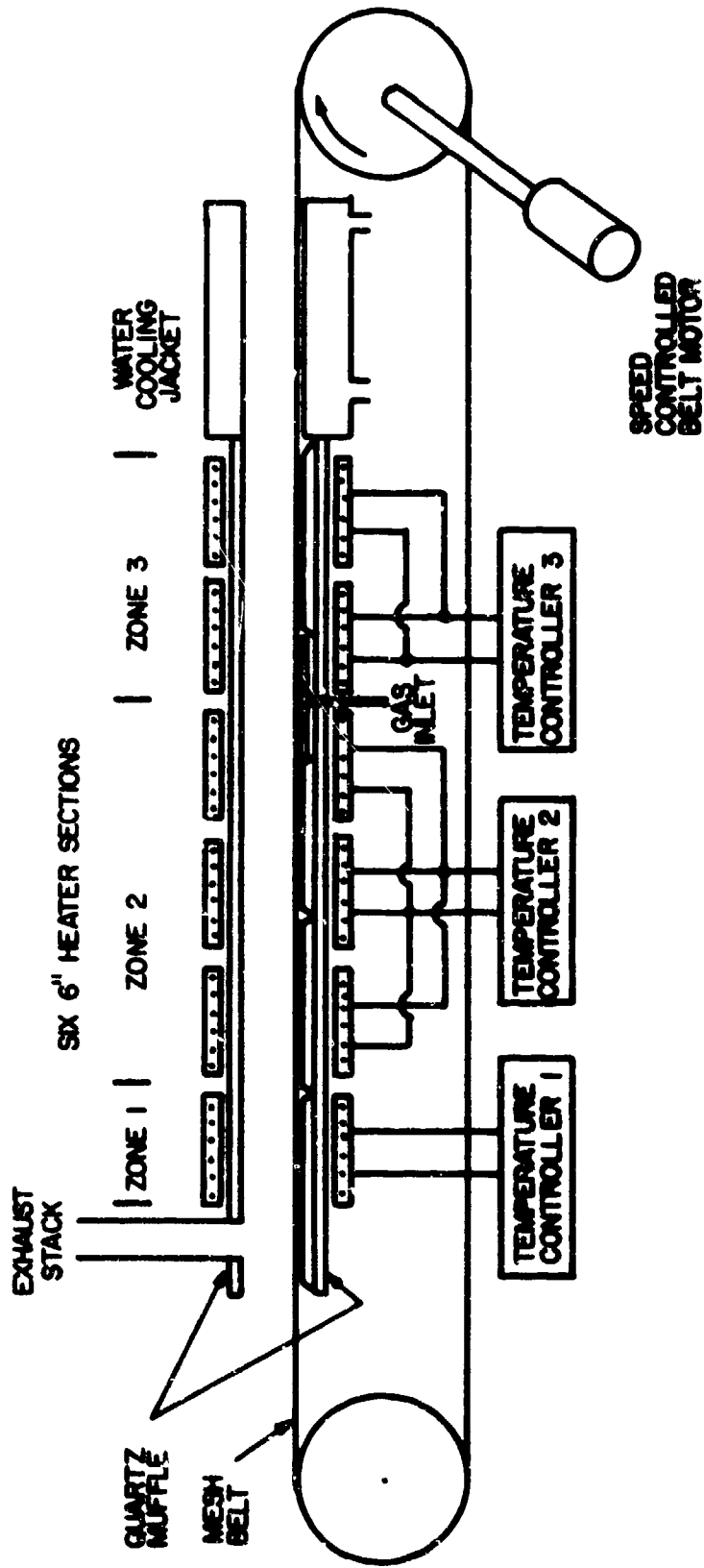
Figure 3.15   Tunnel Kiln Schematic

laboratory phototype tunnel kiln designed for thick film applications. The basic design incorporated a multiple section heating assembly, a speed-controlled belt, and an atmosphere control system.

The heating assembly had six 6 inch sections controlled by three time proportioning temperature controllers adjustable from 200 to 1200°C. The heater sections could be connected to the controllers in any combination. For application to this project the first zone contained one section, the second zone three, and the third zone contained two. Over-temperature protection was provided by a control mater relay driven by a thermocouple that could be installed in any of the six heating elements. The three inch square cross-section fused quartz muffle was used because it would not be a source of contamination and was transparent to infra-red radiation. The output end of the kiln contained a 24 inch long water cooled inconel jacket to cool the substrates to room temperature before exiting the kiln.

Substrates were carried through the kiln on a 2 inch nichrome mesh belt driven by a speed controlled DC motor that could maintain constant belt speeds from 0.3 to 11 inches/sec. Parts were removed by a gravity operated ramp which delivered the parts to a box mounted at the end of the kiln.

The atmosphere could be controlled in the quartz muffle and water cooled jacket by introducing gas beneath the belt between the second and third zones. The atmosphere was contained in the kiln by adjustable openings in the two ends of the kiln and exhausted at the adjustable venting stack. Gas flow rate could be adjusted by a flow meter.

The standard profile established for the kiln was chosen so as to fire 10% RuO_2-glass resistors to a minimum in resistance with a belt speed that was in a convenient and dependable range. Figure 3.16 shows the temperature versus distance profile as determined with an 18 gauge chromel-alumel thermocouple wired to the belt, and Fig. 3.17 shows the variation of room temperature resistance versus belt speed using this profile. A minimum in resistance value is observed at 4.3 inches/min. Previous experiments had determined that resistance value scatter at the minimum was small and, therefore, had the smallest sensitivity to small changes in belt speed. Figure 3.18 shows the temperature versus time
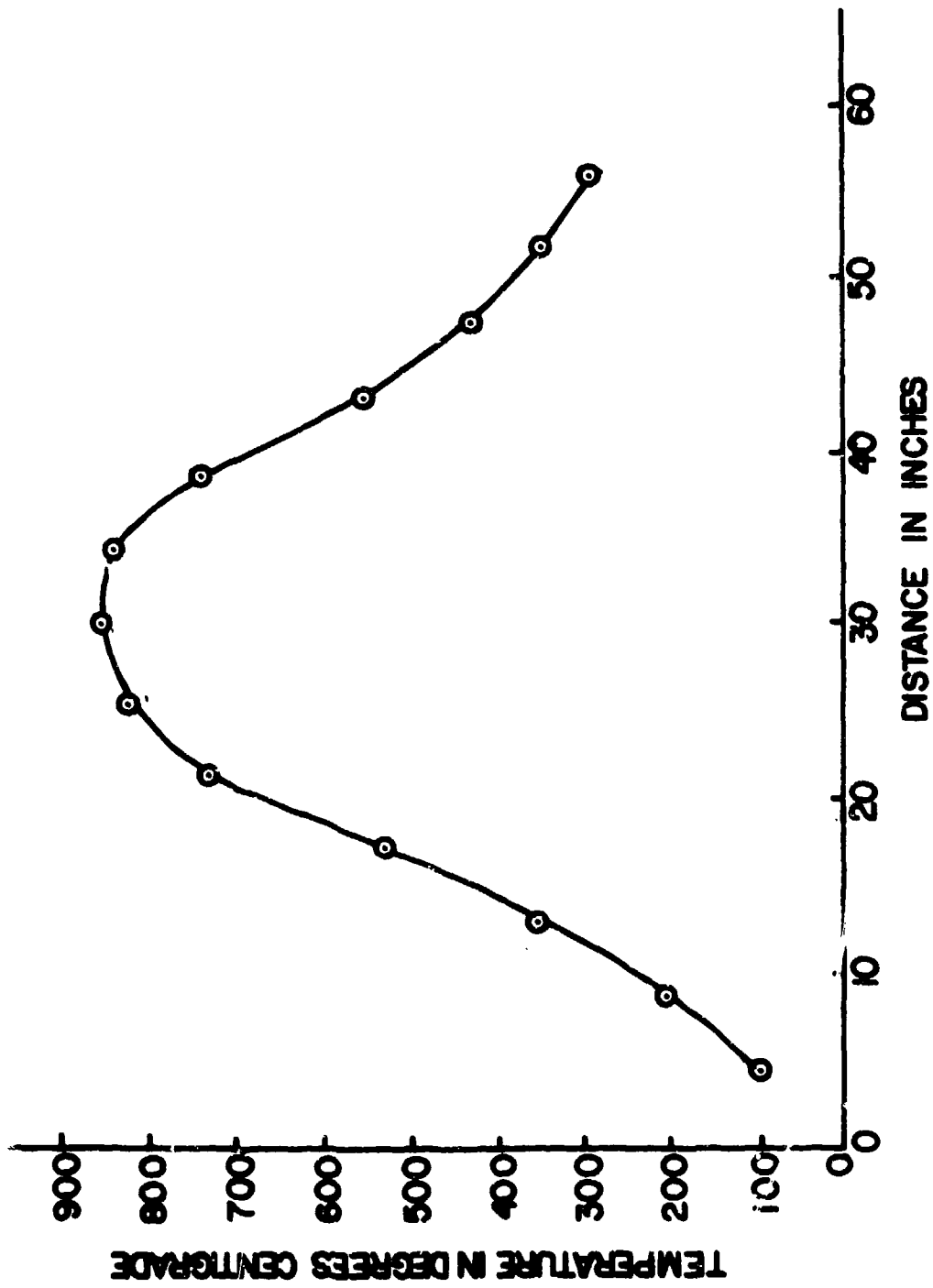
Figure 3.16   Tunnel Kiln Temperature Gradient
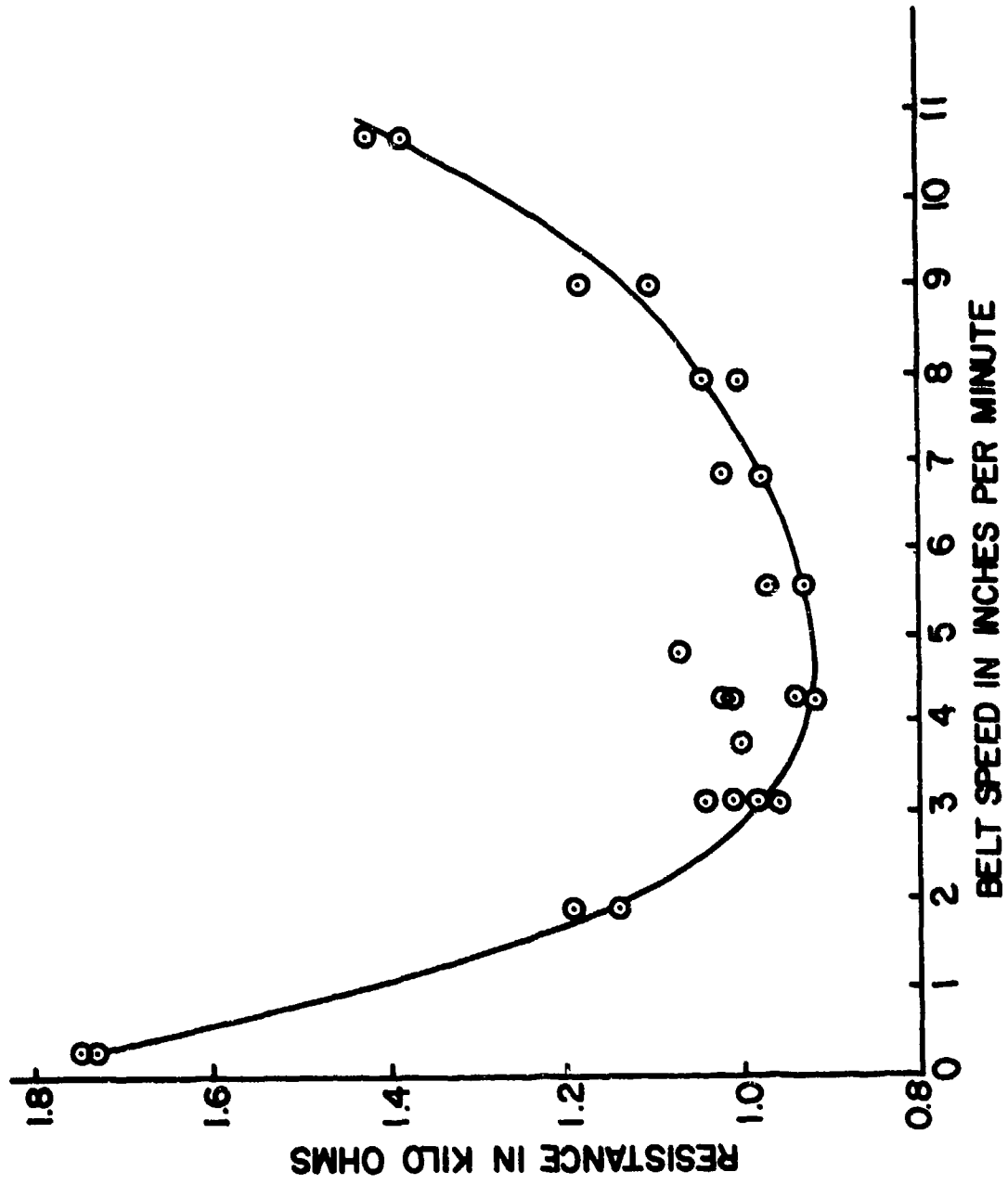
Figure 3.17   Resistance Versus Belt Speed
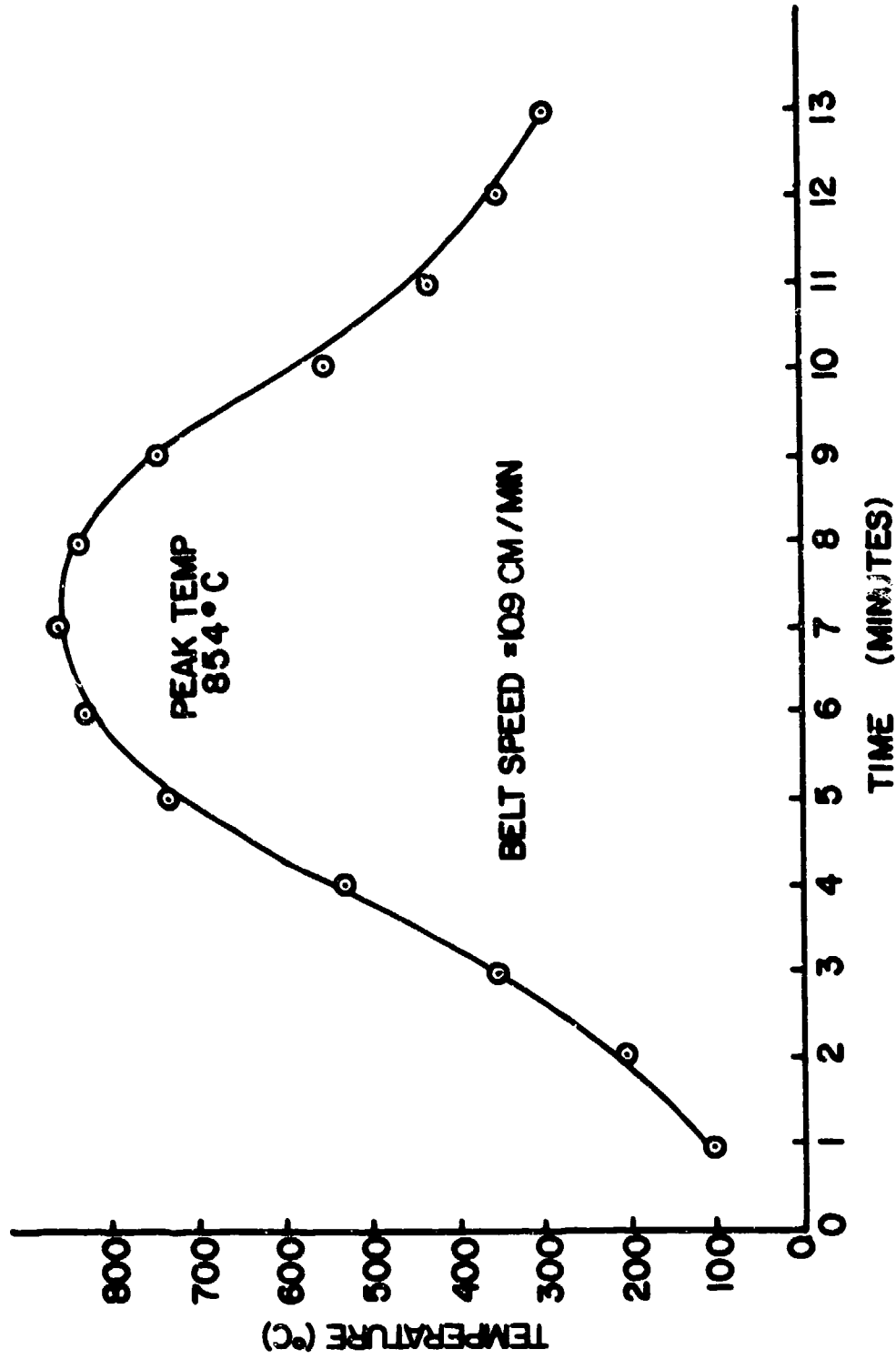
Figure 3.18   Standard Time-Temperature Profile

profile corresponding to the 4.3 inches/minute belt speed; seventy-two substrates fired in random small samples had an average value of 984±3.0 Ω. The profile shown in Fig. 3.18 was chosen to determine the blending curve for the end member pastes, and was used for all standard resistor firings in this project.

SECTION 4
Experimental Results

4.1   Characterization of Ingredient Materials

To maintain the greatest simplicity in all resistor experiments the number of ingredient materials was limited to five; alumina substrate, lead borosilicate glass, platinum conductive paste, ruthenium dioxide, and screening agent.

4.1.1   Substrates

The ceramic substrate chosen for this work was 96 percent alumina. This material was selected because it is common to thick film technology, it seemed adequate for all experiments, and it was low in cost. More specifically, the substrates are made from AlSiMag 614 alumina and have a shape commonly referred to as the 12 pin SLT substrate. The substrates were supplied by the American Lava Corporation with the permission of the IBM Corporation. This shape substrate (0.5 x 0.5 x 0.060 inches) seemed well suited to the experiments; the area dimensions of the substrate were large enough for all samples and were compatible with the substrate fixture of the furnace. The substrates were thicker than typically used throughout the industry. A more typical thickness might be .020-.025 inches, but the thicker substrates had a higher transverse thermal conductance that promoted more uniform temperatures in the linear gradient of the furnace. The thicker substrate also made it possible to form a recessed area in the center of the substrate to be filled with glass for certain experiments. Table 4.1 lists the manufacturer's published characteristics of AlSiMag 614 alumina. To further characterize the material a chemical analysis was

Table 4.1 Thermophysical Properties of AlSiMag 614, 96% Al_2O_3

Property	Unit		
Water Absorption	%		0 Impervious
Specific Gravity	---		3.70
Hardness	Moh's Scale		9
	Rockwell 65 N		78
Thermal Expansion Linear Coefficient	Per °C	25-300°C	6.4×10^{-6}
		25-700°C	7.5×10^{-6}
		25-900°C	7.9×10^{-6}
Tensile Strength	Psi	Kg/cm^2	25 000	1 760
Compressive Strength	Psi	Kg/cm^2	375 000	26 360
Flexural Strength	Psi	Kg/cm^2	46 000	3 230
Resistance to Impact	Inch-lbs.	Meter-Kg	7.0	.081
Modulus of Elasticity	$Psi \times 10^6$	$Kg/cm^2 \times 10^6$	47	3.30
Shear Modulus	$Psi \times 10^6$	$\nu\_/cm^2 \times 10^6$	19	1.34
Poisson's Ratio	---		.22

Thermal Conductivity	25°C	BTU in./ hr. ft^2 °F	cal. cm./sec. cm^2 °C	244	.084
	300°C			119	.041
	500°C			75	.026
	800°C			58	.020

Dielectric Strength 60 Hertz AC Test Discs 1/4" thick	volts per mil	kilovolts per mm	210	8.3

Volume Resistivity	25°C	Ohm-centimeters	$>10^{14}$
	100°C		2.0×10^{13}
	300°C		1.1×10^{10}
	500°C		7.3×10^7
	700°C		3.5×10^6
	900°C		6.8×10^5

		25°C	300°C	500°C	800°C
Dielectric Constant	1 MHz	9.3	9.5	10.8	22.4
Dissipation Factor	1 MHz	.0003	.0027	.0131	.0911
Loss Factor	1 MHz	.0028	.0257	.1415	2.041

obtained with the results shown in Table 4.2.

An average coefficient of thermal expansion such as given in Table 4.1 is insufficient to establish the influence of thermal stress on resistor performance. Therefore, the expansion of the AlSiMag 614 was measured as a function of temperature, and the results are shown in Fig. 4.1.

Procedures were developed for cleaning the substrates and firing to constant weight (within the ability to weigh, about $\pm$ 0.2 milligrams). Two basic methods of cleaning were tested; one using hot acid baths and the other using a detergent, in both cases followed by rinsing and drying. A comparison, based on visual observations, subsequent weighing and firing steps, and discussions with industrial personnel involved with cleaning alumina substrates for thin film circuits indicated that the proper use of a good detergent is adequate and less troublesome than the use of acids. The procedure selected was to ultrasonically clean with a warm detergent solution, rinse repeatedly in increasing purities of water, rinse in reagent grade methanol or isopropyl alcohol and dry for twenty minutes at 250°C. Fortunately, the cleaning requirements of the substrates are lessened by the nature of their manufacture. The high temperature firing required to form the substrates either volitilizes any contaminants or allows them to diffuse into the surface where they can no longer be removed by cleaning, and they are usually handled carefully after firing (nylon gloves, etc.). In fact, the method of cleaning recommended by one substrate supplier is to fire at a temperature greater than 900°C for at least 30 minutes. However, when preceeded by adequate chemical cleaning and drying at 250°C, no further weight or visual appearance changes were observed if the substrates were subsequently fired to a high temperature.

4.1.2   Glass

4.1.2.1   Composition

A lead borosilicate glass having a composition of 63% PbO, 25% B_2O_3, and 12% SiO_2 by weight was chosen as the standard glass for this work for the following reasons:

Table 4.2 Chemical Analysis of AlSiMag 614 Substrate

Element	ppm(wt)
Ba	20
Fe	500
Mn	5
Mg	6000
Na	2000
Ga	200
Ni	5
Ti	200
Li	10
Cr	10
Sn	<10
Cu	<5
Co	<5
Mo	<10
U	<10
Zr	<30
K	1000
Ca	1500
Si	10,000
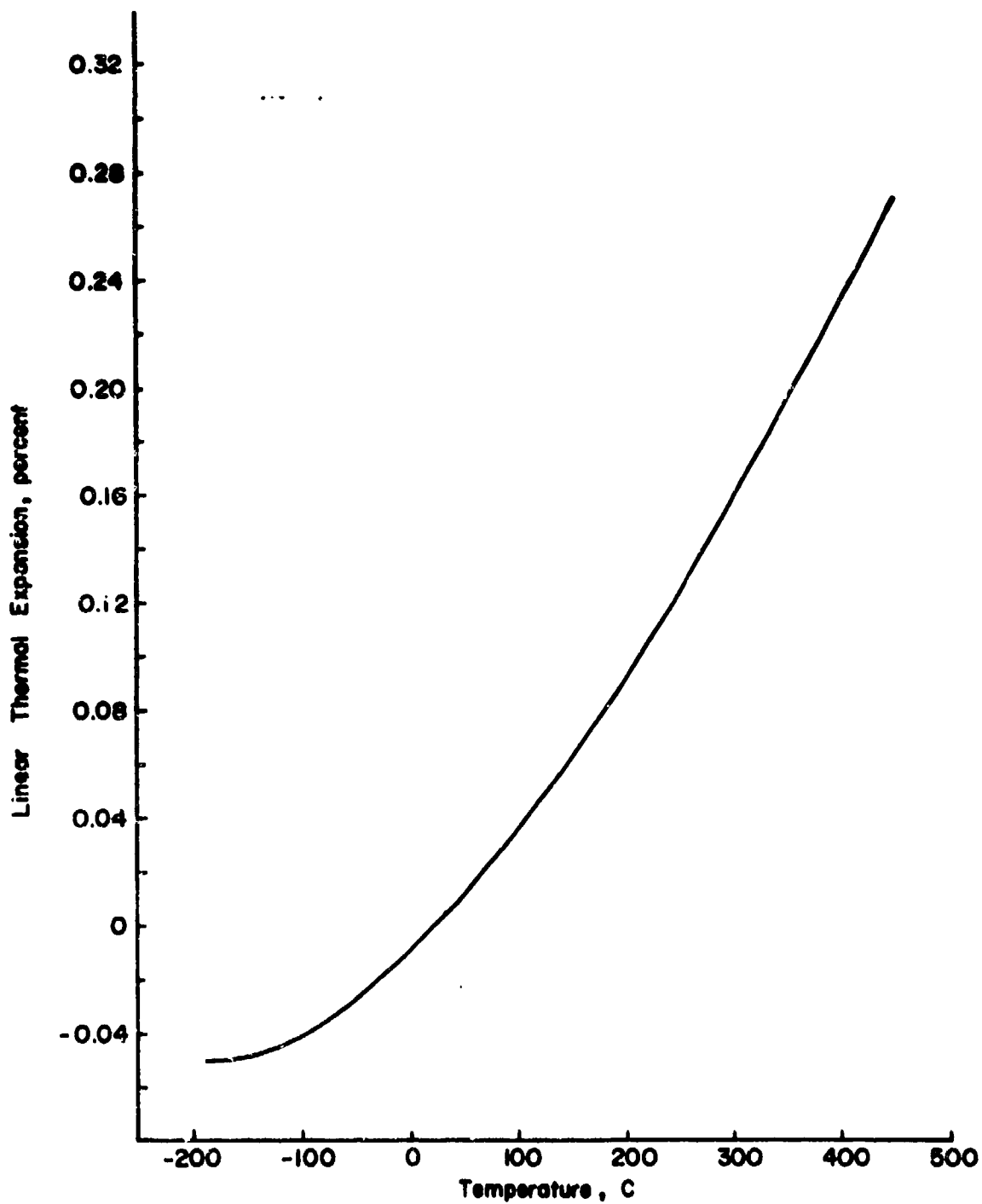
Figure 4.1   Thermal Expansion of AlSiMag   4 Substrate

1. It is known that this glass plus RuO_2 will produce good resistors.
2. It has a low softening temperature (~450°C).
3. The physical properties of the lead borosilicate glass system have been rather thoroughly studied.
4. It is possible to vary the coefficient of thermal expansion by varying the ratios of the three ingredients.

In addition to the 63-25-12 glass, seven glasses with different compositions were required for certain experiments involving thermal stress. Inorganic mixtures containing the constituents in the desired proportions was obtained from Owens-Illinois, Toledo, Ohio. These extremely fine and well dispersed mixtures were heated slowly (<1°C/minute) in platinum crucibles to 1000°C and fritted in distilled water. The composition, annealing point and softening point for each of these glasses is given in Table 4.3. The boron and silicon concentrations were determined by wet chemical analyses, and the lead contents were obtained by difference. Very little uncertainity is introduced by this approach because the glasses were of quite high purity as evidenced by the mass spectrographic analysis (Table 4.4). The glasses were ground in a vibratory agate (99% SiO_2) ball mill, and a sample of the 71-25-4 glass was analyzed for major constituents both before and after grinding (-325 mesh) in order to determine if any pick-up of SiO_2 occured. The 71-25-4 glass was chosen because it had the lowest silica content and hence would be most sensitive to contamination. The results shown in Table 4.3 indicate an increase of 0.03 w/o SiO_2, but this is within the accuracy of the analytical technique. The annealing and softening points given in Table 4.3 were estimated from DTA records supplied with the glasses by Owens-Illinois.

4.1.2.2   Thermal Expansion

The expansion vs. temperature of the standard 63-25-12 glass was measured and the results are shown in Fig. 4.2. The thermal coefficient of linear expansion from room temperature to 300°C calculated from these data is 6.96 x 10^{-6}/°C. The contraction at about 350° is partially due to the force of the measuring system.

Table 4.3

Composition and Properties of the Glasses

Glass	PbO(w/o) (calculated)	B_2O_3(w/o)	SiO_2(w/o)	Softening Point (°C)	Annealing Point (°C)
71-25-4 (unground)	71.05	25.0	3.95	420	510
71-25-4 (-325 mesh)	71.0	25.2	3.98	---	---
50-10-40	51.0	10.0	39.0	440	750
60-10-30	59.9	10.2	29.9	436	580
81-10-9	80.6	10.2	9.2	360	500
76-10-14	75.8	10.2	14.0	390	530
55-10-35	55.6	10.0	34.4	440	700
63-25-12	62.8	25.2	12.0	440	520
71-10-19	70.9	10.1	19.0	420	530

Table 4.4

Mass Spectrographic Analysis of 71-25-4 Glass

Element	ppmw	Element	ppmw
Li	0.02	Y	≤ 0.05
B	High	Zr	0.3
F	< 0.3	Ru	< 0.3
Na	10.	Rn	<15.
Mg	< 4.	Pd	< 0.2
Al	70	Ag	3.
Si	High	Cd	2.
P	0.2	Ba	0.5
S	2.	La	≤ 0.2
Cl	2.	Ce	≤ 0.2
K	1.	Ta	< 0.2
Ca	6.	Os	< 0.3
Sc	< 0.2	Ir	< 0.2
Ti	0.2	Pt	3.
V	< 0.07	Hg	< 0.3
Cr	1	Tl	1.
Fe	10.	Pb	High
Ni	0.5	Bi	100.
Cu	1.	Th	< 0.2
Zn	1.	U	< 0.4
Ga	< 1.		
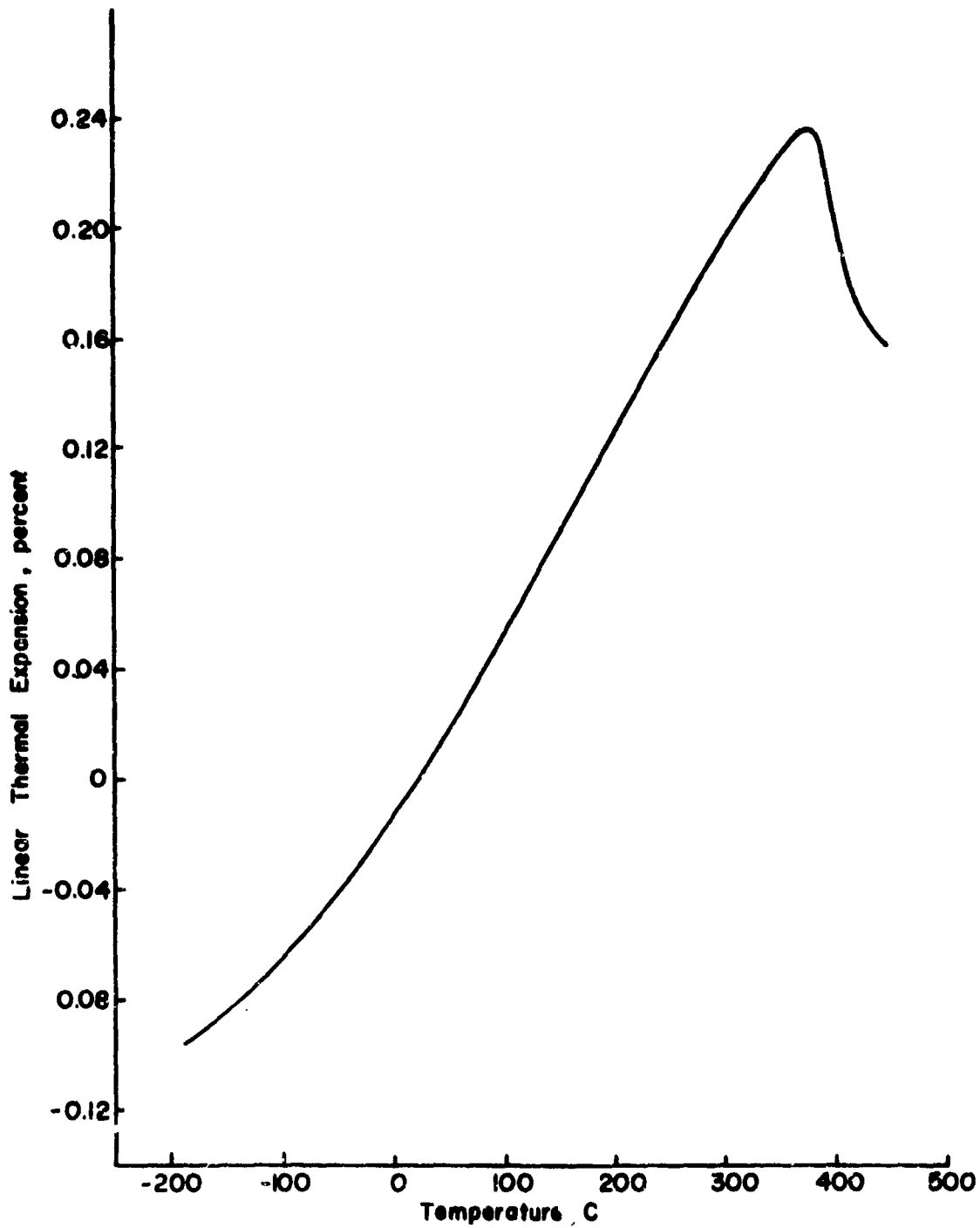
Figure 4.2   Thermal Expansion of 63-25-12 Lead-borosilicate glass

4.1.2.3   Viscosity

High temperature viscosity measurements wer^ carried out on the standard 63-25-12 glass oy the sphere methou [46], which required measuring the rate of movement of a ball in the molten glass. Gold was chosen as the material for the ball because it does not oxidize at the temperatures of study and there is little reaction between gold and the glass. A gold ball 0.86 cm in diameter was prepared by casting the molten gold in a bullet mold.

The apparatus for the measurement of viscosity is shown in Fig. 4.3. The gold ball was suspended by a thin platinum wire from the sample pan of an automatic recording microbalance*. The balance had an accuracy and resolution capability of about 5 μg and an automatic range of 0.1 g. The signal from a linear variable differential transformer whose output was proportional to the beam displacement was amplified and recorded on a strip chart recorder. The chart recorder was calibrated to measure the displacement of the ball in the glass directly as a funtion of time. In this mode of operation full scale on the chart recorder (25.4cm) corresponded to 1.04 mm travel of the ball. A platinum crucible 3.8 cm in diameter and 3.8 cm deep was filled with the glass, placed on a ceramic support and centered in a vertical cylindrical furnace that could be raised or lowered by a lab jack. The temperature of the glass was measured by a chromel-alumel thermocouple placed in contact with the bottom of the crucible. The temperature measured by this thermocouple was found to deviate from the temperature of the glass melt by $1 - 4°C$ over the temperature range of the experiments.

The furnace was heated to the required temperature and sufficient time was given for thermal equilibrium to be reached. Then the furnace was raised until the gold ball was completely immersed in the glass. At this stage, the motion of the ball in the molten glass was initiated by adding weights to the tare weight pan or removing them. Force versus velocity data were calculated from the distance versus time plot obtained at each temperature and plotted for both upward and downward motion of the ball.

*Ainsworth, Inc., Englewood, Colorado.
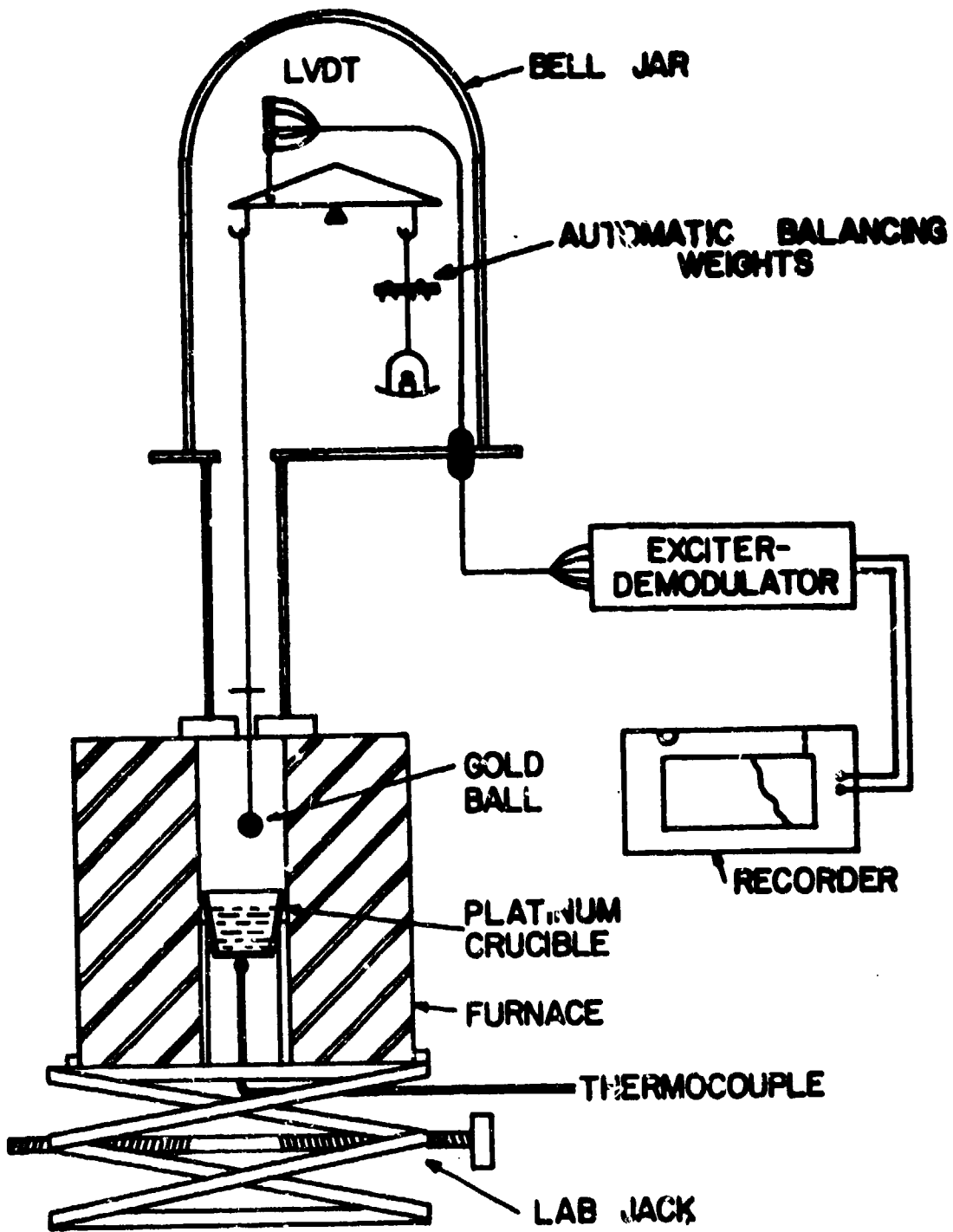
Figure 4.3   Viscosity Apparatus

These plots were straight lines and the slopes were very close in both
the cases. The average of the two slopes was used to calculate the
viscosity directly using the formula [46],

$$\eta = \frac{S_1 \ g \ F}{3 \pi d_1}$$ (4.1)

where S_1 is the average of the slopes from the force versus velocity
plots (g/cm/s), g is the gravitational constant (980 dynes/s), Fa is the
Faxen correction factor

$$[1 - 2.104 \ \frac{d_1}{D_1} + 2.09 \ (\frac{d_1}{D_1})^3 - 0.95 \ (\frac{d_1}{D_1})^5 \ ], \quad d_1 \ \text{is}$$

the diameter of the sphere and D_1 is the diameter of the crucible. In
order to check the accuracy of the experimental method, the viscosity of
a Brookfield standard (Fluid 100,000) was measured and compared with the
reported value of 953.5 poise. The measured value of 1069 poise was
within 12.1%.

The viscosity results are shown in Fig. 4.4. The plot of the logarithm
of viscosity versus reciprocal temperature for the lead borosilicate glass
is linear over the temperature range studied confirming the anticipated
exponential temperature dependence of viscosity. The activation energy
calculated from the slope of the plot is 81 ± 2 kcal/mol. Extrapolation of
this plot gives the softening temperature, i.e. the temperature at which
the viscosity of the glass is $10^{7.6}$ poise, to be 537°C.

4.1.2.4   Surface Tension

The modified dipping cyclinder method [47] was used to study the high
temperature surface tension of the glass. Platinum was selected as the
cylinder material as it neither oxidizes nor reacts with the glass over the
temperature range studied. The cylinder was 1.3 cm in diameter and 1.3 cm
high with a wall thickness of 0.13 mm. The apparatus for the measurement
of surface tension was similar to that shown in Fig. 4.3. The cylinder
was suspended by a platinum hang down wire from the sample pan of the
microbalance (see Fig. 4.5). After the glass reached the required tempera-
ture, the crucible was raised until the bottom of the platinum cylinder was
below the surface of the glass. The crucible was then slowly lowered and
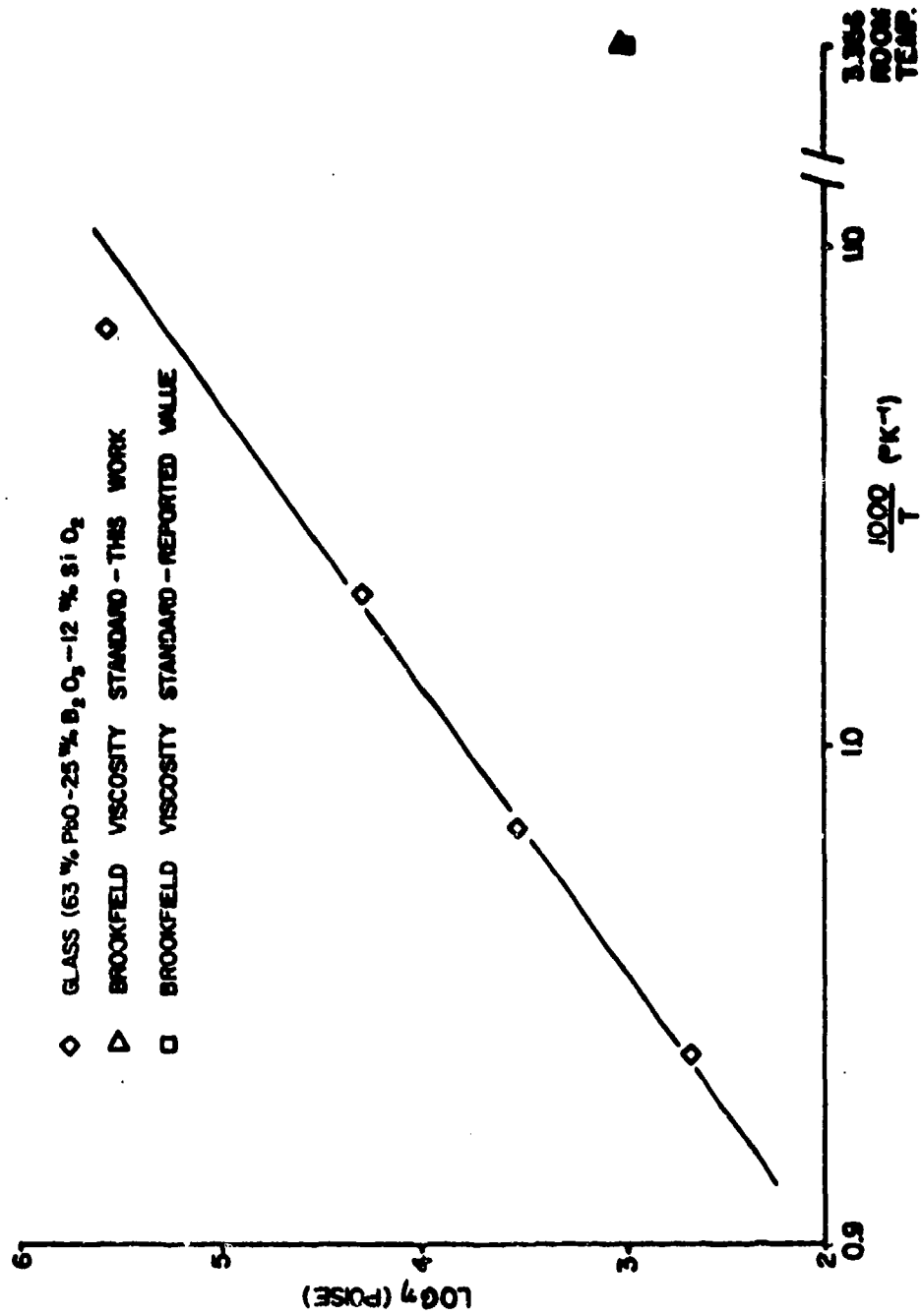
Figure 4.4   Temperature Dependence of Viscosity of
Lead Borosilicate Glass

5 MIL PLATINUM WIRE
TO THE BALANCE

PLATINUM
CYLINDER.

PLATINUM
CRUCIBLE

FURNACE

THERMOCOUPLE

LAB JACK
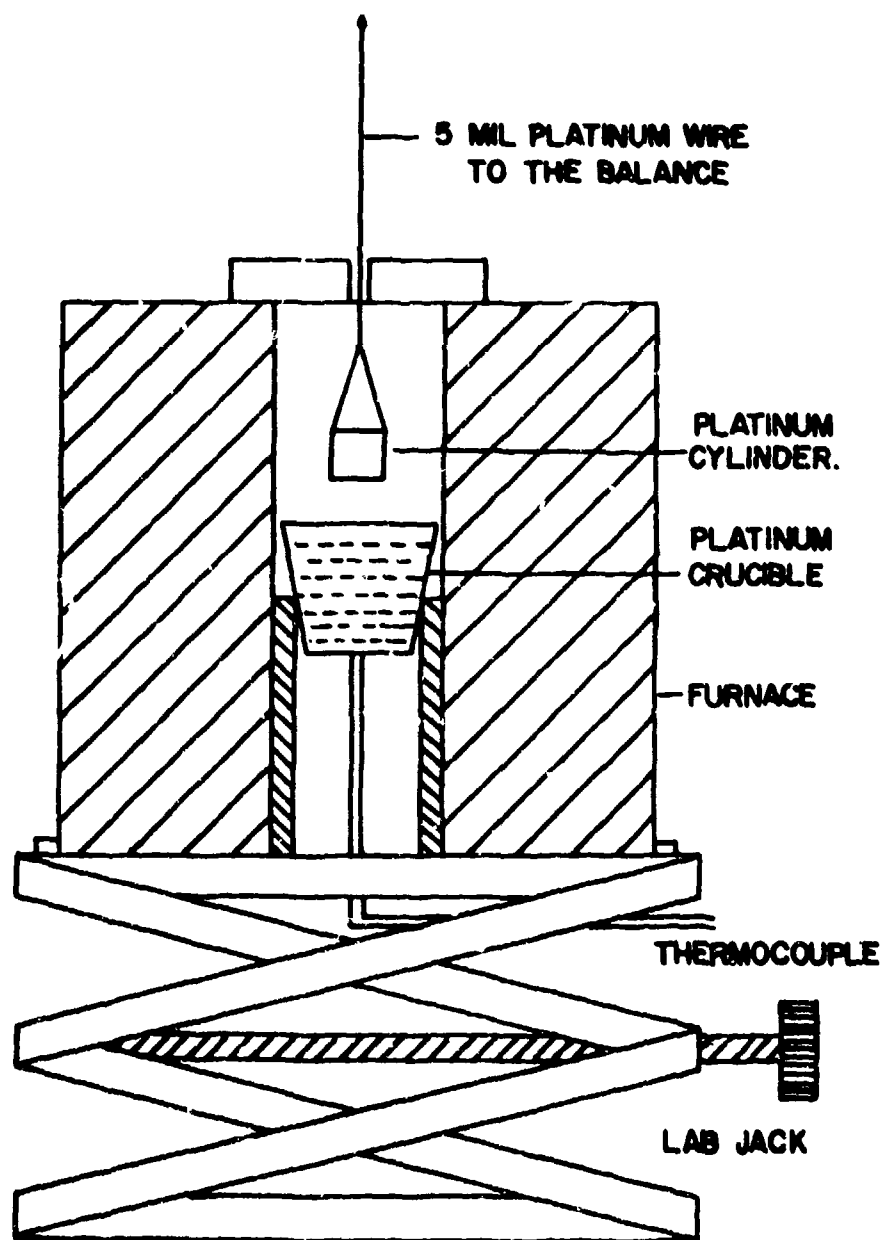
Figure 4.5   Surface Tension Apparatus

the maximum downward force on the cylinder caused by the surface tension of the glass before breakaway was recorded. After the cylinder had separated from the glass, the weight of the cylinder and any glass retained on the rim of the cylinder was substracted from the maximum force before breakaway. This gave the maximum pull exerted on the cylinder, W_{max}, that was used to calculate the surface tension of the glass by the following equation [48].

$$\gamma = \frac{g\ W_{max}}{4\pi R} \left[1 - \frac{2.8284\ \delta_2}{\sqrt{h_1 R}} - \frac{0.6095\ \delta_2}{R} + \frac{3\delta_2^2}{h_1 R} + \frac{2.585\ \delta_2^2}{R\sqrt{h_1 R}} + \frac{0.371\ \delta_2^2}{R^2} \right] \quad (4.2)$$

where γ is the surface tension of the glass (dynes/cm), h_1 is given by $W_{max}/\pi R^2 d_2$, g is the gravitational constant (980 dynes/s), W_{max} is the maximum pull exerted on the cylinder, d_2 is the density of glass, R is the mean radius of the cylinder and $2\delta_2$ is the thickness of the cylinder. The density of the glass at each of the experimental temperatures was estimated by extrapolating the low temperature expansion date (Fig. 4.2).

Preliminary measurements were conducted on a 85.08 w/o PbO - 14.92 w/o SiO_2 glass to verify the experimental technique by comparing the observed data with previously reported surface tension values for similar glasses. The results of the surface tension measurements are shown in Fig. 4.6. The surface tension of the 85.08 w/o PbO - 14.92 w/o SiO_2 glass is consistent with the values reported for similar glasses [48]. The surface tension of the lead borosilicate glass increases with decreasing temperature, especially below 700°C. Such a negative temperature coefficient of surface tension has been reported for PbO - B_2O_3 glasses containing 50-80 w/o PbO [48].

The effects of surface tension were demonstrated on a qualitative but dramatic level during resistor firing experiments. Several samples, particulary those with 5% RuO_2 content, when fired to high temperature developed a characteristic at the interface of the resistor and conductor that consisted of a noticably reduced thickness and reduced content of RuO_2. An example of this is shown in Fig. 4.7a in which the relative lack of the dark RuO_2 is obvious from the photomicrograph. The reduced thickness
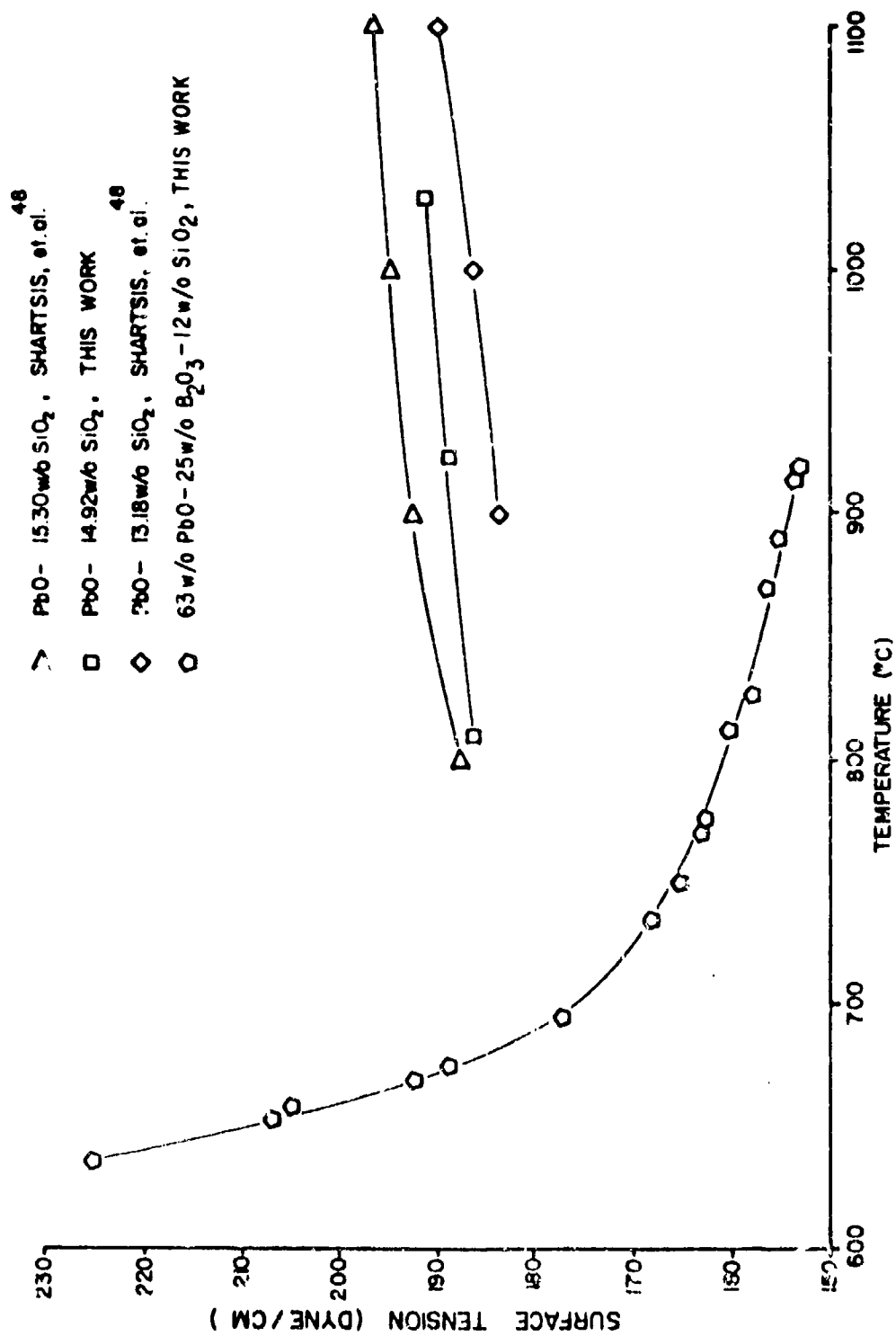
Figure 4.6   Surface Tension of Lead Silicate and
Lead Borosilicate Glasses

86
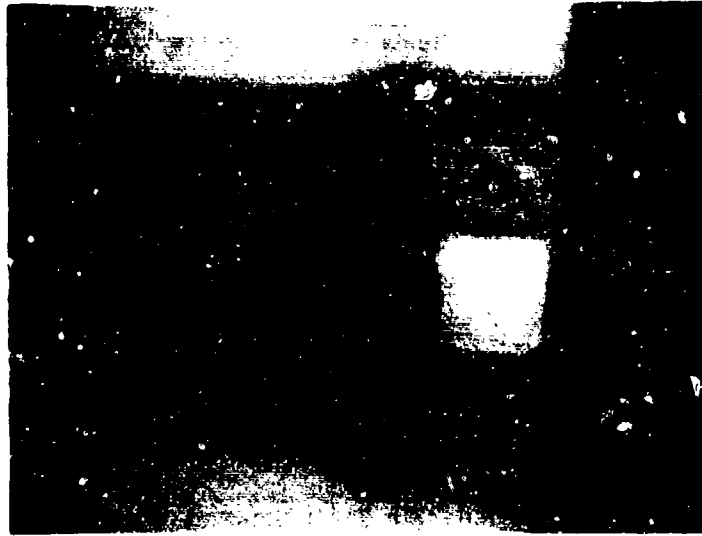
a. Resistor-Conductor Interface
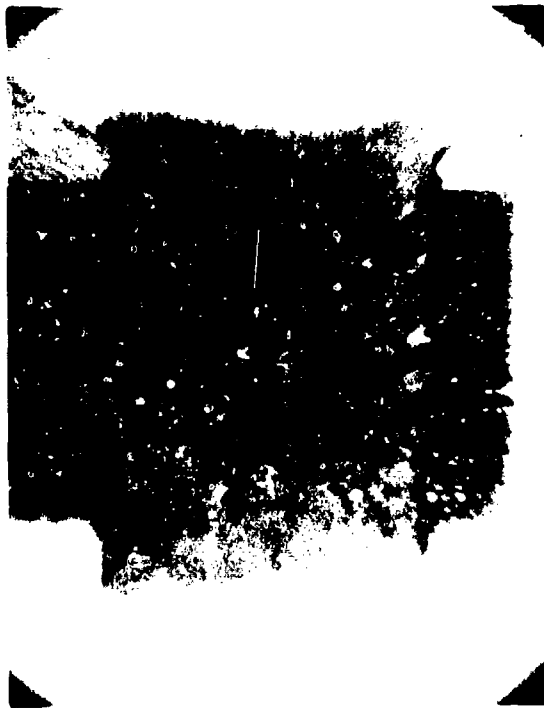
b. Addition of Bi_2O_3
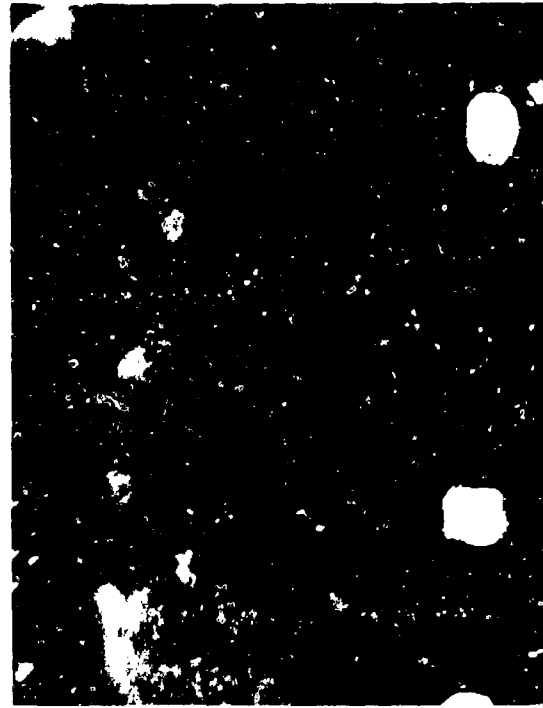
c. Addition of Bi_2O_3

Figure 4.7   Effects of Surface Tension on Resistor Formation

is apparent from direct visual observation and was verified with a
profilimeter. This phenomena produced a severe problem because samples
would appear to be open circuited or very high in resistance when the
bulk of the resistor was otherwise normal. The depletion of glass at
the interface is related to the affinity of the conductor paste for the
glass. This can be seen in Fig. 4.7a where the glass has diffused much
farther into the conductive than it has across the surface of the substrate.
The initial dimension of the resistor can be seen by the black area on
conductive; the RuO_2 does not propagate through the conductive.

The reduced concentration of RuO_2 at the interface must be due to
some phenomenon in addition to the diffusion of glass into the conductive
because the opaqueness is less than can be explained by the reduced
thickness of the glass. In addition to platinum the primary ingredient in
the paste is Bi_2O_3 (see Table 4.5) which acts as a flux to improve
adhesion. It is a glass former not present in the resistor glass and
could, therefore, affect the properties of the resistor glass.

Figure 4.7b and c show the effect of adding Bi_2O_3 to the surface of
a resistor. The quantity added was not weighed but it was a particle
about 0.3 mm in diameter. The large dark area near the left edge of the
resistor (Fig. 4.7b) shows where the particle was placed, the strongly
effected area is much larger than the initial particle size. However,
the influence of this small amount of Bi_2O_3 has extended to some degree
throughout the entire resistor as can be seen by the radial parttern of
small dark spots and "white tails", regions of glass void of RuO_2. Figure
4.7c shows greater detail in the darkened spot. Although most of the
resistor is uniformly dense at this magnification the effected area is
characterized by non-uniform agglomeration of the RuO_2.

4.1.2.5   Sintering

The first model experiments to study the neck growth of particles
undergoing sintering were conducted by Kuczynski [4]. He measured the
neck growth of copper and silver microspheres sintered to a flat plate of
the same material. The procedure adopted for neckgrowth experiments was
laborious. The metallic particles of spherical shape were dispersed

on a flat block and heated in a controlled atmosphere at different temperatures. After heating for different times the samples were mounted in bakelite and the polished diamatral cross-section of the particle in contact with the block was observed under the microscope to measure the neck radius.

The neck growth measurement technique to study sintering was later adopted by many workers. Kingery and Berg [23] observed the growth of contact area between spheres of glass, sodium chloride and copper by hot stage microscopy. They mounted a microscope to focus on the sample in the high temperature furnace and used it in conjunction with a camera for photographs or a filar micrometer eyepiece for direct measurements. This way, they could record the neck growth data at high temperatures, and the labor of quenching and polishing was avoided. Secondly, all the required data for a particular temperature could be taken on the same set of particles. A similar setup was used by Dayer and Ullrich [49] to study liquid phase sintering in the 90 w/o copper - 10 w/o tin system. Only qualitative information on the microstructure development was obtained.

Further improvements in the direct observation of the neck growth at high temperatures were made by Kaufman and coworkers [50] who employed the electron microscope equipped with a hot stage. They used a closed circuit television system integrated into the electron optical system of a Philips EM 200 microscope for direct recording of the neck growth data. In addition to the television camera, a video tape recorder and a monitor were also employed. They used this arrangement to make neck growth measurements on submicron copper and silver spheres. More recently sintering studies have also been conducted in the scanning electron microscope equipped with a hot stage by Fulrath and coworkers [51].

The electron microscope equipped with a hot stage requires either inert atmosphere or high vacuum. Hence this technique has been successfully employed for only a few systems containing mainly metallic particles. For the sintering of glass particles one can not use either vacuum or inert atmosphere because this could result in reduction of glass depending upon the temperature and oxygen partial pressures. Hence the alternative was to use an optical microscope equipped with a hot stage unit (see Section 3.3) that could be used in air even at high temperatures.

Neck growth between two glass spheres was studied under isothermal conditions. The glass spheres were of the size range 150-300 μm and were prepared in the following way. The frit was ground in the agate mill and sieved. The sieved fraction between 149-354 μm was used for making the spheres in the furnace shown in Fig. 4.8. This was a two section tube furnace with an alumina core the lower part of which was wound with nichrome wire and the upper part with platinum-40 w/o rhodium wire. A mullite center tube was used to protect the alumina core from being attacked by the glass particles. The lower part of the furnace was maintained at 800°C and the upper part at 1200°C. The glass particles were placed on the sieve that was being vibrated so the particles would fall down the furnace. Only very few particles were placed on the sieve at a time to avoid the coalescence of the particles as they traversed the tube. As the particles traveled through the furnace, they melted and became spheres to decrease their surface energy, and these spheres were collected at the bottom.

For recording neck growth data during sintering of spheres, a few glass spheres of similar sizes were placed in the platinum pan of the hot stage unit and two particles touching each other were chosen for the neck growth study. The furnace was heated to the required temperature and the neck growth data including time and thermocouple emf were recorded continuously on video tape during the sintering process. Figure 4.9 shows the successive stages during the sintering of glass particles as recorded at one temperature. This method of recording data was useful because it created a virtually continuous and complete record of the sintering process and all the data for a particular temperature could be taken on the same set of samples. The video monitor also offered the additional advantage of observing the rapid coalescence process at high temperatures. This is demonstrated by the four photographs of Fig. 4.9 for which the total elapsed time is only 30 seconds and yet the number of sequential viewing frames (1800) is sufficient for quantitative rate measurements. The data obtained from particles in this size range can be scaled down to obtain rate information for the particle sizes used in resistor formulation once the dominant sintering mechanism is established.
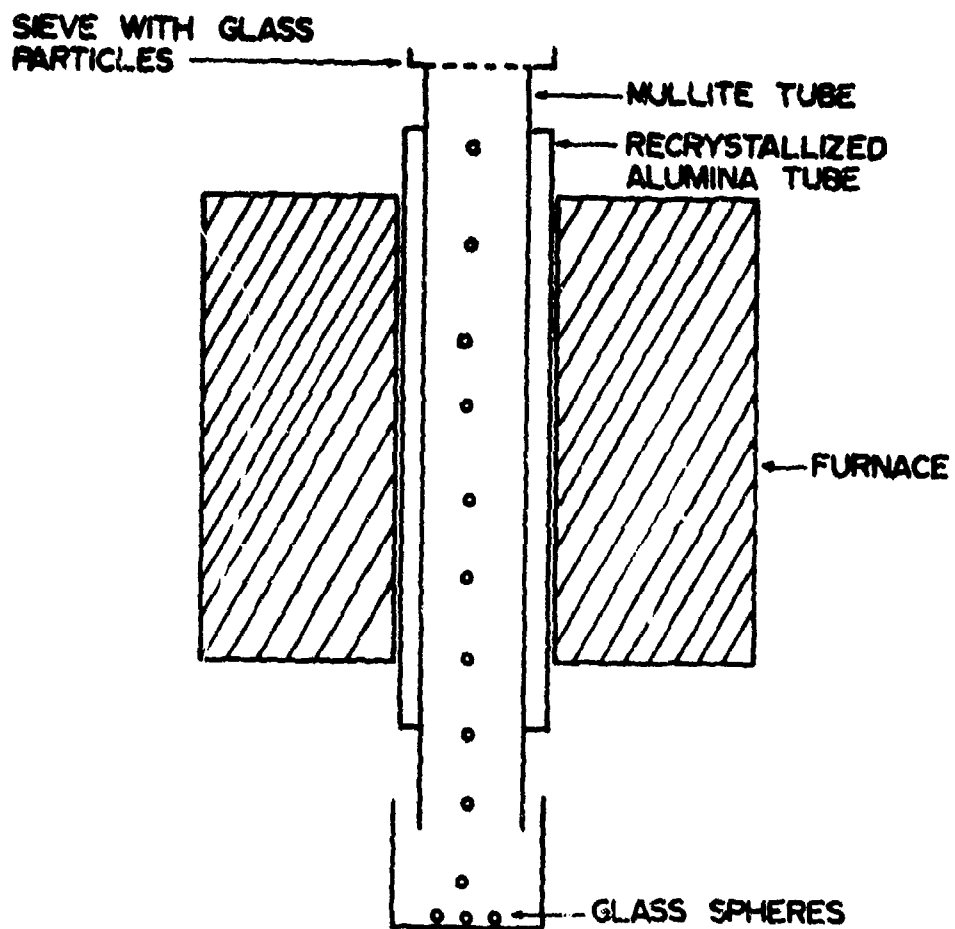
Figure 4.8   Furnace Assembly for Making Glass Spheres

a. b.

c. d.
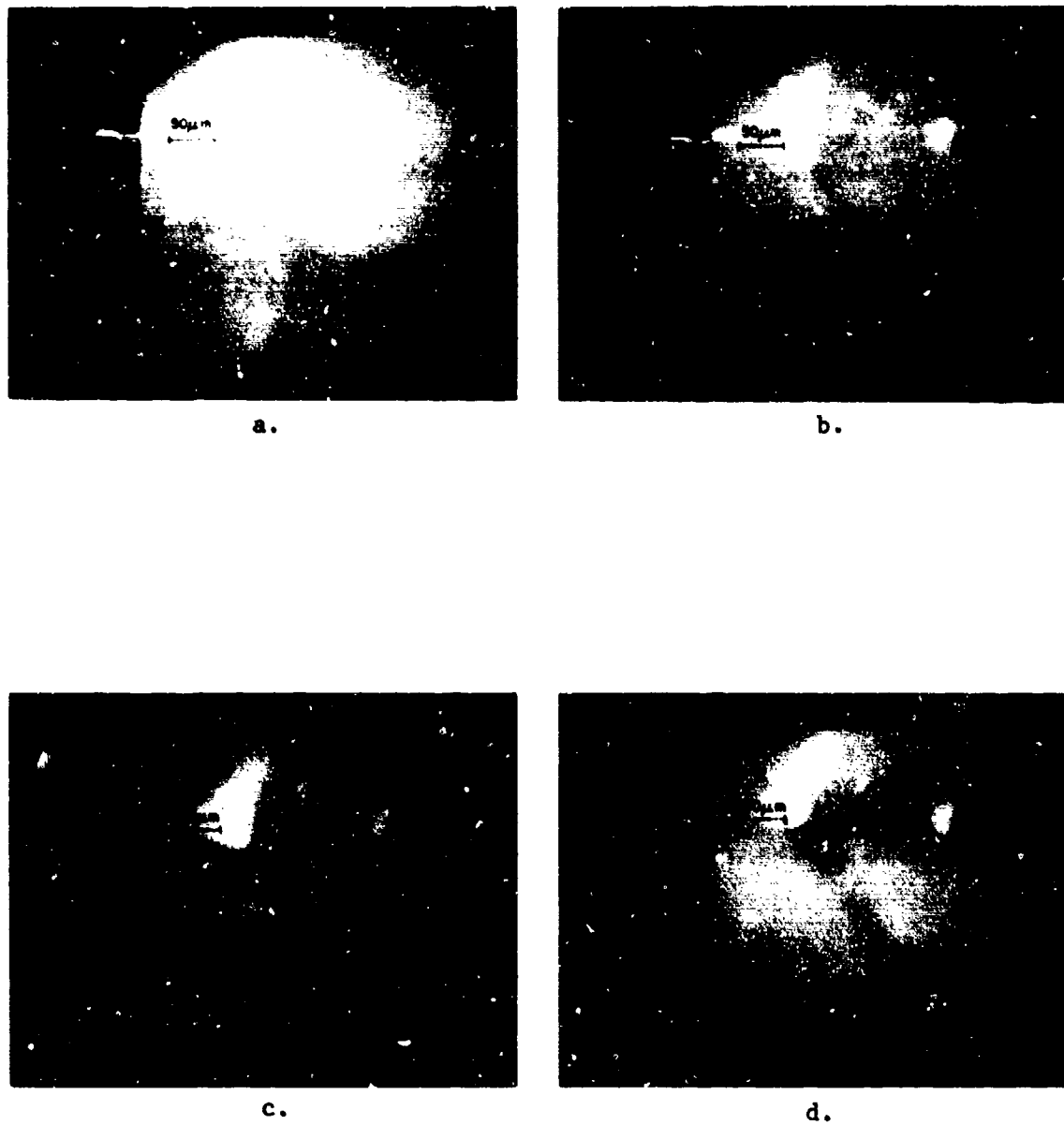
Figure 4.9   Successive Stages of Neck Growth During Sintering
of Lead Borosilicate Glass Spheres

The neck growth between glass spheres ranging from 180-250 μm in diameter was measured as a function of time at five different temperatures from 480 - 550°C. For each case the neck growth data, including time and temperature were recorded continuously during the complete sintering process.

Assuming that Newtonian viscous flow is the predominant sintering mechanism for the glass, the relationship between neck radius and time should follow Eq. 2.12, and a plot of $(\frac{x}{r})^2$ versus t should give a straight line. The predicted behaviour was observed at all five different temperatures as can be seen from Figs. 4.10 and 4.11. It can therefore, be concluded that Newtonian viscous flow is the predominant mechanism for the sintering of the lead borosilicate glass particles. In order to determine the temperature dependence of viscosity, viscosity values were computed from Eq. 2.12 using the slopes of the $(\frac{x}{r})^2$ versus t plots. The surface tension values at the experimental temperatures required for computation of the viscosity were obtained by extrapolating the data in Fig. 4.6. Figure 4.12 shows the viscosity values computed from sintering studies along with those extrapolated from the high temperature viscosity measurements by the sphere method. The magnitudes of the viscosity values obtained by the two methods are in good agreement considering the uncertainties in the extrapolation of the viscosity and surface tension plots, but the temperature dependence of the viscosity calculated from the sintering data is different from the extrapolated values. The activation energy of viscosity by the sintering studies is computed to be 126 ± 3 kcal/mol as compared to 81 ± 2 kcal/mol by the sphere method. The viscosity measurements by the sphere method were carried out at temperatures much higher than the softening point of the glass, whereas the sintering data were obtained at temperatures near the softening point. The differences could well be differences in the activation energies in the different temperature ranges. Such a behaviour was also found by Kuczynski [22] who reported that during the sintering of silicate glasses containing CaO, MgO and Na_2O, the activation energy was 67 kcal/mol for temperatures higher than 700°C and 121 kcal/mol for temperatures less than 700°C. The softening point of the glass (the temperature at which the viscosity is $10^{7.6}$ poise) estimated from sintering data is 533°C.
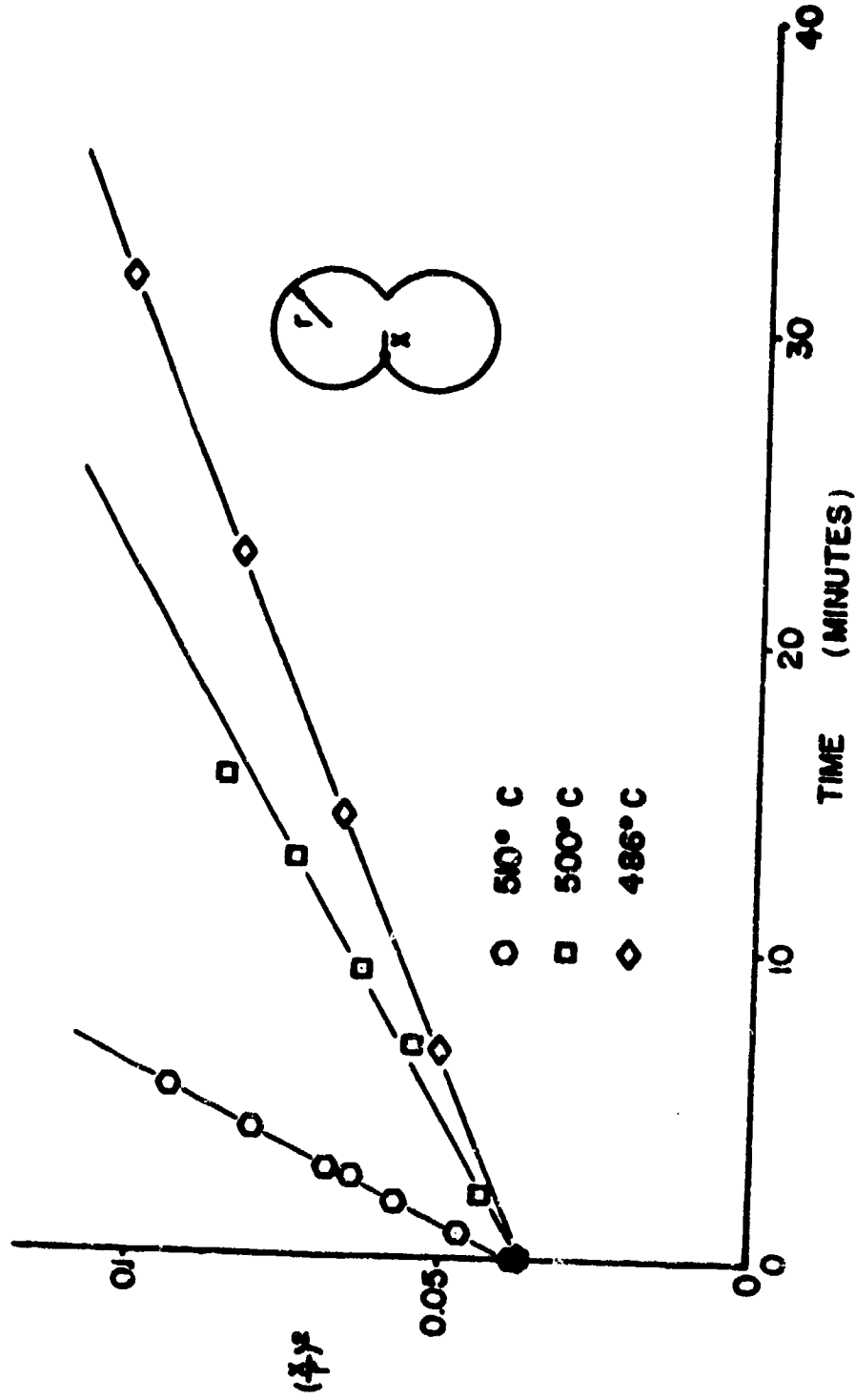
Figure 4.10   Initial Stage Sintering Kinetics for Lead   res.
Borosilicate Glass Spheres

94

Figure 4.11   Initial Stage Sintering Kinetics for Lead
Borosilicate Glass Spheres
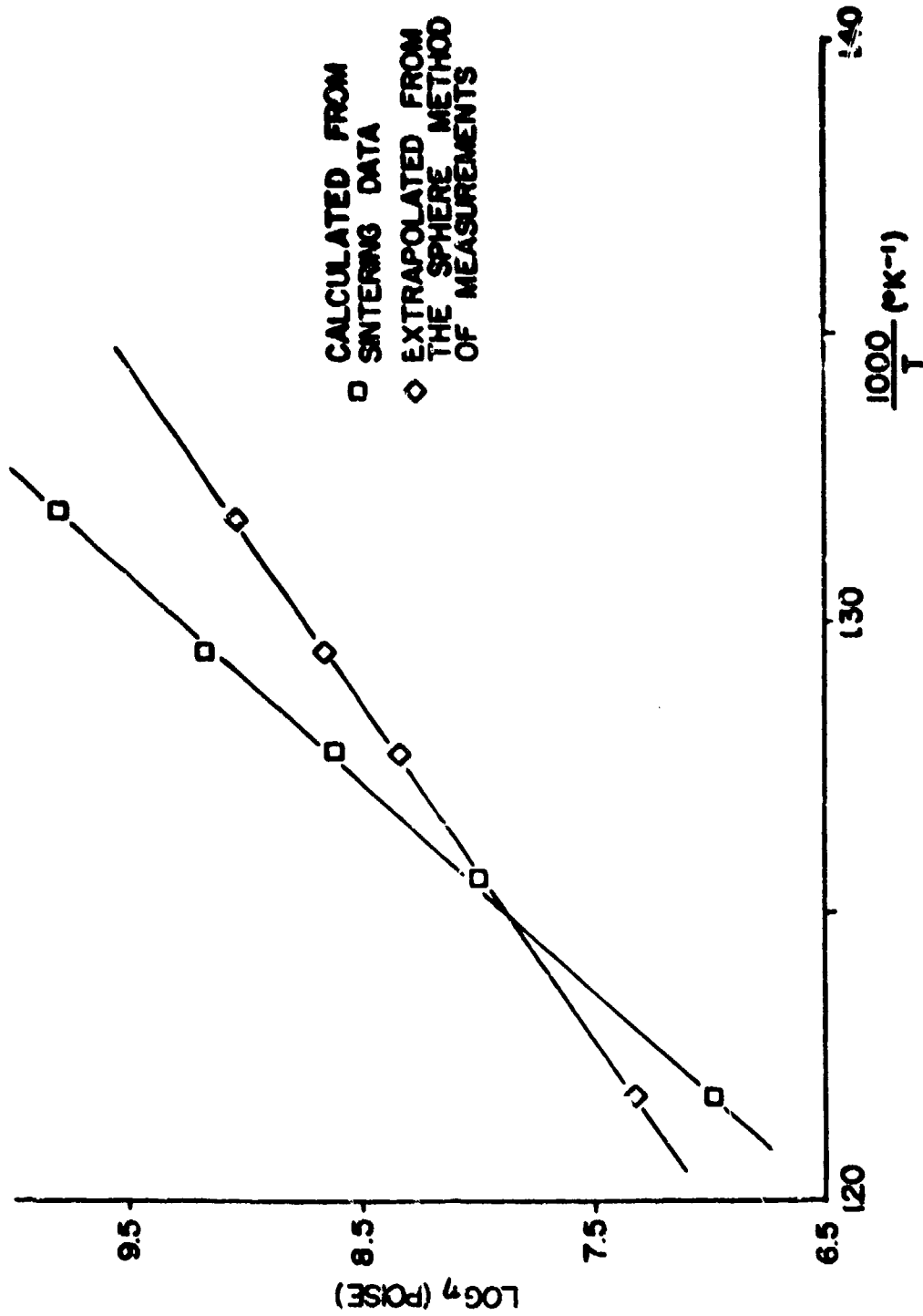
Figure 4.12. Temperature Dependence of Viscosity of Lead Borosilicate Glass

4.1.3   Conductive Paste

Conductive patterns on the substrate and adhesion of crystals to wires were both established with Englehard 6082 fluxed platinum paste. It was chosen because of its moderately good adhesion and electrical resistance, and because it is moderately stable and unreactive at high temperatures. A chemical analysis of the paste after firing to remove the organics is shown in Table 4.5. As can be seen, the flux is Bi_2O_3.

Experience has shown that this paste adheres well to a large variety of ceramic materials provided an adequate technique is used. Particularly with the first application, it is easy, for some ceramic materials, to apply the paste too thick. If the thick paste is dried and fired too quickly a dry film may form on the surface that will be disrupted by volatile materials lower in the film leaving rapidly. This type of failure can be eliminated by more gradual drying and firing. A second mode of failure results from the two stages of coalescence of the conductive. The first volume shrinkage occurs during drying and as most of the organics leave, the particles of material cohere. If the adhesion of the partially wet film to the substrate material is not adequate, the dimensional changes during drying will cause the conductive film to separate from the substrate as it shrinks. The second volume reduction occurs at high temperature as the platinum sinters in the presence of the flux. Again, if the adhesion to the substrate is not adequate at this stage, the dimensional changes of the film will cause it to separate. The best solution to this problem is to apply the film as thin as possible. Once an adhered layer is formed less care is required for additional layers. In general a smooth surface such as crystal faces have the lowest adhesion while more textured surfaces, such as an established film of 6082, are best. The texture of the 96% alumina substrates are intermediate in quality in this respect.

An interesting effect occurs with the combination substrate, glass, and 6082 conductive. After extended times at high temperatures (>800°C) the glass causes the metal film to separate from the substrate and float in the glass. It does not float to the surface and does not move significantly.

Table 4.5   Analysis of Platinum Paste (Engelhard #6082)
(Inorganic Components)

	values in ppma		
Element	Paste	Element	Paste
Li	1	Mn	10
B	5	Fe	350
F	10	Co	5
Na	1500	Ni	<15
Mg	100	Cu	15
Al	100	Zn	50
Si	150	Sr	2
P	3	Rh	20
S	100	Pd	30
Cl	500	Ag	10
K	30	Ba	15
Ca	50	Au	20
Sc	1	Pb	10
Ti	30	Bi	0.3-1%

All other impurities < 1 ppma.

4.1.4   Ruthenium Dioxide

4.1.4.1   Powder Preparation and Characterization

Although thick film resistors have been made with ruthenium added by
metal resinates and ion implantation, all resistor samples in this program
were made with RuO_2 powder. The powder can be made by oxidizing ruthenium
metal, but this requires a long time at high temperature and the resulting
particle size is larger than that obtained by other methods. The more
desirable method for shorter preparation times and smaller particle sizes
is to precipitate a hydrated oxide of small particle size from a solution
of soluble salts, and then dehydrate to form the oxide. The general
technique, with specific examples, has been discussed by Angus and
Gainsbury [15]. They report preparation of the hydrates by precipitating
solutions of ruthenium chloride, sodium ruthenate, and ruthenium tetroxide
with sodium hydroxide, methyl alcohol, and hydrogen peroxide, respectively.
They also report that the temperature of dehydration affects the particle
size of the oxide, and that the particle size of the oxide in turn affects
the resistivity and TCR of thick film resistors. Heating the hydrate for
one hour at 500°C resulted in approximately 0.3μm particles of oxide
whereas heating for the same time at 800°C resulted in 1.5 μm particles.
This comparison is typical and is due to increased grain growth at higher
temperatures; the driving mechanism is a reduction in surface area.

Since ruthenium dioxide hydrate ($RuO_x \cdot xH_2O$) is commercially avail-
able, quantities were obtained from both Englehard and Mathey Bishop for
dehydration to usable oxide. The dehydration is exothemic to the extent
that care must be exercised in order to avoid a spontaneous reaction.
To plan an appropriate dehydration procedure and to better characterize
the hydrate, both DTA and TGA measurements were made during heating.
Qualitative DTA results were obtained with a laboratory assembled instrument
of standard design, and TGA measurements used a system similar to that
shown in Fig. 4.3. In addition to these measurements an electron spec-
troscopy for chemical analysis (ESCA) was done on the surface.

The qualitative DTA results, Fig. 4.13, shows that the two hydrates
are quite different from one another, probably due to different starting
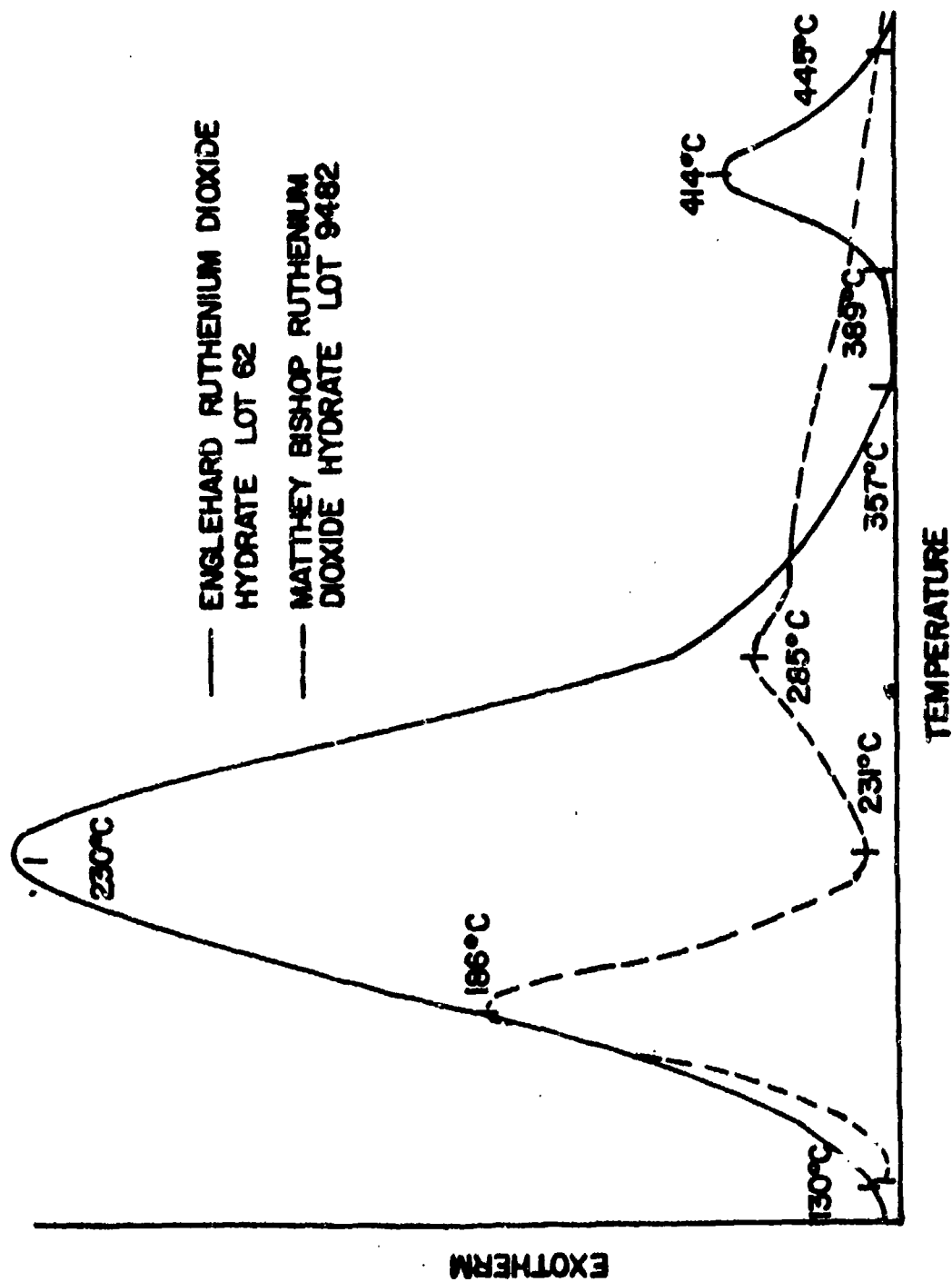
Figure 4.13   Differential Thermal Analysis of the Dehydration
of $RuO_2 \cdot xH_2O$

materials and processing conditions. The single peak at 230°C obtained
with the Englehard hydrate and the double peaks at 186°C and 285°C with
the Mathey Bishop hydrate could represent water loss; this would be
typical of dehydration. Although the patterns are of different form and
the peak for the Englehard material is much larger, the smaller peaks
obtained with the Mathey Bishop hydrate seem to be contained in the larger
peak. The exothermic peak at 414°C obtained with the Englehard material
is uncommonly high in temperature for dehydration. This peak may be due
to the oxidation of carbon since chemical analysis revealed about 2w/o
carbon in the hydrate. The origin of the carbon is not known, but to be
present in such large quantities it would have to have been introduced
somewhere in processing, for example from chemisorbed alcohol. The TGA
measurements on Englehard hydrate, Fig. 4.14, are not consistent with
normal dehydration or with the DTA results since they show a nearly
constant rate of weight loss throughout the same temperature range studied
by DTA. Although there are regions of changing slope for all three heating
rates they do not correspond to the peaks and valleys of the DTA graph.
Assuming that all of the weight loss in Fig. 4.14 was due to water, the
chemical formula of the hydrate would had to have been $RuO_2 \cdot 2.1\ H_2O$.
The TGA measurements do show that adequate drying conditions must be used
for complete water removal, however. Only the slowest heating rate, 1°C/min,
was sufficient to achieve complete water removal with a maximum temperature
of 500°C. At the more rapid heating rates weight loss is continuing at
500°C and additional time at high temperature would be required for complete
water removal. Since TGA measurements during dehydration that have been
reported for other hydrous oxides show a rapid weight loss in the temperature
range corresponding to an exotherm, the results described here are difficult
to interpret. It has been proposed [52] that $RuO_2 \cdot xH_2O$ is not actually
a hydrate but rather very small particles of oxide with chemisorbed water
on the surface. This could explain the TGA results but not the DTA. A
procedure was established for drying the Englehard hydrate in a standard
laboratory oven based on the DTA results. The temperature was increased
every half-hour as indicated in Table 4.6. The maximum temperature
employed was 400°C to avoid rapid particle growth which occurs with further
increase in temperature.
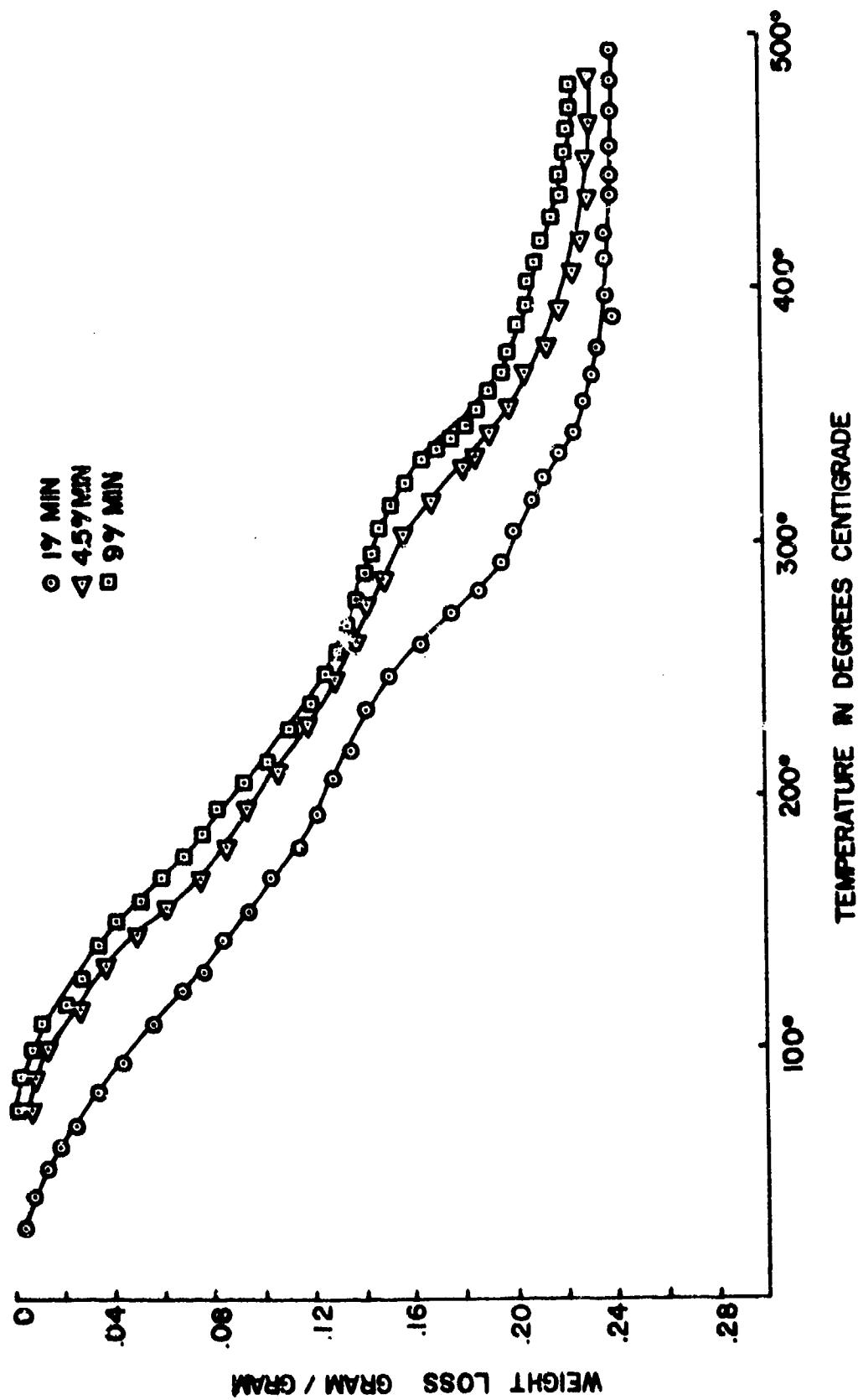
Figure 4.14   Weight Loss of $RuO_2 \cdot xH_2O$ at Constant Heating Rate

Table 4.6 Drying Procedure for Engelhard Hydrate

Time (Hours)	Temperature (°C)
½	80
1	95
1½	115
2	120
2½	125
3	130
3½	136
4	150
4½	164
5	180
5½	200
6	230
6½	280
7	330
7½	360
8	400

The average particle size of the dried powder was estimated by direct observation using a scanning electron microscope (SEM) and a transmission electron microscope (TEM) as well as by indirect methods such as x-ray diffraction line broadening and surface area measurements. The scanning and transmission electron micrographs are shown in Fig. 4.15 (a, c and d). The samples for the SEM observation were prepared either by directly placing the powder sample on an aluminum block or by ultrasonically dispersing the powder in deionized water or alcohols and then placing a drop of this liquid on the aluminum block and letting it dry. All of the different samples yielded similar results.

The samples for the TEM observations were prepared by placing a drop of the liquid containing dispersed RuO_2 on carbon coated copper grids or by making replicas by mixing RuO_2 powder with nitrocellulose in amyl acetate solution.

The average particle sizes estimated by the different techniques are summarized in Table 4.7. The surface area measurements are based upon the extent of nitrogen adsorption on the surface of the powder particles. Because of the clumping of the particles all the area may not be available for nitrogen adsorption thus giving smaller surface area values and hence larger average particle sizes. The average crystallite sizes were computed from the x-ray diffraction line broadening data neglecting the contribution to broadening by internal strains and other defects. This is a fairly good assumption when ceramic powders are considered. For crystallite sizes less than 100 Å or so, one is approaching the lower limit of the crystallite size determination by x-ray diffraction line broadening. In such a case the intensity of the background noise is quite comparable to that of the maximum intensity of the peak, and considerable uncertainty is involved while substracting the contribution from the background noise from the total intensity of the peak. All these factors might result in the computed average crystallite size to be lower than the actual crystallite size.

In spite of the uncertainties involved in the computation of the average particle and crystallite sizes from surface area and x-ray diffraction line broadening measurements respectively, the values obtained were quite comparable. Therefore, it was assumed that the crystallites
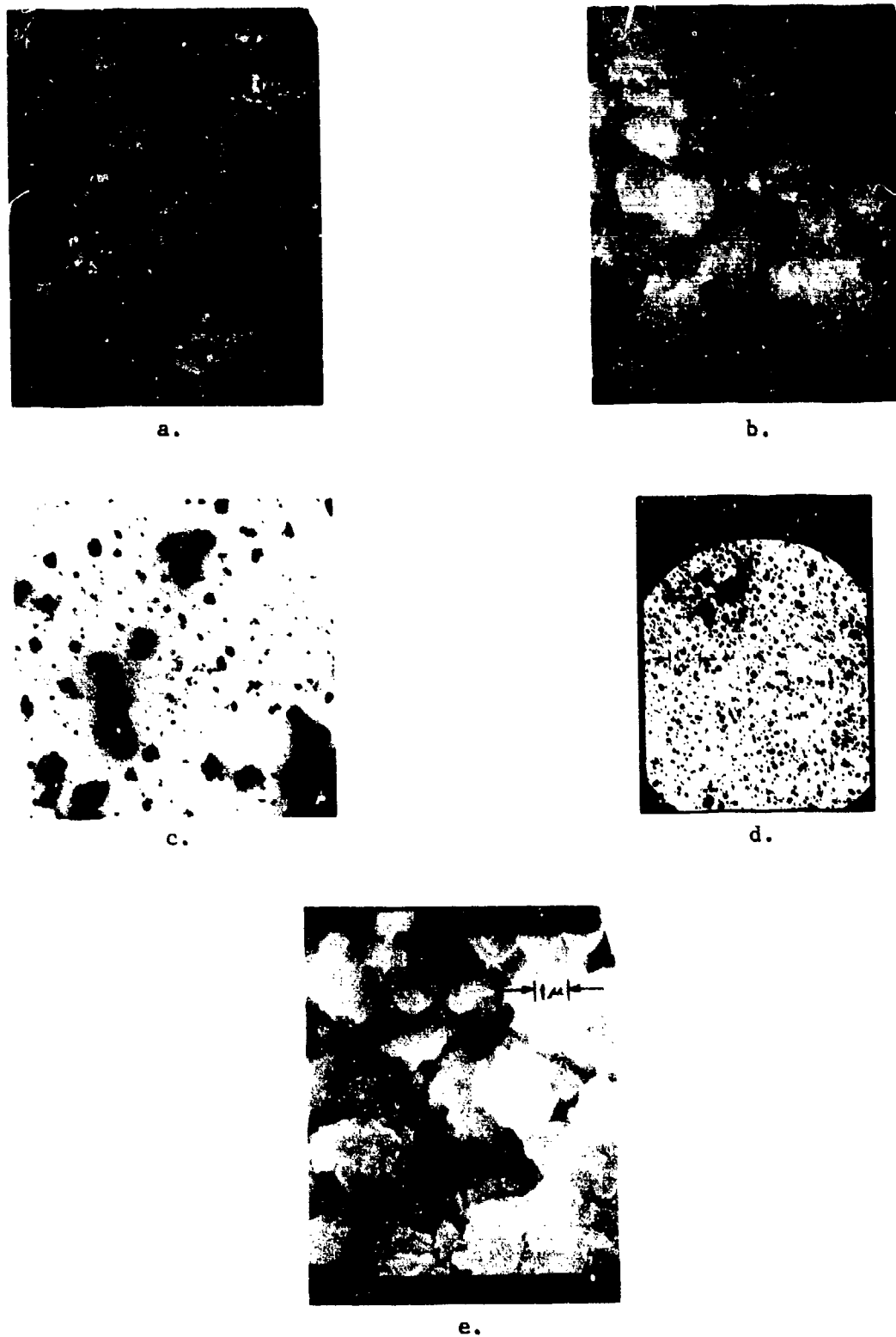
Figure 4.15   Scanning and Transmission Electron Micrographs of RuO_2
Powder (a) Engelhard RuO_2 Powder, Dried-SEM, 5400X;
(b) Engelhard RuO_2 Powder, 800°C, 15 Minutes-SEM, 5400X;
(c) Engelhard RuO_2 Powder Dried-TEM, 26,600X; (d) Englehard
RuO_2 Powder, Dried-TEM, 48,000X; (e) Mathey Bishop RuO_2
Powder-SEM, 5400X.

Table 4.7   Average Particle Size of Dried RuO_2 Powder

Technique	Average Particle Size
X-ray Diffraction Line Broadening	60 Å
Surface Area	120 Å
SEM	1000 Å
TEM	50-1000 Å

are individual particles of sizes between 60-120 Å.

Although fairly good agreement was obtained between particle sizes of dried RuO_2 powder calculated from x-ray and surface area measurements, the correlation with microstructure observations was not good. The SEM photographs in Fig. 4.15a show the particle size of RuO_2 powder to be about 1000 Å. This order of magnitude difference compared to the results obtained from x-ray and surface area results is due to the agglomeration of small RuO_2 particles. The agglomeration problem is evident from the TEM photographs in Figs. 4.15c and 4.15 d. In Fig 4.15c particles in the size range 50-200 Å can be seen along with the larger ones. By observing the periphery of the larger particles, it can be concluded that these are not individual particles but actually clumps of a large number of smaller particles. The photograph shown in Fig. 4.15d was obtained from the sample prepared by putting the upper-most layer of the dispersant (deionized water) in which RuO_2 powder was ultrasonically dispersed. As can be seen, a large number of these particles are in the size range 50-200 Å.

The extensive growth of RuO_2 particles when heated at 800°C for 15 minutes can be noted from Fig. 4.15b. The SEM photograph of the anhydrous RuO_2 powder obtained from Mathey Bishop is shown in Fig. 4.15e. These particles are much larger and the average particle size can be estimated to be about 0.5-1 µm.

4.1.4.2   Structure and Thermal Expansion

Ruthenium dioxide has the tetragonal rutile crystal structure with two formula units per unit cell. Several authors [52-56] have reported unit cell dimensions as shown in Table 4.8. It can be seen that RuO_2 contracts in the c direction with increasing temperature, that is, it has a negative coefficient of linear thermal expansion (α). Expansion vs. temperature is normally anisotropic for non-cubic crystals, and so $\alpha_{||}$ and $\alpha_{\perp}$ (parallel and perpendicular to the c axis) should be different functions of temperature. Based on their measurements, Rao and Iyengar [55] have developed mathematical expressions for $\alpha_{||}$ and $\alpha_{\perp}$. The formulas are:

$$\alpha_{||} = -1.248 \times 10^{-6} - 5.392 \times 10^{-9} \, T - 2.273 \times 10^{-12} T^2 \qquad (4.3)$$

Table 4.8 Crystal Data for Ruthenium Dioxide

	Temperature (°C)	Lattice Parameters (Å)	
		a	b
Cotton and Mague 1966	RT	4.491±.007	3.107±.005
Fletcher, et al. 1968	RT	4.4904±.0001	3.1064±.0001
	190	4.4971	3.1055
	400	4.5074	3.1031
	605	4.5204	3.1002
	795	4.5342	3.0963
Shannon, 1968	RT	4.4906±.0002	3.1064±.0002
Rao and Iyengar 1969	30	4.4908±.0003	3.1064±.0004
	165	4.4958	3.1062
	267	4.5003	3.1051
	361	4.5053	3.1037
	461	4.5109	3.1033
	563	4.5198	3.1012
	608	4.5198	3.1008
	702	4.5258	3.0995
Bowman 1970	RT	4.4919 ±0008	3.1066±.0007

and

$$\alpha_\perp = 6.447 \times 10^{-6} + 1.920 \times 10^{-8}T - 1.075 \times 10^{-11}T^2 \qquad (4.4)$$

where T is the temperature in C°. They indicate that values of $\alpha_{||}$ and $\alpha_\perp$ calculated with these formulas agree to within a few percent of the observed values.

The value of α in any direction may be calculated from $\alpha_{||}$ and $\alpha_\perp$ by the formula:

$$\alpha(h,k,\ell) = \left[\frac{h^2+k^2}{a^2}\ \alpha_\perp + \frac{\ell^2}{c^2}\alpha_{||}\right]\Bigg/\left[\frac{h^2+k^2}{a^2} + \frac{\ell^2}{c^2}\right] \qquad (4.5)$$

where h, k, ℓ are the Miller indices of the direction.

Although knowledge of $\alpha_{||}$ and $\alpha_\perp$ is valuable information for some types of experiments, it is not directly useful when RuO_2 powder is used, such as in thick film resistor formulations. This is because of the random orientation of the small crystals. What is required is an average value of elongation vs. temperature based on volume expansion. This is calculated by the formula

$$\text{Percent elongation (T)} = 100\ \left[V^{1/3}(T) - V^{1/3}(RT)\right]\Big/V^{1/3}(RT) \quad (4.6)$$

where V(T) is the volume at temperature T, and V(RT) is the volume at room temperature. Table 4.9 shows the volume of a unit cell calculated from the lattice parameter data of both Rao and Iyengar [55] and Fletcher, et.al., [52], and the average elongation calculated from Eq. 4.6. In the calculations, the room temperature parameter was assumed to be 4.4905Å. This was chosen based on the values reported by Shannon [54] and by Fletcher, et.al.[52]. The elongation vs. temperature determined from lattice parameter measurements are important because crystals of a size sufficient for accurate dilatometer measurements have not been grown.

The relative values of the thermal coefficients of linear expansion of the glass, substrate, and RuO_2 are important in this material system because they are the best indicator of strains that may be present. The fact that pressure dependent contact resistance has been proposed as an important mechanism determining resistor performance makes it more important than usual. Figure 4.16 shows the measured fractional elongation vs. temperature for the

Table 4.9   Thermal Expansion of Ruthenium Dioxide

Temperature (°C)	Unit Cell Volume (Å)	Percent Elongation
22	62.64	------
30	62.65	0.0594
165	62.78	0.0765
190	62.81	0.0883
267	62.87	0.1315
361	63.00	0.1906
400	63.04	0.2152
461	63.15	0.2693
563	63.28	0.3414
605	63.35	0.3765
608	63.34	0.3741
702	63.49	0.4489
795	63.66	0.5385
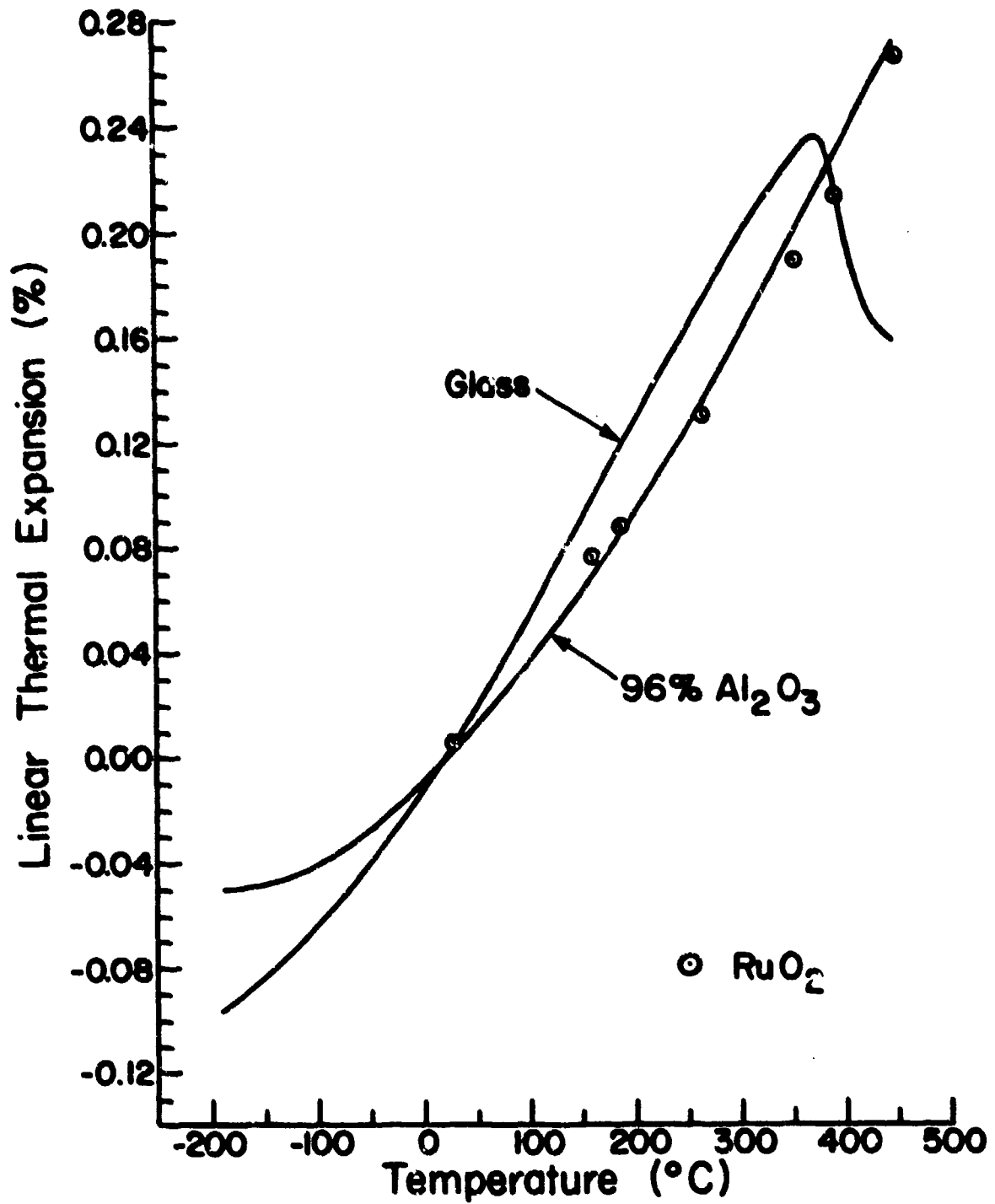
Figure 4.16   Thermal Expansion of Resistor Constituents

glass and subs. rate, and calculated values for RuO_2 at several temperatures. The values for RuO_2 are based on the volume expansion of the unit cell and represent, therefore, the average linear expansion of the RuO_2 powder. The agreement among the three elongations is very close. The best agreement is between the RuO_2 and the substrate, and if it can be argued that the more rigid substrate controls the elongation of the glass for relatively thin, thick film resistors, then the strain in the system should be very low. Even if this is not a valid assumption or if just glass and RuO_2 are used to make a pellet resistor, the change in strain with temperature should be very low in the temperature range between 150°C and the softening point of the glass where the two elongation curves are parallel.

4.1.4.3   Thermodynamic Properties

Several investigations of the chemistry of the ruthenium-oxygen system have been reported dealing with both the thermodynamic properties of RuO_2, and with the formation of other oxides [57-62]. Table 4.10 summarizes the thermodynamic properties of RuO_2 extrapolated to 298°K. A variety of experimental procedures were used to obtain these data including galvanic cell, thermo-balance, and static pressure methods. Although the differences in the reported values of ΔG°_{298} are greater than the individual estimated errors, the agreement to within about one kilocalorie is good.

All the values reported in Table 4.10 were calculated from data measured at higher temperatures. Figure 4.17 compares these data by showing values of the standard free energy of formation, ΔG°, at the measurement temperatures. The data of Chatterji and Vest [62] parallels the data obtained at higher temperatures but is lower; this may be partially due to the $\alpha - \beta$ transformation in ruthenium metal at 1308°K. The data of Pizzini and Rossi [60] shows less agreement.

Figure 4.18 shows the phase fields for the $Ru-RuO_2$ system over the temperature range 600-1500°C. This phase diagram is essential for considerations of the oxygen partial pressures and temperatures during thick film resistor firing. For example, if at 800°C (a nominal temperature for preparing RuO_2 thick film resistors) the partial pressure of oxygen within the film is below 10^{-6} atmospheres, the RuO_2 will be reduced to ruthenium

Table 4.10 Thermodynamic Properties of Ruthenium Dioxide at 298°K

Investigator		ΔH°_{298} (kcal/mole)	ΔS°_{298} (e.u.)	ΔG°_{298} (kcal/mole)	S°_{298} (e.u.)
Bell and Tagami	[57]	−72.2±2.0	−43.3±2.0	−59.3±2.6	12.5±2.0
Shchukarev and Ryabov	[58]	−72.4±.4	---	---	---
Shafer, et.al.	[59]	−71.2	−41.4	−58.9	14.5
Pizzini and Rossi	[60]	−73.36±.35	−41.88±.46	---	---
Latimer	[61]	---	---	---	14.5
Chatterji and Vest	[62]				
Extrapolated		−71.44±.19	−38.97±.1	−58.84±.12	16.93±.1
Corrected		−72.43±.2	−40.44±.2	−60.38±.2	15.46±.2
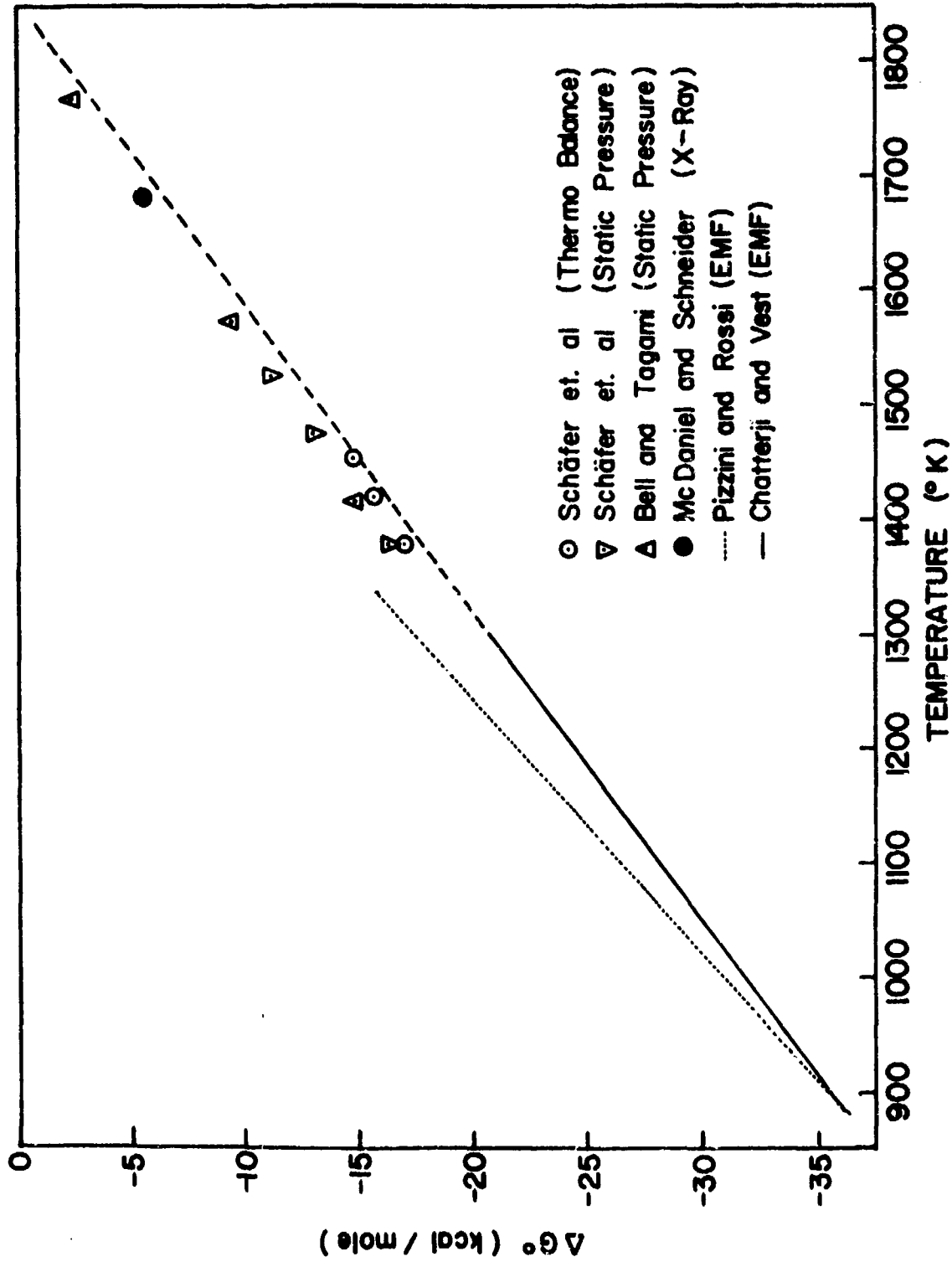
Figure 4.17   Standard Free Energy of Formation of RuO_2
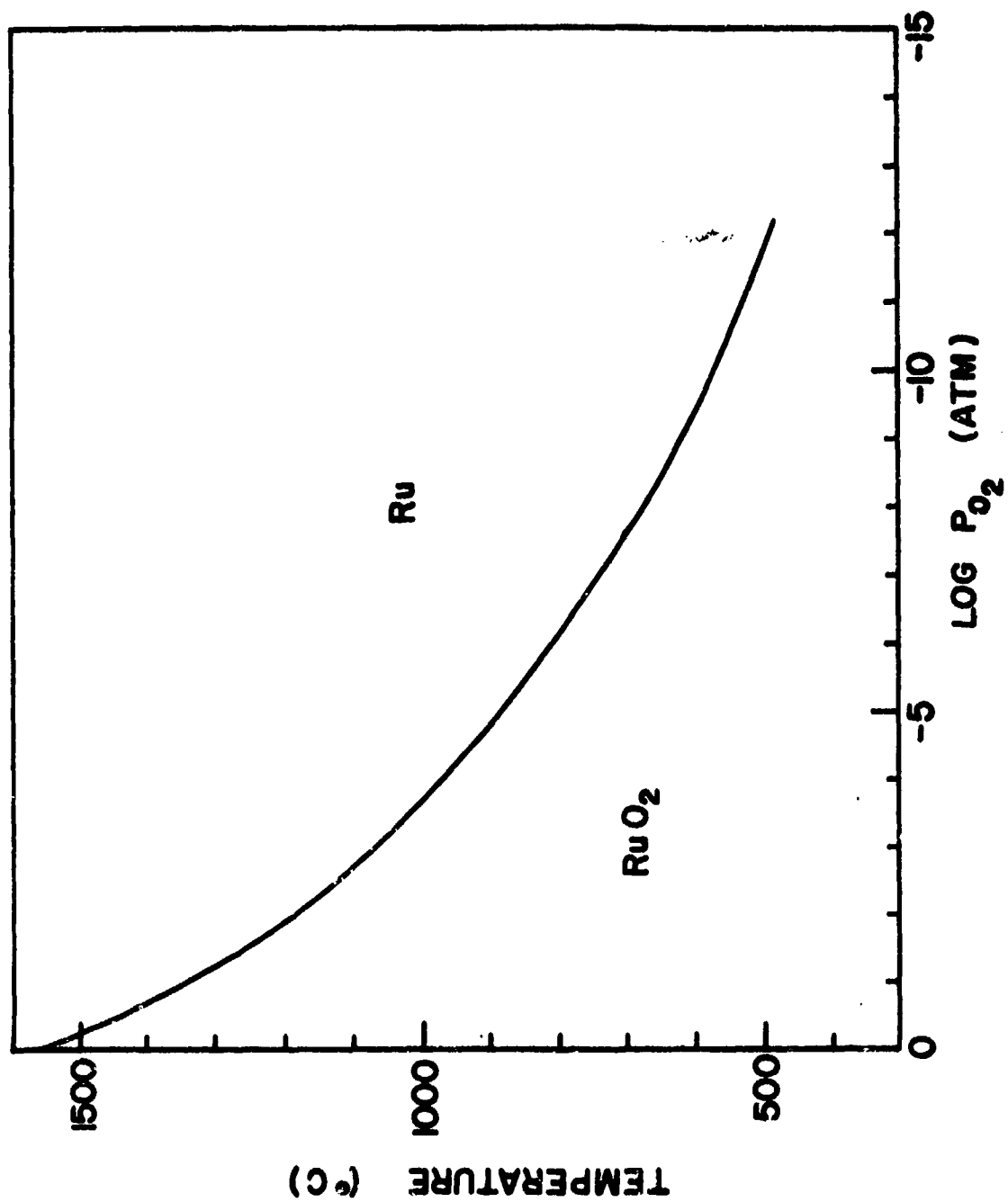
Figure 4.18   Phase Fields for the Ru-RuO$_2$ System

metal. The oxygen partial pressure in the film will be a function of at least the kiln atmosphere and the rate of heating.

Of course, thermodynamics cannot predict the rate at which oxidation-reduction reactions such as $Ru + O_2 \rightleftharpoons RuO_2$ will occur. However, it has been experimentally observed that ruthenium metal oxidizes very slowly. For example, we observed that heating ruthenium metal powder at 1200°C for one hour and at 900°C for 12 hours resulted in 19% oxygen content as compared to 24% required for RuO_2. Similarly, Bell and Tagmani [57] heated the metal several days at 950°C to get within 1% of the theoretical value. The slow rate of oxidation could lead to erroneous conclusions For example, Iles' report [10] that RuO_2 frequently has a significant oxygen deficiency could have resulted from weight gain measurements of the metal when only partial oxidation occurred. The same is true of S...tain's [11] conclusion concerning the existance of Ru_2O_3. In all of the recent thermodynamic work no evidence has been found that there are any anhydrous oxides between Ru and RuO_2.

The reduction of RuO_2 to ruthenium metal is much more rapid than the oxidation of the metal. RuO_2 can be quantitatively reduced in a hydrogen atmosphere in about 5 minutes at 125°C, or in carbon monoxide in about 5 minutes at 300°C.

When RuO_2 is heated to sufficiently high temperatures, two volatile oxides are formed, RuO_3 and RuO_4. At high temperatures both these oxides are in the vapor phase although RuO_4 has been prepared as a liquid at room temperature. Based on transpiration measurements by Bell and Tagmani [57] the partial pressures of RuO_3 and RuO_4 above RuO_2 exposed to air were calculated as functions of temperature; the results are shown in Fig. 4.19. As can be seen, RuO_3 predominates at higher temperatures. The weight loss of RuO_2 due to the formation of these volatile oxides was measured as a function of temperature. The specific surface area of the powder used for these measurements was 15.0 m^2/gm as determined by the BET method. Figure 4.20 shows the rate of weight loss per square meter of surface area; for this particular powder the rate of weight loss in air was 0.01 percent/min at 850°C. These vaporization data are important because the possibility of RuO_2 loss from thick film resistors during processing must be considered.
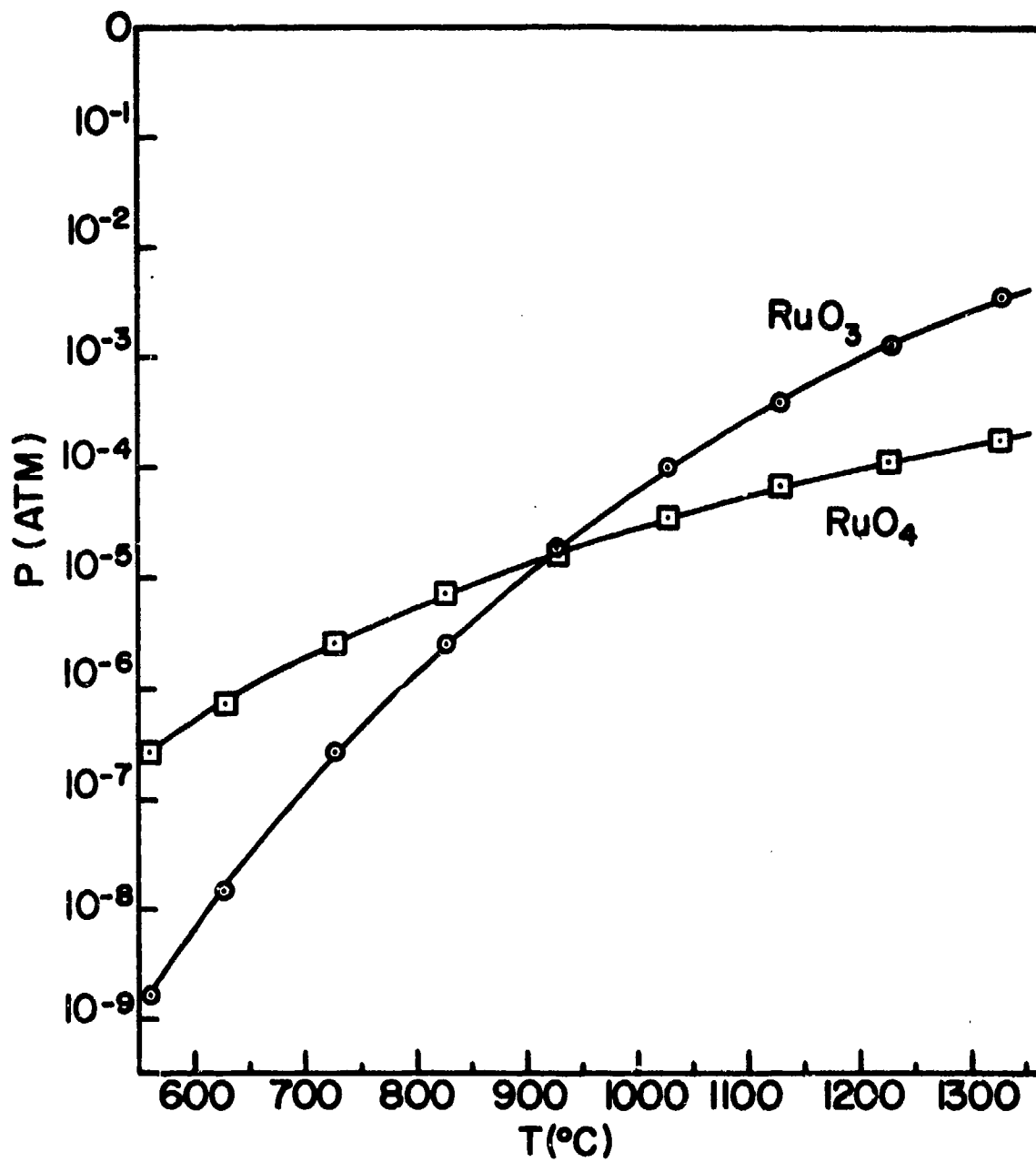
Figure 4.19   Partial Pressure of RuO_3 (g) and RuO_4 (g)
over RuO_2(s) in Air
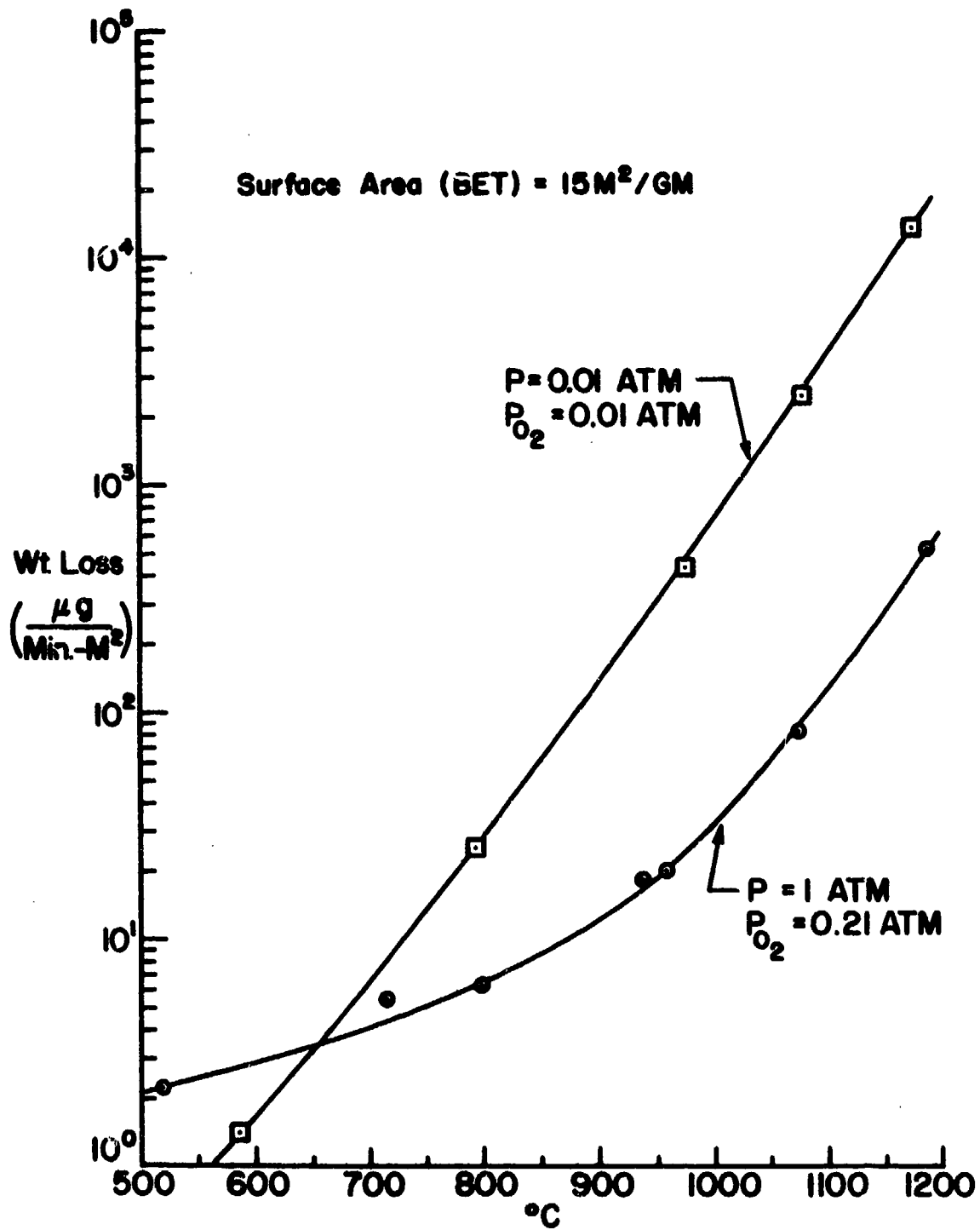
Figure 4.20   Vaporization of RuO_2

4.1.4.4   Electrical Properties of Single Crystals

The most extensive measurements on the electrical resistivity of RuO_2 have been reported by Ryden et.al. [63] from below 4.2°K to 1000°K with several crystals, most of which had residual resistance ratios of 20-50. Based on the results three conclusions are stated: 1) RuO_2 behaves electrically as a transition metal; 2) Matthiesen's rule is not obeyed; and 3) the resistivity of RuO_2 is isotropic. Each of these conclusions will now be discussed.

The conclusion that RuO_2 behaves as a transition metal was based on the ability to fit the resistivity data with the following function for a two band metal with the proper choice of parameters.

$$\rho\ (T)\ =\ \rho_0 + \rho_2 T^2 + \rho_3 T^3\ [J_3(\frac{\Theta_D}{T}) - J_3(\frac{\Theta_E}{T})] \tag{4.7}$$

In Eq. 4.7 ρ_0 is the residual resistivity, $\rho_2 T^2$ represents interband electron-electron scattering, and the last term represents interband electron-phonon scattering, where Θ_D is the Debye temperature and Θ_E is the Wilson temperature. Use of Eq. 4.7 assumes that the intraband electron-phonon scattering which predominates in a one band metal such as copper is negligible in RuO_2.

Figure 4.21 shows the data points reported by Ryden, et.al. (after subtracting ρ_0)compared to the values of $\rho(T)$ calculated with Eq. 4.7 using their reported parameters (dashed line).

As is shown in Fig. 4.21, discrepancies exist in two regions. The discrepancy in the region 10°K to 40°K is slight and is due to a simplifying assumption made in calculating the two terms of the equation. There does not seem to be a reasonable explanation for the discrepancy above 200°C.

Since the reported parameters do not work as well as indicated, a better fit was attempted. Simply increasing ρ_3 is not sufficient because it increases the discrepancy between 10°K and 40°K; a value of ρ_3 that gives agreement at 300°K is about 12% low at T=1000°K. It is not possible to change ρ_2 because below 12°K it is the only significant contribution to the resistivity. Therefore, only Θ_D, Θ_E, and ρ_3 can be varied. Values of $\Theta_D = 1050$°K, $\Theta_E = 110$°K and $\rho_3 = 3.2 \times 10^{-9}$ $\mu\Omega$-cm/°K^2 result in better
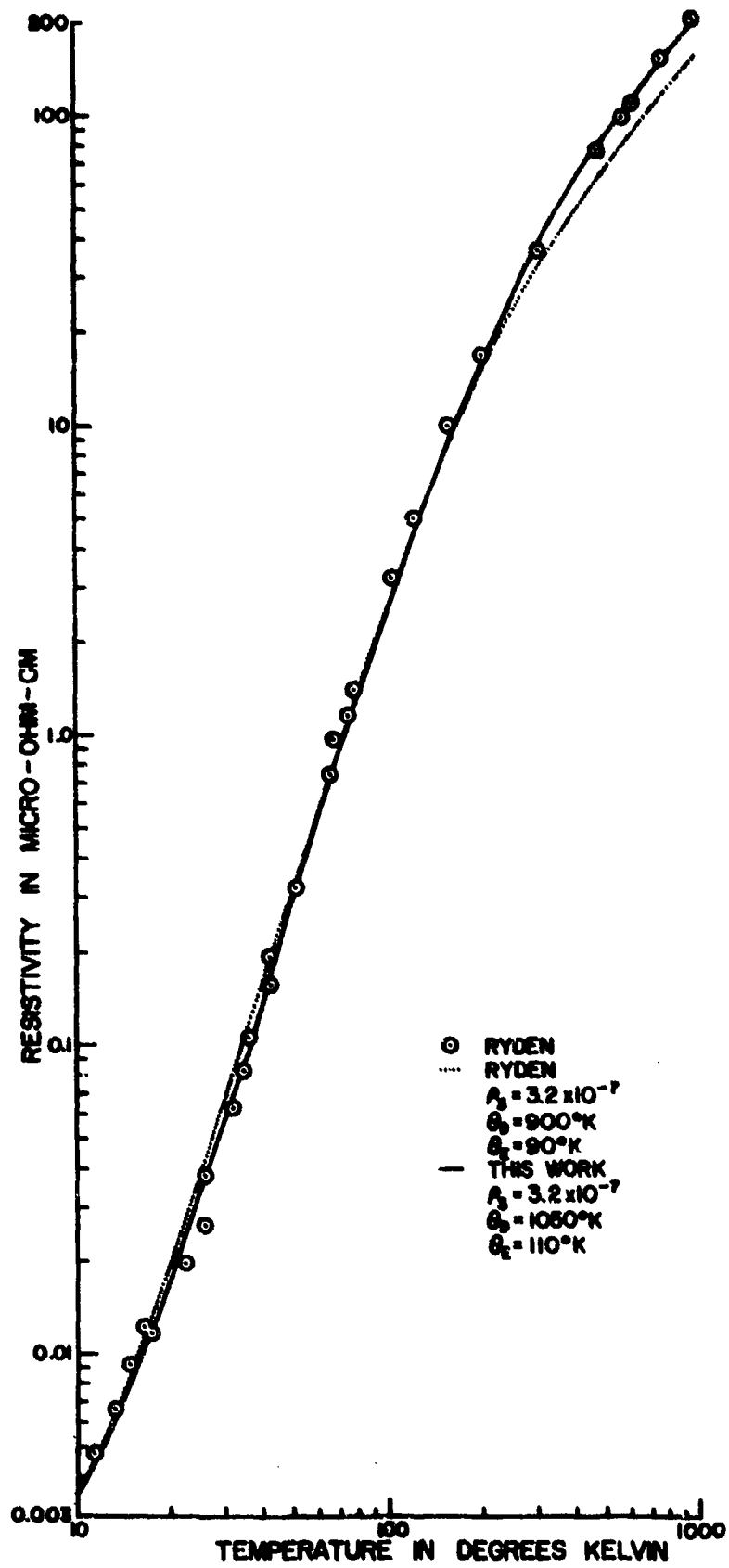
Figure 4.21   Defect-free Resistivity of RuO_2

agreement, as shown by the solid line in Fig. 4.21. The value of θ_D equal to 1050°K disagrees with the Debye temperature of 610-670°K obtained from specific heat measurements [64]. However, it is common for resistivity Debye temperatures to be larger than specific heat Debye temperatures so the discrepancy is not serious.

The band structure implied by the fit to Eq. 4.7 is partially sub-stantiated by the deHass-van Alphen measurements of Marcus and Butler [65]. They report three values of effective mass for RuO_2: 0.51 m_e, 1.7 m_e, 3.5 m_e, where m_e is the rest mass of the electron. However, Ryden [63] argues that the band containing the 1.7 m_e electrons probably has a very low population whereas the other two bands are more heavily populated. Thus, the s band corresponds to the band with the .51 m_e electrons and the d band corresponds to the band with the 3.5 m_e electrons. The difference between the qualitative band structure [54] and that proposed by Ryden can now be understood. The qualitative model has one conduction band, which presumably would have a T^5 dependence at low temperatures and a T dependence at high temperatures, whereas the transition metal model requires two bands that can both be partially filled.

As part of this work the resistivity of a single crystal of RuO_2 was measured above room temperature. The crystal had a diameter of about 70 μm and a distance between potential leads of about 1090 μm. All four leads were cemented in place with Englehard 6082 platinum paste. Figure 4.22 shows the results, normalized at 200°C, obtained over several measurement cycles using the automatic resistance measuring system. The data show a decreasing slope for increasing temperatures resulting in a small curvature throughout the temperature range. The solid lines drawn through the data points are two straight line segments that approximate the curvature.

The two straight line segments are shown again in Fig. 4.23 for comparison with data by Osburn [66] and Ryden [63]. In order to compare defect free resistivities, the straight lines representing Fig. 4.22 have been modified assuming that the defect free resistivity would be 35.2 μΩ-cm as reported by Ryden; a similar correction was made for Osburn's data. The dashed line on Fig. 4.23 is the calculated resistivity discussed earlier using the parameters obtained as part of this work.

Although Osburn's data are somewhat scattered, they agree well with
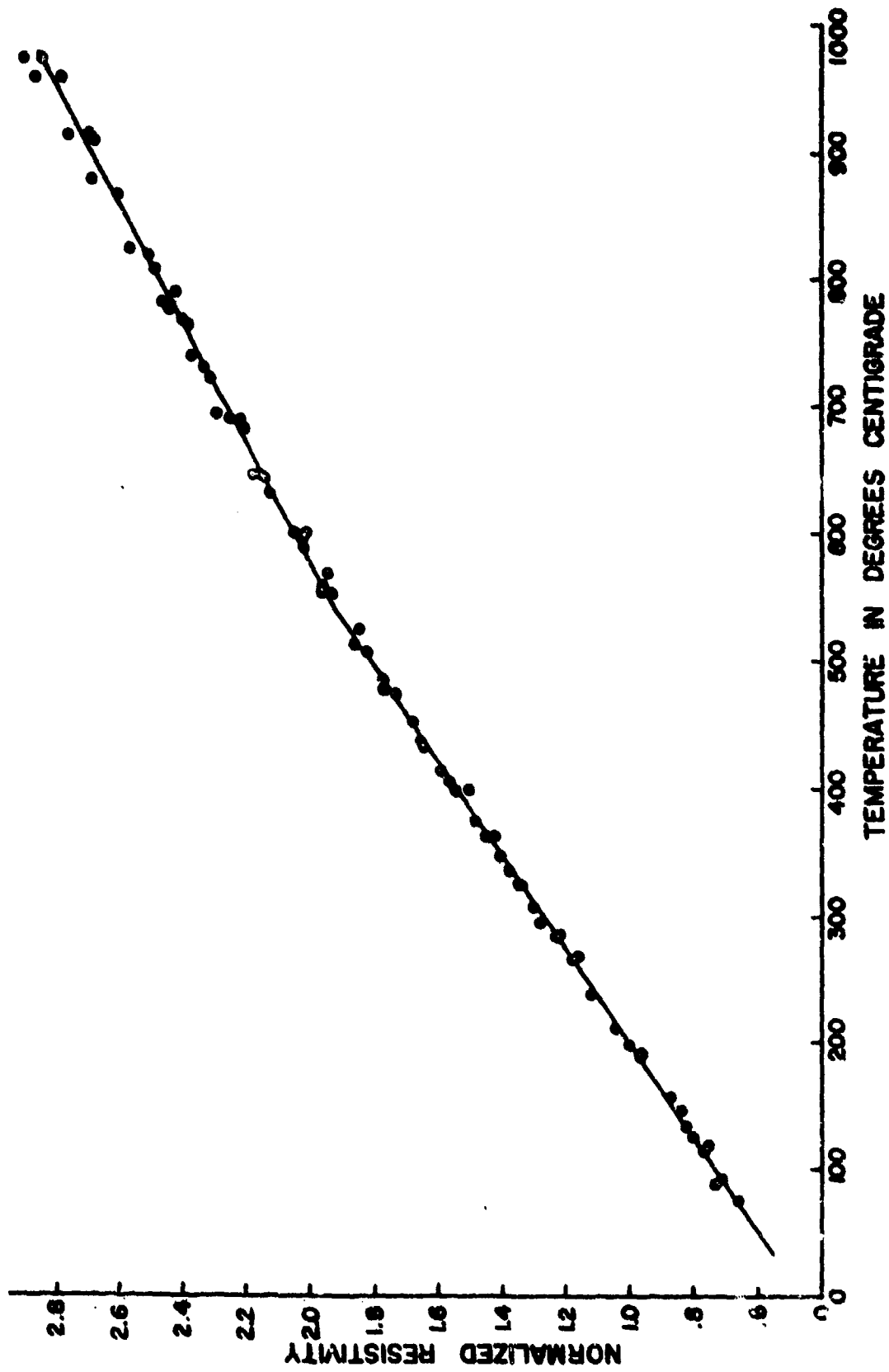
Figure 4.22   High Temperature Normalized Resistivity of RuO_2
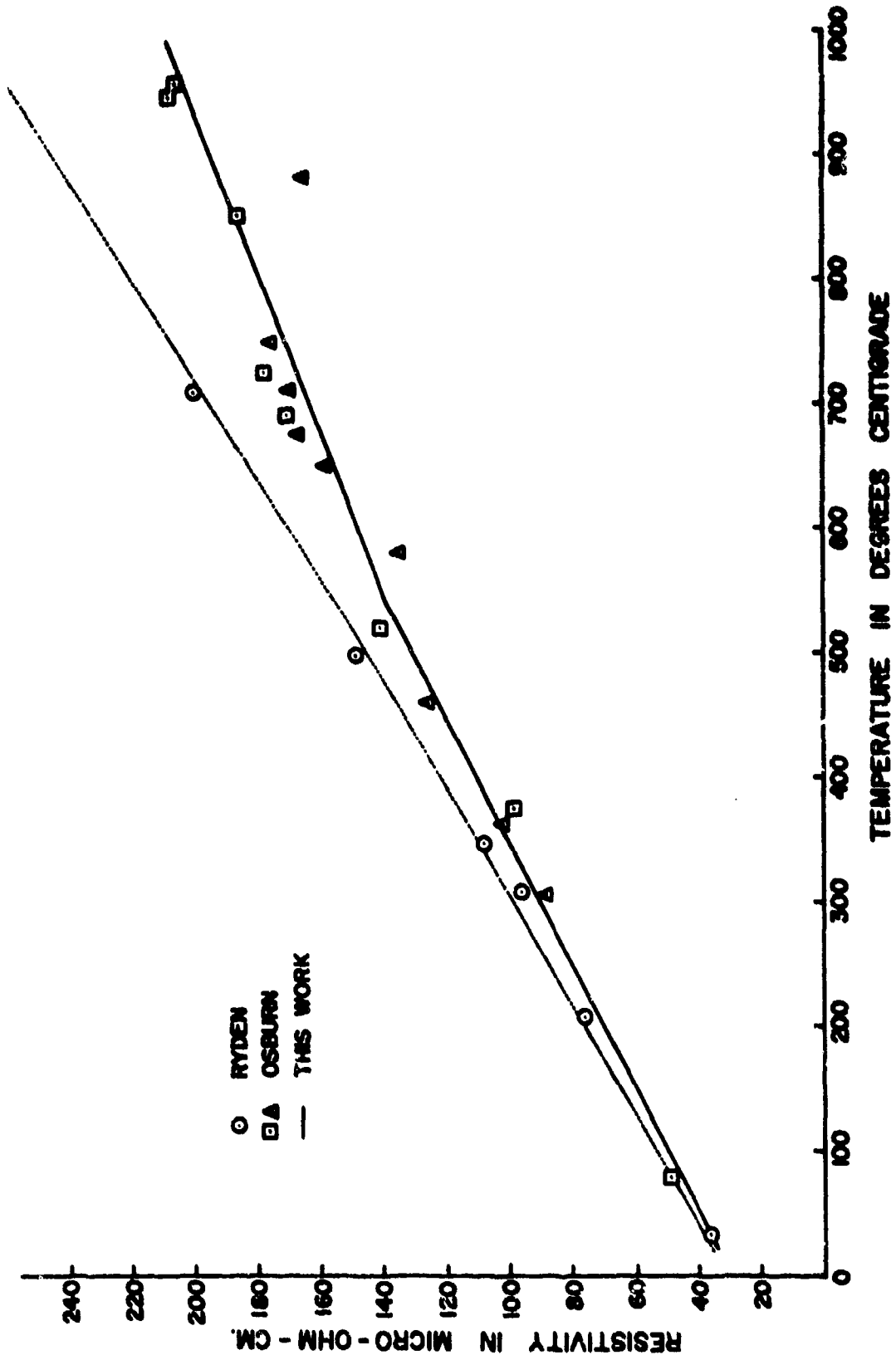
Figure 4.23 High Temperature Resistivity of RuO_2

the results obtained in this work. Ryden's data are clearly different, having an increasing slope for increasing temperature. The calculated resistivity matching Ryden's data has an increasing slope because of the $\rho_2 T^2$ term, that is, because of the electron-electron scattering. A decreasing resistivity as observed here is not common among metallic conductors but the resistivity of platinum and palladium has a similar temperature dependence.

It should also be mentioned that the low temperature (<300°K) data of Ryden et.al. plus the high temperature resistivity data obtained as part of this work can also be fit by including a non-trivial electron-phonon intraband scattering term. The fit is only good up to about 550°C where the decreasing slope causes a deviation. However, the curving high temperature resistivity as represented by the two straight line segments of Fig. 4.23 can be approximated well by having the value of the interband electron-phonon scattering term be constant. The significance of this would be that interband scattering becomes saturated and constant above 540°C leaving only intraband electron-phonon scattering and interband electron-electron scattering to be temperature dependent. A phenomena such as this might happen slowly resulting in curvature rather than an abrupt change in slope. Unfortunately, there is presently no theoretical support for such a model.

The conclusion that RuO_2 does not obey Mattheisson's rule was based on the resistivity measurements of just one crystal. Several other crystals with smaller residual resistance ratios were measured, and all obeyed Mattiesson's rule. The crystals measured in this study were also observed to obey Matthiesson's rule. Final resolution of this question must await a more quantitative description of scattering mechanisms in RuO_2.

The conclusion that RuO_2 has isotropic resistivity was based on a comparison of samples cut from platlet habits of RuO_2 crystals to the more common rod shape oriented along the c axis. The data points shown in Fig. 4.21 were obtained from both types of samples. This disagrees with the results of Fletcher, et.al., [52] who report anisotropy. They obtained resistivities in the 101 plane of 48.4 $\mu\Omega$-cm in the a direction and 67.9 $\mu\Omega$-cm in a direction at right angles. Several parameters, such as effective masses [67] of electrons have been found to be anisotropic so it would not

be surprising if the resistivity was also anisotropic.

4.1.4.5   Contact Resistance of Powder

Since one of the proposed models for the conduction mechanism in thick film resistors involves changes in contact resistance between adjacent conductive particles, it is important to determine the change in contact resistance with temperature and pressure in the absence of extraneous factors such as interactions between the conductive and the glass in order to determine the relative contribution of this mechanism. To obtain the necessary data, the resistance of RuO_2 powder compacts was measured as a function of isostatic pressure and temperature.

The samples were fabricated by isostatically pressing RuO_2 powder in a 5 mm diameter cylindrical rubber mold to 55,000 psi in order to develop sufficient green strength. Two 0.13 mm diameter, platinum wires were wrapped around the sample along its axis to serve as potential leads, and two platinum plus 10% rhodium wires were wrapped around the sample near its ends to serve as current leads, and also, in conjunction with the platinum wires, as a temperature measuring thermocouple.

It was necessary to encapsulate the sample in a pliable mold so that isostatic conditions could be realized when immersed in the pressure transmitting fluid. After consultation with the supplier it was learned that Silastic 733RTV is completely impervious to hydrocarbons, and this material was then used as a sample encapsulent. A solution of 26.5 w/o diphenyl and 73.5 w/o diphenyl oxide (purchased as Dowtherm A) was found to be more dense than water (the pressure transmitting fluid) at all temperatures and pressures of interest. The sample was then placed in a high pressure cell fitted with electrical feed - throughs and filled with Dowtherm A. No mixing of the water and Dowtherm A was observed throughout the experimental program.

The resistivity at room temperature as a function of pressure for one sample is shown in Fig. 4.24. The magnitude of the resistivity in Fig. 4.24 when compared to that of crystalline RuO_2 at room temperature (3.4×10^{-5} Ω-cm) indicates that only contact resistance is being measured. As would be expected for samples of this type the repeatability of the
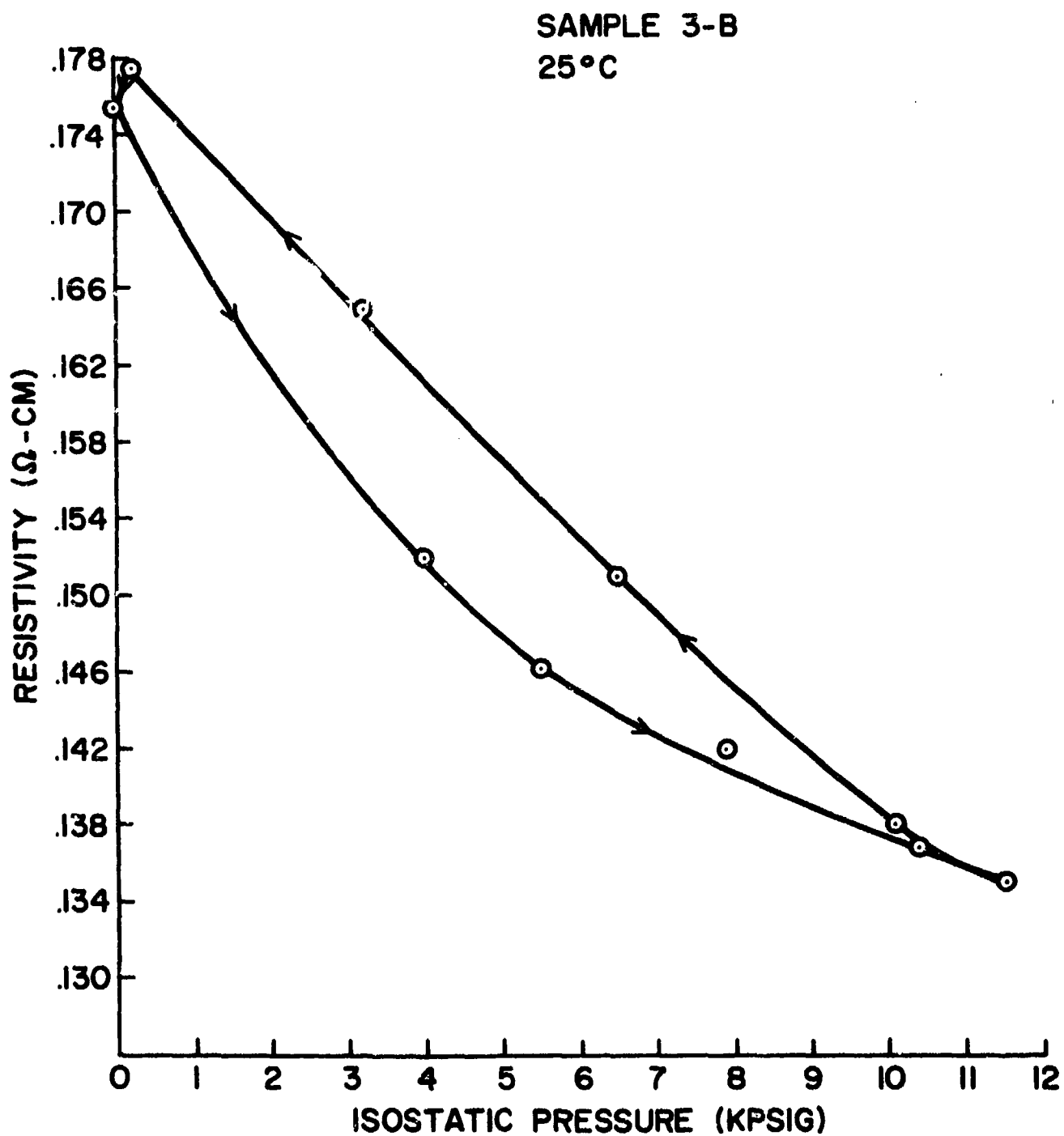
Figure 4.24   Resistivity versus Isostatic Pressure of a
                Compacted Sample of RuO_2 Powder

reaistivity - pressure data was poor. Howeyer, for four different samples,
each of which was cycled many times, the resistance change was never as
great as a factor of two and usually much less over the pressure range
0-12,000 psi.

The ratio of the resistivity at zero pressure to the resistivity at
12,000 psi for sample 3E is given in the following table for various
elevated temperatures.

Run No.	$T(°C)$	$R_o/R_{12,000}$
4	101	1.08
5	64	1.09
6	35	1.09
7	36	1.06
8	104	1.08
9	115	1.09
10	125	1.06
12	50	1.02

The pressure coefficient of contact resistance is small and essentially
temperature independent. Accurate values for the temperature coefficient
of contact resistance at constant pressure could not be obtained because
the changes in contact resistance resulting from pressure cycling were
greater than the changes due to temperature. However, it can be concluded
that the temperature coefficient of contact resistance is near zero and
in no case can it be greater than $\pm$ 300 ppm/°C.

4.1.5   Screening Agents and Formulations

Screening agents are organic liquids blended with the glass and other
inorganic powders so that the resulting formulation or ink will have the
proper rheological characteristics to be deposited onto the substrate in
the desired patterns. Screening agents usually consist of at least a
polymer dissolved in a solvent so that the films can be dried to be
mechanically durable.

The rheological properties of the complete formulation, screening
agent plus inorganic powder, influences the screen printing operation, and

there are two, somewhat separate steps to this operation. One is the transfer of fluid through the screen; this creates a non-uniform film consisting of cylinders separated by depressions caused by the screen wires. The second step is the leveling of the surface, hopefully without bleeding that would increase the area of the pattern. The viscosity requirements for these two steps are not necessarily the same.

Trease and Dietz [68] have estimated that the shear rate during screen printing is about 1000 sec^{-1}, and that the shear rate during leveling is about 0.1-0.01 sec^{-1}. They then evaluated the printing quality of several commercial formulations and compared the results with viscosity measurements at 100 sec^{-1} and 0.1 sec^{-1}, a convenient range for their instrument. They found that good transfer of material to the substrate required viscosities less than 500 poise at 100 sec^{-1} and that good leveling without bleedout required viscosities greater than 30,000 poise at 0.1 sec^{-1}. This approach is oversimplified; for example, leveling and viscosity are only partially related to one another since leveling is a surface phenomena and viscosity is a bulk property. That is, leveling can be changed with surface active (leveling) agents that do not appreciably affect viscosity. Nevertheless, their conclusions furnish a useful starting point in formulation development.

Screening agents for use in thick-film formulations are commercially available; presumably, they have been blended for optimum performance in terms of bleed-out, leveling, etc. Unfortunately, these materials are propietary and chemically complicated so that their effect on the screened films during drying and firing is not clear. To minimize this type of uncertainty a screening agent was developed that is chemically simple though not optimum in other respects. Ethyl cellulose was chosen as the resin because its use in thick film formulations has been reported frequently in the past. The name ethyl cellulose does not represent an exact chemical formula, rather a family of materials that differ in the percent ethoxyl content. The substitution that takes place in the formation of the material is oxygen bonded ethyl groups in place of three hydroxyl groups per monomer unit. In general, the useful range of substitution is about 2.15 to 2.60 ethoxyl groups per unit or 43 to 50 w/o. The ethyl cellulose used in experimental formulations was obtained from Hercules and is classified as

N-300, designating an ethoxyl content of 47.5-49 w/o, and implying that
a 5% solution in 80/20 toluene/ethanol has a viscosity of 300 centipoise.
Some work was also done with ethyl cellulose of lower ethoxyl content
but it did not dissolve as well in the chosen solvent. No attempt was
made to work with higher ethoxyl contents. The solvent chosen for use
in the screening agent, diethylene glycol monobutyl ether (butyl carbitol)
is not as commonly used but it has a desirable vapor pressure versus temper-
ature relationship, and seems to be adequate for use with the resin. A
solution is formed by mixing the ethyl cellulose powder into heated
butyl carbitol to accelerate the dissolution.

To characterize the screening agent a Brookfield Synchrolectric
Model HET micro-viscometer was purchased along with the set of spindles
that are commonly used in the thick-film industry. This permits a com-
parison of the prepared formulations with those that are commercially
available. A Wells-Brookfield cone-plate viscometer attachment was also
obtained in order to measure viscosity or shear stress versus shear rate.
The combination of cones and drive mechanisms permitted the measurement of
viscosity from 216 cps to 1.08×10^6 cps over the range 1 sec^{-1} to 750 sec^{-1}
although, of course, the two parameters are interdependent.

Figure 4.25 shows the viscosity versus shear rate for three different
concentrations of ethyl cellulose in butyl carbitol. The slopes of the
lines indicate that the screening agents are slightly pseudoplastic, and a
plot of shear rate versus stress shows that there is no observable yield
value. An attempt was made to form a ten percent solution but there was
some indication that not all of the ethyl cellulose dissolved.

Figure 4.26 shows the viscosity versus shear rate of a formulation
consisting of a volume ratio of glass to screening agent of 40% using a
screening agent that is 5% by weight ethyl cellulose. Based on earlier
work [68] the formulation is not as pseudoplastic as is desirable but it
has performed adequately and was selected as the standard for formulation
rheology.

Presumably after deposition all of the organics are removed by
evaporation, decomposition, etc. However, to say that the screenings
agent's only contribution to the manufacturing process is to facilitate
printing is, in general, an oversimplification because the polymer may
not have been completely removed at temperatures where the glass begins
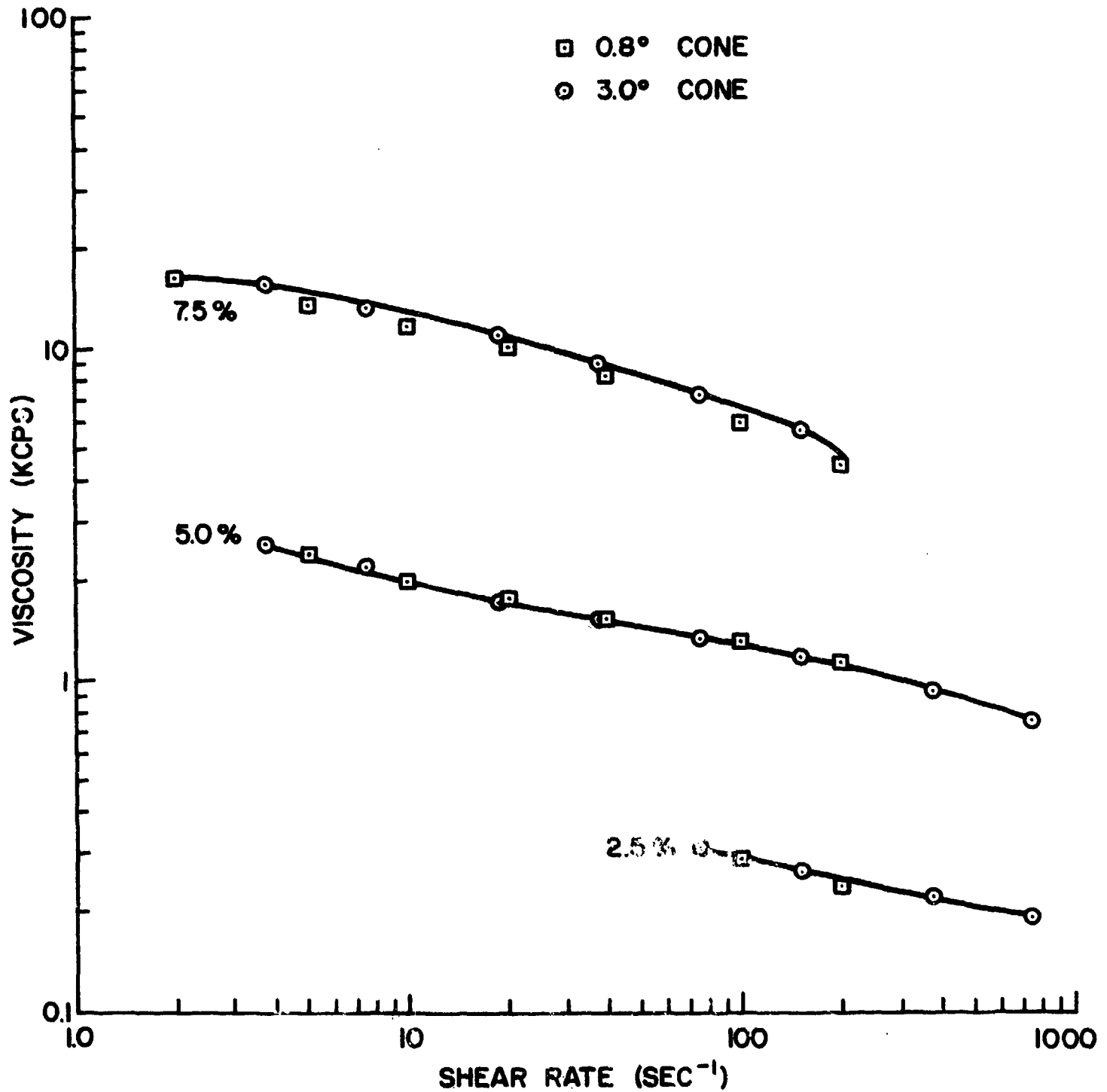
Figure 4.25   Rheological Behavior of Ethyl Cellulose-
Butyl Carbitol Solutions
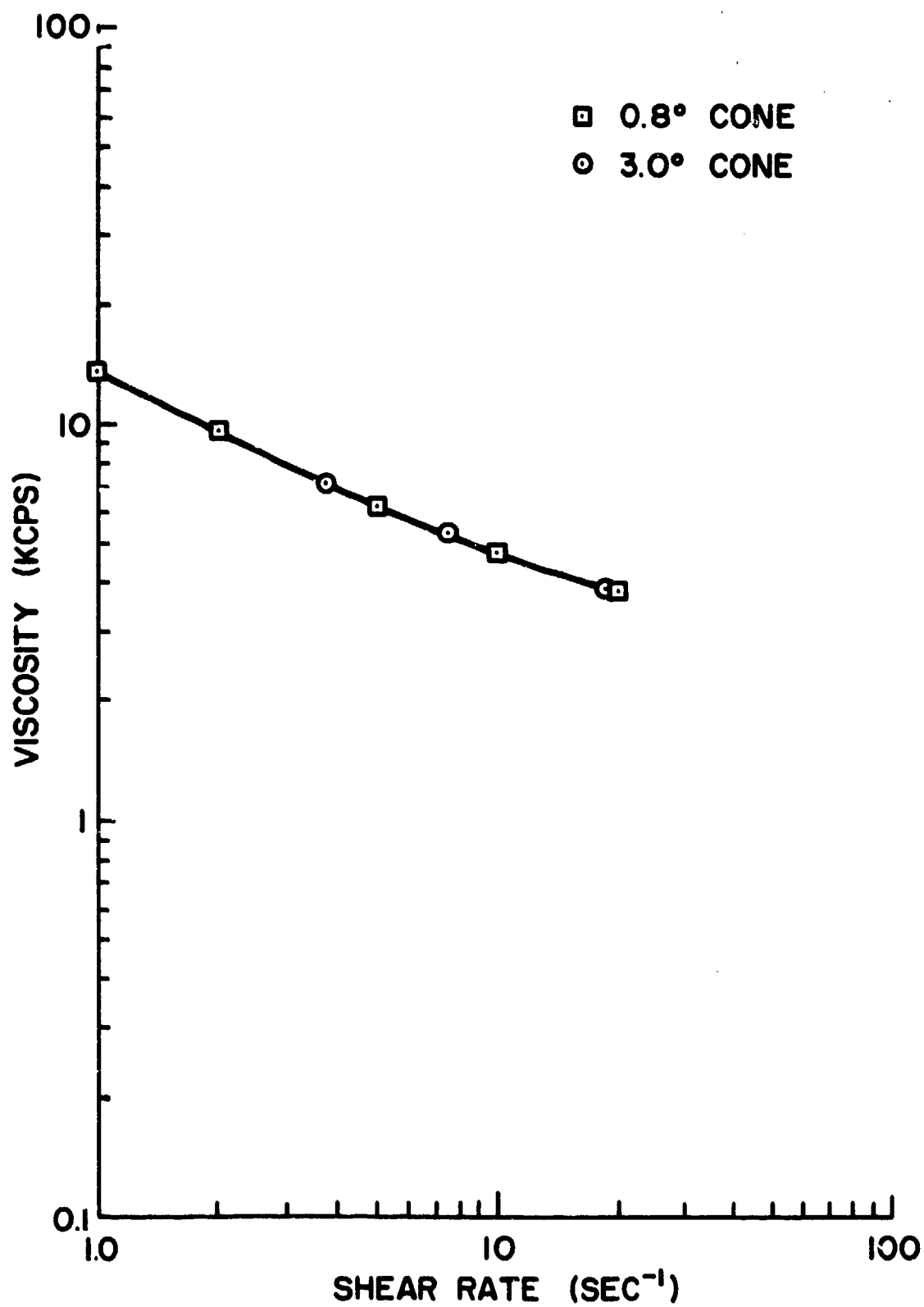
Figure 4.26   Rheological Behavior of a Formulation
Containing 40 v/o Glass

to sinter and/or the polymer must leave by a decomposition process that may require oxygen. It is easy to envision conditions in which some of the oxygen required for the decomposition reaction would come from inorganic compounds in the film thereby changing the composition of the film.

In order to determine the rate of organic removal, a double pan TGA system was constructed that enabled accurate, simultaneous measurements of both sample weight and temperature. The basic system, shown in Fig. 4.27, consisted of two identical pans symmetrically located in a furnace. The sample pan was attached to an automatic, recording Ainsworth microbalance which, with the sample suspended in air, had an accuracy and resolution capability of about 50 µg and an automatic range of 100 mg. All weight changes are detected by a linear variable differential transformer (LVDT), and recorded as a function of time. The second pan was rigidly attached at the same height as the sample pan and a small thermocouple was located adjacent to the duplicate sample to determine the temperature of the sample on the balance pan. Previous tests with various samples and heating rates demonstrated temperature agreement between the two pans to be within 4°C. A thermocouple could not be used on the balance pan during weight measurements because the stiffness of the thermocouple leads from the crucible or hangdown wire to the walls of the system would cause unacceptable errors in weight measurements.

The most meaningful form of weight loss experiment would be with films screen printed onto substrates. However, it was not possible to measure the removal of the last few percent of screening agent, the quantity that is of greatest interest. Consequently, all weight loss measurements were carried out with approximately 40 mg of formulation in small crucibles, 7 mm ID and approximately 10 mm high. The materials investigated by TGA were: (1) butyl carbitol solvent; (2) the screening agent; and (3) screening agent plus $40^V/o$ glass powder (the inorganic content of all printing inks used in other experiments). Evaporation measurements were made under both isothermal and constant heating rate conditions, and in the case of liquid samples, (1) and (2) above, it was possible to determine evaporation rates per unit surface area. Evaporation studies were begun with the volatilization of the solvent.
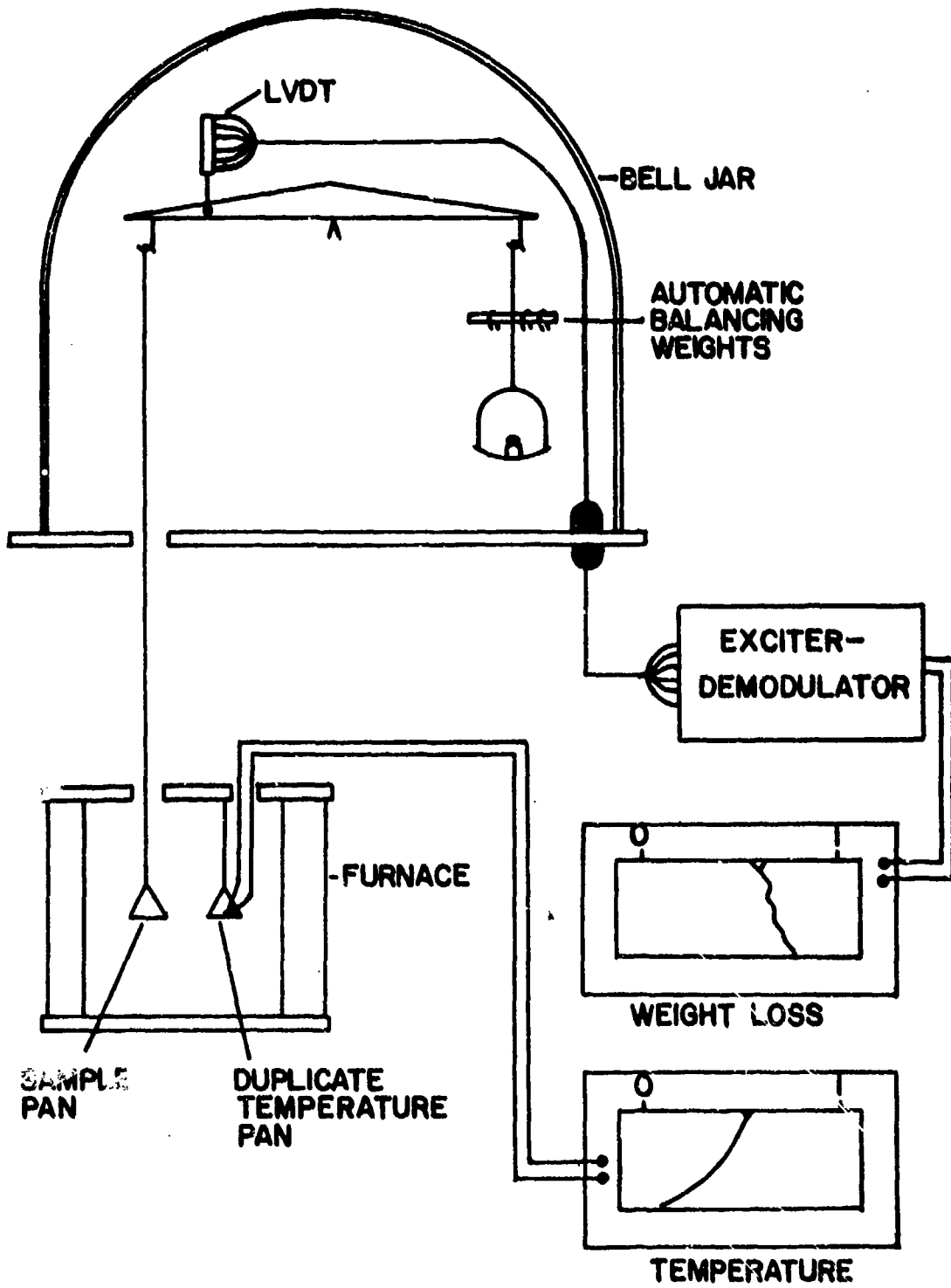
Figure 4.27   Thermogravimetric Analysis Apparatus

For a liquid in equilibrium with the gas phase the kinetic theory of gases gives the evaporation rate (μ) of the liquid as

$$\mu = P \left(\frac{M}{2\pi RT}\right)^{\frac{1}{2}} \text{ gm/cm}^2 - \text{sec} \tag{4.8}$$

where P is the vapor pressure and M is the molecular weight of the gas. The Clausius - Claperon equation relating vapor pressure and temperature,

$$\frac{d \ln P}{dT} = \frac{L}{RT^2} \tag{4.9}$$

where L is the latent heat of vaporization, can be integrated to give

$$P = Ae^{-L/RT} \tag{4.10}$$

where A is the constant of integration. Substituting Eq. 4.10 into Eq. 4.8 gives

$$\mu = Ae^{-L/RT} \left(\frac{M}{2\pi RT}\right)^{\frac{1}{2}} \tag{4.11}$$

which can be rearranged into the form

$$\ln \left(\mu T^{\frac{1}{2}}\right) = \frac{-L}{RT} + \frac{1}{2} \ln \left(\frac{A^2 M}{2\pi R}\right) \tag{4.12}$$

for a graphical determination of the constants L and A; a plot of $\ln \left(\mu T^{\frac{1}{2}}\right)$ versus 1/T should be a straight line with a slope of -L/R and an intercept of $\frac{1}{2} \ln (A^2 M / 2\pi R)$. Figure 4.28 shows the isothermal evaporation rates of butyl carbitol at constant temperature plotted in the form of Eq. 4.12 for temperatures low enough for convenient equilibrium conditions, and it can be seen that the solvent evaporates in the predicted manner. However, other measurements have shown that in the presence of ethyl cellulose and glass the evaporation of the solvent does not obey the relationship of Eq. 4.12.

Figure 4.29 shows the reciprocal of the evaporation rate of the solvent at constant temperatures versus percent of solvent remaining, and shows that the rate is constant until the last few percent when the surface area decreases. In an ideal evaporation process a solution of ethyl cellulose and solvent should evaporate at a constant rate equal to the solvent alone until only ethyl cellulose remains, in this case, $5^w/o$. However, Fig. 4.29 shows that the presence of the ethyl cellulose decreases the evaporation rate (the graph shows the reciprocal) especially
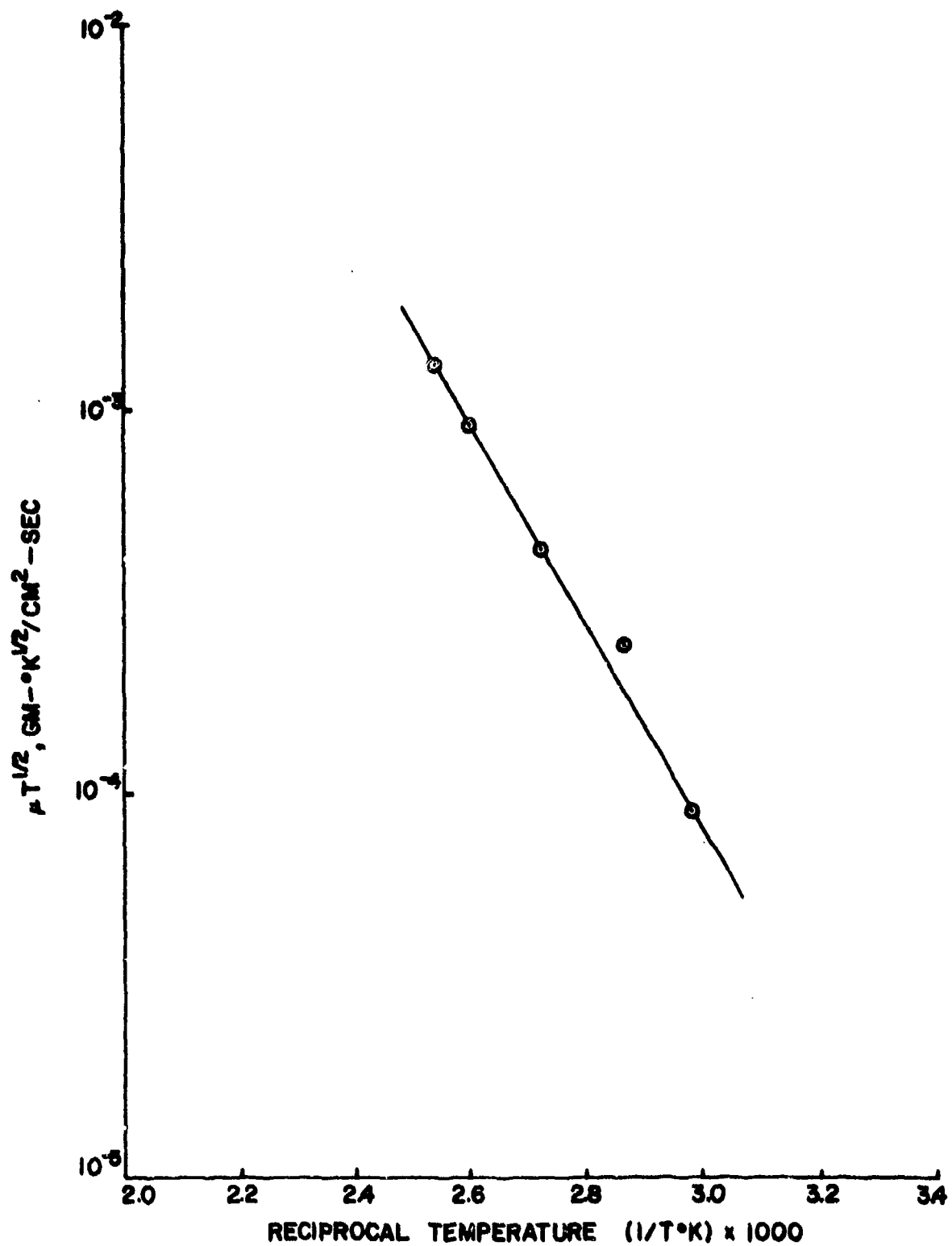
Figure 14

Figure 4.28   Isothermal Evaporation Rate of Butyl Carbitol
Versus Reciprocal Temperature
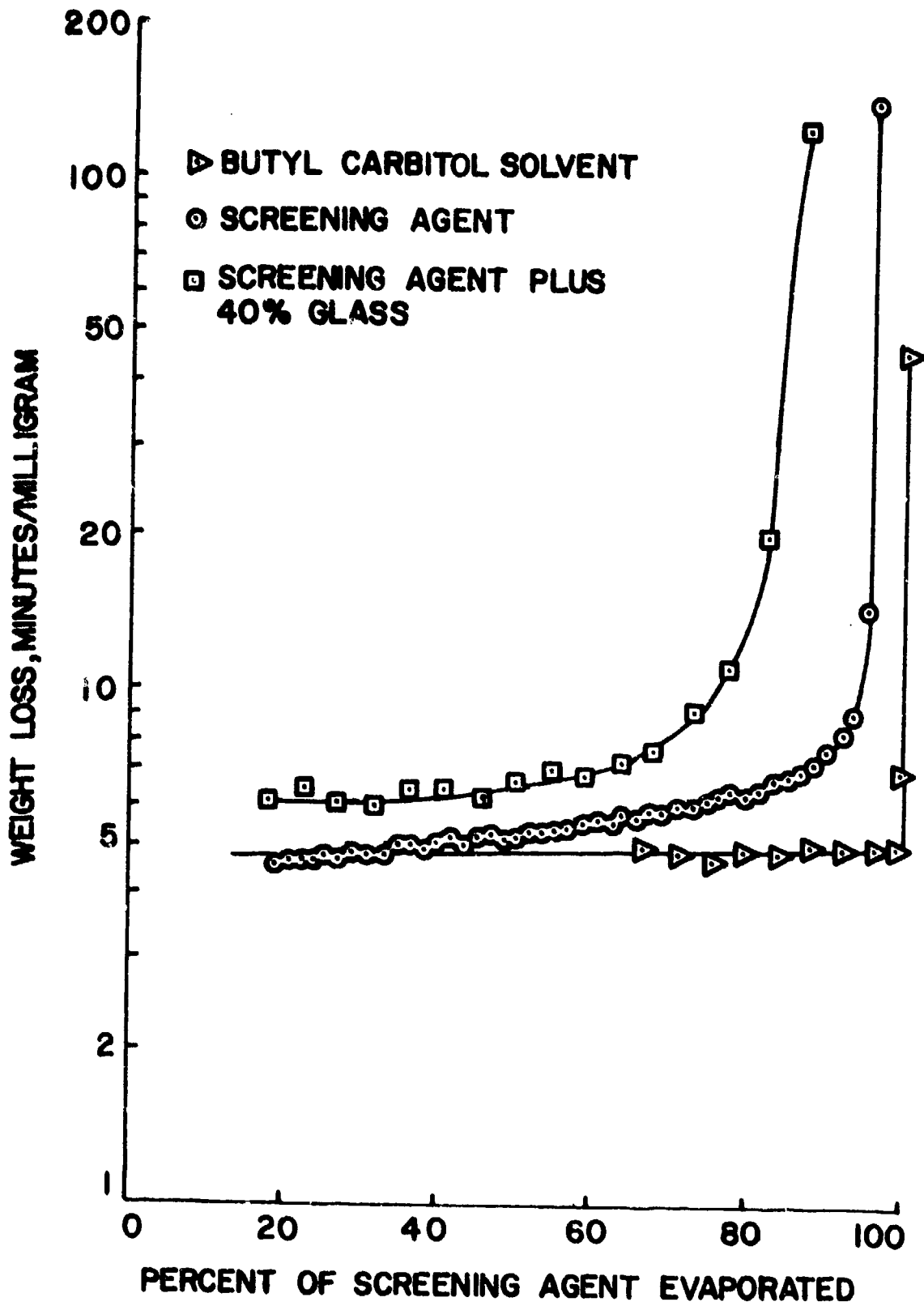
Figure 4.29   Isothermal Evaporation Rate of Screening Agent

at lower solvent contents. This changing rate could be due to a uniform solution that is not ideal or, more likely, to a dry surface layer of ethyl cellulose that impedes the vaporization. The presence of glass has an even greater effect on evaporation rates; the rate begins to decrease significantly when 50% of the solvent has evaporated.

Because of the dependence of evaporation rates on composition of the formulation it was not possible to fit the data to a simple theoretical expression such as Eq. 4.12 and a detailed, scientific study of the vaporization phenomenon was beyond the scope of this project. Therefore, it was decided to adopt an emperical approach to the development of optimum drying procedures. To this end, a sample of screening agent plus 40^V/o glass was dryed at a constant heating rate of $9°C/min$; the results are shown in Fig. 4.30. The weight indicated is total sample weight including glass. At this heating rate it can be seen that the solvent begins evaporating quickly at about 150°C and evaporates at a nearly constant rate from about 180°C to 220°C. The weight change from 260°C to 340°C represents the loss of the ethyl cellulose. This loss of ethyl cellulose has been studied more carefully to determine the rate of loss. For the small samples of glass and screening agent used for all these experiments the rate increased from about 25 μ gram/min at 250°C to about 200 μgram/min at 300°C. Thus, at 300°C all measurable quantities of ethyl cellulose can be removed in several minutes. Unfortunately, visual observation of the dried samples shows that trace amounts of residue from the ethyl cellulose exist even after very long dryings at 300°C. Temperatures in excess of 500°C are required to remove the last traces of organic residue.

In order to make the large number of samples required for the various experiments, several hundred grams of 5 ^{W}/o RuO_2 /glass and 40 ^{W}/o RuO_2 / glass end member pastes were formulated. Pastes with RuO_2 glass content between these end values were then obtained by mixing appropriate quantities of the 5% and 40% pastes. Figure 4.31 shows the viscosity as a function of shear rate for both end members and for a 10% mix prepared by blending appropriate amounts of the end members. These curves agree with that obtained for the glass formulation defined earlier as the viscosity standard. It was necessary to add a small amount of solvent to the 40% RuO_2 paste after formulating with measured quantities of ingredients in order to
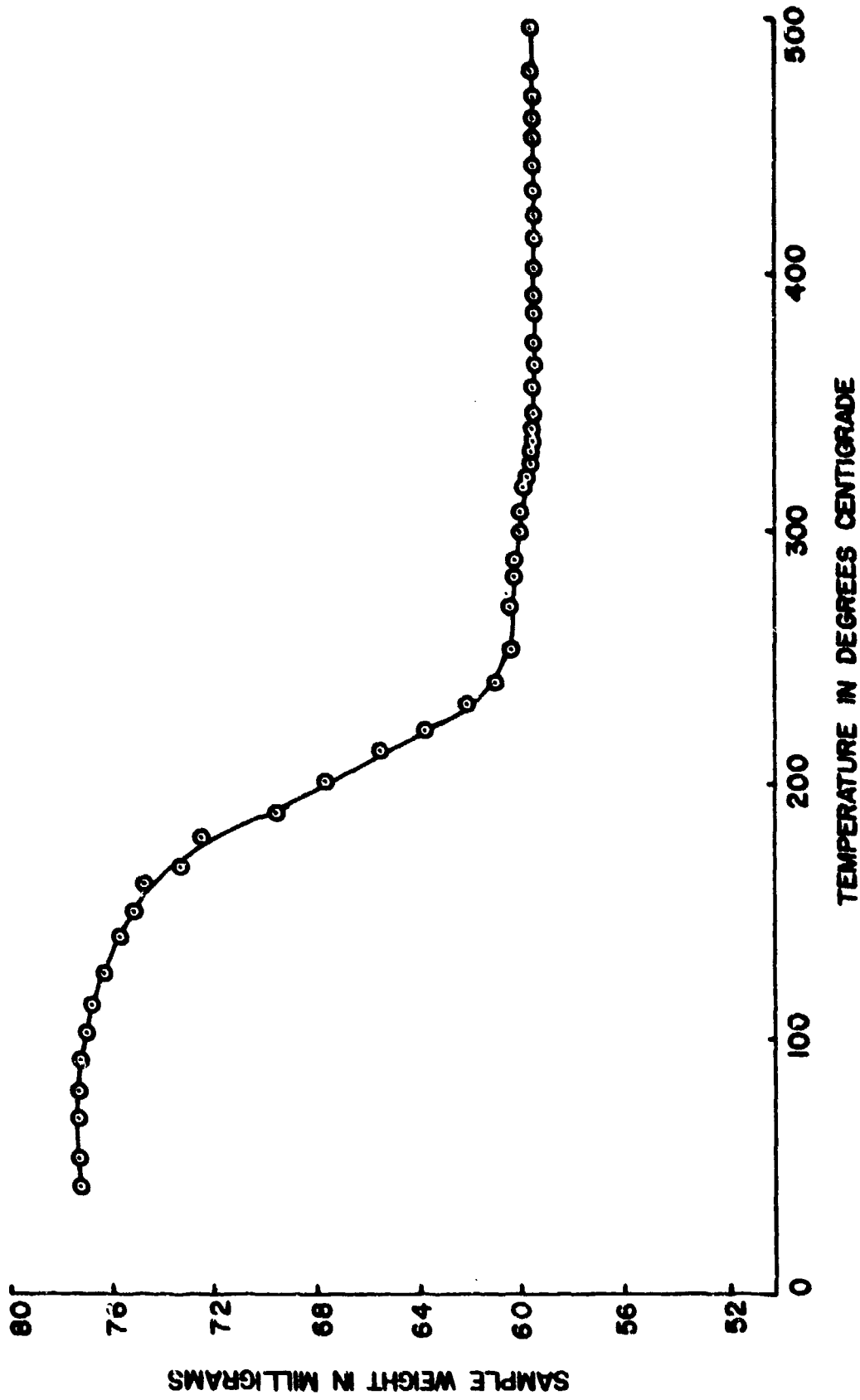
Figure 4.30   Evaporation of Screening Agent at Constant
Heating Rate
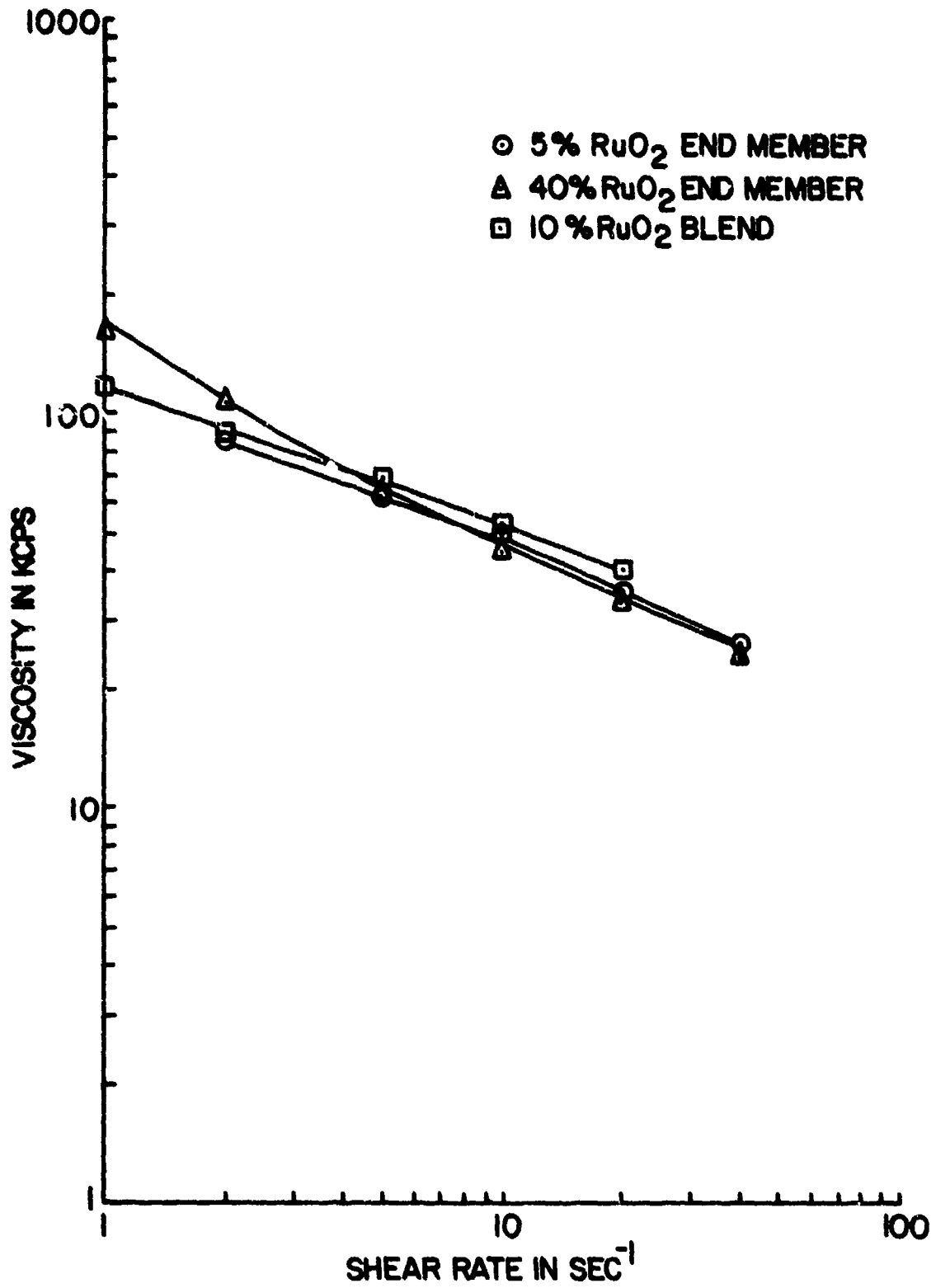
Figure 4.31   Rheological Properties of Resistor Pastes

achieve a match with the viscosity standard, but it is not surprising
that RuO_2 powder imparts different rheological properties to the paste
than does the glass.

4.2 Microstructure Development

4.2.1 Microscopy

The microstructural changes taking place during firing of resistors
were observed with the hot stage video metallograph. The samples for
this purpose were 10 w/o RuO_2 formulation printed on the substrate and
dryed at 300°C for one hour. The samples were then placed in the hot
stage and heated to a maximum temperature of 800°C. The observations
were recorded using either reflected or transmitted light after the sample
temperature reached the softening point of the glass. The turbulent
nature of the resistor during firing was dramatically shown on the video
records. After the glass reached temperatures greater than 600°C,
escaping gas bubbles caused the surface to heave up to tens of microns.
The bubble density at 700°C can be estimated from Fig. 4.32 which shows
the surface of a resistor that had been heated slowly for about 1 hour.
As the temperature was increased (and the glass viscosity decreased) the
bubbles were released with less surface upheaval, but the bubbles were
still observed up to 800°C. In fact, the release of bubbles was observed
for 60 minutes at a constant temperature of 800°C.

Figure 4.33 shows the sequential development of a resistor being
heated at about 10°C/minute, viewed with transmitted light to show the
RuO_2 (dark areas). The primary feature that could be observed was the
agglomeration of RuO_2 resulting in increasing white areas (glass).

Seven resistors containing 10^w/o RuO_2 were screen printed on sub-
strates, dried at 300°C for 20 minutes, and placed in a furnace at 640°C.
The samples were removed from the furnace after 2.5, 4.5, 6.5, 10, 21,
and 72 (2 samples) hours in order to directly analyze the developing
microstructure. The sequential optical photomicrographs (transmitted
light) of Fig. 4.34 show the same type of development shown earlier in
Fig. 4.33. The increasingly larger white areas show a decrease in the
uniformity of RuO_2 dispersion. The magnification of the photomicrographs
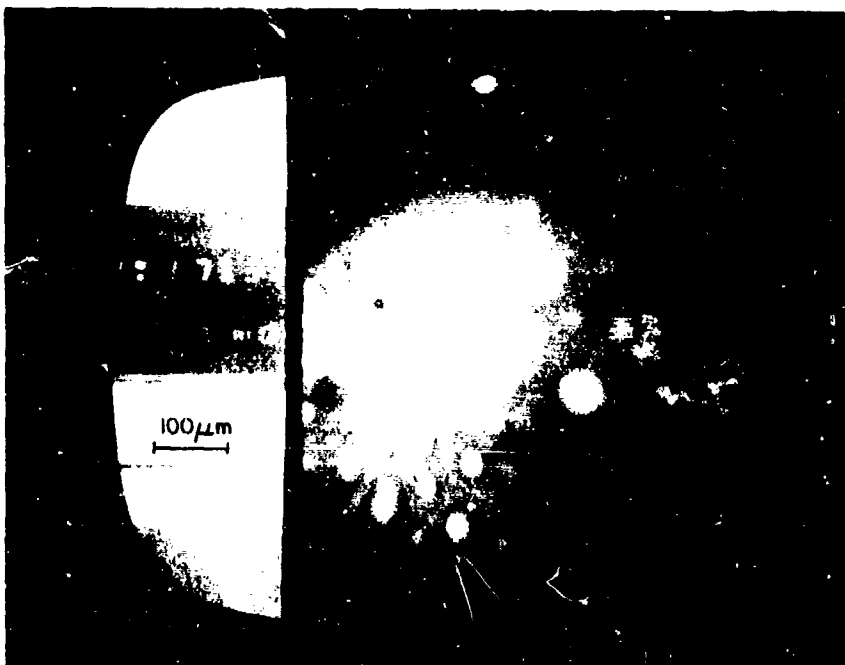
Figure 4.32   Resistor Surface at 700°C Showing
Gas Bubble Density
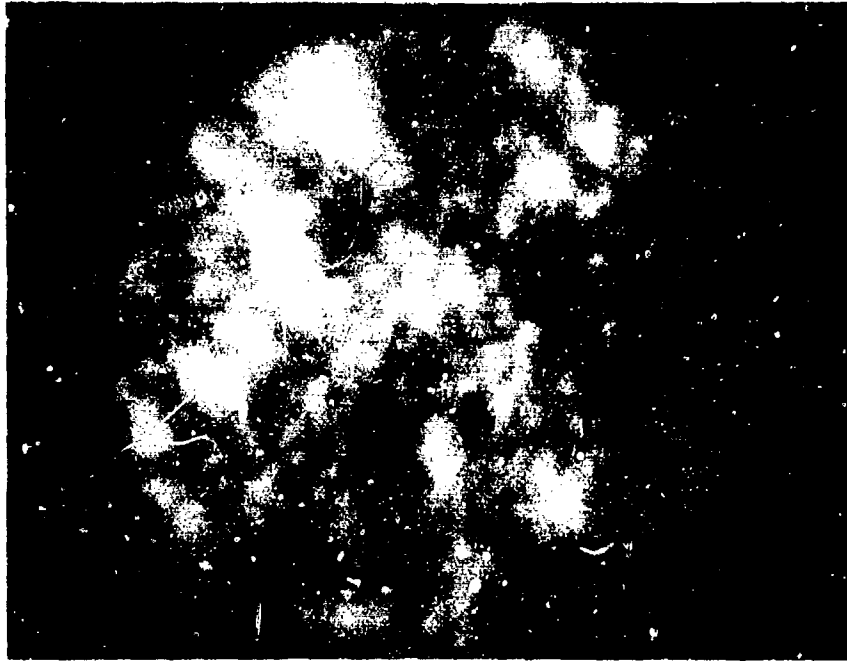
Figure 4.33   Resistor Network Development

a. 4.5 hours
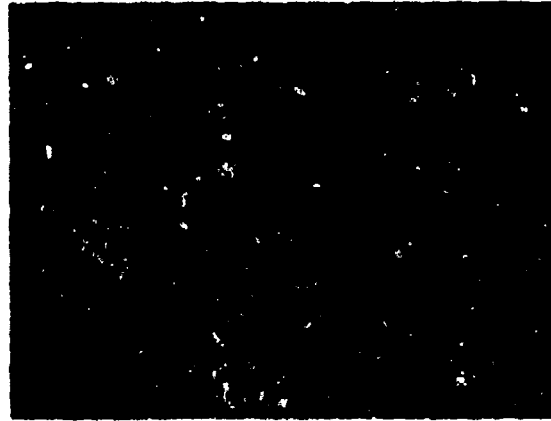
b. 6.5 hours
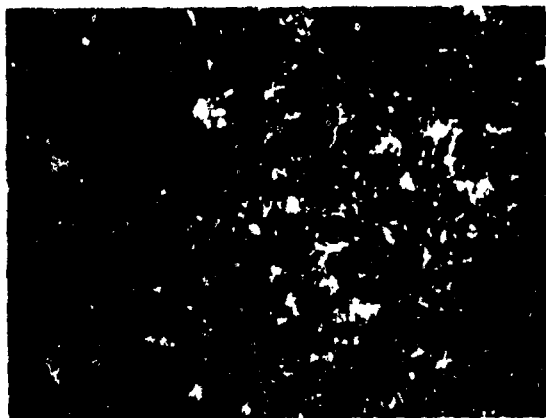
c. 10 hours

d. 21 hours

Figure 4.34   Resistor Macrostructure Development at 640°C (40X)

is only 40X, and details of the microstructure cannot be seen, but the increasing open areas that are void of RuO_2 do represent coursening of the conductive network.

The RuO_2 networks seen in Fig. 4.34 were observed to be continually moving and forming during firing. Figure 4.35 shows four sequential photographs taken from the video monitor on the hot stage. The resistor was at a constant temperature of 800°C, and the elapsed time from Fig. 4.35a to 4.35d is 1 minute, 44 seconds. It was not possible to determine if the branches of the network are actually joining or simply passing above or below each other because of the lack of depth perception, but the rapid motion is evident.

In general, the thick film resistors under consideration consist of a network of ruthenium dioxide particles imbedded in a glass (63% PbO-25% B_2O_3 - 12% SiO_2) matrix, and the glass often masks the structure of the RuO_2, particularly for observations with the SEM. Attempts to apply standard metallographic procedures for producing specimens to be examined with the SEM were not successful, and very few microstructural details of the RuO_2 network could be observed on fractured samples.

An ideal solution to the problem of the glass masking the micro-structure would be to etch the resistor so as to remove some of the glass while leaving the RuO_2 unchanged. Ruthenium dioxide is quite inert, and is not soluble in most etchants, while the lead-borosilicate glass is readily attacked by HCl, NaOH, and to some extent by HNO_3. Sodium hydroxide (concentrated-warm) is extremely reactive with the glass; for example, a resistor completely disappeared after being immersed for one minute in NaOH. Because of this very fast reaction, the concentrated NaOH solution is not a suitable etchant for exhibiting resistor microstructure. The preferred etchant appears to be HCl; etching high lead optical glass with HCl was one of the earliest methods of producing low reflection surfaces, apparently by leaching the lead from the glass surface and leaving behind a surface layer of SiO_x with a refractive index between that of the glass and air. An example of how HCl exposure influences the resistance of a particular resistor is shown by the following results:

Before HCl (concentrated) etch	R = 138 ohms.
After 15 min etch	R = 182 ohms.
After 30 min etch	R = 279 ohms.
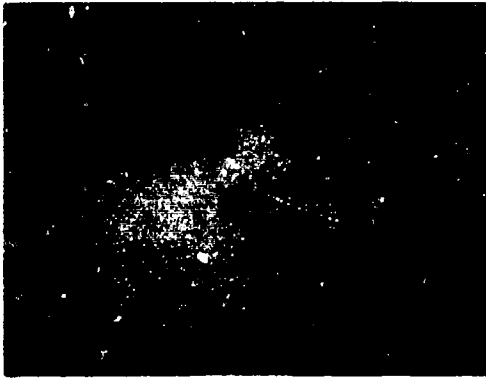
a. 43 minutes, 24 seconds   b. 43 minutes, 48 seconds
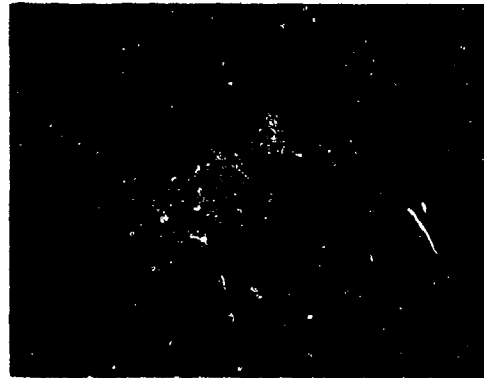
c. 44 minutes, 8 seconds   d. 45 minutes, 8 seconds

Figure 4.35   Macronetwork Formation During Resistor Firing
              on the Hot Stage at 800°C

These and subsequent experiments have shown that for the sample preparation techniques studied the best results on microstructure using the SEM or the optical microscope with reflected light are obtained after heavy etching of the resistor with HCl. If the etching is sufficient, very little lead (in the glass) remains; x-ray spectra for a typical resistor after heavy etching show the presence of Ru, very little Pb, and a significant amount of Si.

Resistor microstructure can be studied using the optical microscope with transmitted light simply by thinning the substrate on a diamond grinding wheel to approximately 10 mils provided the resistor is sufficiently dilute in the conductive phase.

A $5^w/o$ RuO_2 test resistor was printed on the substrate, dried at 220°C for 15 minutes followed by 45 minutes at 300°C, and fired using the standard profile. The sheet resistance of this resistor was 100,000 ohms per square.

The resistor was broken into two parts, and one half was etched in 1:1 HCl for 5 minutes for observation with reflected light. The two photomicrographs of Fig. 4.36 represent regions dilute and concentrated in RuO_2. The grey areas in the photomicrographs are regions rich in RuO_2, but which are out of focus due to the low depth of field at this magnification (720 x). The second half of the resistor was prepared for observation in transmitted light by grinding away the bottom of the substrate to a thickness of approximately 10 mils. The photomicrographs of Fig. 4.37 show the RuO_2 network at four different magnifications (720x, 900x, 1080x, and 1800x). The highest magnification is at the ultimate resolving power of the microscope, but the general structure of the conductive network can be determined.

Some examples of resistor microstructure obtained with the scanning electron microscope (SEM) are shown in Fig. 4.38. The resistors were etched with HCl to remove the lead from the surface of the glass as described above. The glass below the surface of the photographs still contains lead and is therefore opaque. As with the optical micrographs a microstructure of interconnected loops of RuO_2 particles can be observed. Many of the loops appear to be unconnected because they do not lie in the plane of the photograph and part of them is obscured by the opaque, lead containing glass which is responsible for the black background.
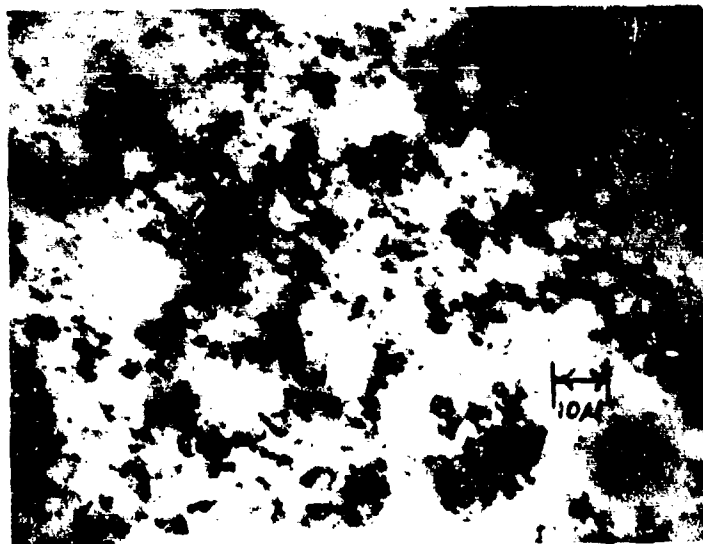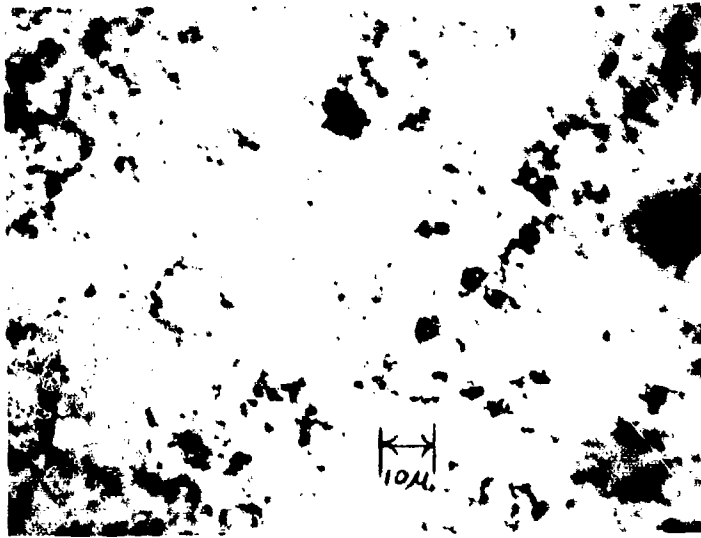
Figure 4.36   Resistor Microstructure: Reflected Light
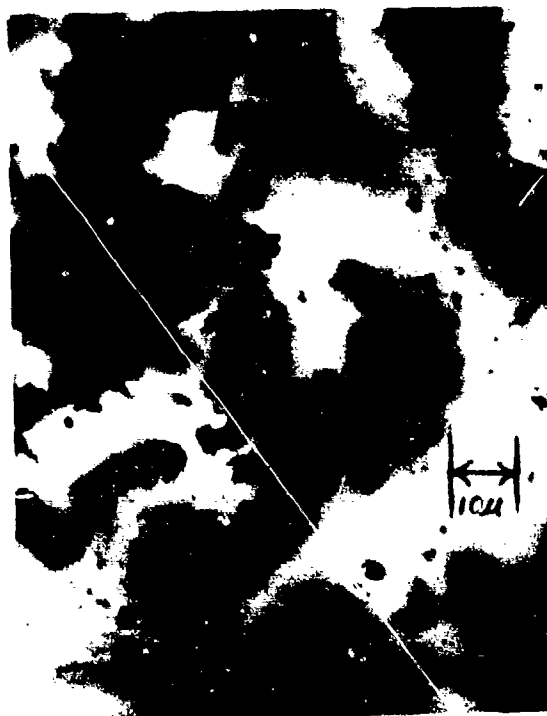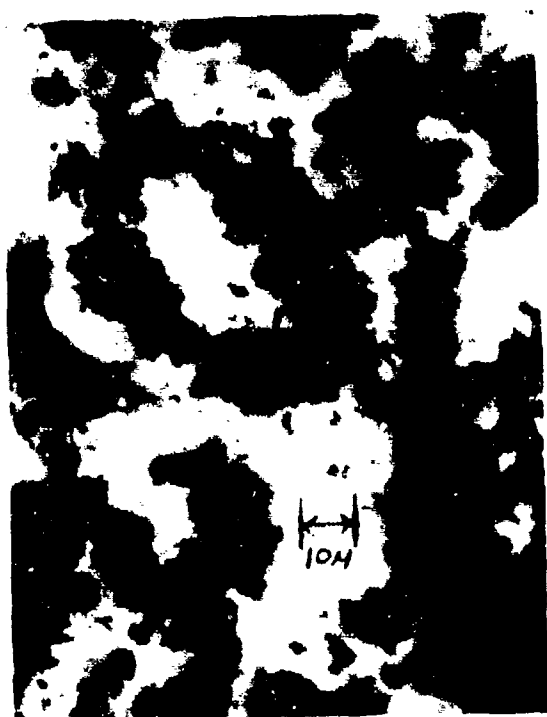
Figure 4.37   Resistor Microstructure: Transmitted Light
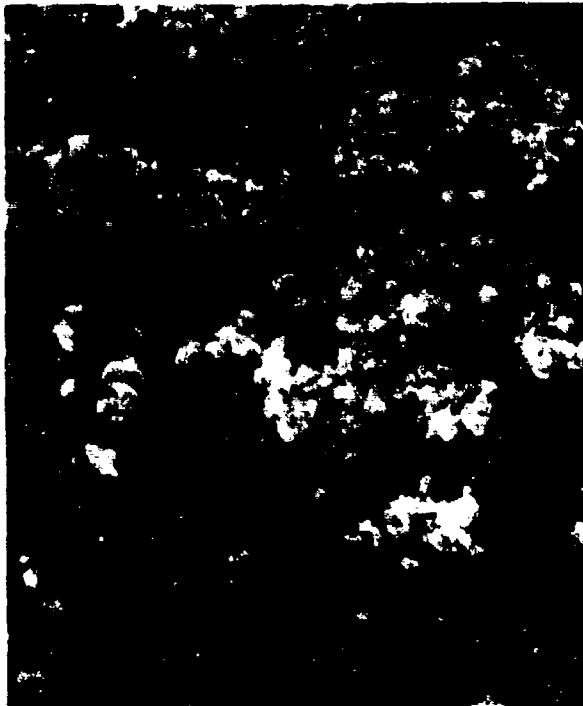
a. 3000x
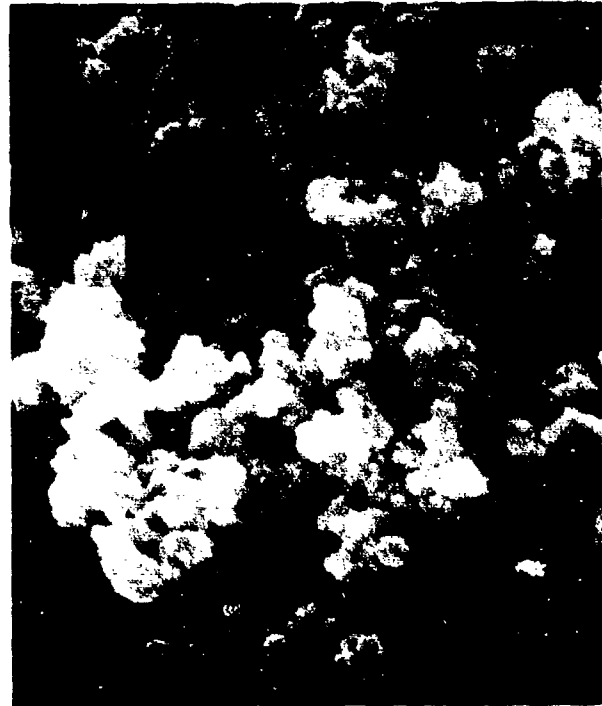
b.10,000x

c. 20,000x

d. 10,000x

Figure 4.38   Scanning Electron Micrographs of Etched Resistors

4.2.2   Solubility of RuO_2 in the Glass

The solubility of RuO_2 in the lead borosilicate glass appears in three of the sintering rate equations, and in two of the ripening equations. The only reported solubility measurements of RuO_2 in any glass were for a family of soda silicate glasses [69, 70]. It was reported that the solubility increased with increasing temperature and with increasing soda content [69], and the solubility at the lowest soda content (20 w/o) and at the lowest temperature (1000°C) was about 50 ppm.

Solubility measurements were made using the RuO_2 powder prepared by drying the hydrate, and lead borosilicate glass frit finely ground in the agate mill. Mixtures containing 10 w/o RuO_2 in the glass were dispersed thoroughly in the ball mill and separated into approximately 10 g samples. These samples were heated in platinum crucibles for either 15 minutes to approximate a typical tunnel kiln firing or 13 hours to obtain the equilibrium solubility. The firing temperatures used for both time intervals were 600, 700, 800, 900 and 1000°C. This temperature range, which was chosen to include the range of maximum temperatures used in kiln profiles, is well above the softening point of the glass. Previous work [71] suggested that the composition of the glass would change very little under these firing conditions. Separate measurements were also conducted to check the weight loss by volatilization. This loss was negligible during 13 hours heating at 600°C and only about 2.15 %/o even after heating for 13 hours at 1000°C. Although RuO_2 can volatalize from the glass [70], it was assumed that the excessive amount of undissolved RuO_2 in the sample replaces any that is lost.

At the end of the heating period the platinum crucibles were quenched in cold water in order to minimize the possibility of any reprecipitation of RuO_2. The quenched samples were treated at room temperature for 24 hours with a solution of 30 ml HCl + 25 ml HF + 25 ml H_2O, including 4 hours of ultransonic agitation. Ruthenium dioxide is not dissolved by either of these acids, but, it was assumed that the dissolved ruthenium in the glass does go into solution along with the constituents of the glass. This assumption was also the basis for the study of solubility of ruthenium in soda silicate glasses investigated by Biswas and Mukerji [69]. The resulting

solution was filtered twice to remove the residue (RuO_2, $PbCl_2$, PbF_4) and the filtrate was heated at $100°C$ until its volume decreased to about 10 ml. The concentrated filtrate was filtered again to remove the residue ($PbCl_2$, PbF_4) and then analyzed for Ru. The residue was also treated with HCl and analyzed for Ru. A blank solution was prepared by treating the RuO_2 powder with HF and HCl in a manner identical with that used for the composite.

The amount of Ru in these solutions was determined using a Perkin-Elmer 303 Atomic Absorption Spectrophotometer after calibration with a ruthenium solution standard. For the concentrations and sample sizes of the experiment the minimum detectable limit for an accuracy better than $\pm 5\%$ was 2 ppm. No detectable amount of ruthenium was found in either the blank solution (verifying an insignificant solubility of RuO_2 in HF and HCl) or in the solutions prepared by subsequent treatment of the precipitate.

The results of the test samples are plotted in Fig. 4.39. As can be seen, the average concentration of Ru in the glass fired for 15 minutes at $800°C$ (typical tunnel kiln firing) is about 5 ppm and even at $1000°C$ the solubility is less than 35 ppm. The Ru concentration measurements for the samples fired at $1000°C$ were repeated starting with a new RuO_2-glass composite to verify the cross-over of the curves. The data points at $1000°C$ in Fig. 4.39 are the averages of the two values obtained and the error symbols show the discrepancy. The larger error occurs at the lower concentration, as expected.

The solution concentration measured by this technique averages the Ru concentration for the glass in the sample both near and far, on a microscopic scale, from the particles of RuO_2; it is unlikely that the concentration of Ru in the glass is uniform after the 15 minutes firing. The activity of RuO_2 at the surface of smaller particles is enhanced leading to an increase in the concentration of solute. Therefore, although all concentrations measured were low, it is possible that the concentration of Ru in solution is large at the particle-glass interface.

The effect of a small particle size on solubility would explain why the concentration of Ru in the glass fired at $1000°C$ is greater after 15 minutes than after 13 hours. During the initial heating, the smallest particles dissolve rapidly creating a super-saturated solution in their
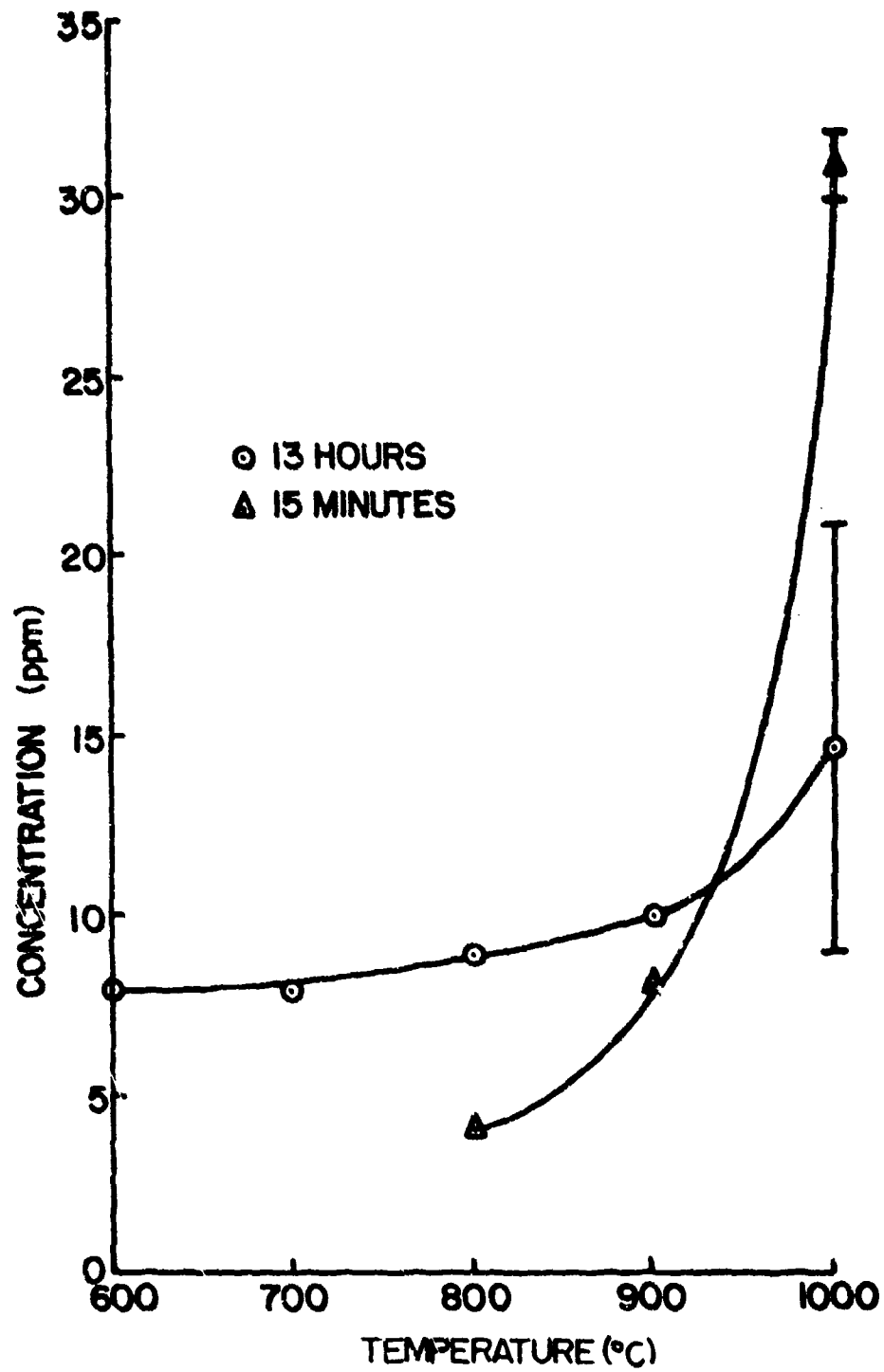
Figure 4.39 Solubility of RuO_2 in Lead Borosilicate Glass

vicinity. Ruthenium then diffuses through the glass and precipitates as RuO_2 on the surfaces of larger particles, eventually decreasing the total ruthenium dissolved in the glass to the equilibrium value.

Figure 4.39 indicates that for fixed time the solubility increases with increasing temperature and the equilibrium solubility varies from 8 ppm at 600°C to about 15-20 ppm at 1000°C. The results seem to be consistent with the earlier work of Mukerji and Biswas [69] for soda silicate glasses. Their prediction for the soda silicate glasses containing 20 w/o Na_2O was about 50 ppm at 1000°C and the trend was one of decreasing solubility with decreasing soda content. Hence one can expect the solubility in lead borosilicate glass to be much lower.

4.2.3   Glass Spreading

The wettability of glass to RuO_2 was studied by contact angle measurements. The RuO_2 single crystals prepared in this study were very small (0.2 mm by 2 mm) and hence could not be used for the contact angle measurements. Instead, it was decided to use sintered compacts made from RuO_2 powder. The powder was pressed in an uniaxial press at 4.1×10^9 dynes/cm^2 in the form of cylindrical pellets 0.5 cm in diameter and about 0.2 cm high. These pellets were heated at 1000°C for 25 hours to obtain sufficient mechanical strength.

The glass frit was placed on the RuO_2 compacts and heated at 700, 800, 900 and 1000°C for different times and photographs of the cooled samples were taken. The schematic of the sample arrangement for making contact angle measurements is shown in Fig. 4.40. As can be seen this arrangement gives the side view of the sample placed between aluminum reference bars.

The photographs of contact angle measurements are shown in Fig. 4.41. As can be seen from Fig. 4.41 (a-d), the contact angle continually decreased on successive heating at 800°C until almost complete wetting was achieved. The observed time dependence was probably due to the high viscosity of the glass at 800°C and hence its slow flow rate. At higher temperatures complete wetting can be seen in much shorter times i.e. with 5 minutes of heating at 900°C (Fig. 4.41e) and 1000°C (Fig. 4.41f). At
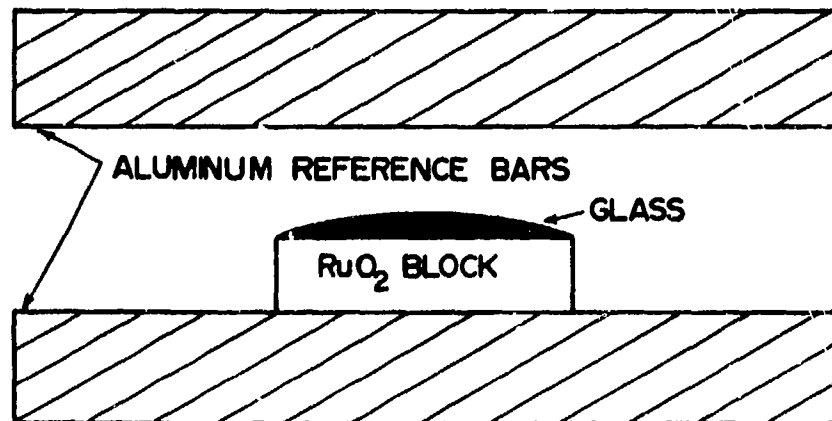
Figure 4.40   Schematic of Sample Arrangement for Wettability Study

154

a. 800°C, 3 minutes
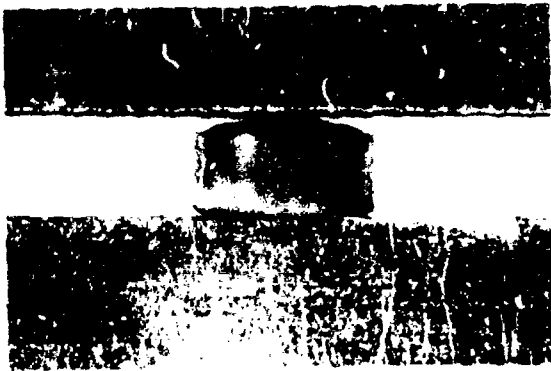
b. 800°C, 8 minutes

c. 800°C, 18 minutes

d. 800°C, 28 minutes
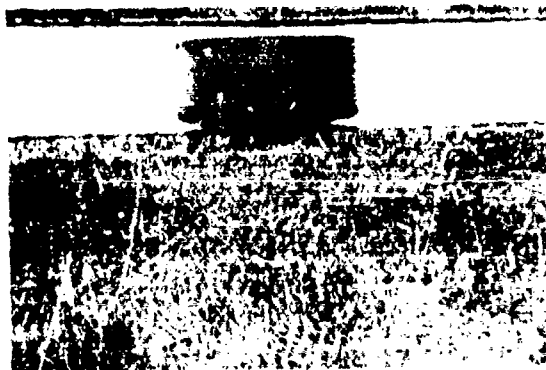
e. 900°C, 5 minutes
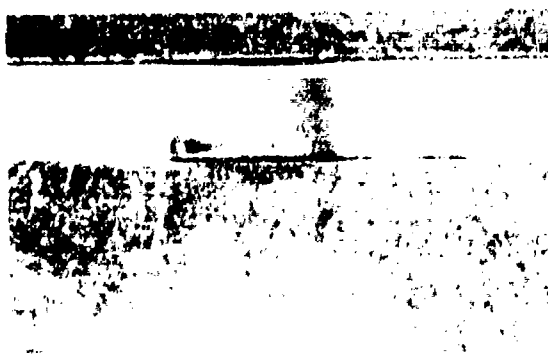
f. 1000°C, 5 minutes

Figure 4.41   Wetting of RuO$_2$ by Lead Borosilicate Glass

lower temperatures, the viscosity of the glass is very high and hence a long time is required for it to flow completely.

The glass heated at the lower temperatures on RuO_2 had small air bubbles entrapped inside. These closed pores due to entrapped air will be eliminated only if the capillary pressure is greater than the air pressure and the kinetics of this process are mainly controlled by the viscosity. Even after heating for 30 minutes at 700°C, the contact angle remained high. Heating for very long times resulted in the flow of glass through the pores of the RuO_2 compact and no glass remained on the surface. This penetration of the RuO_2 particles by glass would not have been possible without good wetting.

The above observations indicated that the glass completely wets RuO_2, the flow of glass being controlled by viscosity. Pask and coworkers [34] reported that the contact angle under chemical equilibrium conditions could be different from the contact angle under nonequilibrium conditions due to the saturation of the liquid phase with the dissolved phase. This is an important factor because the change in the wetting characteristics due to dissolution of RuO_2 in the glass could affect further microstructure development. In order to study this effect, glass saturated with dissolved ruthenium was prepared by heating a well dispersed mixture containing 1 w/o RuO_2 and 99 w/o glass in a platinum crucible at 900°C for one hour and 16 hours and quenching in distilled water to make the frit. Quenching ensured that the dissolved ruthenium did not precipitate out. Contact angle measurements were conducted using this frit and the results obtained on the samples heated at 800°C are shown in Fig. 4.42, and are seen to be similar to those obtained without any dissolved RuO_2 in the glass (Fig. 4.41 [a-d]). At 800°C there was a gradual decrease in the contact angle on successive heating whereas at 900 and 1000°C complete wetting occurred in a very short time. Hence, it can be concluded that there is no effect on the wetting characteristics of the glass due to dissolution of RuO_2 in it.

Addition of impurities can also change the wetting characteristics [72]. The only impurity addition in this system occurs from the substrate material during the firing of the resistors. The glass-substrate interactions might change the composition of the glass and the wettability. In order to check for this possibility, contact angle measurements were conducted using glass previously treated with the substrate material.

800°C, 3 minutes   800°C, 8 minutes   800°C, 18 minutes

a.   Glass Treated with RuO_2 for 1 Hour

800°C, 3 minutes   800°C, 8 minutes   800°C, 18 minutes
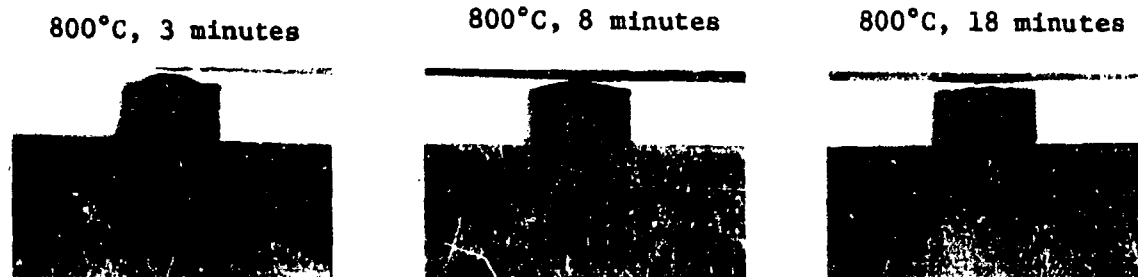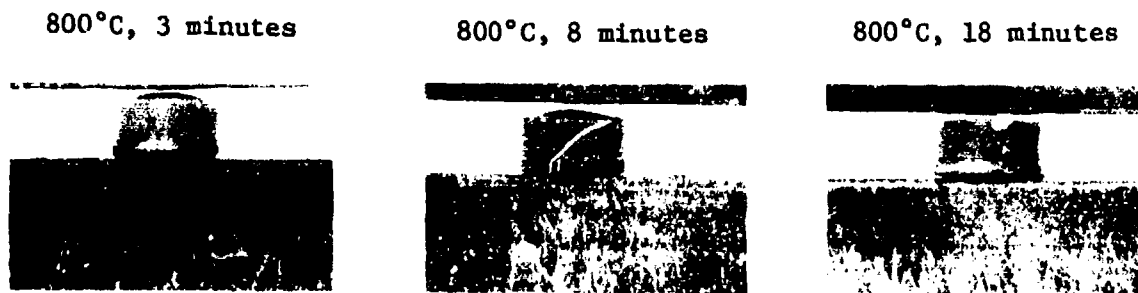
b.   Glass Treated with RuO_2 for 16 Hours

Figure 4.42   Wetting of RuO_2 by Lead Borosilicate Glass
                Treated with 1 w/o RuO_2.

AlSiMag 614 (96 w/o alumina) substrates were ground and sieved to pass through a 325 mesh screen and mixed with the glass. This well dispersed mixture containing 10 w/o substrate material and 90 w/o glass was placed in the platinum crucible, heated at 800°C for 16 hours, and quenched to make the frit. The resulting glass did not indicate the presence of any undissolved substrate material or the formation of any new crystalline phases. The results of the contact angle measurements with this glass (Fig. 4.43) also showed that the contact angle decreased on successive heating at 800°C. As can be seen, it takes a longer time at 800°C for the glass to flow completely as compared to the case where no substrate material is involved (Fig. 4.41 [a-d]).This observation is probably associated with the higher viscosity due to the addition of the substrate material. Complete wetting was achieved in 5 minutes when heated at 900 and 1000°C.

Though this study has been qualitative in nature, it does give all the necessary information about the wettability of glass to RuO_2. In general, it can be concluded that at equilibrium the glass completely wets RuO_2 and the equilibrium wetting is not affected by either the saturation of the glass with ruthenium or the dissolution of the substrate material.

4.2.4   Sintering of RuO_2

Most of the initial stage liquid phase sintering studies have been conducted by shrinkage measurements. Investigations involving the direct observation of the neck growth between the solid phase particles in the presence of the liquid phase have not yet been reported. This type of study involves dispersing the solid phase particles in the binder phase and observing the neck growth between the particles that are touching each other at temperatures beyond the melting point of the liquid phase. Hot stage microscopy is a good tool for such an observation. The preliminary experiments conducted to observe neck growth between RuO_2 particles (~100 μm) using the hot stage video metallograph are described below.

The RuO_2 particles were mixed with formulation containing only glass and organic screening agent. This mixture was applied to the AlSiMag 614

a. 800°C, 15 minutes
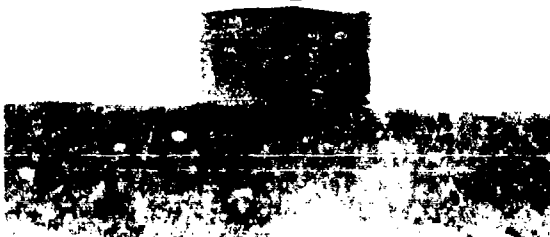
b. 800°C, 30 minutes

c. 800°C, 45 minutes

Figure 4.43   Wetting of RuO_2 by Lead Borosilicate Glass Treated
with 10 w/o AlSiMag 614 Substrate Material

substrate 0.0375 cm thick, dried at 300°C for 20 minutes, and fired subsequently in the hot stage. The molten glass being optically transparent and the substrate being optically translucent, the RuO_2 particles could be easily observed in transmitted light. During initial heating, beyond the softening point of the glass, considerable gas bubbles were observed to form, grow and break at the surface causing the RuO_2 particles to move around in the molten glass. Fig. 4.44 shows a before and after result of the movement on the relative position of the RuO_2 particles.

The set of particles shown in Fig. 4.44 was chosen to observe the neck growth and the heating was continued for about 3 hours at 800°C, but no indication of neck growth was observed. After this experiment it was decided to carry out the heating in an ordinary furnace and to observe the neck growth on the quenched samples. The motive behind this study was to obtain information about the time required for initial neck growth by using many sets of particles at the same time. Having this, one should be able to conduct the same study using the hot stage and obtain more precise data.

Samples were prepared by mixing RuO_2 particles (50 - 300 μm) with either the formulation containing only glass and screening agent or just glass powder. This mixture was placed on the substrate and heated at temperatures as high as 1000°C up to about 100 hours. The samples were pulled out frequently to observe under the optical microscope for any neck growth. In some cases new glass additions were made. The microscopic observations indicated certain changes in the neck area as can be seen in Fig. 4.45. In order to check if these were associated with the neck growth between the particles, the samples were treated with HCl, HF and hot H_2O to remove the glass, whereupon the particles fell apart suggesting that no appreciable degree of sintering between the conductive particles had taken place. Still higher temperatures could not be employed as RuO_2 loss becomes appreciable, and significantly smaller particles could not be used because of limitations in the resolving power of the optical system. Hot stage SEM or TEM could not be easily adopted for the RuO_2-lead borosilicate glass system as the use of vacuum or any inert atmosphere reduces the glass and RuO_2. It was concluded that it
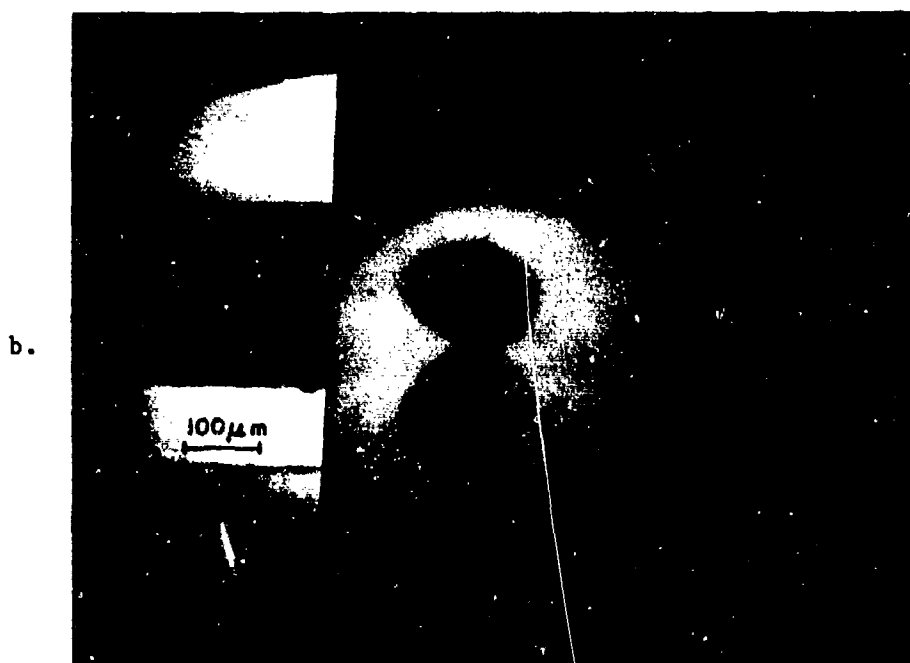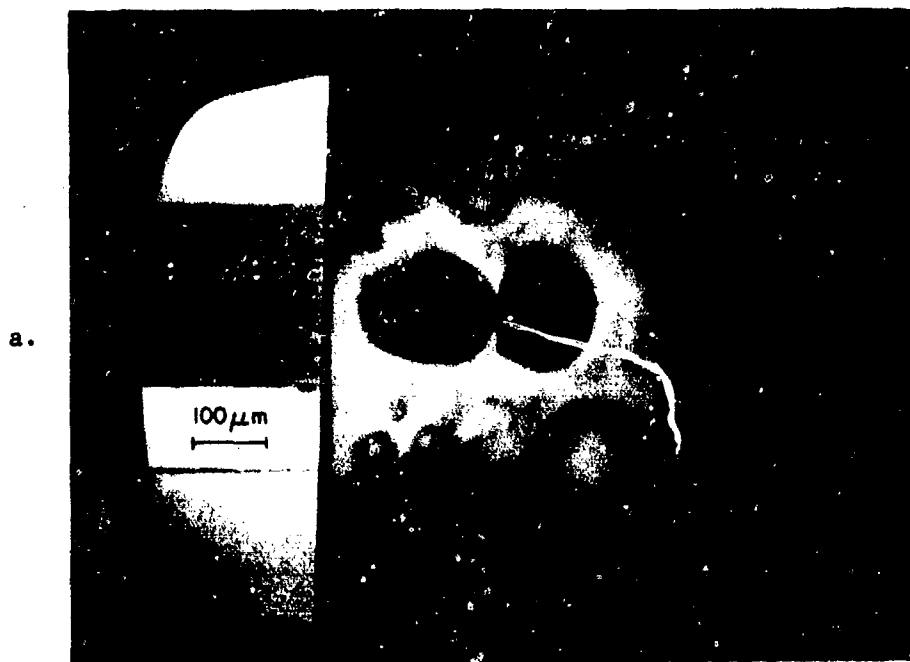
Figure 4.44   Movement of RuO$_2$ Particles in Lead Borosilicate Glass
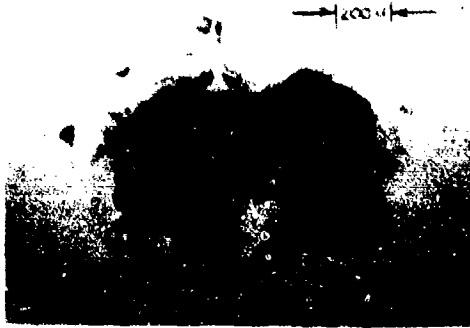
a. 700°C, 10 minutes

b. 800°C, 10 minutes

c. 800°C, 10 Hours
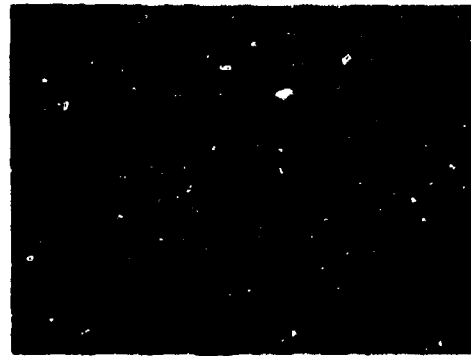
d. 800°C, 50 Hours

Figure 4.45   Successive Stages of Sintering of RuO_2 Particles

would not be possible to get initial stage sintering information by direct observation of neck growth.

Measurements of density and dimension changes of compacts upon heating have the potential of providing information about the initial stages of liquid phase sintering [73]. In order to study the feasibility of this approach for the RuO_2-glass system, preliminary experiments were conducted to record the density changes of compacts of RuO_2 and glass powders after sintering. The mixtures of RuO_2 and glass powders (40 - 80 V/o RuO_2) were dispersed thoroughly in the agate mill and pressed in the form of cylindrical pellets in an uniaxial press or an isostatic press at pressures varying from 2×10^9 - 6×10^9 dynes/cm^2. The pellets were, in general, 0.5 cm long and 0.625 cm in diameter with green densities ranging from 40 - 70% of the theoretical value. These pellets were placed in a platinum boat and fired in a tube furnace at temperatures ranging from 800 to 1000°C. The dimensions of the cooled samples were measured using a micrometer. Figure 4.46 shows the density as a function of time at 800°C for a sample containing 33 v/o glass isostatically pressed at 3.3×10^9 dynes/cm^2 and dried at 300°C for 1 hour. The density in the as dried condition was 46.4% of the theoretical value. As can be seen from Fig. 4.46 the density increase is negligible after 17 hours of heating at 800°C, and even after that the increase is very small. The density changes at much longer periods of heating are not useful to study initial stage sintering because this change is probably associated with the particle growth.

Further experiments were conducted using different compacting pressures and different amounts of glass. The green density increased with increasing compacting pressures, but the change in the density upon initial heating remained negligible.

Microstructural investigation of the fired compacts using SEM revealed considerable closed porosity in the samples as can be seen from Figs. 4.47a and 4.47b. As the firing time was increased the pores increased in size, but the total pore volume did not decrease appreciably. Grinding and reheating the samples increased the density to some extent, but these data do not give any information regarding initial stage sintering.
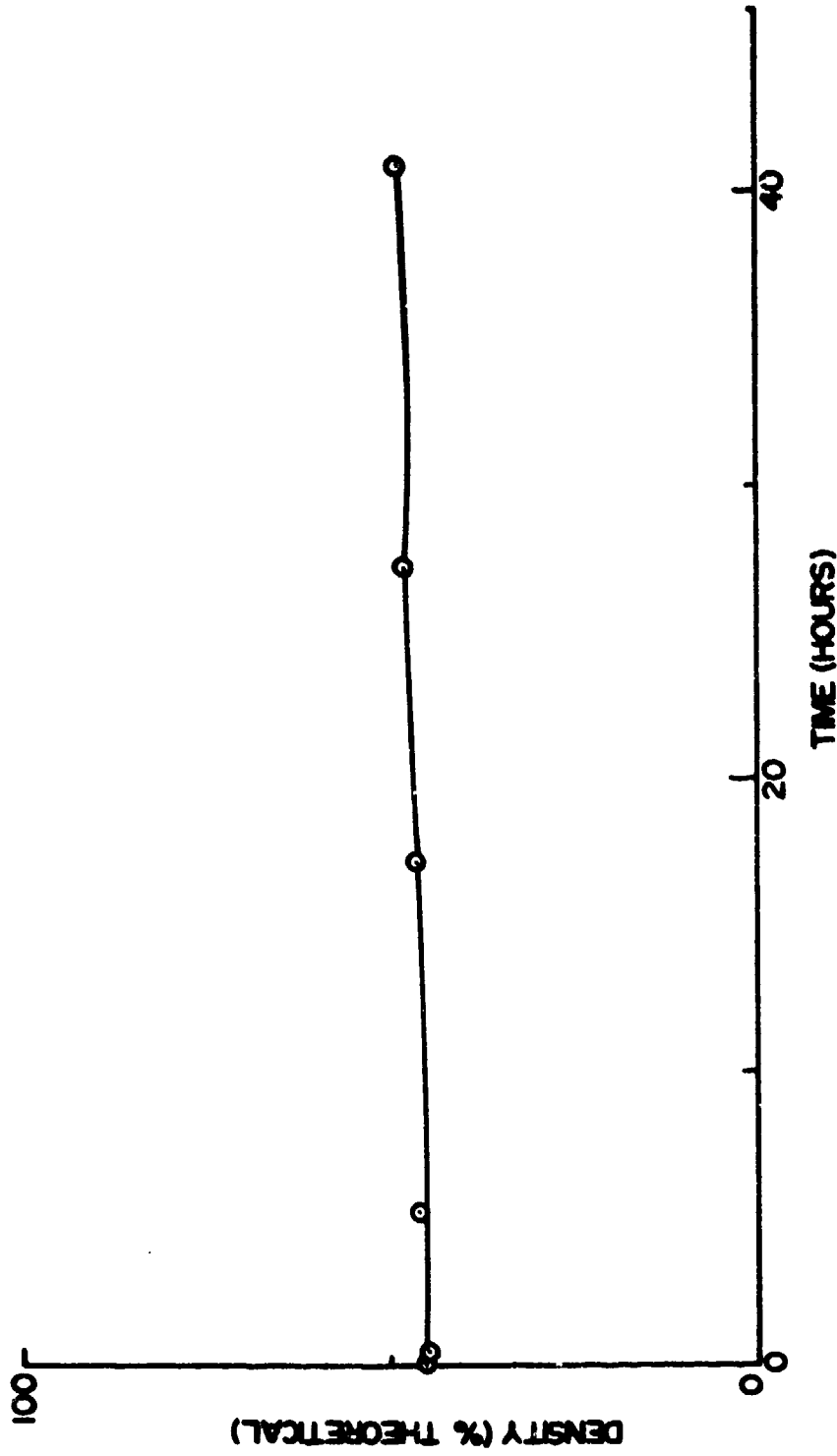
Figure 4.46 Density Changes During Isothermal Heating of a
RuO_2-Lead Borosilicate Glass Compact at 800°C.
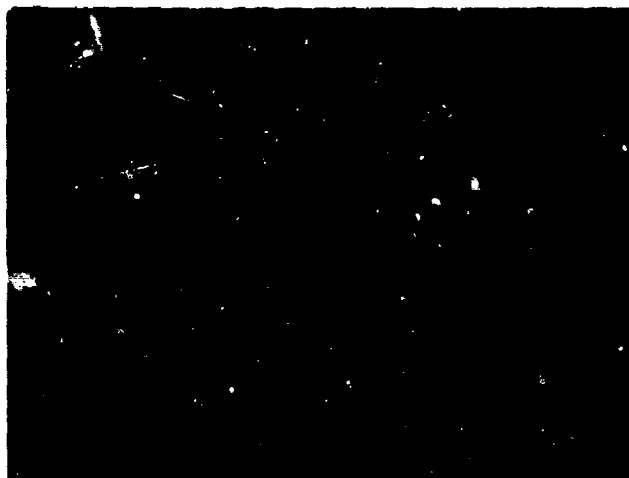
a. Polished Surface – 80 v/o RuO$_2$, 800°C, 10 minutes
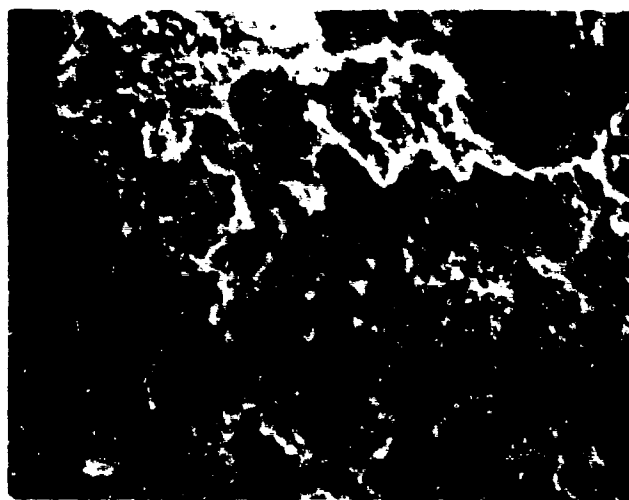
b. Fracture Surface – 40 v/o RuO$_2$, 1000°C, 2 hours

Figure 4.47   Microstructure of Shrinkage Samples–SEM, 800X.

The conclusion drawn from the density measurements was that the density did not change to a great extent after firing even though the samples contained substantial amounts of the liquid phase. The starting porosity remained even after long hours of heating. For the pores to close, the capillary pressure must be greater than the gas pressure inside. The capillary pressure is directly proportional to the surface tension of the glass and inversely proportional to the radius of the pores. At higher temperatures the surface tension decreases and hence the driving forces may not be enough to overcome the gas pressure. The pore coalescence resulting in the formation of the larger pores reduces the capillary pressure due to the increase in the radius of the pores. At lower temperatures where the surface tension is high, the viscosity is also very high, and because of this the pore elimination will be a very slow process.

Density measurements on fired and cooled compacts of RuO_2 and glass, showed very little shrinkage during the initial stages of heating. This type of study has two disadvantages: (1) the dimensional measurements on the cooled samples may not always give all the information about the various processes that take place during heating; and (2) since the dimension changes involved in this case are small, it is not possible to follow them accurately using a micrometer.

A better method would be to record the dimension changes at high temperatures using a more sensitive instrument such as a dilatometer. Shrinkage measurements of compacts during heating can be related to the microstructure changes using the appropriate kinetic relationships provided there is no large increase in the average particle size due to the ripening process. Therefore, it was decided to study the shrinkage of the RuO_2-glass compacts under isothermal conditions using a horizontal dilatometer.

The samples for shrinkage measurements were prepared in the following way. A mixture of RuO_2 and glass (30 w/o glass) was dispersed thoroughly and pressed in an uniaxial press at 4.1×10^9 dynes/cm^2. The pressed samples were about 0.5 cm long and 0.625 cm in diameter. All samples were preheated at 250°C for one hour in order to allow the initial contraction due to loss of moisture and glass sintering to be completed.

The shrinkage data at six different temperatures are shown as a

function of time in Fig. 4.48. Four stages can be identified in the time dependence of the relative shrinkage. Stage 1 is an initial rapid expansion shown at all six temperatures. This stage is simply the result of the thermal expansion of the sample as it approaches thermal equilibrium in the furnace. Data at very short times do not have quantitative significance because approximately 5-10 minutes are required for the sample to reach thermal equilibrium.

Stage 2 is a contraction which occurs: (1) over the full time span measured at 565 and 605°C; (2) up to 6 or 7 hours at 648°C; (3) up to 20, 5 and 2 minutes at 695, 722 and 752°C respectively. This contraction is probably due to a rearrangement of the RuO_2 particles in the glass and initial stage sintering of RuO_2.

Stage 3 is an expansion which can be observed: (1) as a slight increase in relative length at the longest times at 648°C; (2) at 695°C over the time period 20 minutes to 2.5 hours; (3) at 722°C over the time period 5-15 minutes; (4) at 752°C over the time period 2-5 minutes. It is believed that stage 3 is associated with either the presence of closed pores with entrapped air pressure greater than the capillary pressure, and/or formation of gases due to oxidation of RuO_2 to higher valence, volatile oxides. The phenomenon is not observed at the lower temperatures because the glass may not have closed pores or because the rate of oxidation of RuO_2 is much slower at these temperatures. The expansion is observed only at very short times at the higher temperatures because the glass viscosity has decreased to a sufficiently low value that the gas bubbles are released as rapidly as they are formed.

Stage 4 is a further contraction which is observed after 2.5 hours at 695°C, after 15 minutes at 722°C and after 5 minutes at 752°C. It is believed that this stage is a continuation of the sintering of RuO_2 in the presence of the glass. Weight loss measurements have shown that the loss of RuO_2 and/or glass by vaporization is insufficient to account for the observed changes during stage 4.

There are two different types of processes occurring during isothermal heating of the RuO_2-glass compacts: (1) processes leading to contraction due to rearrangement, sintering of RuO_2 particles and their growth; and (2) processes opposing the contraction either due to the entrapped air
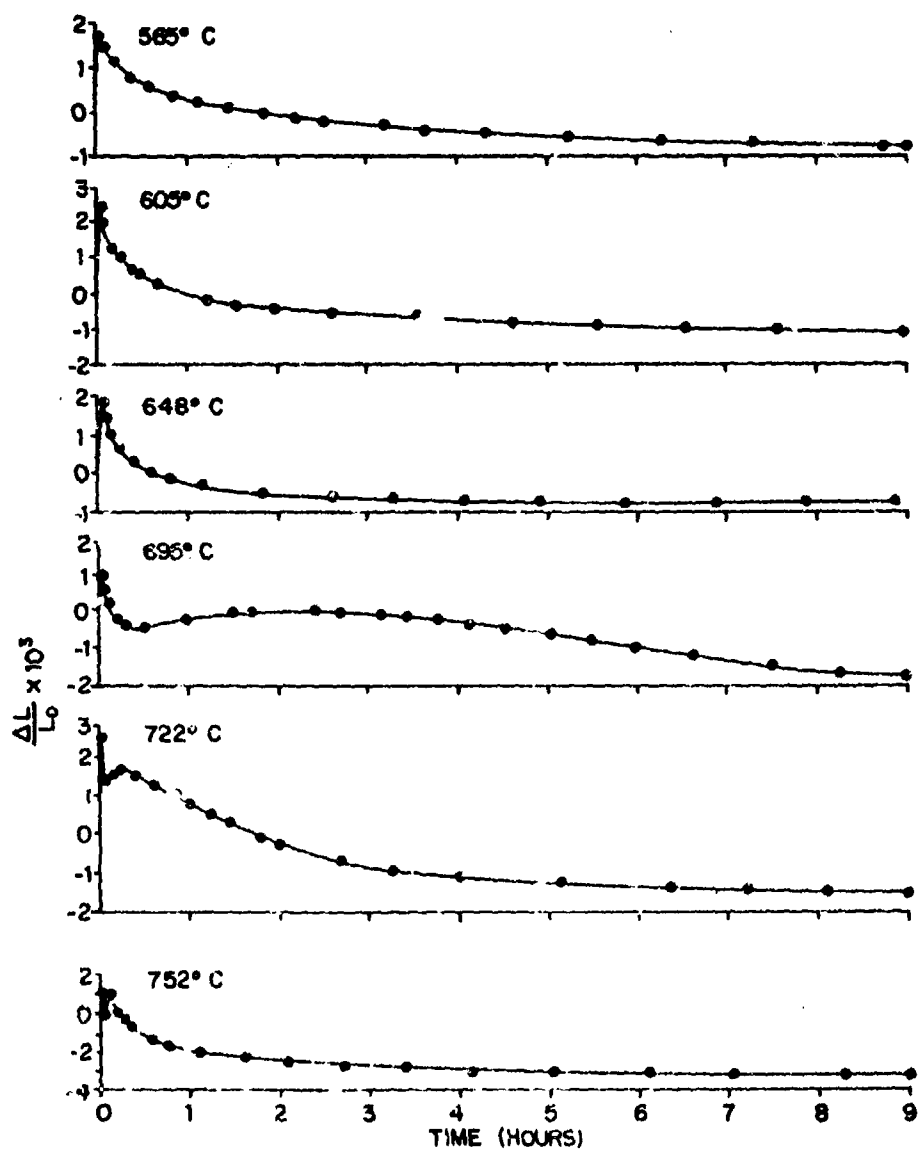
Figure 4.48   Relative Shrinkage of RuO₂-Lead Borosilicate Glass
Compacts During Isothermal Heating at Different Temperatures

in the closed pores or evolution of gases by oxidation of RuO_2. The shape of the shrinkage curves depends on the relative magnitudes of these processes. The kinetic expressions relating time dependence of the shrinkage (Table 2.2) are applicable only for the contribution from the processes causing contraction during initial stages of sintering. Since the relative magnitudes of the different processes are not known, it is not possible to determine the contributions from those resulting in contraction only and hence any quantitative analysis of the shrinkage data to determine the predominant sintering mechanisms is difficult.

In general, the total shrinkage observed was very small in agreement with the results obtained from density measurements. Referring to the geometry in Fig. 2.3, the total relative shrinkage ($\Delta L/L_o$) after the completion of the initial stage sintering ($\frac{x}{r} = 0.3$) should be 4.5 x 10^{-2} whereas the observed relative shrinkage was about 4 x 10^{-3} i.e. less than 10% of the expected value even after long hours of heating. Kingery [19] has reported that it should be possible to obtain final density by rearrangement process alone if the sample contains more than 35 v/o liquid. In the compacts studied, even though th glass content was about 39 v/o, there was little change in the density and the final density obtained was only 50-60% of the theoretical density. This is obviously due to closed pores inside the compacts. The capillary forces of surface tension are not enough to eliminate the pores and hence the porosity remains in the sintered compacts.

4.2.5 Ripening of RuO_2

The study of the growth of solid phase particles in a liquid phase can also provide information on the predominant mechanisms controlling the kinetics of liquid phase sintering [72]. The direct measurement of the grain size from microstructure examination has been employed as a tool for such an investigation by many workers [72, 74, 75]. The kinetic expressions involved in such a study are given by Eqs. 2.38 and 2.39.

Samples for microscopic observation were prepared from either a formulation containing 40 w/o RuO_2 relative to glass with ethyl-cellulose-butyl carbitol screening agent, or a dry mixture of RuO_2 and glass powder

(30 w/o RuO_2). The powders were thoroughly dispersed in the agate mill before use. The RuO_2 in both the cases was made by drying the hydrate. Whenever the formulation was used, the samples were dried at 125 and 250°C for half an hour before the final firing. The firing temperatures used were 800, 900, 1000 and 1100°C.

Samples were prepared in five different ways and will subsequently be referred to as sample types 1-5.

1. The paste screen printed in the form of a square pattern (1 cm by 1 cm) on AlSiMag 614 substrates and fired.
2. The paste hand printed on platinum foil and fired.
3. The paste heated in a platinum boat.
4. Mixture of RuO_2 and glass powders heated in a platinum crucible.
5. Mixture of RuO_2 and glass powders along with pieces of AlSiMag 614 substrates heated in a platinum crucible.

Since the aim was to look at the growth of RuO_2 particles only, all the glass was completely leached out as described for the solubility studies and only the RuO_2 remaining was used for the analysis. Removal of all the glass was confirmed by energy dispersive x-ray analysis of the SEM, and x-ray diffraction phase analysis. The dried samples were placed on either aluminum or graphite blocks and observed using SEM.

Figures 4.49 and 4.50 show the sintering and growth of RuO_2 particles at 1000°C with increasing firing time for sample types 3 and 4 respectively. Figure 4.49a shows the RuO_2 powder after leaching out the glass but prior to any sintering or particle growth. Two features can be observed with increasing time at 1000°C in Figs. 4.49 and 4.50 for both sample types: a sintered network of RuO_2 particles and large crystals of RuO_2 both begin to form with increasing time. The material for the formation of these crystals must come by partial dissolution of the sintered network. Figure 4.49 shows that the sintered mat of RuO_2 co-exists with the larger crystals after sufficient time at 1000°C. The two growth habits of the RuO_2 crystals (platelets and needles) can also be seen in Fig. 4.49d. It can also be noted by comparing Figs. 4.49 and 4.50 that essentially identical crystal growth patterns are obtained, starting with a typical thick film formulation or starting with only the mixture of inorganic powders.

In addition to being a function of time at temperature, the sintering and growth are also functions of temperature. Figure 4.51 shows the

a. Dried, 250°C
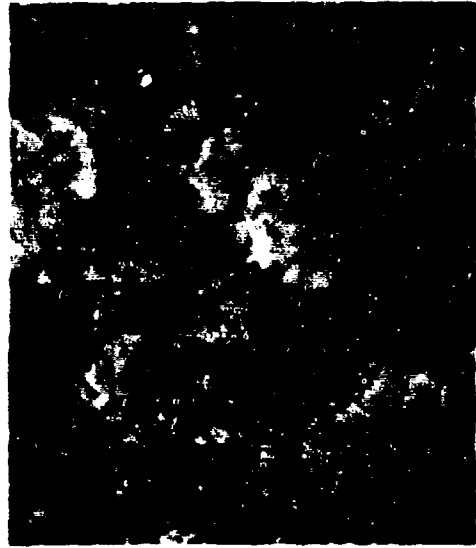
b. 1000°C, 30 minutes
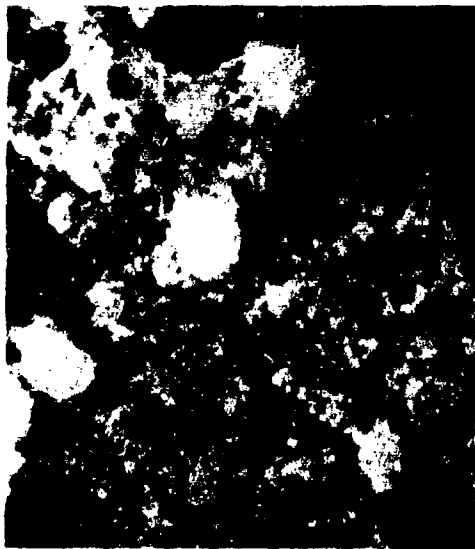
c. 1000°C, 2 hours

d. 1000°C, 6 hours

Figure 4.49   Sintering and Growth of RuO$_2$ Particles–Paste
(Sample Type 3), SEM, 7000X^2

a.   1000°C, 5 minutes
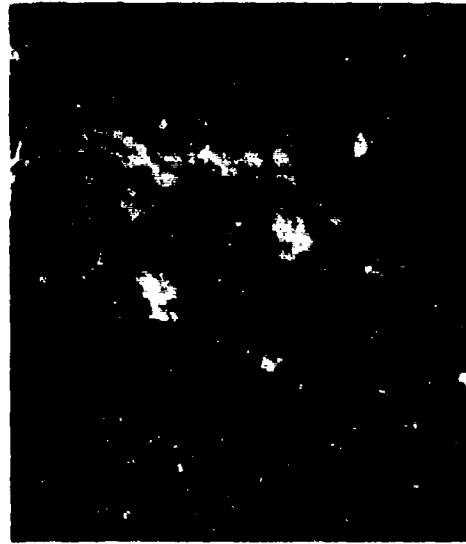
b.   1000°C, 10 minutes
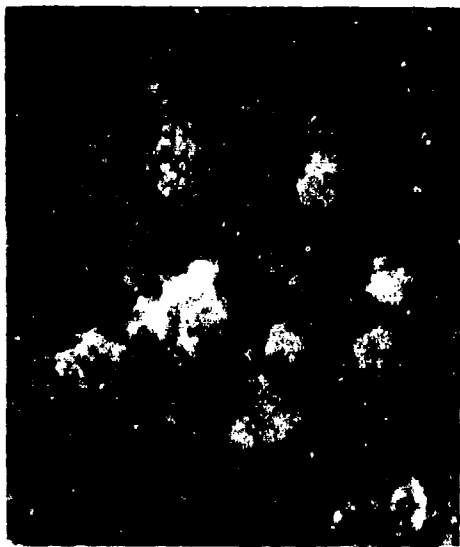
c.   1000°C, 30 minutes

d.   1000°C, 6 hours

Figure 4.50   Sintering and Growth of RuO_2 Particles-Powder Mixture (Sample Type 4), SEM, $7000X$
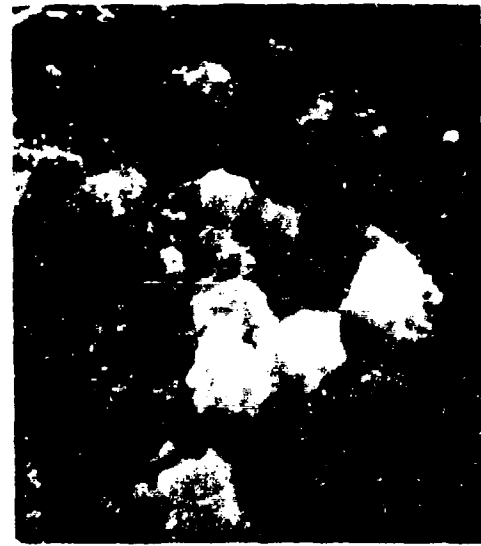
a. 800°C, 22.5 hours   b. 900°C, 6 hours

Figure 4.51   Sintering and Growth of RuO_2 Particles-Powder Mixture
(Sample Type 4), SEM, 7000X

microstructure obtained after two experiments using sample type 4 at 800 and 900°C firing temperatures. Even after 22.5 hours at 800°C there is almost no indication of particle growth (Fig. 4.51a); whereas extensive particle growth is apparent after 6 hours at 900°C (Fig. 4.51b).

The results using sample type 1, which approximates an actual thick film resistor did not agree with those obtained for sample types 3 or 4. Figure 4.52 shows the microstructure obtained at 900°C (Fig. 4.52a), 1000°C (Fig. 4.52b) and 1100°C (Fig. 4.52c) for differing times and even at 1100°C, only very limited crystal growth can be detected. Figure 4.52b can be compared with Figs. 4.49d and 4.50d which represent comparable time-temperature conditions for sample types 3 and 4. There is evidence of extensive sintering in Figure 4.52b, but essentially no crystal growth.

In order to separate possible effects due to geometry of the sample from those resulting from chemical interactions with the substrate, a sample was prepared by printing the formulation on platinum foil (sample type 2) and the microstructure observed after 6 hours at 1000°C is shown in Fig. 4.53a; the crystal growth observed is comparable to that seen in Figs. 4.49d or 4.50d and certainly far more extensive than that observed with the film on the alumina substrate.

In order to study chemical interactions without geometry effects sample type 5 was prepared in a manner identical to sample 4 with the exception that pieces of AlSiMag 614 substrates were added to the RuO_2 and glass powders in the platinum crucible. Figure 4.53b shows the microstructure obtained when sample type 5 was fired at 1000°C for 6 hours. The sintered mat with the absence of any appreciable crystal growth is identical to that of sample type 1 (Fig. 4.52b), and clearly demonstrates that the inhibition of the growth of RuO_2 is the result of a chemical interaction with the substrate.

An important observation that can be made from the study of the micrographs is the presence of a wide distribution of particle sizes. Referring to Fig. 4.49c, it is evident that the particle sizes vary from less than 0.1 µm to greater than 1 µm. In fact, the typical behaviour after long hours of heating at higher temperatures is the presence of a very large number of small crystals sintered onto a few big crystals. Any technique for determining the average particle size by quantitative

a. 900°C, 18 hours

b. 1000°C, 6 hours

c. 1100°C, 1.5 hours

Figure 4.52   Sintering with Limited Growth of RuO_2 Particles-
Screen Printed Samples (Sample Type 1), SEM, 7000X
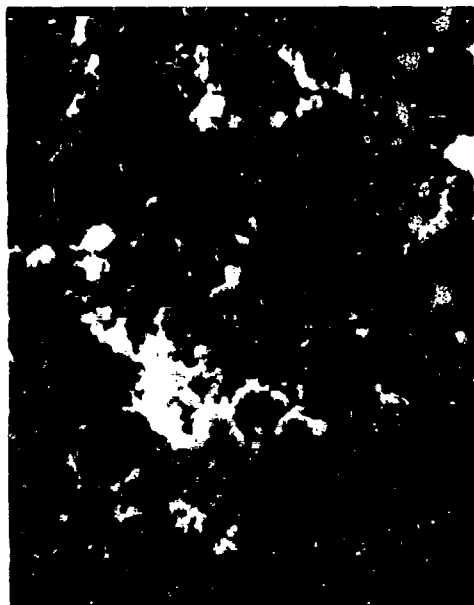
a. Sample Type 2 – 1000°C, 6 hours   b. Sample Type 5 – 1000°C, 6 hours

Figure 4.53   Effect of the Substrate on Growth of RuO_2 Particles-
SEM, 7000X

microscopy deals with the measurement of size as well as number of particles in a particular size range [76]. In this particular system, even though the size and number of large crystals can be computed, it is extremely difficult to incorporate all the small crystals. As explained before, many of these particles are agglomerates of a large number of extremely fine particles. Although the particles in the powder treated at lower temperatures for shorter periods of time may not have a very wide size distribution, the tendency of the fine particles to agglomerate makes it very difficult to separate them and measure the size of the individual particles either by SEM or TEM. All these considerations made quantitative microscopy techniques unsuitable for studying the increase in average particle size in this system particularly when the starting RuO_2 powder is made up of extremely fine particles.

In order to avoid the problem of dealing with extremely fine particles, samples of type 4 were prepared using anhydrous RuO_2 powder obtained from Mathey Bishop. The average particle size of this powder was about 50-100 times larger than the powder prepared from the hydrate. The microstructure results obtained after treating the anhydrous RuO_2 powder with the glass at 1000°C for differing times are shown in Fig. 4.54. As can be seen, the average particle size remained almost the same even after heating at 1000°C for 10 hours. This is obviously due to the slow kinetics resulting from the larger particles.

Since the quantitative microscopy approach was not feasible to determine the increase in the average particle size with time and temperature, it was necessary to adopt indirect techniques such as x-ray diffraction line broadening and surface area measurements [77]. The x-ray diffraction line broadening technique can be used to determine average crystallite sizes provided one is concerned with crystallite sizes below 0.2 μm [78]. The increase in the average particle size also decreases the surface area of the sample, and the average particle size can be obtained from the surface area values assuming the particles to be uniform in size and shape [77]. Results of the x-ray and surface area measurements on sample types 1, 3 and 4 mentioned above are described in the discussion that follows.

Specimens for x-ray diffraction study were prepared by placing the

a. 1000°C, 10 minutes
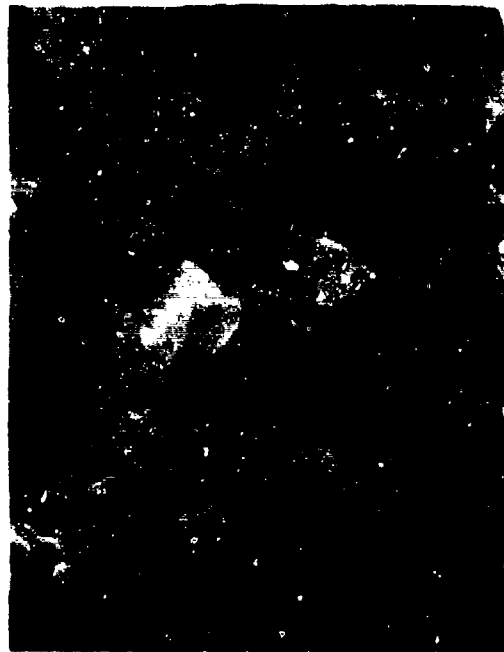
b. 1000°C, 30 minutes

c. 1000°C, 10 hours

Figure 4.54   Sintering With Limited Growth of RuO_2 Particles-
Mathey Bishop RuO_2 Powder, SEM, 7600X

RuO_2 powder from sample types 1, 3 and 4 on a microscope slide in the form of a thin layer. The peak due to the (110) reflection was scanned using copper radiation at a speed of 0.125°/minute in a Philips Norelco diffractometer. The average crystallite sizes were calculated from the Scherrer equation [79] after the breadth at half intensity was corrected for instrumental and $K\alpha$-doublet broadening according to the method outlined by Bartram [79]. The broadening caused by internal strains and other defects was neglected. The average crystallite size was assumed to be the same as the average particle size for the reasons explained before.

The average x-ray crystallite sizes for sample types 3 and 4 were found to be similar, in agreement with the SEM studies, (compare Figs. 4.49 and 4.50), but those for sample type 1 were much smaller, particularly at the higher temperatures. Data for sample types 1 and 4 as a function of time at temperatures are shown in Fig. 4.55. The presence of the substrate appears to buffer the crystallite size after an initial rapid increase. This effect is probably due to a reaction between the substrate material and the glass causing changes in the properties of the glass, and will be discussed in Section 4.2.7.

The x-ray data on these samples gave hope that this technique could be used for studying ripening kinetics. Hence, more samples of type 4 were prepared by heating the mixture of 30 w/o RuO_2 powder and glass powder for differing times in a platinum crucible. The firing temperatures employed were 800, 850, 900, 950 and 1000°C. After firing, all the glass was leached out and only the RuO_2 remaining was used for the analysis. The average crystallite sizes were determined by the x-ray diffraction line broadening technique on powder samples using a Type F Siemens diffractometer with a curved crystal monochromator; 3 different peaks due to (110), (101) and (211) reflections were scanned, using copper radiation at a speed of 0.1°/minute to investigate the possibility of different growth behaviour in different crystallographic directions.

The procedure for calculating the average crystallite size from line broadening data utilized integral line breadth instead of the half maximum line breadth. Corrections for instrumental and $K\alpha$-doublet broadening were carried out according to the method outlined by Bartram [79]. The pure diffraction breadth was obtained by the graphical method from the curves corresponding to skewed distribution of crystallite sizes [80].
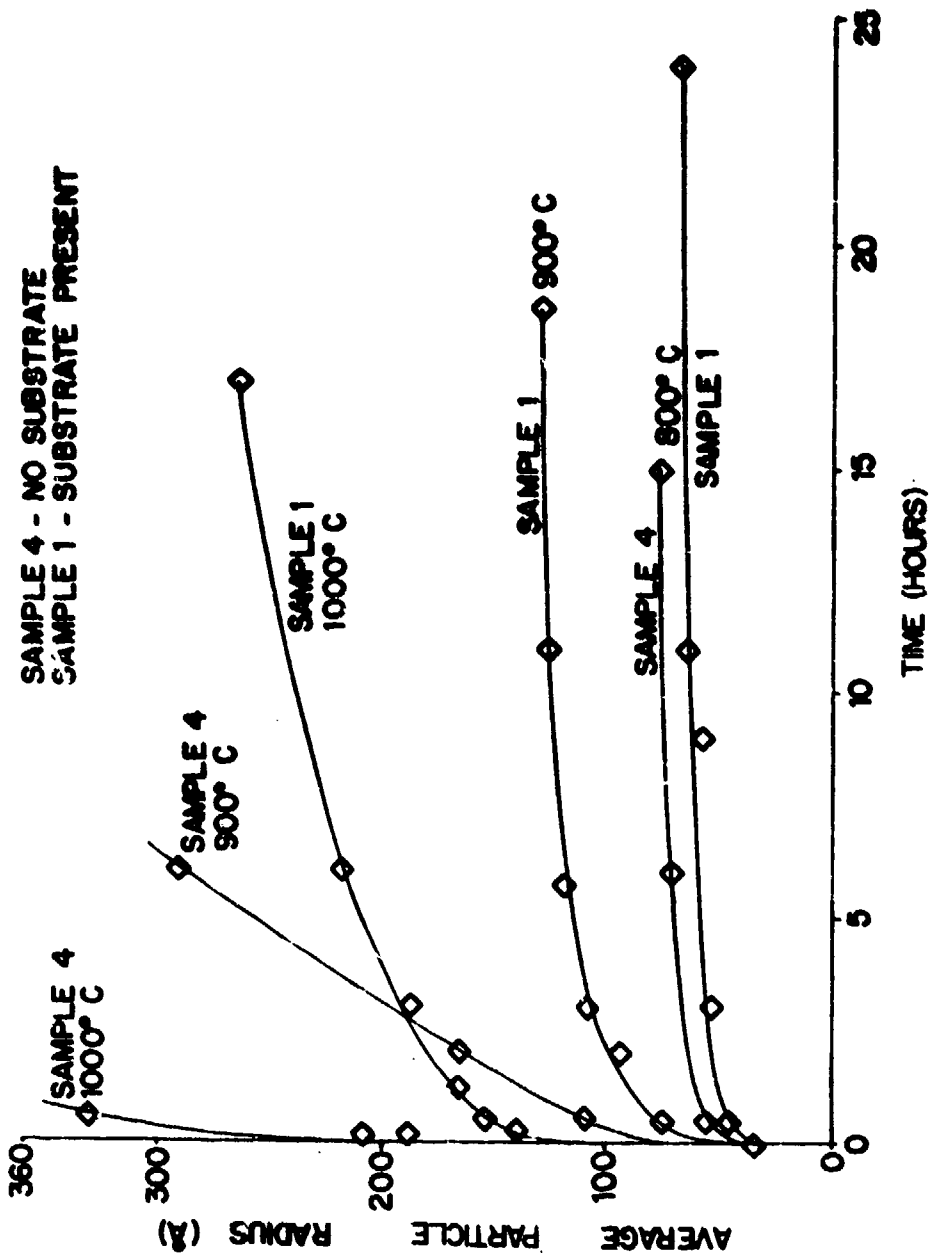
Figure 4.55   Average Particle Size From X-ray Line Broadening

The results from the x-ray measurements are shown in Figs. 4.56-
4.60. The minor differences between these results and those reported
previously (Fig. 4.55) are due to the difference in the method of
computation. The growth pattern is similar in all the 3 crystallographic
directions studied. The mean values of the average crystallite sizes
from the three different reflections are shown in Fig. 4.61.

Surface area measurements were conducted using an Aminco Sor-BET
helium carrier surface area meter. The RuO_2 powder was placed in the
sample holder of the surface area meter and evacuated at 100°C for about
24 hours to ensure the removal of all the moisture from the samples.
The surface area was determined by the amount of nitrogen adsorbed at the
sample surface at liquid nitrogen temperature. A direct measurement of
nitrogen adsorption was made from the highly sensitive pressure gauges
incorporated in the surface area meter. The uncertainty in the surface
area values obtained was about $\pm 5\%$.

The surface area values obtained were used to calculate the average
particle sizes assuming that all the individual particles were uniform
spheres. The results are shown in Figs. 4.56 - 4.61 along with the average
particle sizes obtained from x-ray measurements. The average particle
size calculated from the surface area measurements is greater than that
obtained from x-ray measurements in the untreated powder for the reasons
discussed in Section 4.1.4.1. The average particle size calculated from
either x-ray or surface area data show a similar increase with time and
temperature at shorter times of treatment.

After long hours of treatment at 850, 900, 950 and 1000°C there is a
discrepancy in the average values calculated by the two methods. The
x-ray results seem to indicate an exaggerated growth, but this is because
the x-ray diffraction line broadening technique is applicable only for a
fairly uniform distribution of sizes. For a powder sample composed of
crystallites of a wide distribution of sizes, the average size calculated
from the line breadth is weighted towards larger sizes [81]. For cubic
crystals, if there are n particles of size D

$$\text{observed mean size} = \frac{\Sigma \, n \, D^4}{\Sigma \, n \, D^3} \qquad (4.13)$$
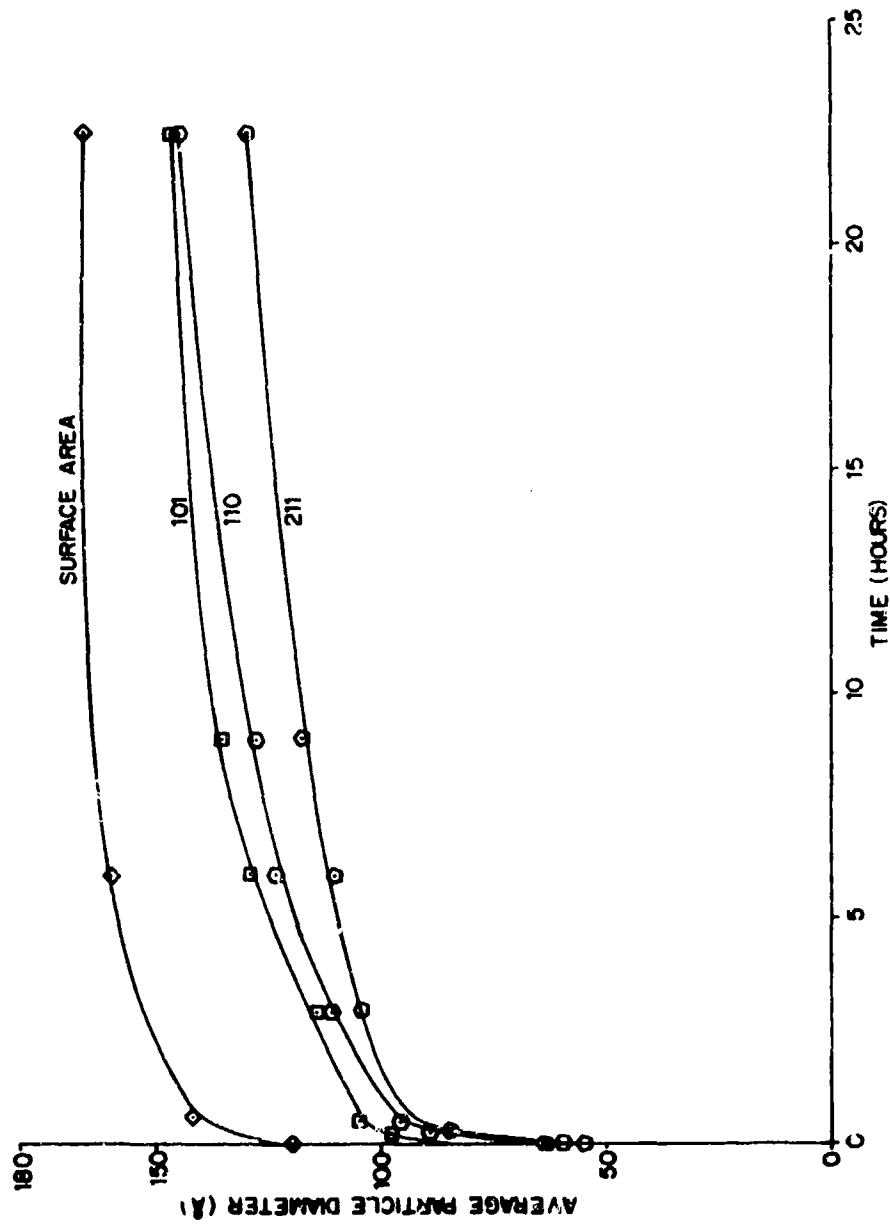
Figure 4.56　Average Particle Size of Sample From X-ray Line Broadening and Surface Area–800°C
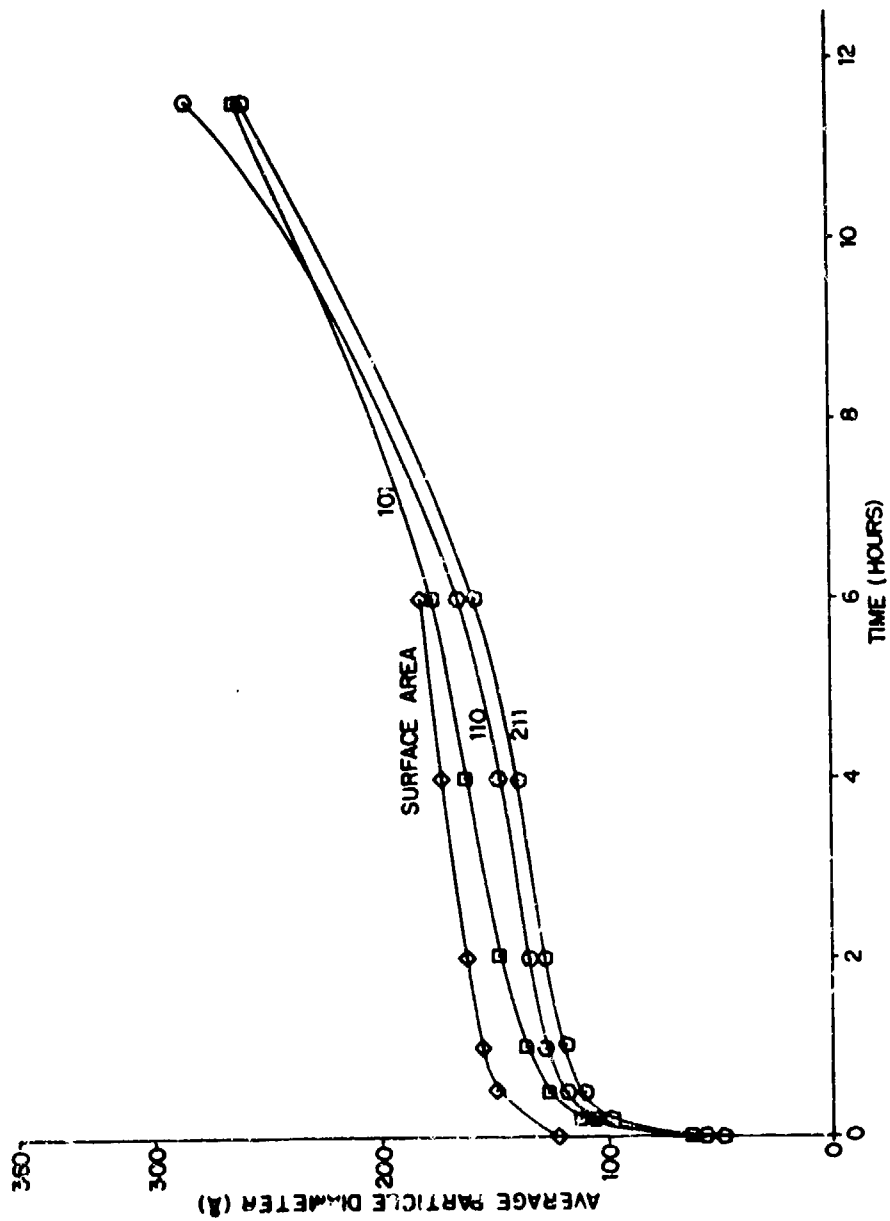
Figure 4.57   Average Particle Size of Sample From X-ray Line
Broadening and Surface Area-850°C
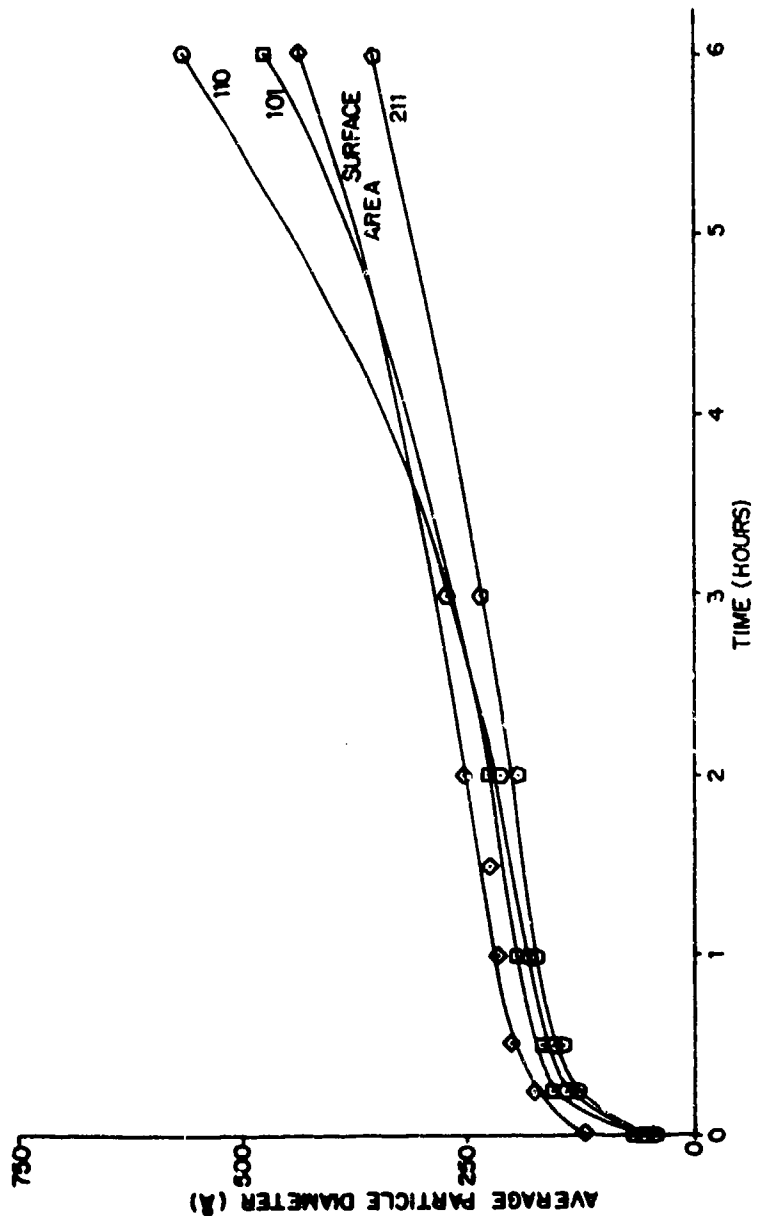
Figure 4.58 Average Particle Size of Sample From X-ray Line
Broadening and Surface Area–900°C
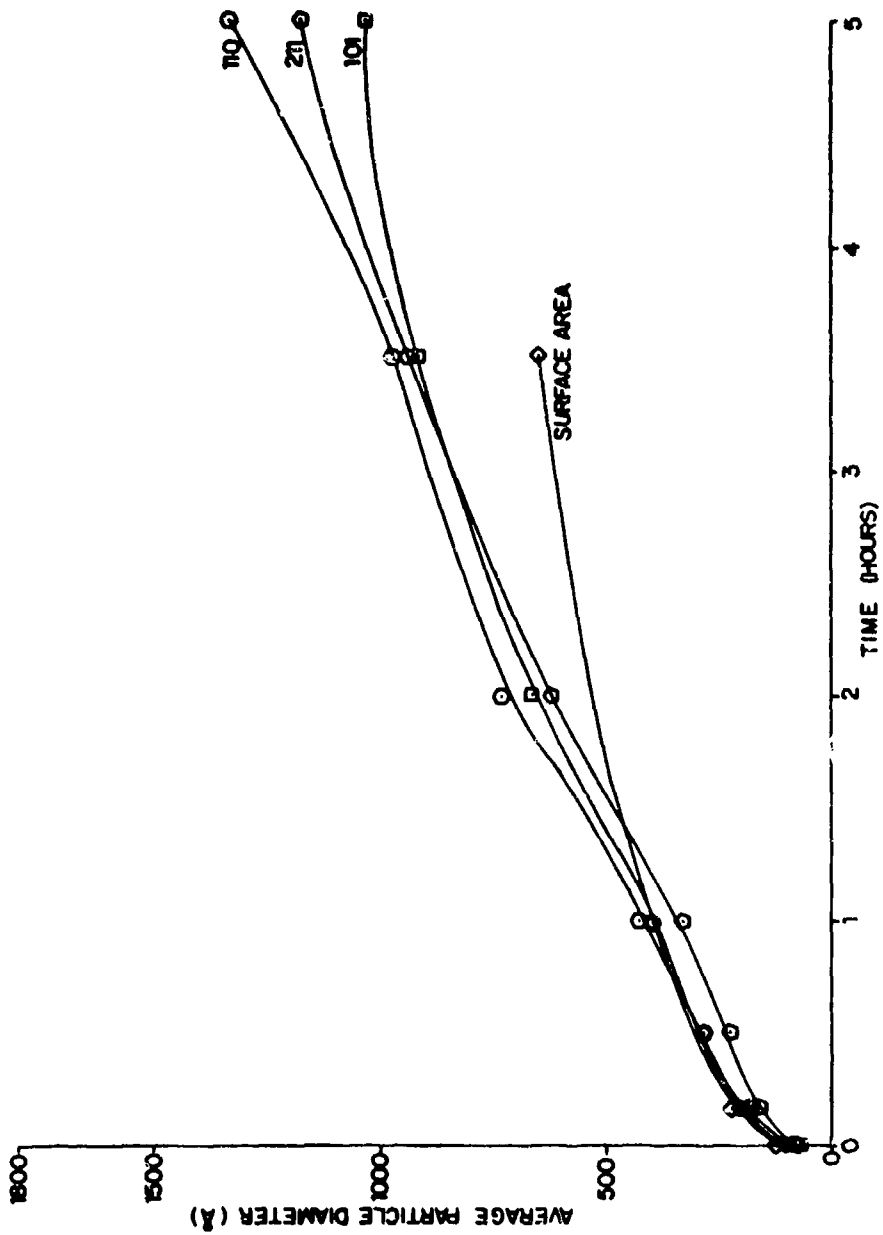
Figure 4.59   Average Particle Size of Sample From X-ray Line
Broadening and Surface Area–950°C
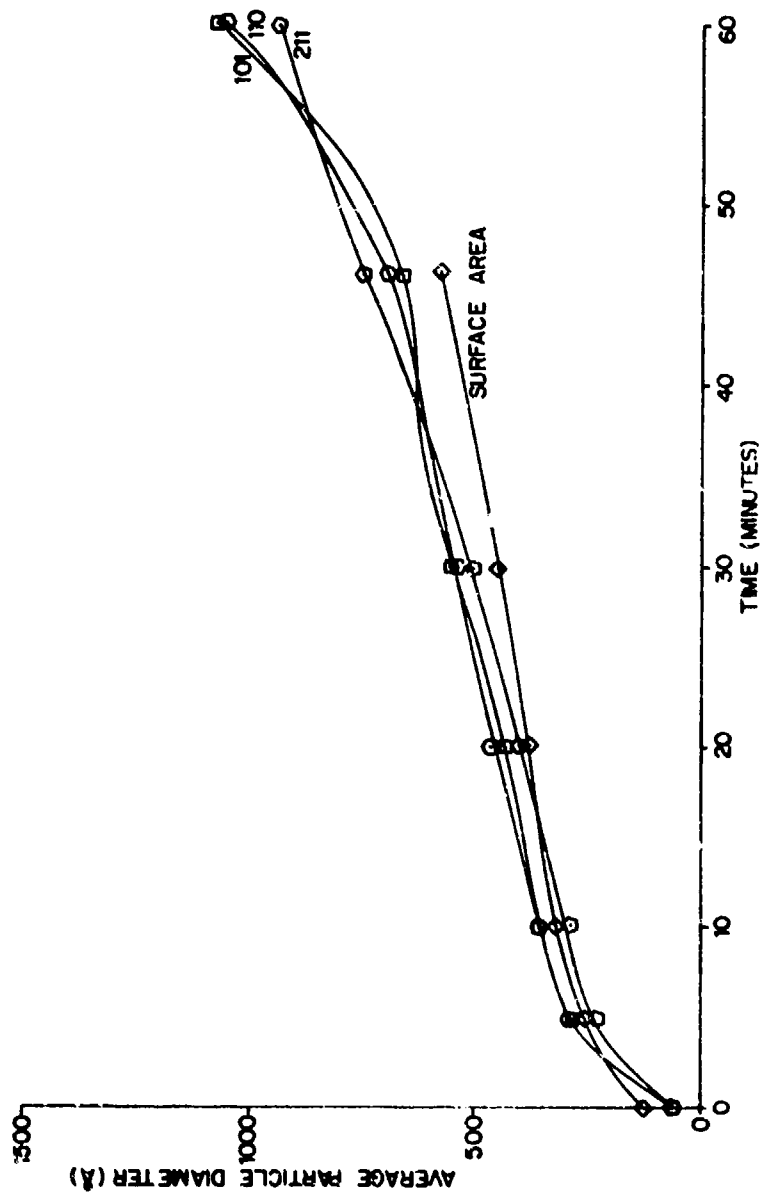
Figure 4.60   Average Particle Size of Sample From X-ray Line
Broadening and Surface Area–1000°C
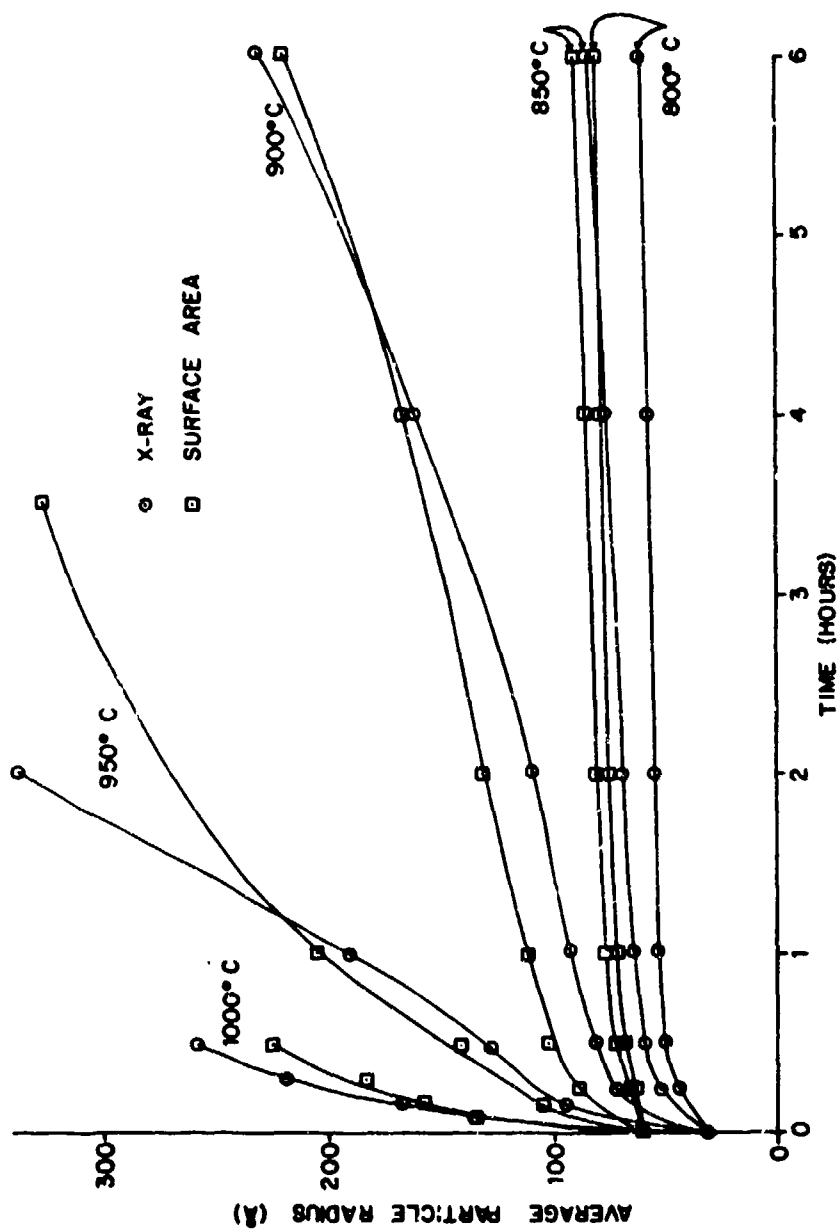
Figure 4.61   Average Particle Size of Sample From X-ray Line
Broadening and Surface Area

whereas,

$$\text{true mean size} = \frac{\Sigma \, n \, D}{\Sigma \, n} \tag{4.14}$$

The difference between the observed and true mean sizes increases as the
distribution becomes more wide and particularly if a few large crystall-
ites and a large number of small crystallites are present, which is
exactly the situation in these sampes as evidenced by SEM investi-
gation (Figs. 4.49 - 4.50). This fact has to be considered while
analyzing the data.

In order to study the effect of the amount of glass on the growth
kinetics, samples of type 4 were also prepared by using 6 and 18 w/o RuO_2
in the powder mixture. The samples were fired at $1000°C$ for 10 minutes,
0.5 hours and 6 hours and after removing all the glass checked for
microstructure, surface area and x-ray particle Size. The results of
these experiments were similar to those obtained for the samples containing
30 w/o RuO_2. As indicated in Fig. 4.62, the decrease in surface area of
RuO_2 powder upon treatment for different times is almost the same for
samples containing 18 and 30 w/o RuO_2. Average x-ray particle size
increases for the samples containing 6 and 18 w/o RuO_2 also followed the
same behaviour as the samples containing 30 w/o RuO_2. The microstructure
results are shown in Figs. 4.63 - 4.64. Comparing Figs. 4.63 - 4.64 with
Fig. 4.50, it is clear that the growth of RuO_2 particles is independent of
the amount of glass for the range of glass concentration studied.

4.2.6   New Phases

The ingredient materials for our thick film resistors are RuO_2, lead
borosilicate glass, organic screening agents and the substrate. Since
the resistors are fired at temperatures as high as 800 - 900°C, the
possibility of the formation of new phases due to interactions between the
different constituents had to be considered. Although, most of the
screening agent is removed during the initial drying operation at around
300°C, the last traces remain at temperatures as high as 500°C. The
reducing atmosphere created by the gases during burnout of the organic
agents could reduce RuO_2 and the glass. At higher temperatures the other
possible interactions are between RuO_2-substrate, substrate-glass and
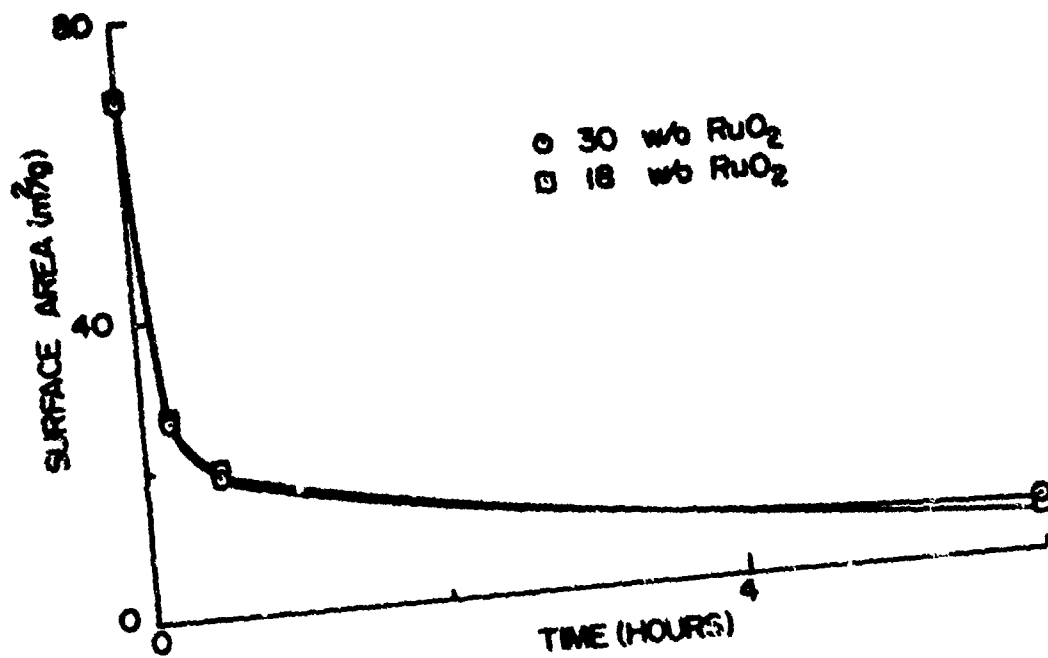
Figure 4.62   Surface Area Change For Samples Containing
18 and 30 w/o RuO$_2$
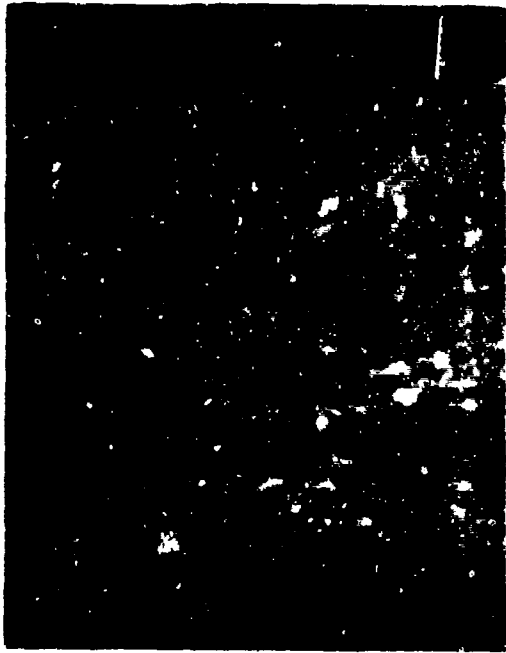
a.   1000°C, 10 minutes
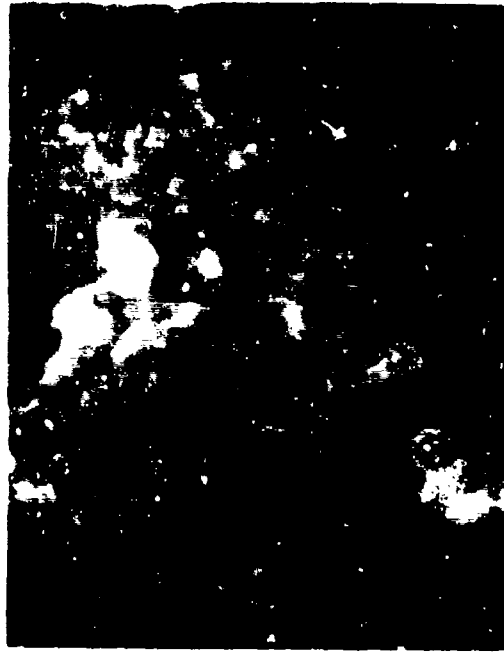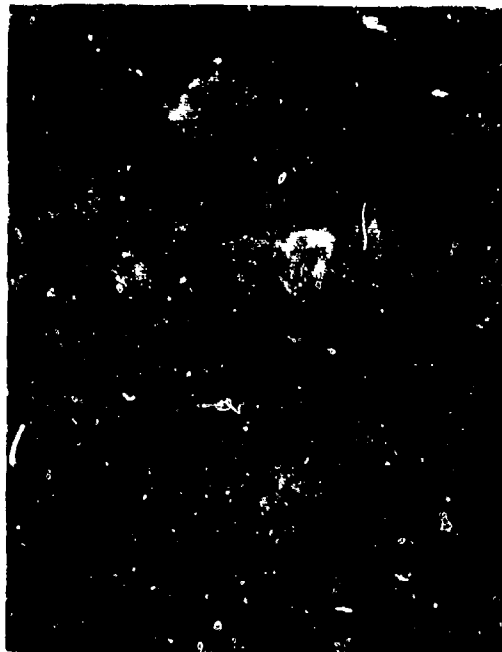
b.   1000°C, 30 minutes

c.   1000°C, 6 hours

Figure 4.63   Sintering and Growth of RuO_2 Particles-Powder
Mixture, 18 w/o RuO_2, SEM, 7000X
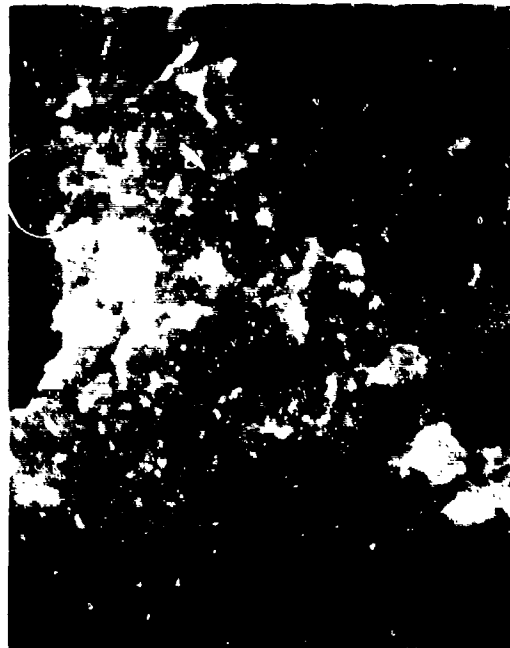
a. 1000°C, 10 minutes   b. 1000°C, 30 minutes

c. 1000°C, 6 hours

Figure 4.64   Sintering and Growth of RuO_2 Particles--Powder
Mixture, 6 w/o RuO_2, SEM, 7600X

RuO_2-glass. The experiments reported below were directed towards a qualitative study of the above interactions.

In isolated cases such as very long firing times, SEM investigations have revealed a variety of shapes that are neither vitreous lead boro-silicate glass nor RuO_2 particles. Some of these are shown in Fig. 4.65. The small size of the configurations caused a problem in using the SEM x-ray analyzer to identify the composition of a specific region in the resistor. The penetration depth of the electron beam was greater than the dimensions of the new phases and so elements below the new phase were detected also. For example, analyses of the crystals of Fig. 4.65d typically indicated the presence of ruthenium and aluminum. (Significant amounts of aluminum are to be expected in a fired resistor because of the substrate.)

Several different types of samples were prepared to take into consideration all possible interactions utilizing either mixtures of dried RuO_2 powder and lead borosilicate glass or the formulations containing 10 w/o RuO_2. In general the samples fell into four broad categories.

I. The formulation containing 10 w/o RuO_2 was hand printed on AlSiMag 614 substrates, dried at 300°C for 20 minutes and fired at 800, 900 and 1000°C for different times ranging from 15 minutes to 100 hours. Blank samples were also prepared by giving the same treatment to the substrates alone and the substrates with the formulation containing only glass and screening agent hand printed on them. The x-ray diffraction phase analyses were performed on the heat treated samples.

The samples fired for short times showed peaks for only RuO_2 and the substrate material (Al_2O_3) for those containing RuO_2, and peaks for only the substrate material for those with no RuO_2. Heating for a long period of time (more than 50 hours at 900°C) indicated certain extra phases; but, they were present in the samples with or without RuO_2 indicating that they were due to interactions between glass and the substrates only.

II. Mixtures containing 10 w/o RuO_2 and 90 w/o glass were dispersed thoroughly in the agate mill. This mixture was placed in platinum boats and heated at temperatures of 800, 900 and 1000°C for different times up
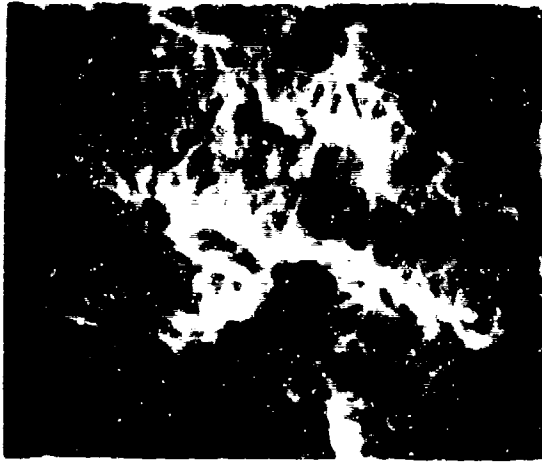
a.
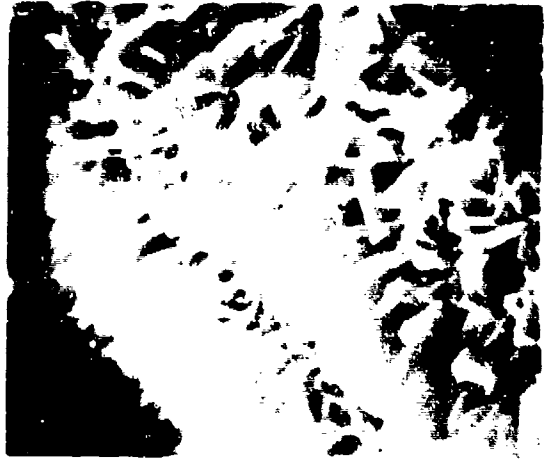
b.
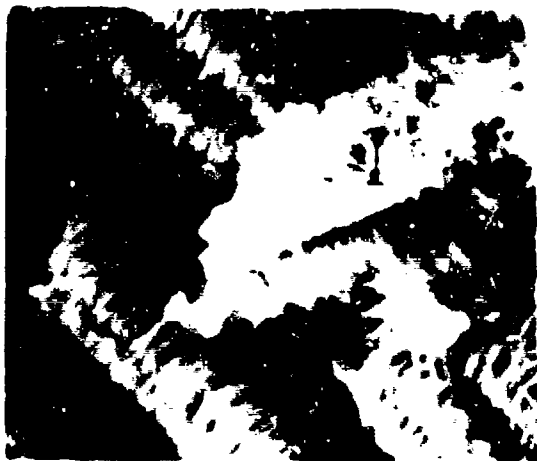
c.
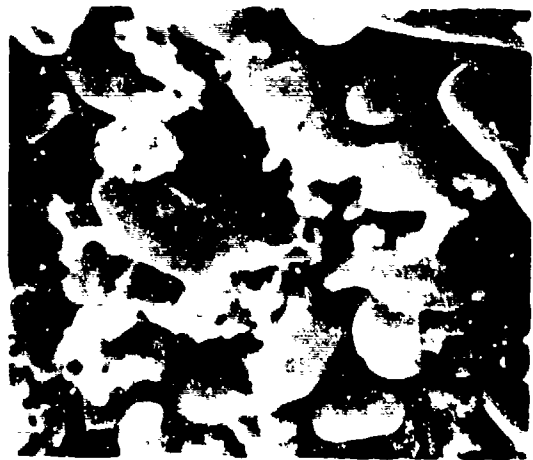
d.

Figure 4.65   Crystalline Structures Formed During
Extended Resistor Firing

to about 20 hours at 1000°C. After the heat treatment the powder diffraction specimens were prepared either by finely grinding the composites or by removing the glass by selective leaching. The selective leaching process involved: (1) treating with HCl to form $PbCl_2$; (2) rinsing with hot water to remove the $PbCl_2$; (3) treating the residue with HF and removing the SiF_4 formed; and (4) rinsing with hot water to remove the B_2O_3.

For both types of samples the diffraction patterns indicated only the presence of RuO_2 suggesting that either: (1) no crystalline phases were formed by the interactions of RuO_2 and glass; or (2) that the new phases formed were in a quantity or size that was below the detection limit of the diffractometer.

III. The formulation containing 10 w/o RuO_2 was screen printed on the substrates, dried at 300°C and then fired at 500°C for 30 minutes, 625°C for 30 minutes and 800°C for 15 minutes. The samples heated at 800°C were treated with HCl until all resistor material was removed from the substrates. The resulting solution was placed on glass slides and dried to form a powder residue for x-ray diffraction analysis. Blank samples were also prepared by using the identical process with a formulation containing glass but no RuO_2 in order to check for any phases formed due to glass-substrate interactions or the glass and HCl reaction. The Al_2O_3 phase was observed in both the cases and additional peaks due to RuO_2 were observed in the samples containing RuO_2, but no new phases were found.

The samples fired at 500, 625 and 800°C were treated with HCl to remove the resistor material from the substrate, then treated with hot water, HF and hot water successively to remove the glass. The resulting samples gave patterns for only RuO_2. Some samples were also checked directly after the firing. These samples indicated the presence of only RuO_2 and the substrate material.

IV. The formulation containing 10 w/o RuO_2 was placed in a platinum boat, dried at 300°C for 20 minutes and heated at 800°C for times ranging from 15 minutes to 20 hours. Some of these composites were ground and checked directly for the phases and others were treated with HCl, HF and water to remove all the glass. The results indicated the presence of ruthenium metal along with RuO_2 for samples treated for shorter time

periods. As the heating was continued further the intensity of ruthenium peaks decreased and finally only RuO_2 remained.

Several observations and conclusions can be made from these experiments.

a. The x-ray diffraction phase analysis experiments failed to indicate the formation of any new crystalline phases due to the interaction of RuO_2 either with the substrate or the glass.

b. Some new phases formed because of the interaction of the glass and the substrate, but these were observed only after long hours of heating. Hence the amount of new crystalline phases formed during normal tunnel kiln firing of RuO_2-glass thick film resistor can be considered to be extremely small.

c. The resistor paste that was heated in the platinum boat contained metallic ruthenium in early stages of heating. The ruthenium metal is believed to be formed through reduction of RuO_2 by the decomposition products of the screening agent. The reduction of RuO_2 to Ru is much faster than the oxidation of Ru to form RuO_2. Because of the large surface area to volume ratio in the screen printed samples, most of the organic material is removed during the initial drying and hence no ruthenium metal was detected in any screen printed samples.

d. In all the samples it was observed that the RuO_2 peaks in the diffraction pattern gradually became narrower as the time and temperature of firing were ' -reased. This could be due to: (1) an increase in the average particle size caused by growth of larger particles at the expense of the small particles or the dissolution or evaporation of small particles; (2) grain growth within each particle; and/or (3) a decrease in the internal strain of the particles. It was also observed that the RuO_2 powder underwent similar line narrowing when heated at 800°C in the absence of the glass.

4.2.7   Substrate Effects

As previously discussed, the growth of RuO_2 particles is inhibited by the presence of the substrate. The factors responsible for this feature were studied by considering the effect of the interactions between the ingredient materials on the different parameters controlling the microstructure development.

X-ray phase analysis results did not indicate any new crystalline phases formed due to interactions between either RuO_2 and substrate or RuO_2 and glass for the time-temperature conditions employed in the ripening studies. New crystalline phases observed after long periods of heating (more than 50 hours at 900°C) were attributed to substrate-glass interactions.

It was observed from the SEM investigation that alumina went into solution in the glass after an initial period of firing at 800°C thus changing the composition of the glass. Any change in the composition of the glass could lead to changes in the parameters controlling the microstructure development such as wettability of glass to RuO_2, viscosity of the glass and solubility of RuO_2 in the glass. These possibilities are discussed below.

As discussed previously, contact angle measurements using glass with 10 w/o substrate material dissolved in it showed complete wetting to RuO_2. This would imply that even after 10 w/o substrate material is dissolved in the glass, the glass would still penetrate the RuO_2 particles and the driving forces responsible for microstructure development would remain essentially the same assuming that the change in the surface tension of the glass is negligible.

The next consideration is the effect of changes in the composition of the glass on the viscosity of the glass. In order to determine the change in the viscosity of the glass, shrinkage measurements were conducted on compacts of glass powder with and without substrate material dissolved in it. The time dependence of the linear shrinkage of a compact consisting of spherical particles undergoing initial stage sintering by Newtonian viscous flow is given by Eq. 2.13. From the slope of the plot of $\Delta L/L_o$ versus t, γ_{sv}/η can be determined.

Samples for the shrinkage measurements were prepared by pressing glass particles in the size range 37–74 μm in an uniaxial press at 7×10^8 dynes/cm^2. Results of the isothermal shrinkage measurements gave straight lines when plotted for $\Delta L/L_o$ versus t (Fig. 4.66). The surface tension to viscosity ratios determined by substituting the slopes of the plots from Fig. 4.66 in Eq. 2.13 are shown in Fig. 4.67. The shrinkage data were obtained on compacts consisting of particles that were not spherical in
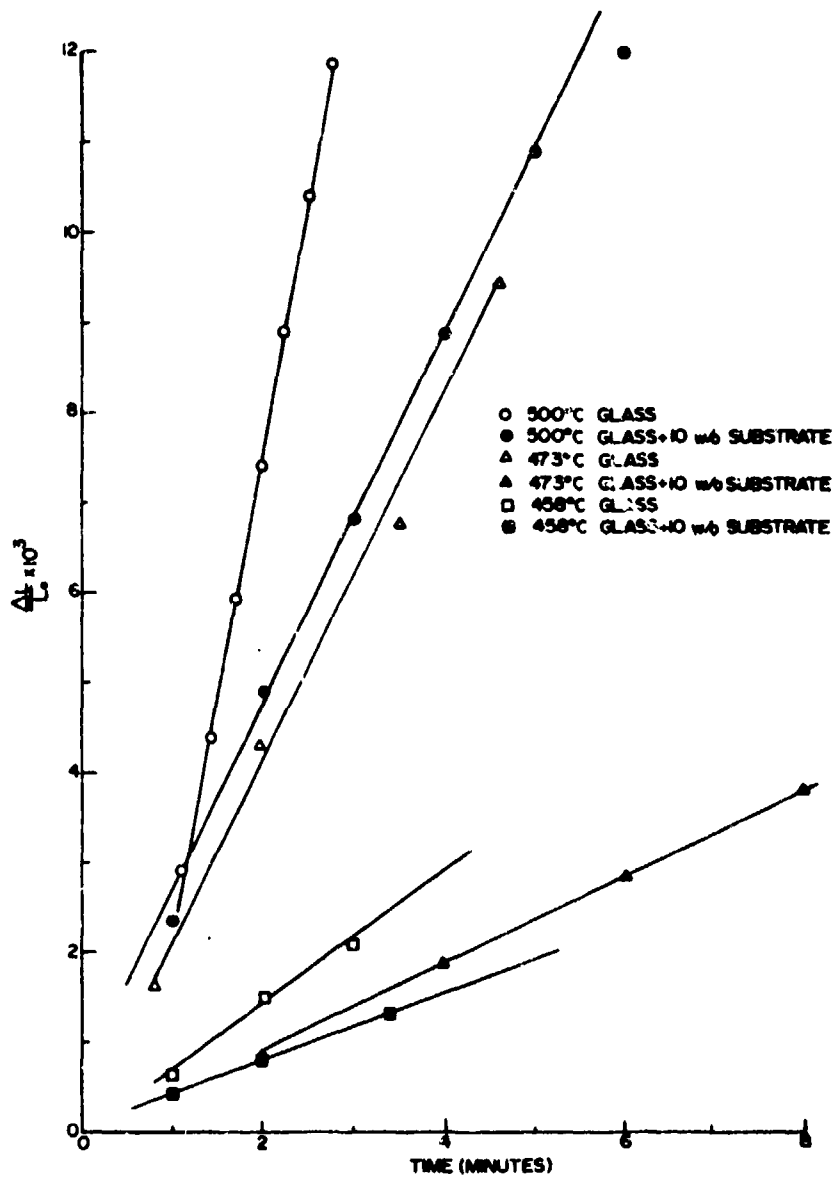
Figure 4.66   Relative Shrinkage of Lead Borosilicate Glass Compacts
During Isothermal Heating at Different Temperatures.
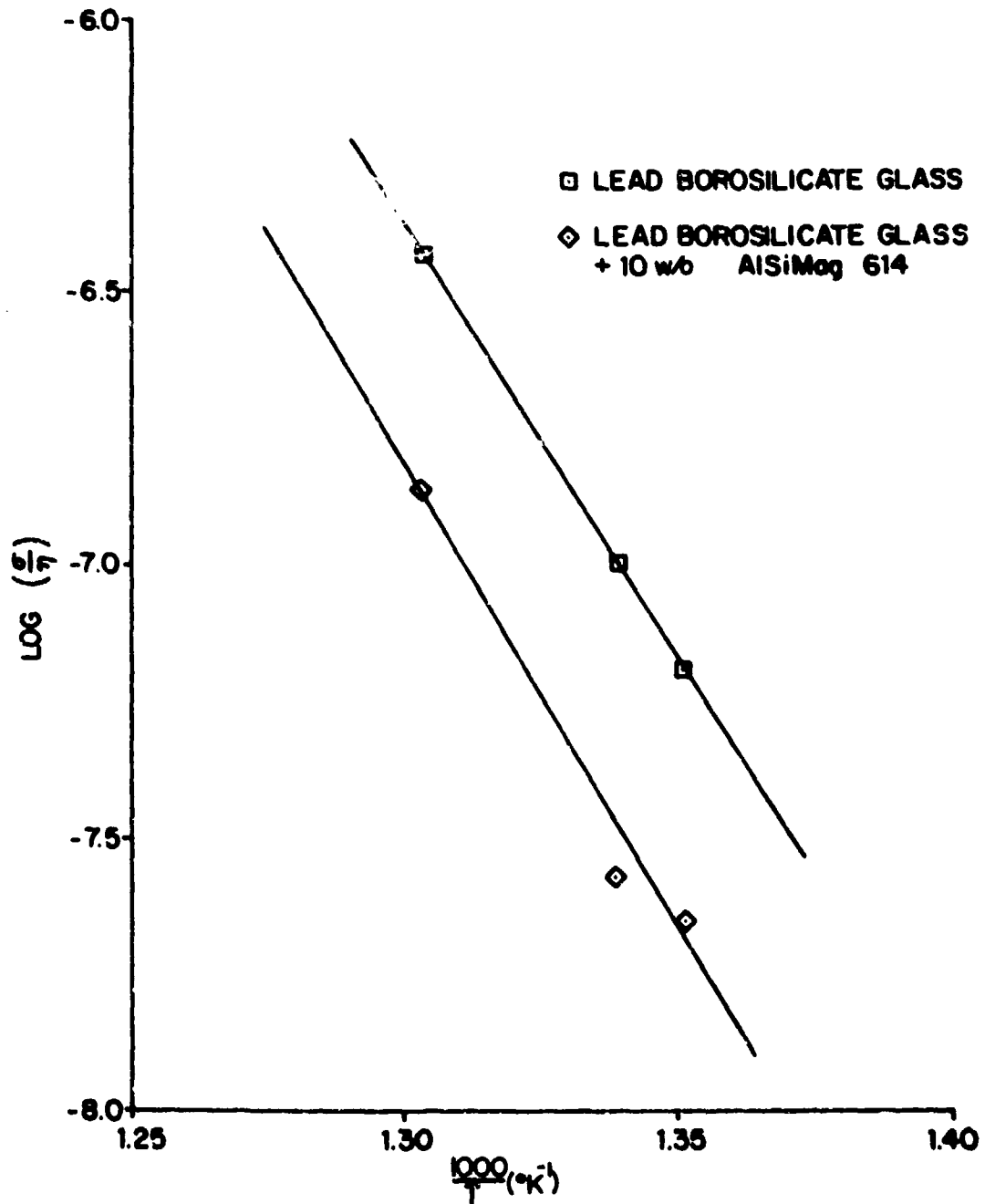
Figure 4.67   Ratio of Surface Tension to Viscosity of Lead
Borosilicate Glass From Shrinkage Measurements

shape whereas Eq. 2.13 is valid for spherical particles only. Hence
results obtained from Fig. 4.67 are not an absolute measure of surface
tension to viscosity ratios. This information was obtained only for
relative comparison of the values from the two types of glasses.

Assuming that the changes in the surface tension of the glass due
to dissolved substrate material to be negligible, it follows from
Fig. 4.67 that the viscosity increases by about 3-5 times due to the
dissolved substrate material. According to Eq. 2.40 any increase in the
viscosity decreases diffusion coefficients, thus introducing the possibility
that the rate of particle growth will decrease if the diffusional process is
rate controlling. In order to check for this possibility, diffusion co-
efficients were calculated assuming the viscosity of the glass to increase
by 5 times and substituted in Eq. 2.38 to compute the time required for the
average particle size to attain a particular value. These values were
compared with the observed values and the results indicated that the diffusional
process was about 50-200 times faster than the observed growth behaviour and
hence could not be rate controlling.

Since the results of neither the contact angle nor the viscosity measure-
ments using the glass with 10 w/o substrate material dissolved in it can
explain the observed effect of substrate-glass interactions, it is believed
that the substrate-glass interactions change the composition of the glass
such that the solubility of RuO_2 in the glass is drastically reduced.

4.3   Charge Transport

4.3.1   Single Crystals of RuO_2 in Glass

Early in the project an attempt was made to prepare samples for
measurement of diffusion and solubility of RuO_2 in glass by following
changes in electrical resistivity. The procedure was to mount single
crystals on wires so electrical measurement could be made, then encapsulate
the crystals in glass. It was hoped that measurements of the resistance
vs. time would yield data on diffusion and solubility of RuO_2, and would
also provide a clue to any new phases being formed between RuO_2 and glass
ingredients. When samples were prepared with crystals having a diameter

of 25-100 μm, no unusual effects were observed. As measured with the automatic resistance measuring system, the crystals did not change in resistance after substantial periods of time at high temperatures and no change in resistance vs. temperature was observed. If any effects were to be observed, they would be most apparent with crystals of very small diameter. The increase in resistance due to the dissolution of a thin surface layer would be greater and the higher resistance of the small crystals would improve the possibility of observing a new electrically active phase.

The crystals used for experiments reported here varied in diameter from about 2 μm to about 3.5 μm and had a length from about 1 mm to about 1.5 mm. The crystals were mounted on four 1 mil platinum wires bonded to conductive pads in a recessed area of an alumina substrate (see Fig. 4.68a). Preparing a sample involved selecting a crystal, transporting it to mounting wires, positioning it in the desired location and cementing the crystal to the four wires with the platinum paste. The crystal was then encapsulated in glass. A mounted crystal without glass is shown in Fig. 4.68b. The entire procedure required a steady hand and good luck.

The crystal was mounted in a recessed area of the substrate so that the glass could be contained better in the vicinity of the crystal. The glass could not be added by covering the crystal with powder because the glass sinters and undergoes a volume shrinkage near 600°C when the viscosity is still high. This shrinkage can break the crystal and remove the cemented wires. A procedure that produced better results was to add the glass to the well in the substrate by placing the powder around the side of the well to form a cone shape with no glass in contact with the lead wires, and then fire to 700°C for a short time to cause the volume shrinkage. This procedure was then repeated three or four times until a conical shape of fired glass extended from near the crystal to the rim of the well. When this point was reached, the sample was heated to 800°C or above where the glass became low enough in viscosity to flow to the center and encapsulate the crystal by rising up around it. Once the crystal was encapsulated, the well could be filled by adding powder and heating to 700°C.

Steady-state data, either resistance vs. time or resistance vs.

a. Recess in Substrate with 1 mil
    Platinum Wires Attached
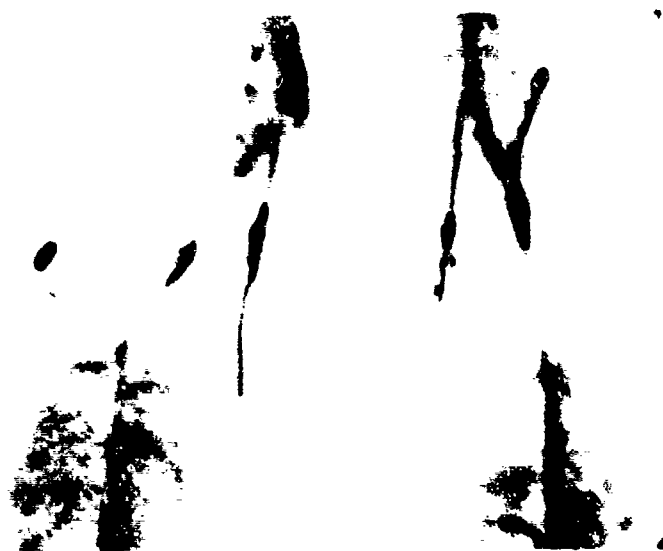
b. Mounted RuO_2 Single Crystal

Figure 4.68   Mounting of Small RuO_2 Single Crystals

temperature could not be obtained with the desired repeatibility at high temperatures because the glass would "creep" out of the recess and across the surface thereby decreasing the amount between the measurement electrodes, and the motion of the glass produced stresses on the RuO_2 crystals which eventually led to fracture in all cases.

Measurements consisting of sample resistance as a function of time and temperature were obtained for four small crystals. The data for all samples were similar to those shown in Fig. 4.69 for Sample 19 during three heating and cooling cycles. The changes in resistance at lower temperatures after thermal-cycling are primarily due to changes in lead wire geometry.

The resistance is seen to increase with increasing temperature with a TCR characteristic of RuO_2 up to a temperature between 600 and 800°C where a maximum occurs followed by a rapid decrease in resistance with further increase in temperature. This region of negative TCR is due to the parallel conductivity of the glass. The scatter of data in the high temperature region is due to the fact that the quantity of glass in the neighborhood of the electrodes is constantly changing due to creep of the glass out of the recessed area of the substrate and the necessity to periodically add new glass. Sample 19 fractured after 40 minutes at 970°C in its final thermal cycle. The base up triangle data points shown on Fig. 4.69 were obtained after the crystal had fractured and represents glass resistance only. The activation energy for glass conduction is 1.5 ev.

In summary, the series of experiments performed with small crystals in glass did not detect the formation of any electrically active phase between RuO_2 and glass under the time-temperature conditions important in thick film resistor processing, and no change in resistance due to dissolution of RuO_2 in the glass could be detected.

4.3.2   Crossed Single Crystals of RuO_2

To measure the resistance of a single contact between two small crystals of RuO_2 in the presence of glass, the crystals were each mounted on two 0.005 inch diameter platinum wires bonded to conductive pads on an alumina substrate. One wire on each crystal served as the potential lead
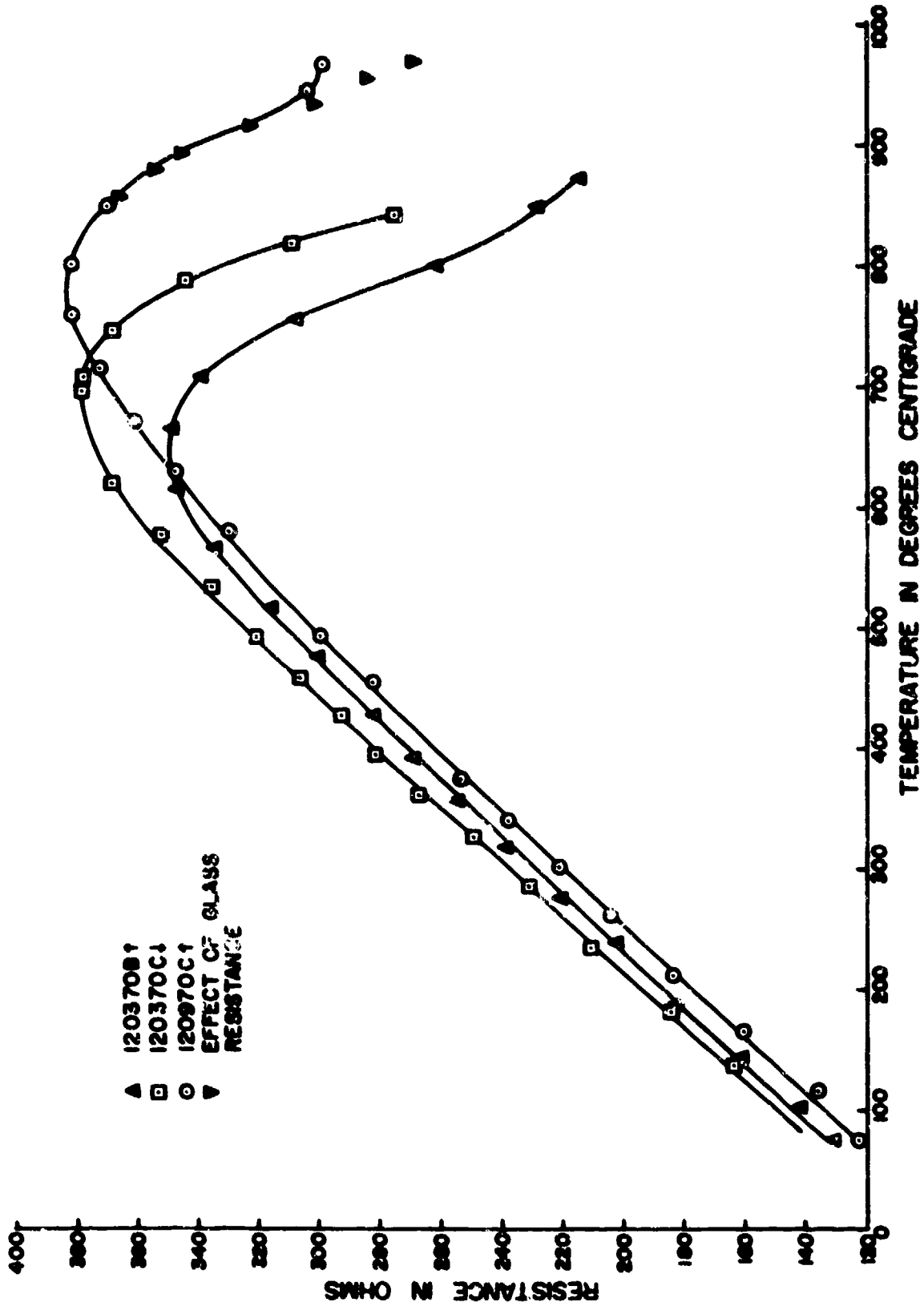
Figure 5.69 Temperature and Thermal History Dependence
of the Resistance of Sample 19

and one for the current lead, in a configuration such that the crystals crossed at a point of contact near one end. Thus, the measured resistance was the sum of the contact resistance and single crystal resistances between the potential leads and the point of contact. The 0.005 inch wire was used to mount the crystals in order to provide sufficient rigidity to maintain contact but to allow enough flexibility for the negative coefficient of thermal expansion of the RuO_2 in the c direction, the growth direction of the single crystal rods. Two additional leads were attached to the ends of the crystals beyond the point of contact. These extra leads permitted four terminal resistance measurements of each crystal with the point of contact serving as one potential lead, and allowed for the determination of crystal resistance up to the point of contact. The mounted crystals are shown in Fig. 4.70. The lead wires were attached to the crystals with platinum paste conductive.

After the crystals and lead wires were attached, the 0.005 inch platinum mounting wires w .e bent slightly to create a contact between the crystals. Glass powder was then mixed with butyl carbitol (diethylene glycol monobutyl ether) to form a paste and applied to one side of the region of intersection. With glass at the area of contact, the sample was exposed to increasing temperatures from 600° to 800°C and then recycled to 800°C. The thermal history of the crossed single crystals of RuO_2 is given in Table 4.11. Figure 4.71a shows the resistance-time behaviour during the early portion of the first firing cycle (600°C maximum temperature) for the temperature-time cycle shown in Fig. 4.71b. The sample resistance was unstable in the early portion of the cycle as might be expected for the "point" contact of two hard surfaces. The resistance oscillated from about 7 to 30Ω often with frequencies up to the response limit of the chart recorder (5Hz). At approximately the softening point of the glass (∿500°C) the resistance decreased almost an order to magnitude, and remained low and relatively noise-free for the remainder of the cycle. A visual observation of the sample after Cycle A showed that the glass had sintered with entrapped air bubbles, and showed some wetting to the crystals.

Upon reheating the sample for the next and all subsequent firing cycles, the sample resistance remained well behaved up to about the softening temperature of the glass as shown in Fig. 4.72. At this point

Figure 4.70   Crossed Single Crystals of RuO_2 (40X)

Table 4.11 Thermal History of Crossed Single Crystals of RuO_2

Firing Cycle (30°C/min)	Maximum Temperature (°C)	Measurement Cycle	TCR (ppm/C°)	Comments
012671A	600			Add glass before cycle
012871A	700	A	3770	
020371A	800	B	2980	
020471A	800	C	3260	
		D	2750	Removed the sample from the furnace to obtain crystal resistance. Sample resistance became erratic.
021271A	800			Add glass before cycle. Sample resistance became infinite at the completion of the firing cycle.
021271B	800	E	3400—3800	Add glass before cycle. Heating and cooling rate of 60°C/min near 800°C
				Sample resistance was not stable versus temperature
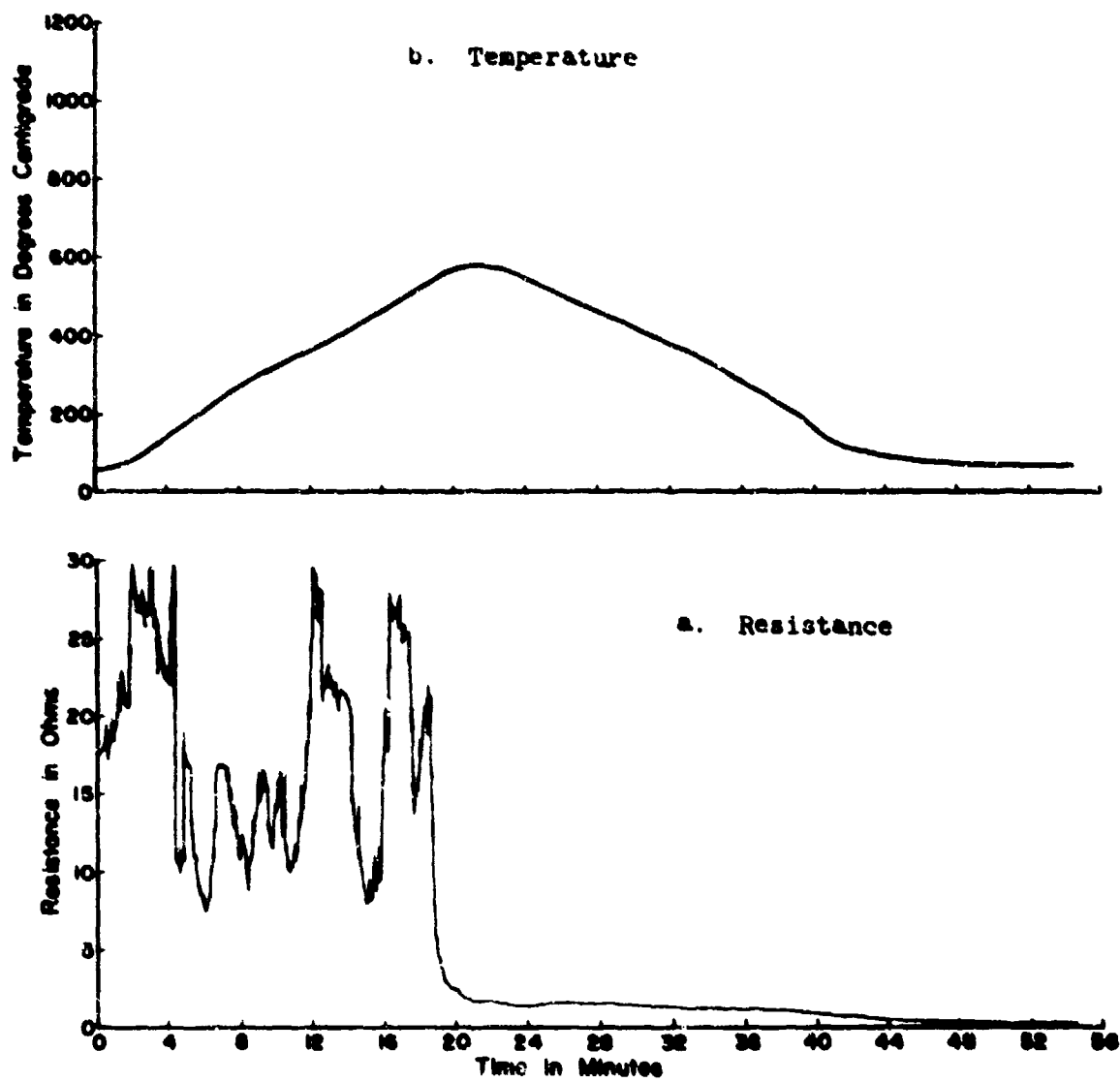
Figure 4.71   Initial Firing of Crossed Single Crystals of RuO_2
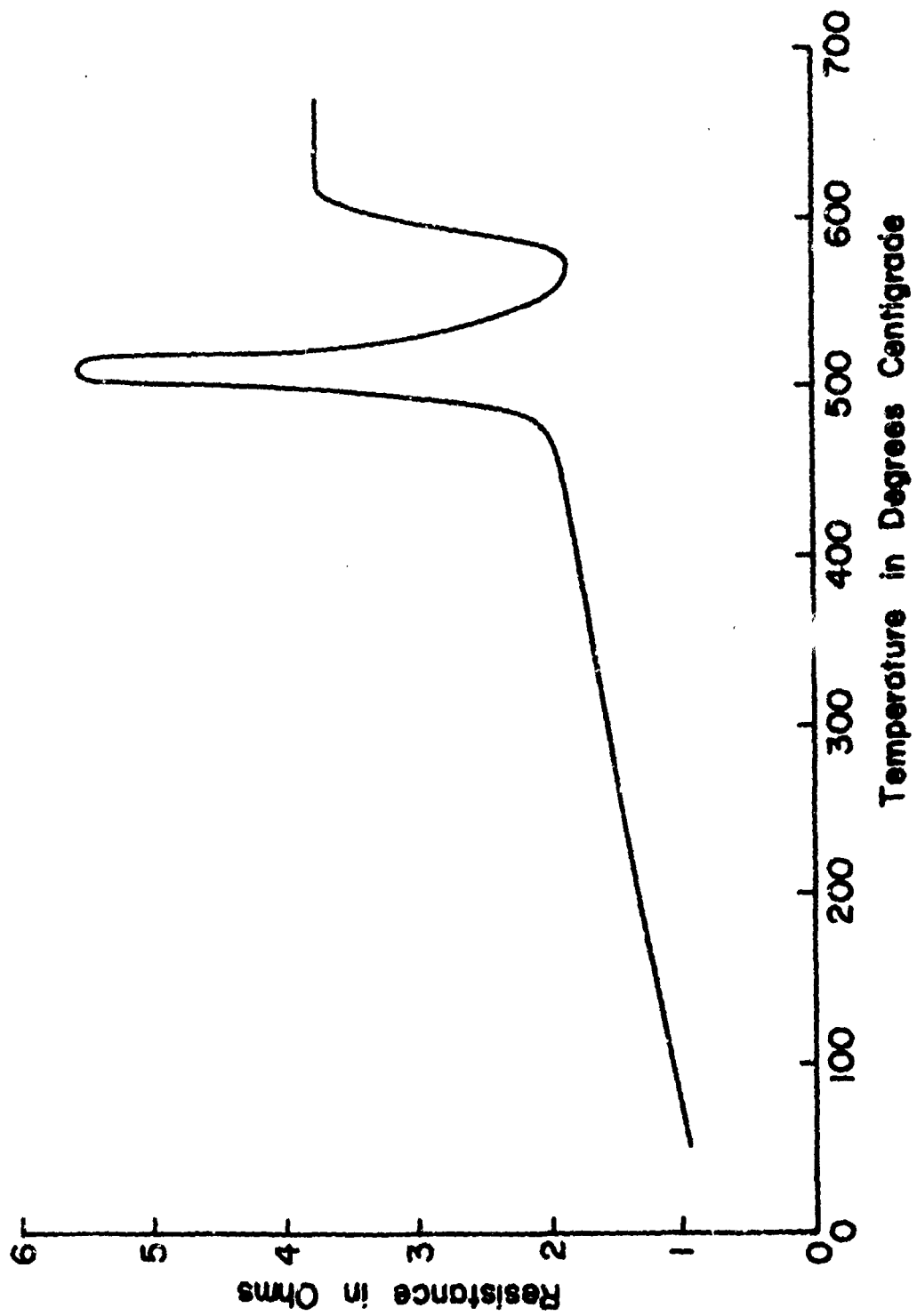
Figure 4.72   Resistance of Crossed Single Crystals of RuO_2 During Refire

the sample resistance increased several fold over a temperature range
of about 50°C, and then decreased to near the original value. Above
600-700°C the resistance was nearly constant with some low frequency
erratic behaviour.

For all cycles the sample resistance was accurately measured from
70° to 250°C, and these results are shown in Fig. 4.73; the TCR's
(extrapolated to room temperature) of the contact resistance are given
in Table 4.11. The sum of the resistances of the two crystals is about
0.01Ω and 0.02Ω at 80° and 250°C respectively, so the measured resistance
is almost entirely due to the contact. With the exception of the erratic
behaviour observed during Cycle E, the resistance of the contact at any
terperature increased by a factor of two during the life of the sample.

The sample was removed from the firing facility after measurement
cycle D to determine the room temperature resistivity of the crystals.
It was observed that although the crystal resistance measurements were
repeatable, the contact resistance was not. A visual observation failed
to clearly show the presence of any glass near the point of contact
although the observation after the 700°C firing cycle (Cycle B) showed
that the glass had completely wet the RuO_2 and had completely encircled
the point of contact. Therefore, it was assumed that insufficient glass
was present at the point of contact to maintain the bond under the stress
resulting from the negative thermal expansion coefficient of RuO_2. More
glass was added for additional exposures to 800°C but some additional
erratic behaviour was noted as summarized in Table 4.11.

Figure 4.74 compares the normalized resistance of the contact to the
resistance of single crystal RuO_2. Although there was a monotonic increase
in resistance, the TCR, as indicated by the slopes of the lines, was more
random. However, all cycles had significantly smaller slopes than single
crystal RuO_2, the minimum slope corresponding to almost half the TCR.

A second set of experiments were performed using crossed crystals
precoated with glass in order to measure resistance values very early in
contact formation. To accomplish this, a single crystal of RuO_2, approx-
imately 80 μm in diameter by 2 mm long, was mounted on two 5 mil platinum
wires and held in place with platinum paste, and 1 mil platinum wires
wrapped around both the crystal and the 5 mil lead wires. Glass powder
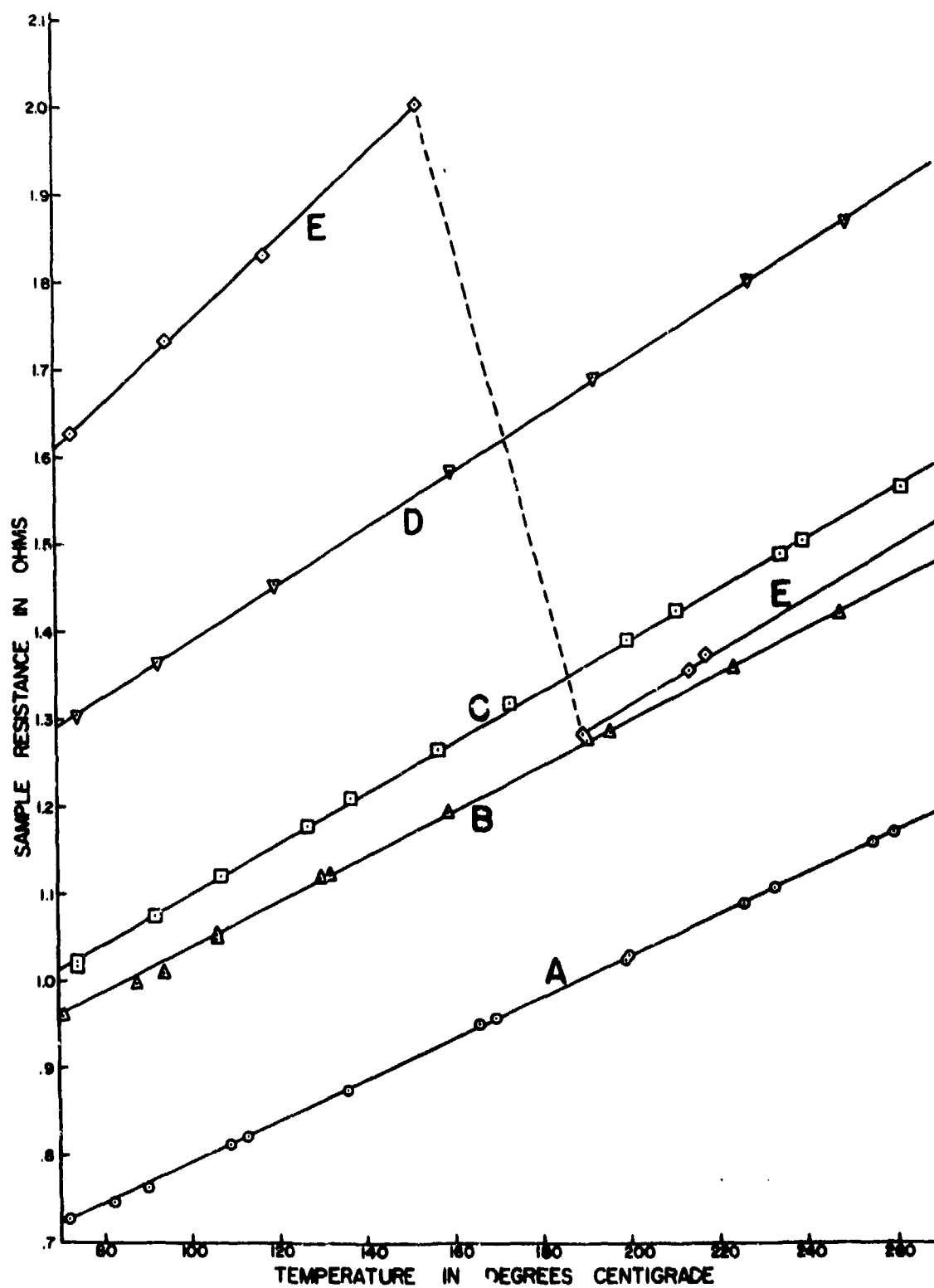
Figure 4.73 Temperature and Thermal History Dependence of the
Resistance of Crossed Single Crystals of RuO_2
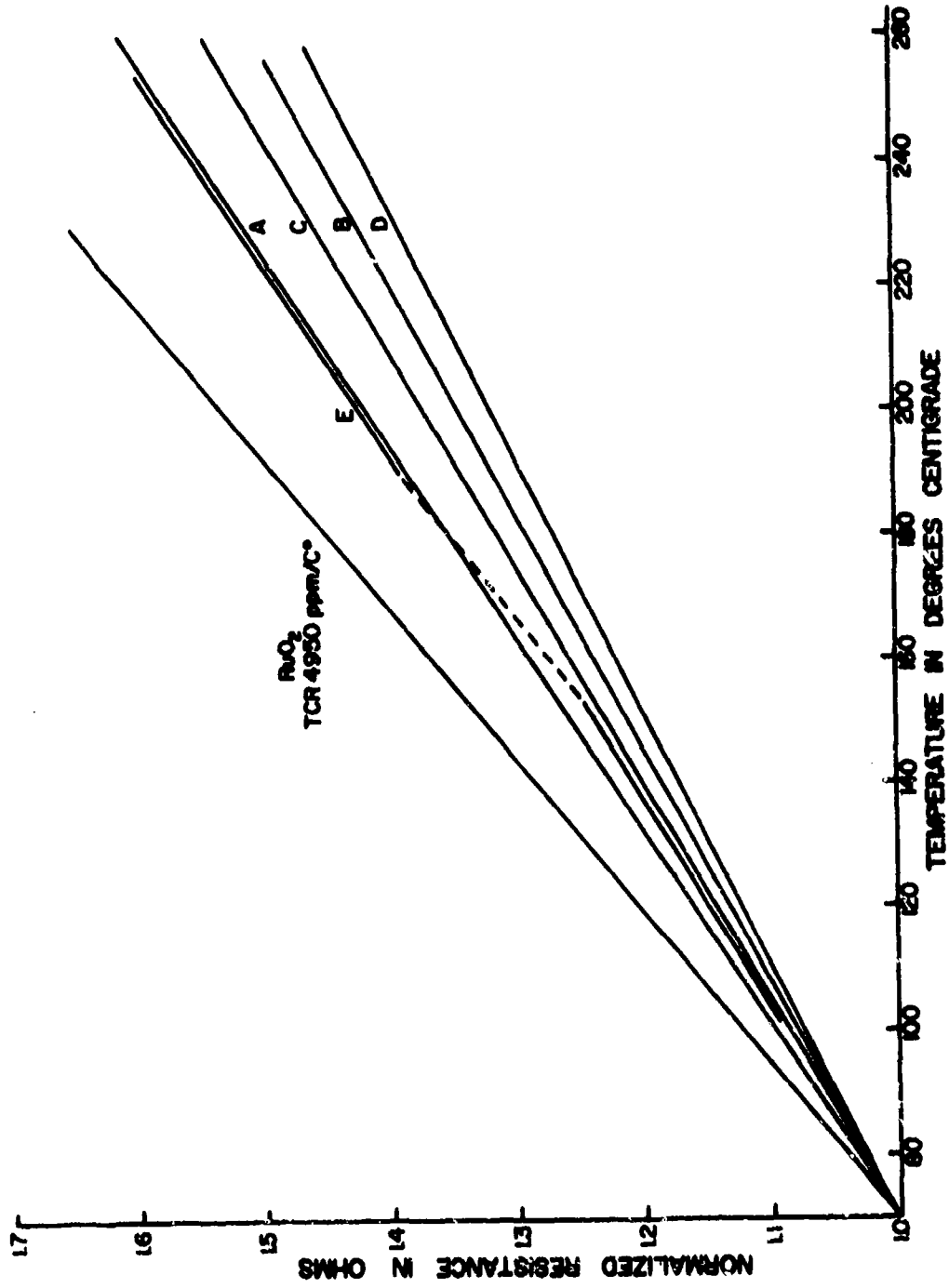
Figure 4.74 Normalized Resistance as a Function of Temperature
For Crossed Single Crossed Single Crystals of RuO_2

was then applied and heated to form a thin insulating film over the surface of the crystal. A second crystal of similar size was mounted in the same manner and then placed in contact with the first crystal. Figure 4.75 shows one set of mounted crystals after several firings with some additional glass added at the point of contact for increased strength.

The crystals were heated to about 720°C and maintained at constant temperature until the measured resistance decreased from initially infinite resistance. The decreasing resistance associated with initial contact formation was detected with a micro-switch mounted on the resistance chart recorder that detected the motion of the pen unit. At this time (after about 1½ days of firing time) the sample was quenched to study the behaviour near room temperature by moving the sample in the push rod furnace. Although the TCR was always significantly lower than +5000 ppm/°C, the early quenchings resulted in erratic resistance at temperatures above room temperature. Considerable improvement in sample life was obtained by quenching to the annealing temperature of the glass (~440°C) and holding for 8 hours. Figure 4.76 shows typical behaviour of two crossed crystal samples plotted as normalized resistance versus temperature after repeated firing cycles. TCR's calculated from these data varied from approximately 1000 ppm/°C early in the sample life to 4800 ppm/°C after several firing cycles to 720°C although the increase was not monotonic. Earlier in the life of both samples, when the resistance could not be accurately measured near room temperature due to instability, slightly lower TCR's were observed.

At several times during the life of the samples measurements were made to detect any time dependence and/or non-linearity in resistance. Time dependence measurements were made with an oscilloscope to detect time constants as small as 1 msec, and with DC current measurements for as long as 120 minutes. No time dependence was observed. The resistance was linear (voltage proportional to current) from 1 μa to 1 ma to within 0.5%. Higher current caused some non-linearity but this is believed to be due to local heating at the point of contact and an increase in resistance due to the TCR of the RuO_2. Small signal resistance versus DC bias current was also measured with the results that any change in resistance was less than 1%.

Figure 4.75   Photomicrograph of Massive Crystals with Single
Point Contact (50X)
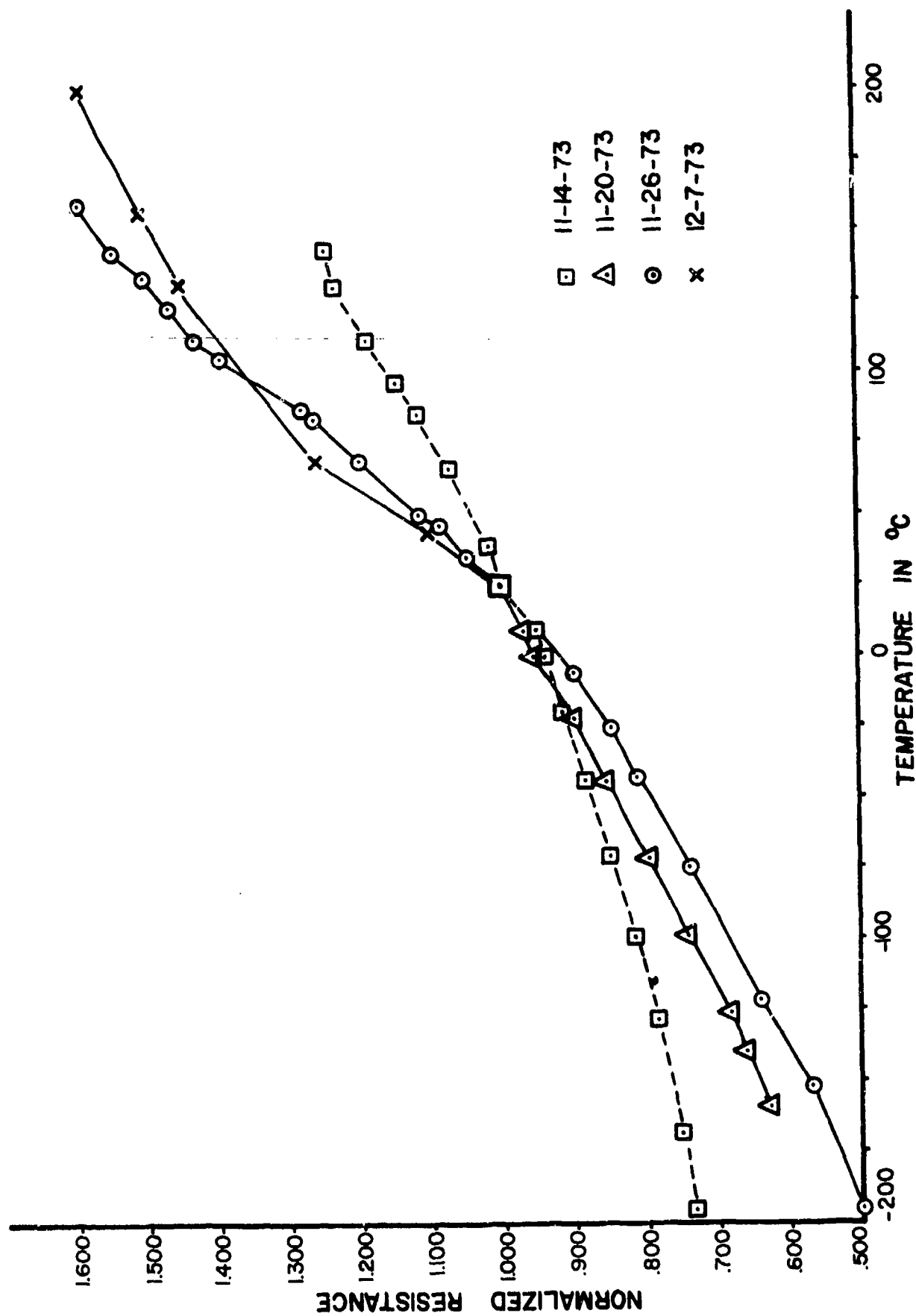
Figure 4.76 Resistance Versus Temperature of Crossed Crystals

A third series of crossed crystal experiments were performed using much smaller crystals of RuO_2 mounted on 1 mil platinum wires with a single point of contact as shown in Fig. 4.77. The thinner crystal is about 3 μm in diameter and 1 mm in length, and the other crystal is about 8 μm in diameter and 0.8 mm in length. A small quantity of glass encapsulates the region of contact; it was added after both crystals were mounted and in mechanical contact. There were a sufficient number of lead wires to enable four-wire measurement of the contact resistance.

Figure 4.78 shows the resistance near room temperature (86°C) and the high temperature TCR of the small crossed crystals extrapolated to room temperature as a function of firing time at 740°C. The resistance was initially just under 3 ohms and increased, mostly after one hour, to 4-5 ohms. During the same time the TCR decreased from approximately 4000 ppm/°C to 1200 ppm/°C. From 100 to 500 hours both the resistance and TCR remained almost constant. The contact resistance was erratic before the sample reached the softening point of the glass and the TCR was relatively large at the beginning of the firing process, close to the value of the contacting material. The influence of the glass during firing was both to increase the resistance and decrease the TCR of the contact.

4.7.3 RuO_2-Glass Composites

Massive composites of RuO_2-glass were studied in order to eliminate any effect of the substrate. The ideal experiment would have been one in which the coefficient of linear thermal expansion (α_ℓ) of the glass was the only independent variable, but this was impossible. The best compromise was decided to be the use of lead borosilicate glasses of varying composition in order to achieve a range of α_ℓ values. In addition to chemical composition, other non-controlled variables introduced by this compromise were softening temperature, annealing temperature, viscosity, and surface tension of the glass. Eight glasses were prepared for the project; the composition, annealing point, and softening point for each of these glasses is given in Table 4.3. The glass pellets to be used for thermal expansion measurements were cast in a Pt foil boat by heating rapidly to about 200°C above their respective softening points, and then cooling rapidly to room temperature.

Mounting Wires on Substrate.

Mounted Crystals.

Figure 4.77   Photomicrographs of Small Crossed Single Crystals

216
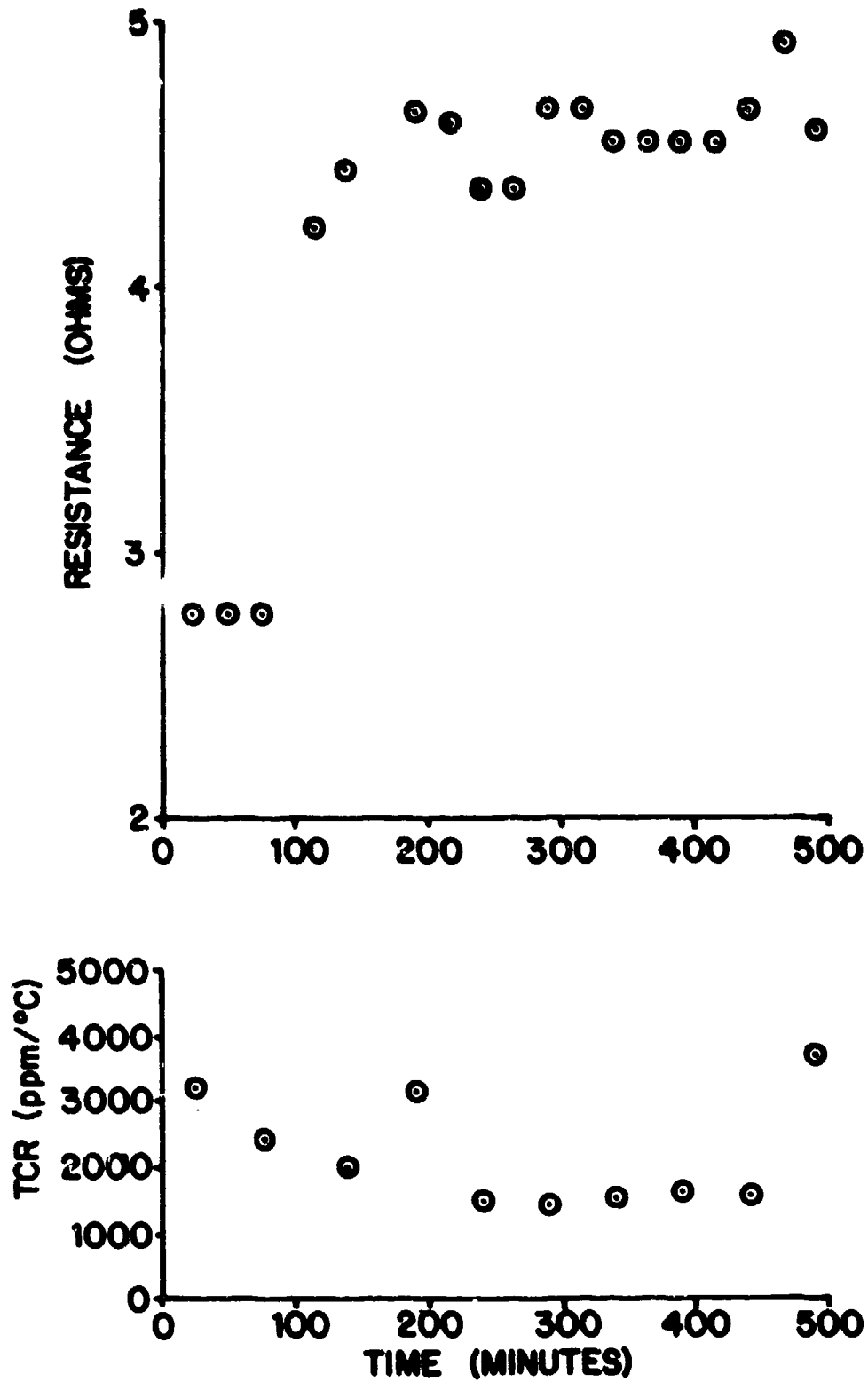
Figure 4.78   Re_ _tance and TCR of Small Crossed Crystals

The samples were then removed from the Pt boats and annealed for 1 hour at their respective annealing points. The glasses for the RuO_2 composites were first ground in a vibratory agate ball mill until they passed through a 325 mesh screen. RuO_2 powder was mixed with the glasses in the proportion of 15:100 by weight, and the mixture wet ground in butyl carbitol for 10 minutes. After grinding, the mixture was dried at 180°C for 3 hours to remove the butyl carbitol. The soft pancake of resistive mixture which resulted was broken up, the powder packed in a cylindrical rubber mold, and isostatically pressed up to a pressure of 18,000 psi. After compacting, the pellets were placed in a boat shaped Pt foil crucible, heated at a rate of 12.5°C/min to 900°C, held at 900°C for 16 minutes, cooled at a rate of 50°C/min to the annealing point of the respective glasses, held at the annealing temperature for 1 hour, and cooled to room temperature at 50°C/min. The fired resistor pellets were hand polished to shape them roughly into parallelopipeds (about 80 mm x 30 mm x 10 mm), and grooves were made on both sides of the resistor (using a diamond saw) to help lodge four Pt wires (5 mil) to be wound across the resistor. Four circumferential bands of silver epoxy paint were painted onto the resistor along the Pt wires to serve, together with the Pt wires, as the electrodes for four terminal measurements.

Thermal expansion measurements were made with a fused quartz dilatometer. For all runs it was found that the coefficient of the quadratic term in the expansion equation was at least three orders of magnitude less than the coefficient of the linear term from room temperature to 360°C; α_ℓ could therefore be taken as a constant for each glass. The results of these measurements and calculations are given in Table 4.12. The α_ℓ values given in Table 4.12 are in quite good agreement with those previously reported [82] for glasses in this system.

The resistance versus temperature plots for all of the composites were quite linear over the temperature range measured (-55°C to 125°C). The normalized resistance versus temperature plots are shown in Fig. 4.79, and the TCR for each composite is tabulated in Table 4.12. The code letters of the composites in Fig. 4.79 refer to the glass compositions given in Table 4.12. No attempt was made to determine absolute resistivities.

Table 4.12

Linear Coefficients of Thermal Expansion
of the Glasses and TCR of the Composites

Composite	Glass	α_ℓ (ppm/°C)	TCR (ppm/°C)
A	50-10-40	4.52	286
B	55-10-35	4.72	353
C	60-10-30	5.53	443
D	63-12-25	6.45	307
E	71-10-19	7.23	455
F	71-25-4	7.50	258
G	76-10-14	8.40	409
H	81-10-9	9.55	829
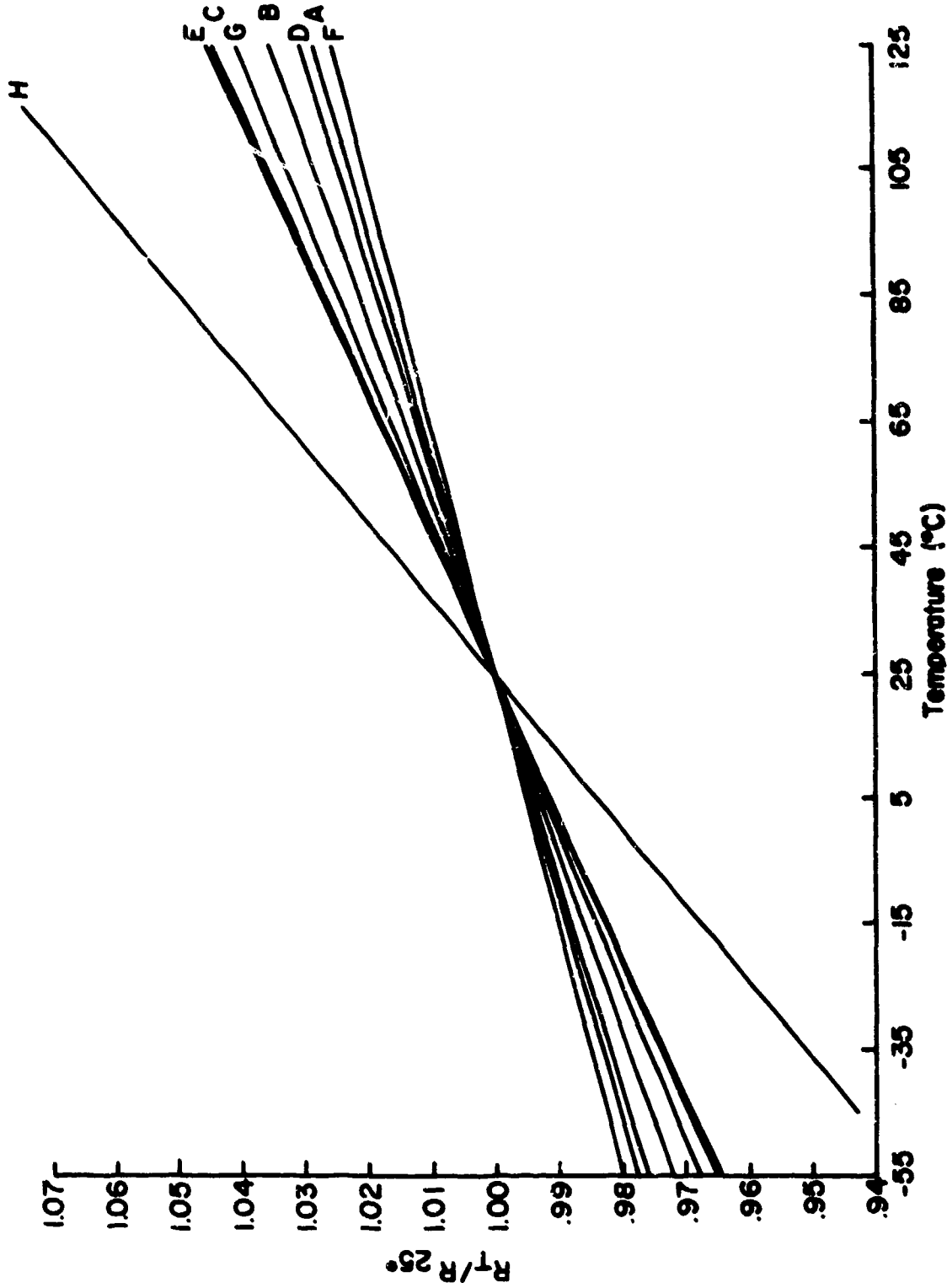
Figure 4.79   Normalized Resistance as a Function of Temperature
for Eight RuO_2-Glass Composites

4.3.4 Large Particle Resistors

Two resistor-like samples were prepared using particles of RuO_2 in the size range of 150 to 180 μm. The particles were mixed with the glass powder and a small amount of screening agent and this formulation was applied with a pick in a thin, nearly uniform layer to a substrate with four conductive terminals; screen printing was not feasible because of the particle size. Figure 4.80 shows the first sample, sample 85, after several high temperature firings.

Firing to 650°C for 2¼ hours failed to result in electrical continuity. At this stage the sample had a very large concentration of bubbles and small fractures throughout the resistor structure. Firing to 730°C for 15 minutes removed most of the bubbles and allowed the glass to flow away from the RuO_2 area resulting in a more compact film, and the resistance decreased to about 20 ohms at room temperature. Fractures of the glass were still prevalent in the cooled sample, as can be seen in Fig. 4.80b. These fractures always existed at room temperature throughout the life of both samples and, because of the small number of contacts in the conducting paths, influenced resistance value. During temperature changes of the resistor, step changes in resistance value were frequently noted; these are assumed to be due to the occurance of one or more fractures. Figure 4.81 shows resistance versus temperature for sample 85; it had a TCR of 3750 ppm/°C at room temperature. Figure 4.82 shows resistance versus temperature for the second sample, sample 88, that was measured during heating to 510°C and subsequent cooling to room temperature. From room temperature to 200°C (the same as the range for Fig. 4.81), the TCR was +3700 ppm/°C in agreement with the results obtained with sample 85. Above this temperature the TCR was negative; however, at approximately the softening temperatures of the glass (430°C), the resistance increased by several orders of magnitude going beyond the range of the resistance measuring circuit being used. On cooling, the sample was approximately ten times higher in resistance value than on heating but had a TCR with respect to room temperature of only 1460 ppm/°C. There was a step change in resistance value at 210°C that terminated the usefulness of the sample.
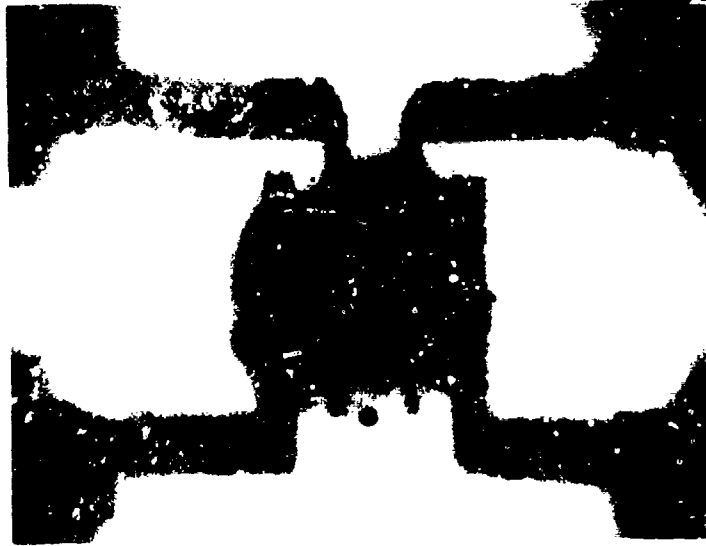
a. Resistor Geometry.
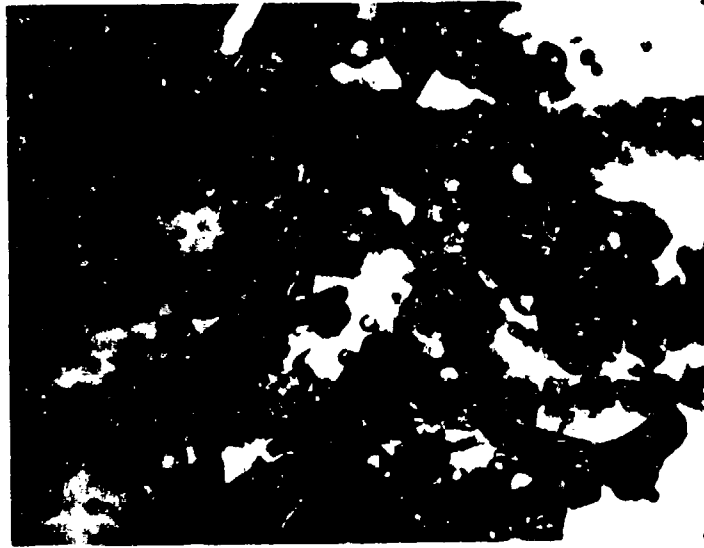
b. Detailed View Showing Fractures.

Figure 4.80   Large Particle Resistors
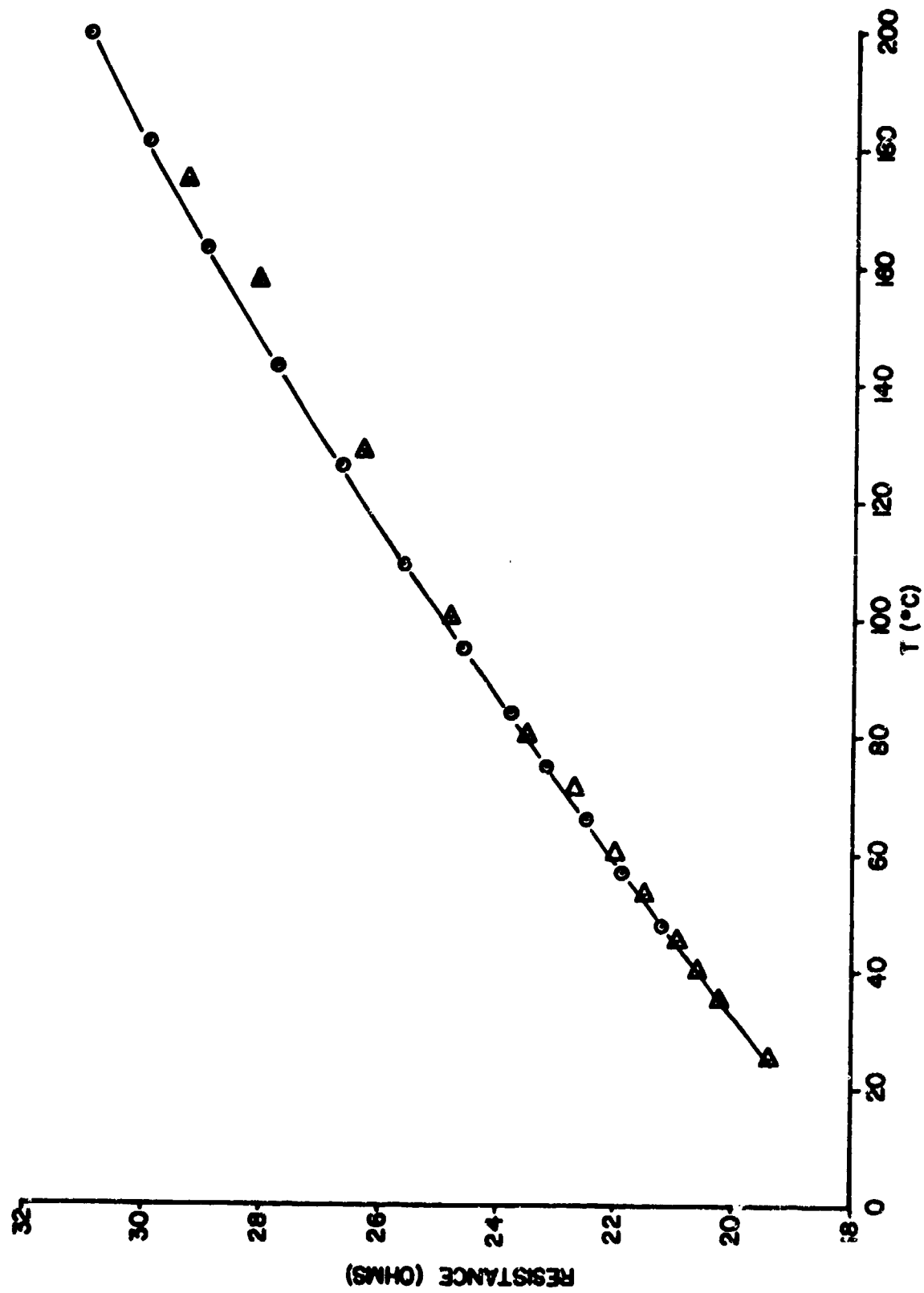
Figure 4.81   Resistance Versus Temperature of Large Particle Resistors
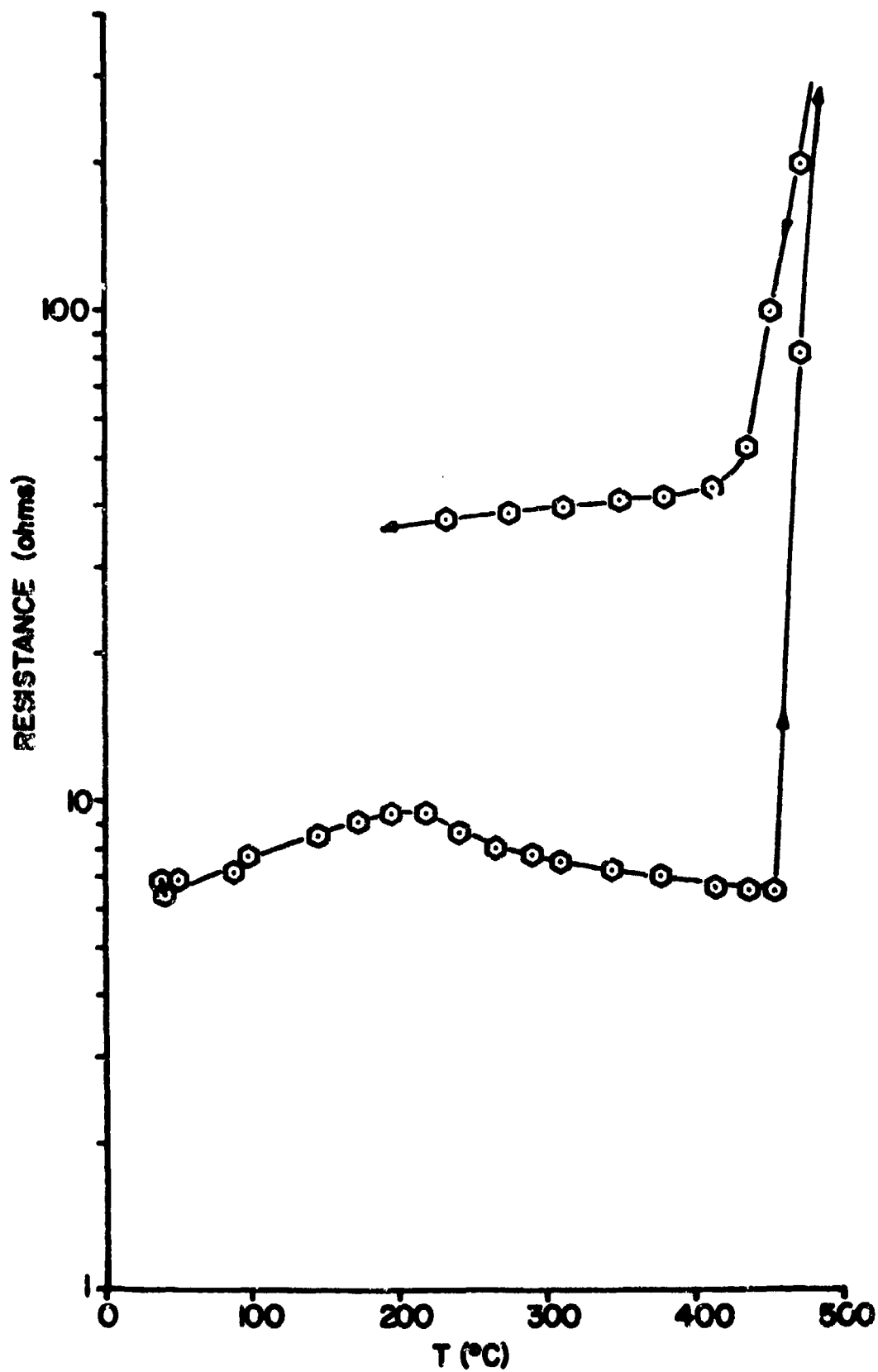
Figure 4.82   Resistance Versus Temperature During Firing of Large
Particle Resistors

4.3.5   Blending Curve

End member thick film resistor formulations were prepared by combining 5 wt.% (3.3 vol.%) RuO_2 to glass and 40 wt.% (30.2 vol.%) RuO_2 to glass powders with a 5% ethyl cellulose in butyl carbitol screening agent. The RuO_2 and glass (63% PbO-25% B_2O_3-12% SiO_2) powders used were those previously characterized. Intermediate value resistor formulations (10, 20, 30 wt.%) were prepared by combining suitable aliquots of the two end members. Each formulation was blended on the 3-roll laboratory mill described previously, and the rheology of the formulations was adjusted to the specifications previously developed. Platinum conductives were printed on AlSiMag 614 substrates $\frac{1}{2}$" x $\frac{1}{2}$" x 0.025", and fired. The resistors were then printed on these electroded substrates in a one-square pattern (0.175" x 0.175") using the modified Aremco semi-automa   screening machine and a 165 mesh stainless steel screen. The settings for snapoff distance, squeegee overtravel, and squeegee speed were those which had been determined to be optimum during the studies of repeatability of screen printing. The screened resistors were dried in a laboratory type oven for 15 minutes at 130°C to remove the volatile organics and then fired in a Lindberg tunnel kiln, using the standard time-temperature profile. Resistance of each of the resistors was determined by a 4-terminal measurement technique, averages and standard deviations calculated, and the sheet resistance normalized to a resistor thickness of 0.001". These data are given in Table 4.13 and are plotted in Fig. 4.83.

Attempts were made to prepare higher value resistors by blending the 5 wt.% end member with a glass-screening agent combination to obtain 1.5 and 3 wt.% (1 and ? vol.%) RuO_2 to glass. All resistors made from the 1.5 wt.% blend measured greater than 10^{13} ohms, and the resistance of resistors made from the 3 wt.% blend varied from 6 x 10^6 ohms to greater than 10^{13} ohms (the upper limit of our measurement capabilities). The blending curve of Fig. 4.83 is not extended to the 2 vol.%; the sheet resistance of that composition is shown as extending from 6 megohms per square to 10^{17} ohms per square, the sheet resistance of the glass.

4.3.6   Resistance During Resistor Firing

Table 4.13 Blending Curve Data

	wt% (vol.%) RuO_2/RuO_2 + glass				
	5 (3.3)	10 (6.7)	20 (14.0)	30 (21.7)	40 (30.2)
Number of Resistors	11	11	11	11	11
Average Sheet Resistance ($K\Omega$/square)	157.15	2.986	0.1669	0.04087	0.01317
Standard Deviation ($K\Omega$/square)	56.88	0.696	0.01242	0.00190	0.00038
Standard Deviation (%)	36.2	23.3	7.4	4.6	2.9
Normalized Sheet Resistance ($K\Omega$/square-mil)	106.86	2.120	0.1605	0.0358	0.01304
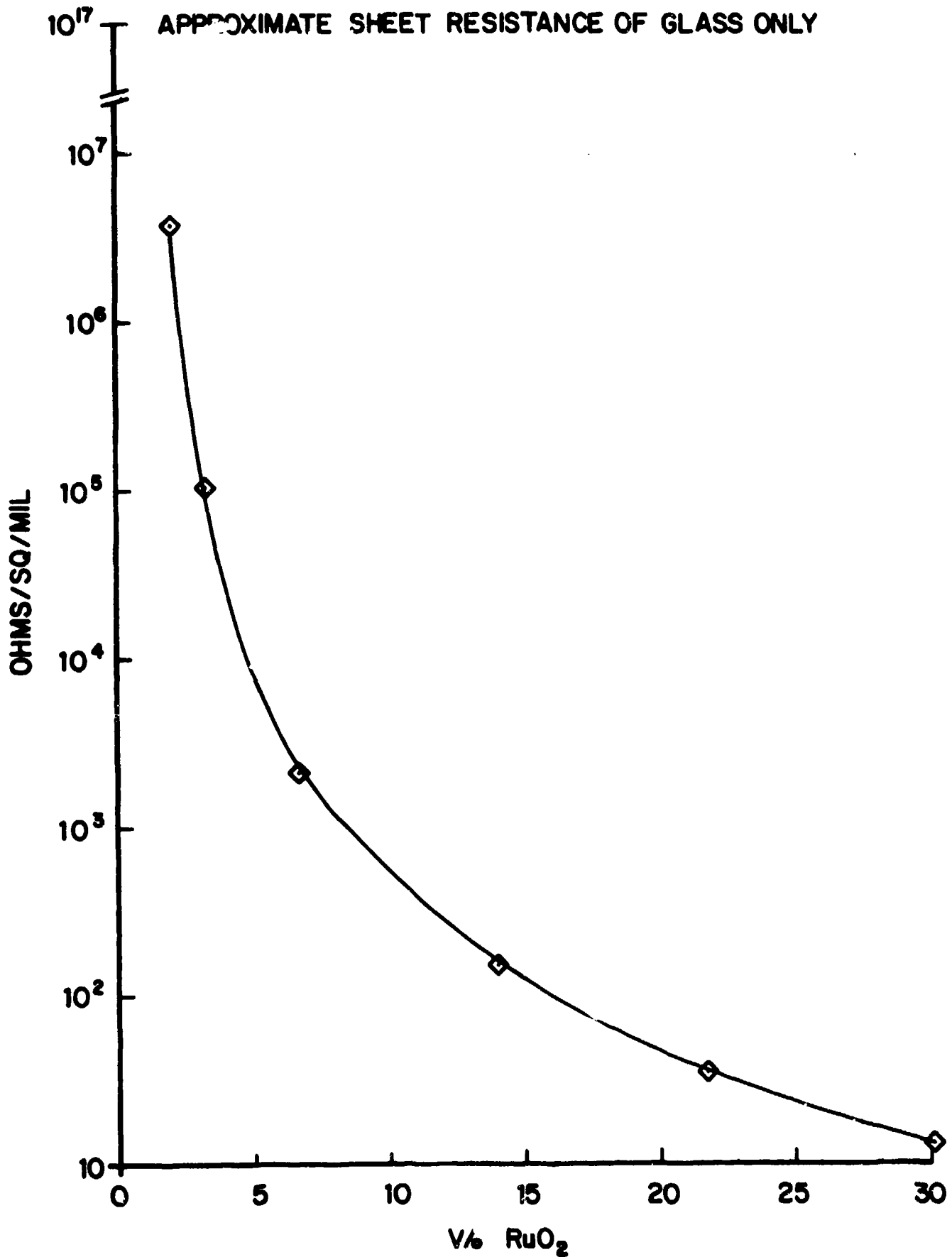
Figure 4.83   Blending Curve for 30.2 v/o and 3.3 v/o RuO_2 End Members

4.3.6.1   Low Value Resistors

The samples were prepared by screen printing 40 w/o RuO_2 formulation on the AlSiMag 614 substrates. Prior to this, platinum electrodes were put on the substrates by screen printing the platinum conductive paste and firing at 800°C for 10 minutes. After the resistor formulation was screen printed, the samples were dried for 30 minutes at 250°C. Platinum and platinum-10 w/o rhodium wires (0.0125 cm) were attached to the platinum electrodes to provide connection between the measuring system and the sample for the electrical resistance as well as temperature measurements. Electrical resistance (DC) was measured using a four probe technique employing a Data Precision 2540-Al digital voltmeter which had the capabilities of measuring resistance values from 0.1 ohm to 10^6 ohms.

Two different types of electrical resistance measurements were conducted:

a. The resistance changes under isothermal conditions were recorded as a function of time at different temperatures and the results are shown in Fig. 4.84 The resistance of the sample was about 60-70 ohms in the as dried condition prior to firing. During firing, there was a rapid initial decrease in resistance followed by a rapid increase. The rapid increase in resistance was followed by a slow decrease and then an increase in resistance at longer times. Only this final stage of increasing resistance was observed at 1120°C (Fig. 4.85).

b. The second set of measurements involved changes in the room temperature electrical resistance of the samples after they were heated at 600, 625, 650, 675, 700, 800, 900 and 1000°C for varying times. The sample fixture used is shown in the cutaway diagram of Fig. 4.86. Four spring loaded probes insulated by teflon make contact to the conductive pads on the substrate, and wires from the probes lead to the digital voltmeter.

The results are shown in Figs. 4.87 - 4.68 and are similar to the results obtained at high temperature (Fig. 4.84). Figure 4.89 gives a comparison of room temperature and high temperature resistance values as a function of time at three different temperatures.

The initial peak is seen only at 600°C in the room temperature data;
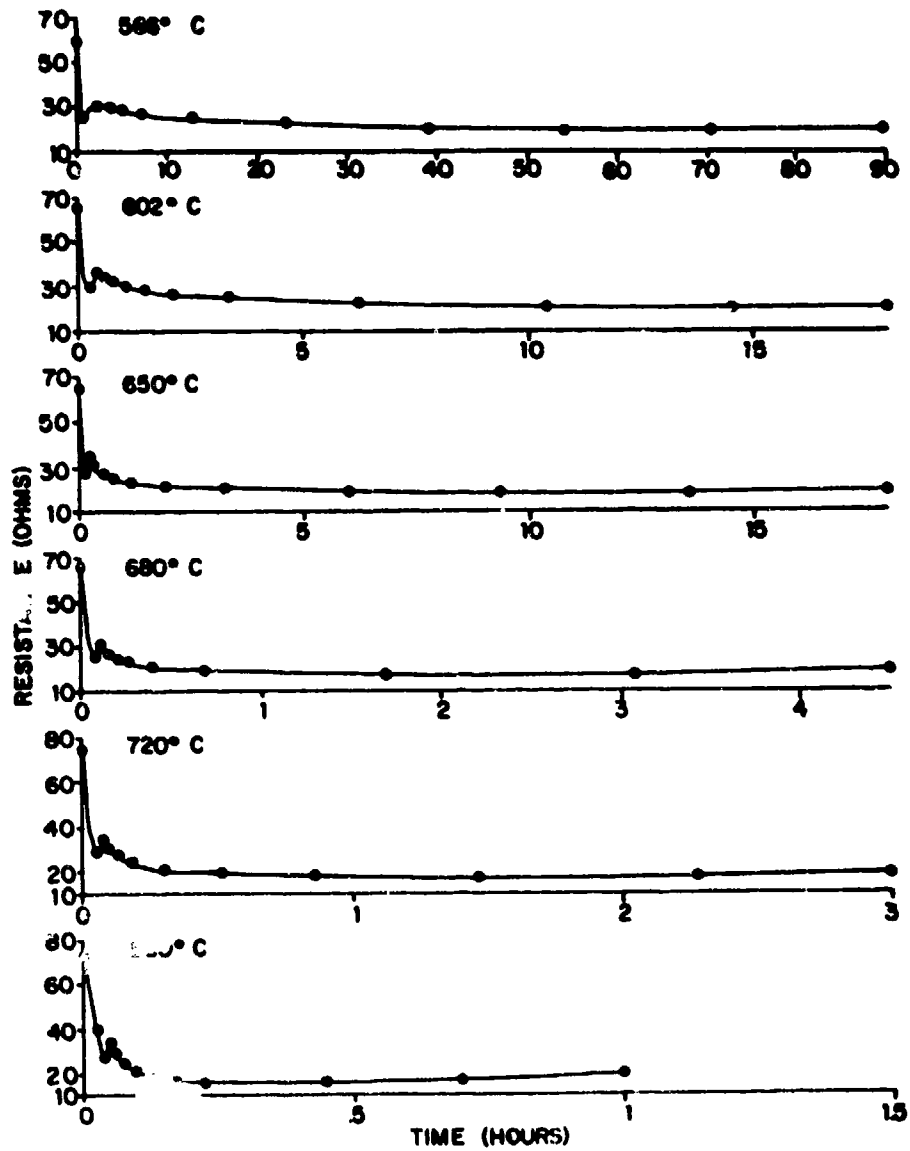
Figure 4.84   Isothermal Electrical Resistance Change During Firing
40 w/o RuO$_2$ Thick Film Resistors at Different Temperatures
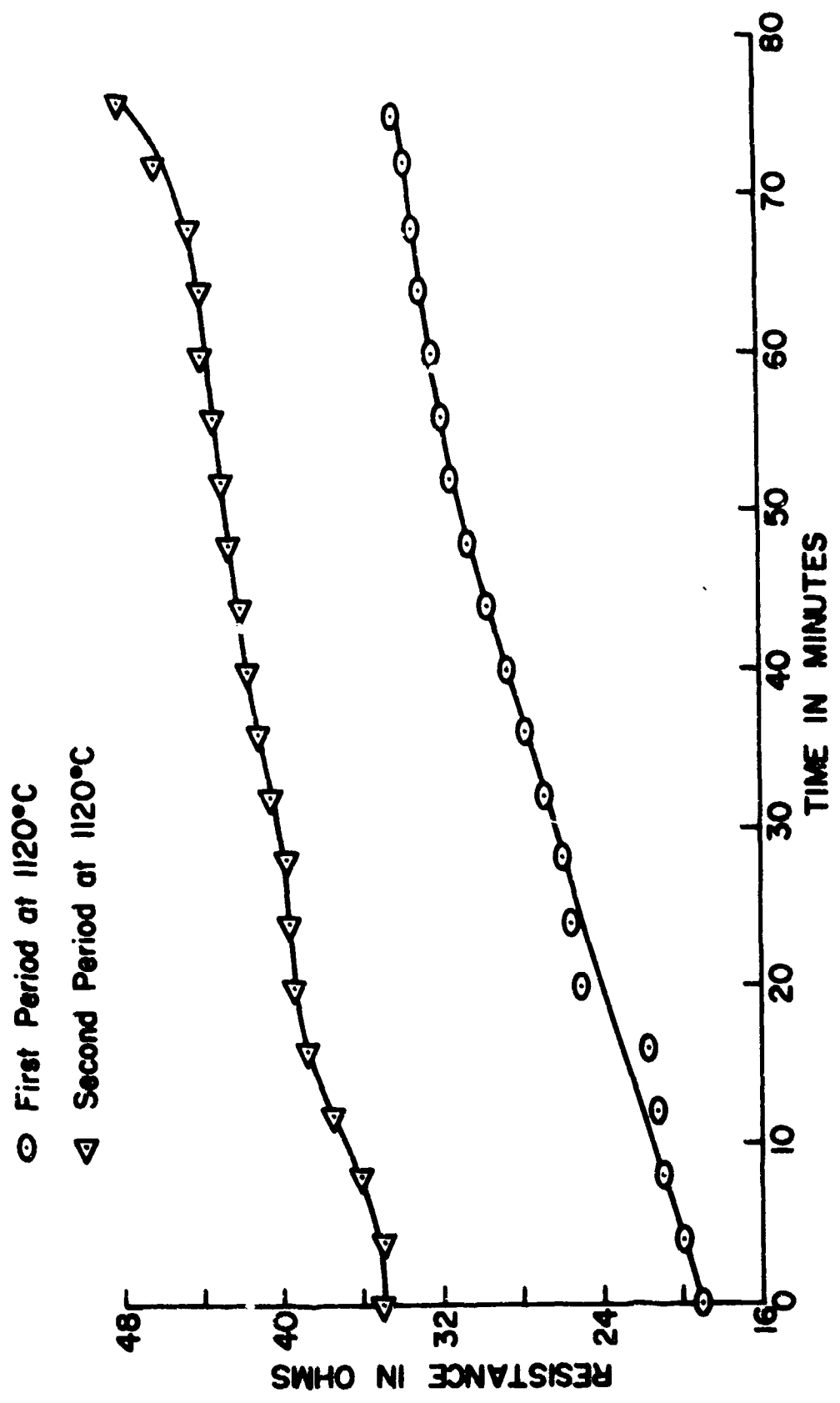
Figure 4.85   Isothermal Resistance Changes for a 40% RuO$_2$ Resistor

SAMPLE LEADS TO MEASUREMENT SYSTEM

TEFLON INSULATORS

SPRING LOADED CONTACT PROBES

THERMOCOUPLE LEADS

TO HEATER POWER SUPPLY

SAMPLE SUBSTRATE

THERMOCOUPLE

HEATER WINDING
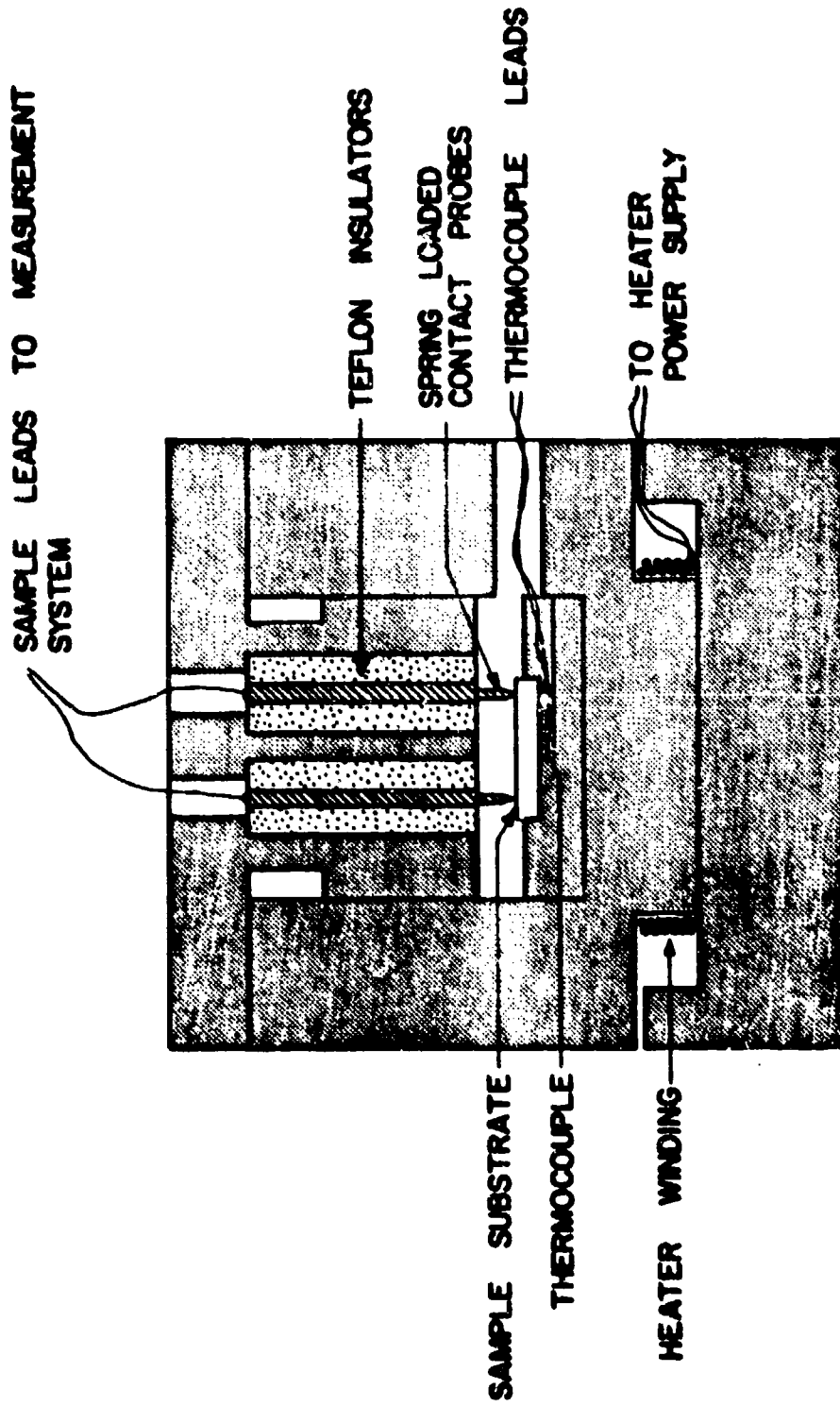
Figure 4.86   Assembly for Room Temperature Electrical
Resistance Measurements
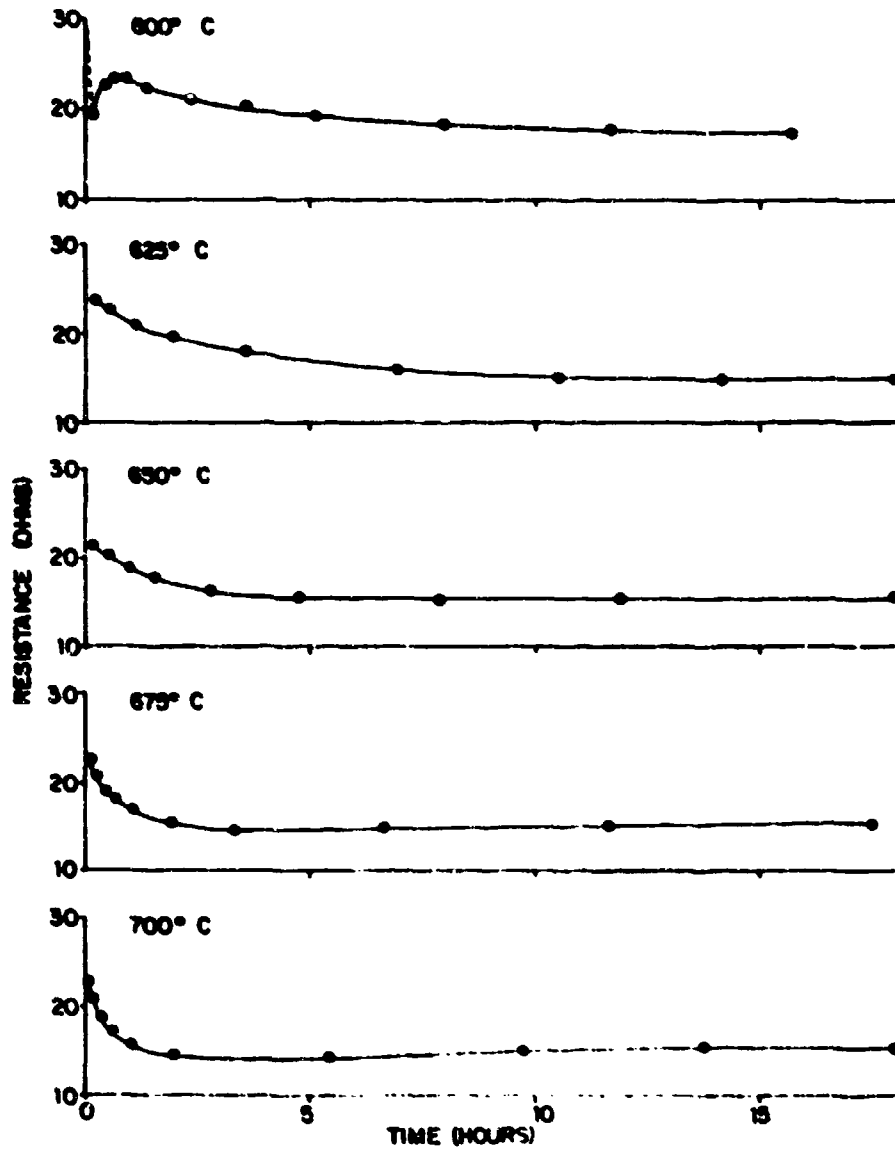
Figure 4.87   Room Temperature Electrical Resistance Versus Time
of Firing for 40 w/o RuO_2 Thick Film Resistors at
Different Temperatures
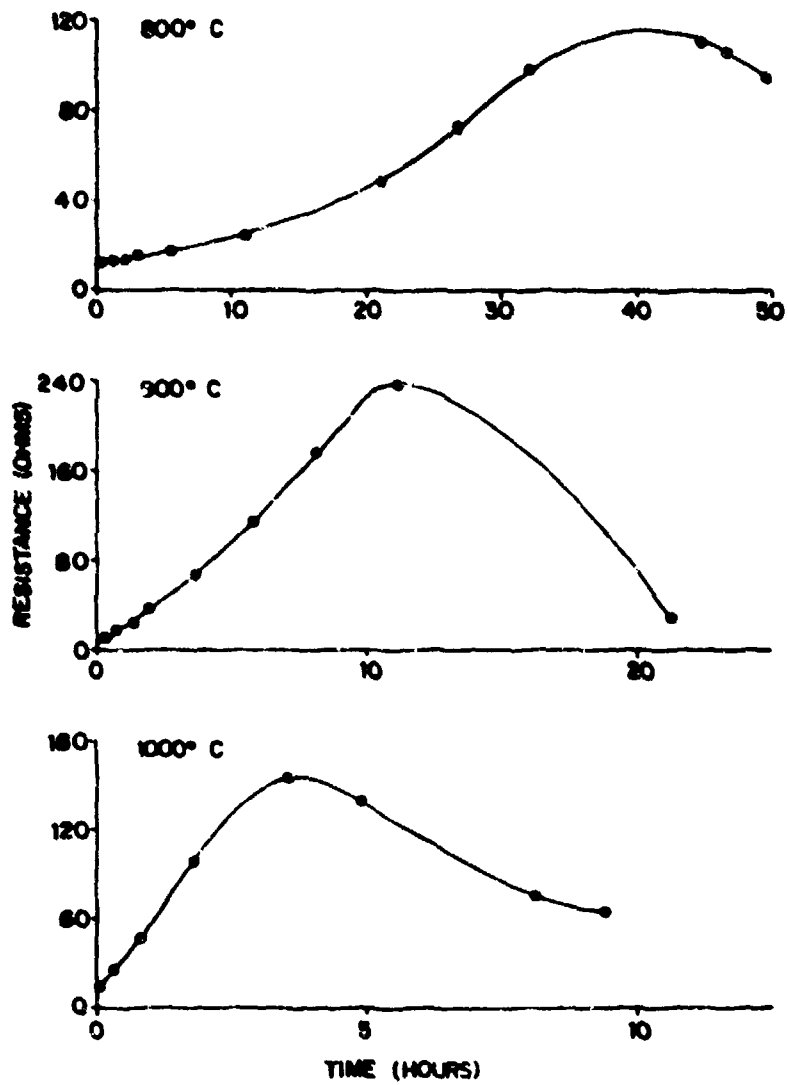
Figure 4.88   Room Temperature Electrical Resistance Versus Time
               of Firing for 40 w/o RuO_2 Thick Film Resistors at
               Different Temperatures
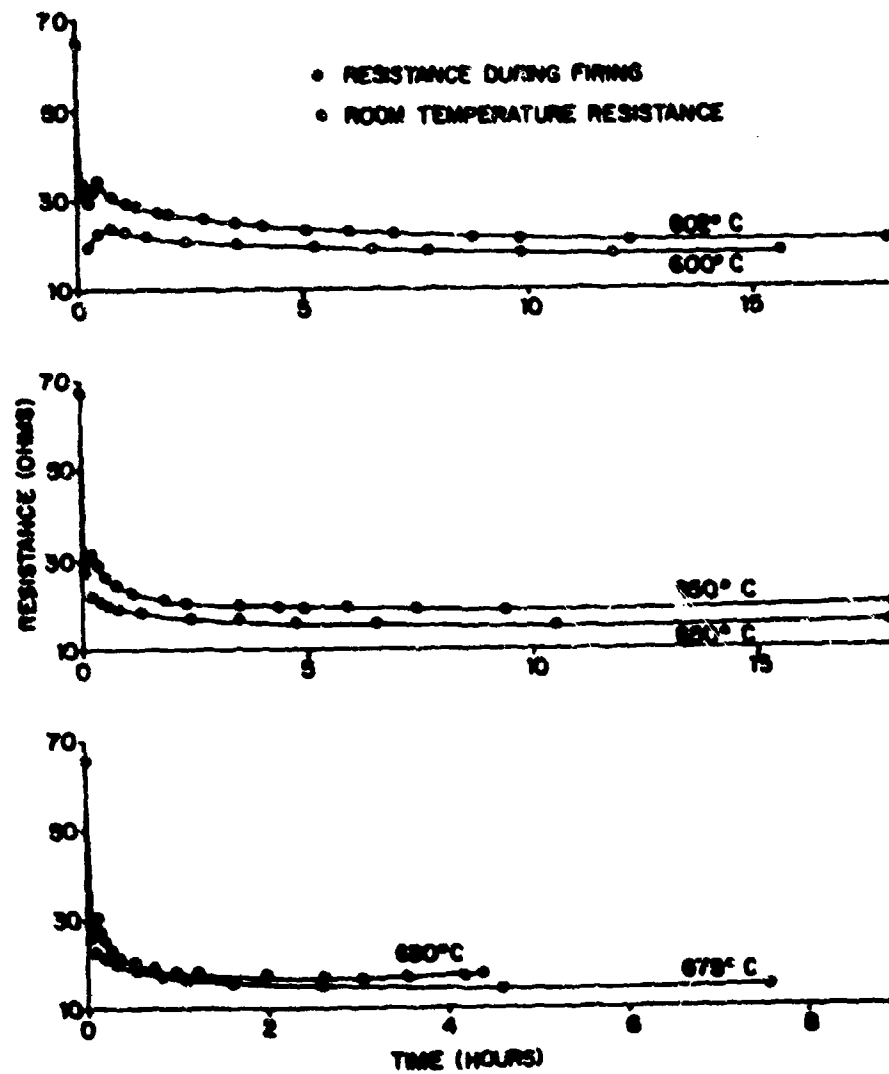
Figure 4.89   Comparison Between Electrical Resistance Change During
Firing and Room Temperature Electrical Resistance After
Firing for 40 w/o RuO_2 Thick Film Resistors

at the higher temperatures the peak occurs over such a short period of time that either the resistance has increased and decreased before the initial datum point is obtained, or the first datum point is before the peak and the second after the peak. At higher temperatures (800, 900 and 1000°C) the initial stages occur in a very short time and the resistance increase can be easily observed. At still longer times at the higher temperatures the resistance is seen to decrease again.

4.3.6.2   High Value Resistors

The properties of resistors having a low RuO_2 content relative to glass are much more sensitive to processing parameters than low value resistors. This is a good situation for determining the effects of time and temperature during firing, but unfortunately effects due to variations in starting powders and formulation blending are also more pronounced. This situation limits quantative correlations, but the data are still extremely useful in developing models for microstructure development and charge transport mechanisms.

Using the standard profile and measuring the resistance of 3-10 w/o RuO_2 resistors during firing with the push rod facility, the resistance was observed to remain very high until a critical temperature (650-750°C depending on the formulation) at which point it dropped very rapidly. In order to slow down the kinetics of resistor formation, resistance was measured as a function of time at a constant temperature below the critical temperature. The test temperatures were chosen, after preliminary experiments with each formulation, in order to maintain network development times long compared to the time required to quench the samples to obtain room temperature resistance measurements at periodic intervals during the firing. More than fifty resistor samples (5 - 10 w/o RuO_2) were fired with concurrent resistance and temperature measurements using a variety of time-temperature profiles. Taken as a group the results indicated the variations in time and temperature that result in electrically conductive and low TCR resistors (e.g. < 2 megohms/square,< $\pm$ 400 ppm/°C) and have shown that the firing process and the creation of a conductive network has certain repeatable characteristics regardless of other minor details.

Figure 4.90 shows the resistance at 50°C versus time at 640°C for seven samples. The same basic behaviour was observed for all samples: the resistance decreased from an initial infinity to a minimum at approximately 10 hours and then increased monotonically. The TCR increased early in the life of the sample but remained negative throughout the firing period. This negative TCR behaviour was typical of this particular formulation; positive TCR's were observed after the minimum resistivity was reached with other formulations. Part of the resistance increase at times greater than 10 hours was due to a high resistance interface at the platinum conductive and the TCR and resistance data were not valid representations of the resistor for times in excess of 20-25 hours.

The samples represented in Fig. 4.90 were prepared to demonstrate that the room temperature resistance versus firing time is repeatable for identical samples and firing profiles and, therefore, that samples can be prepared in definable stages of development. The seven samples were terminated at firing times of 2-1/2, 4-1/2, 6-1/2, 10, 21, and 72 (2 samples) hours in order to directly analyze the developing microstructure; four of these microstructures were discussed earlier (Fig. 4.34). It can be seen from Fig. 4.90 that the spread in sample resistance minimizes at the minimum in resistance value, and that the resistances do not diverge greatly from that point on. However, the resistance spread before the resistance minimum is much greater; in some cases they differ by a factor of ten.

Further insight into resistor formation can be obtained by measuring resistance versus temperature after varying times at a test temperature where the kinetics of resistor formation are sufficiently slow so that periodic withdrawal from the furnace for resistance measurements will not perturb the results. For this study a resistor was fired at 590°C for a total of 350 hours. The room temperature resistance remained very high up to 30 hours at which time it was approximately 8×10^6 ohms. The resistance then showed a steady decrease between 30 and 100 hours, a minimum resistance of 3×10^5 ohms at 150 hours, and then a gradual increase in resistance up to 350 hours. The test temperature (590°C) was high enough for the resistance of the glass to be measured with the measurement system; it was approximately 3 megohms as taken from the
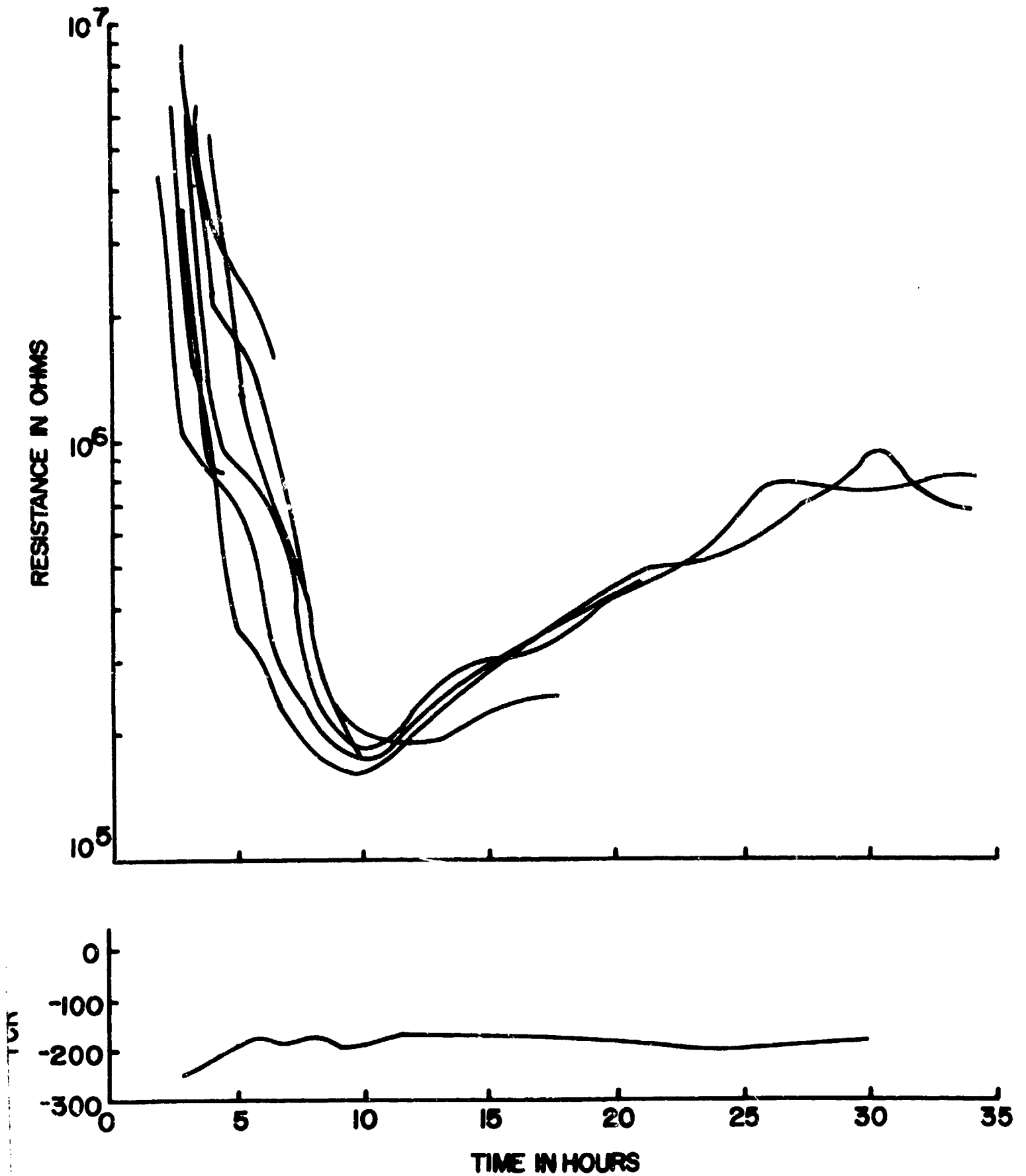
Figure 4.90   Resistance at 50°C and TCR Versus Firing Time At 640°C

measured resistance at the beginning of the experiment. The resistance
at 590°C monotonically decreased by a factor of four during the first
350 hours.

At various times during the experiment the sample was withdrawn from
the furnace and then reinserted while continuously measuring its resistance.
Some results of these experiments are shown in Fig. 4.91. Before the
resistor began to form, the glass furnished the only conduction mechanism,
probably ionic. This is shown in Fig. 4.91a after 20 hours of firing
time where the resistances during both heating and cooling increased
rapidly at lower temperatures. At 26 hours, Fig. 4.91b shows a resistance
versus temperature behaviour that appears to be as characteristic of
initial resistor formation. The resistance measured at room temperature
was considerably lower than that observed after 20 hours. During the
heating portion a dip in the graph develops at a temperature a little
lower than the softening temperature of the glass. Later, at 42 hours,
(Fig. 4.91c), when room temperature resistance measurements indicated
that the resistor was more completely developed, the dip that existed at
26 hours has become more apparent because the resistance at lower temp-
eratures is lower, and because a "bump" has formed at a slightly higher
temperature. Also, at this stage of development a dip now appears
during the cooling period. Still later in resistor formation, for example,
56 hours, dips and bumps exist in both the heating and cooling profiles,
but they are always more pronounced in the heating cycle. Figure 4.91d
does not emphasize the magnitude of the dip because it is located near
the zero of a linear axis.

For the development of microstructure and charge transport models
it is desirable to measure both the resistance versus temperature behaviour
to low temperatures and the current voltage characteristics as a function
of the degree of resistor development. For these experiments resistors
were screen printed using a formulation containing either 5 or 10 w/o RuO_2.

Figures 4.92 and 4.93 represent typical characteristics of the 10 w/o
RuO_2 formulation. Figure 4.92 shows that the resistance at room temperature
decreased from an initial very high value to a minimum at 8 hours and
then increased slowly. The TCR, shown on Fig. 4.93 was originally highly
negative, on the order of -450 ppm, and increased rapidly with firing. The

238
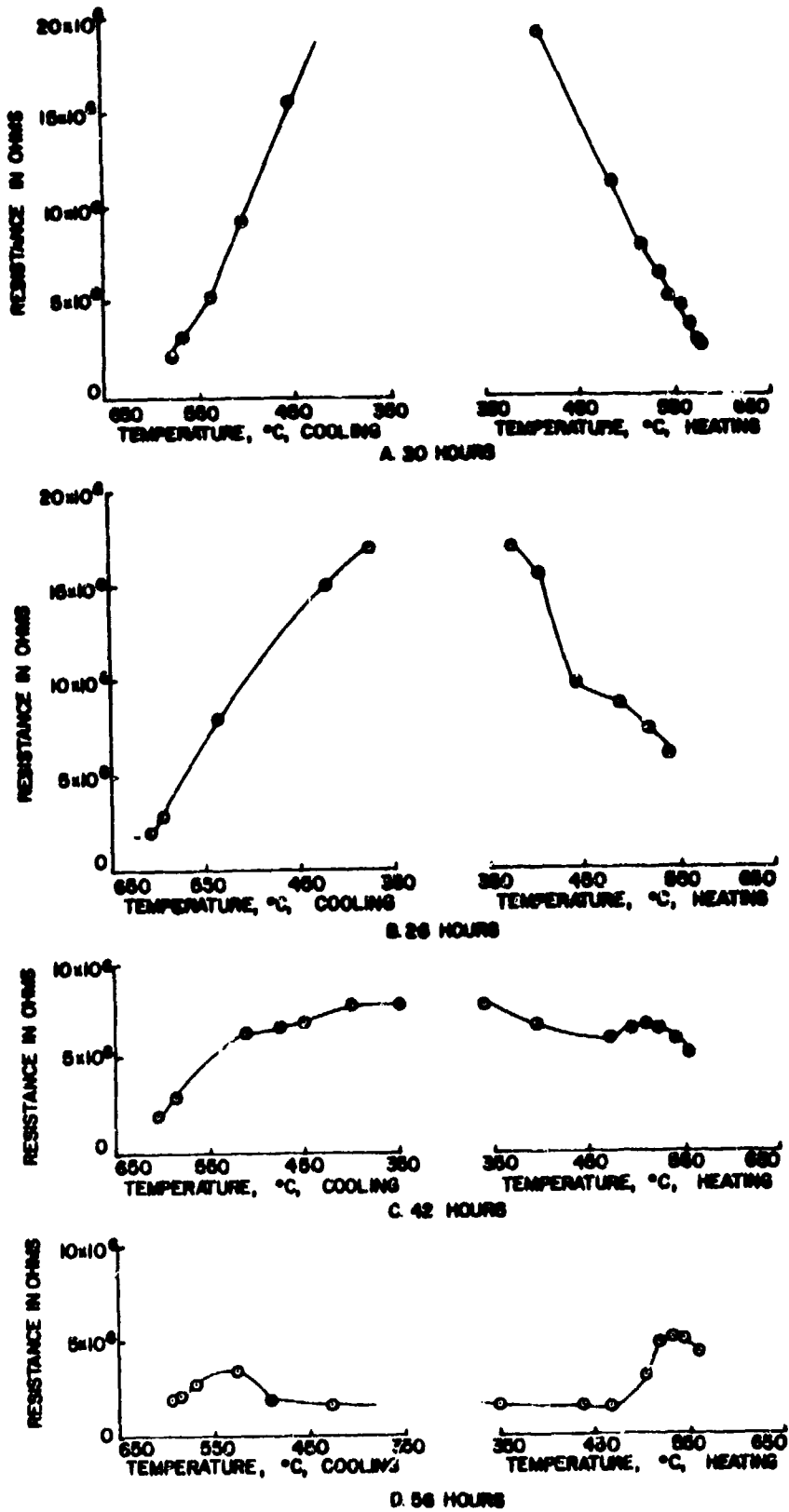
Figure 4.91 Temperature and Thermal History Dependence of Sample 35
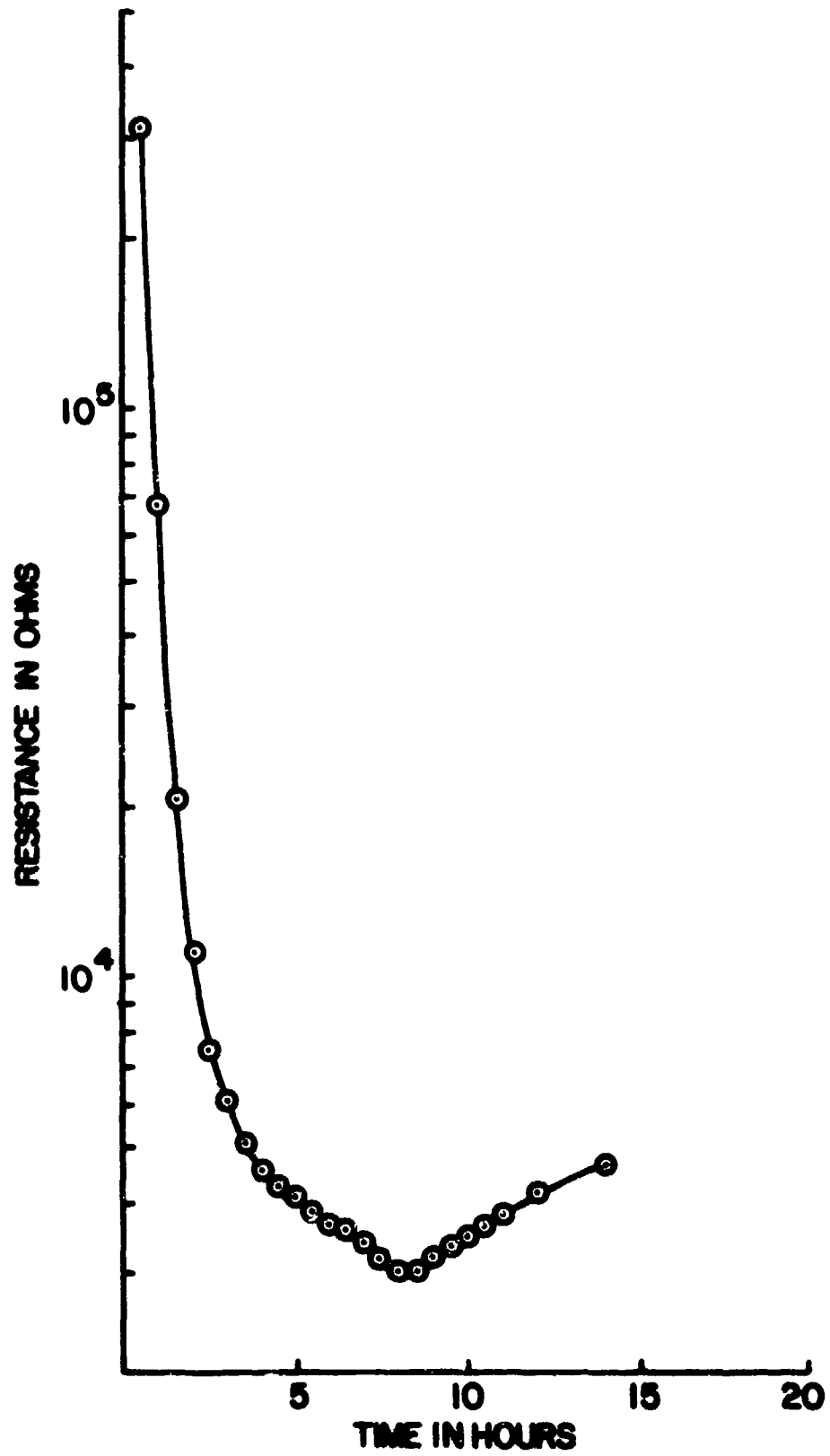
Figure 4.92 Resistance Versus Firing Time for 610°C Maximum Temperature
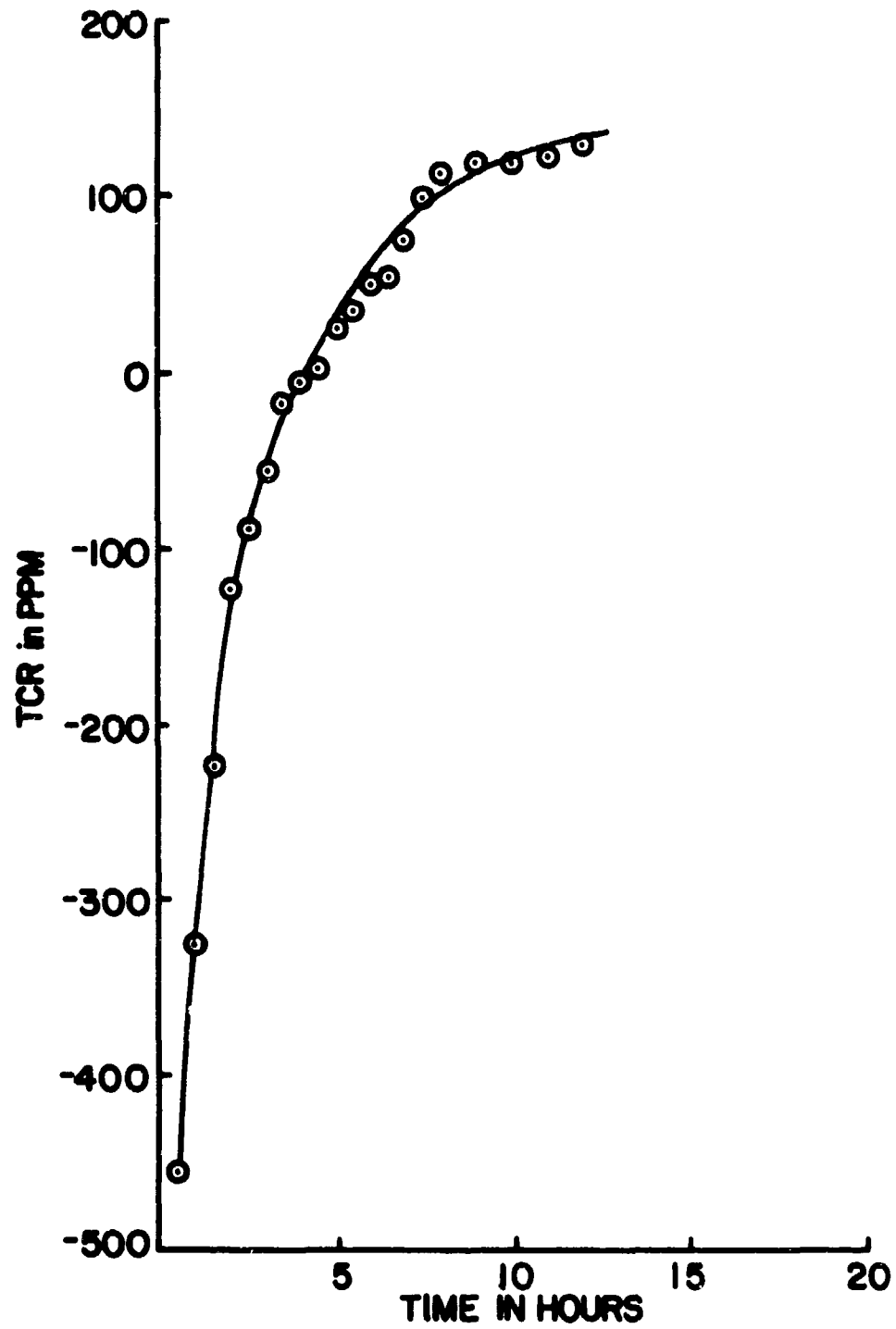
Figure 4.93 TCR Versus Firing Time for 610°C Maximum Temperature

The TCR crossed zero before the resistance was a minimum and continued positive until it reached about +125 ppm at 10 hours, after which it was approximately constant.

Resistance versus temperature measurements for resistors in various stages of development were extended to lower temperatures by utilizing the sample fixture shown in Fig. 4.86. The fixture was lowered into a dewar which was then filled with liquid nitrogen to completely cover the sample fixture. After the data point at -196°C was taken, the fixture was removed from the dewar and allowed to warm slowly in a room temperature environment while the resistance was continually recorded. The rate of temperature increase was consistent with the ease of measurement in reasonable time except above -50°C where the heater was used. Figure 4.94 shows the normalized resistance versus temperature of three resistor samples fired for varying times at 630°C. Sample 78 was fired for 20 minutes and has the most negative TCR at room temperature; sample 74 was fired for 40 minutes and has an intermediate TCR; sample 77 was fired for 90 minutes with a resultant positive TCR at room temperature. The data points at -296°C (approximately 4°K) were taken with the sample immersed in liquid helium using a different sample measuring system.

Numerous investigations of the current-voltage characteristics of thick film resistors fired in the normal way have always shown linear behaviour over many orders of magnitude. Typical results for a 5 w/o RuO_2 resistor are shown in Fig. 4.95 (resistor A). Linear behaviour was also invariably observed for resistors fired at lower temperature for times beyond the minimum in the curve (e.g. Fig. 4.92).

Current-voltage measurements were made on two resistors which had been fired for times corresponding to the rapidly decreasing portion of Fig. 4.92. Four terminal measurements were made, and the resistor area between the potential leads corresponded to one square. For the resistors prepared with firing times of 30 minutes and 60 minutes at 610°C the measurements were started at the lowest possible electric fields consistent with the measurement capabilities for current and voltage. The field was gradually increased and then returned to the initial low value to check for reproducibility. Having established the reproducibility of a certain range of electric fields, the field would then be increased to some new value, again reduced, and the reproducibility examined.
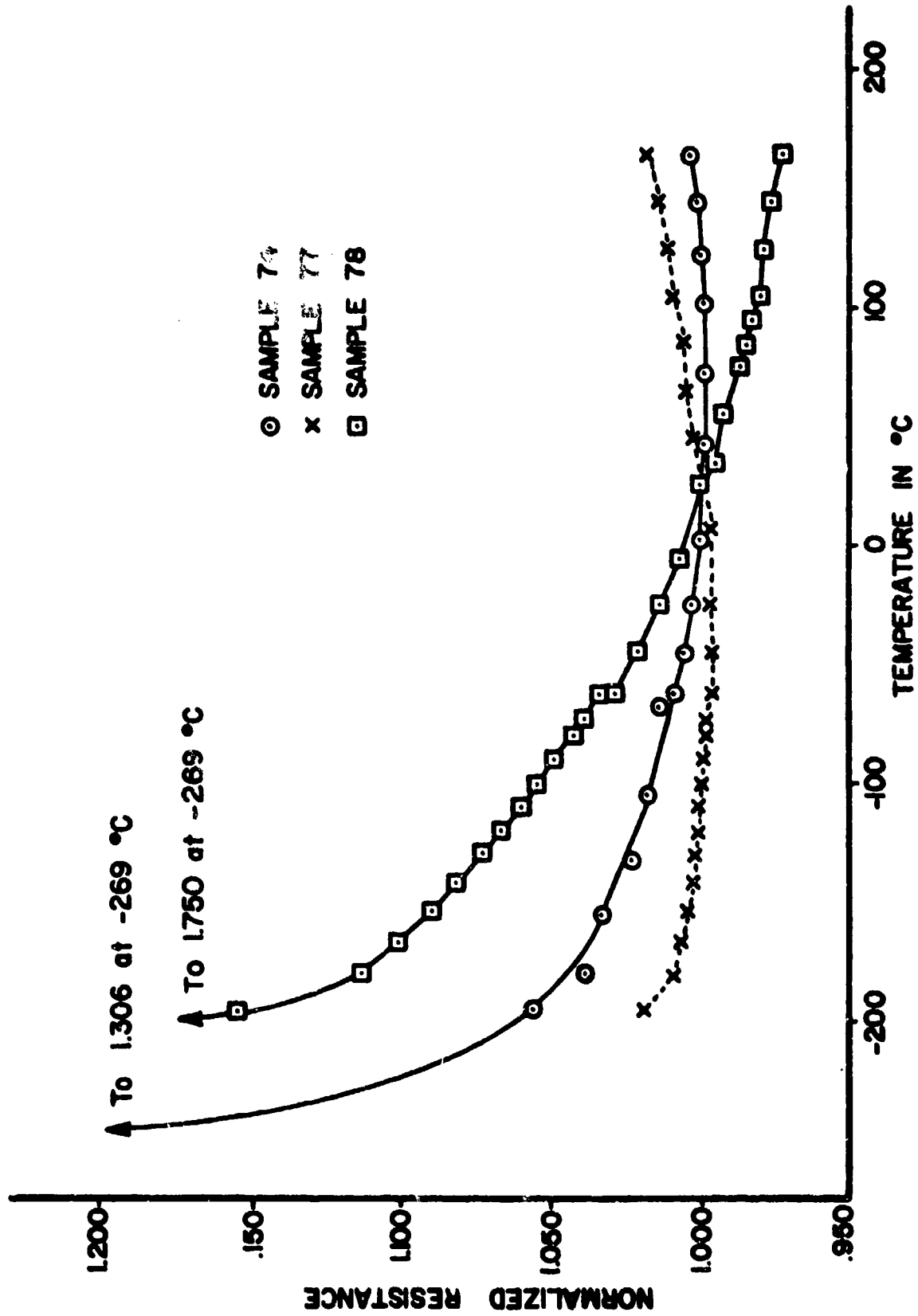
Figure 4.94 Normalized Resistance of Resistors Versus Low Temperature
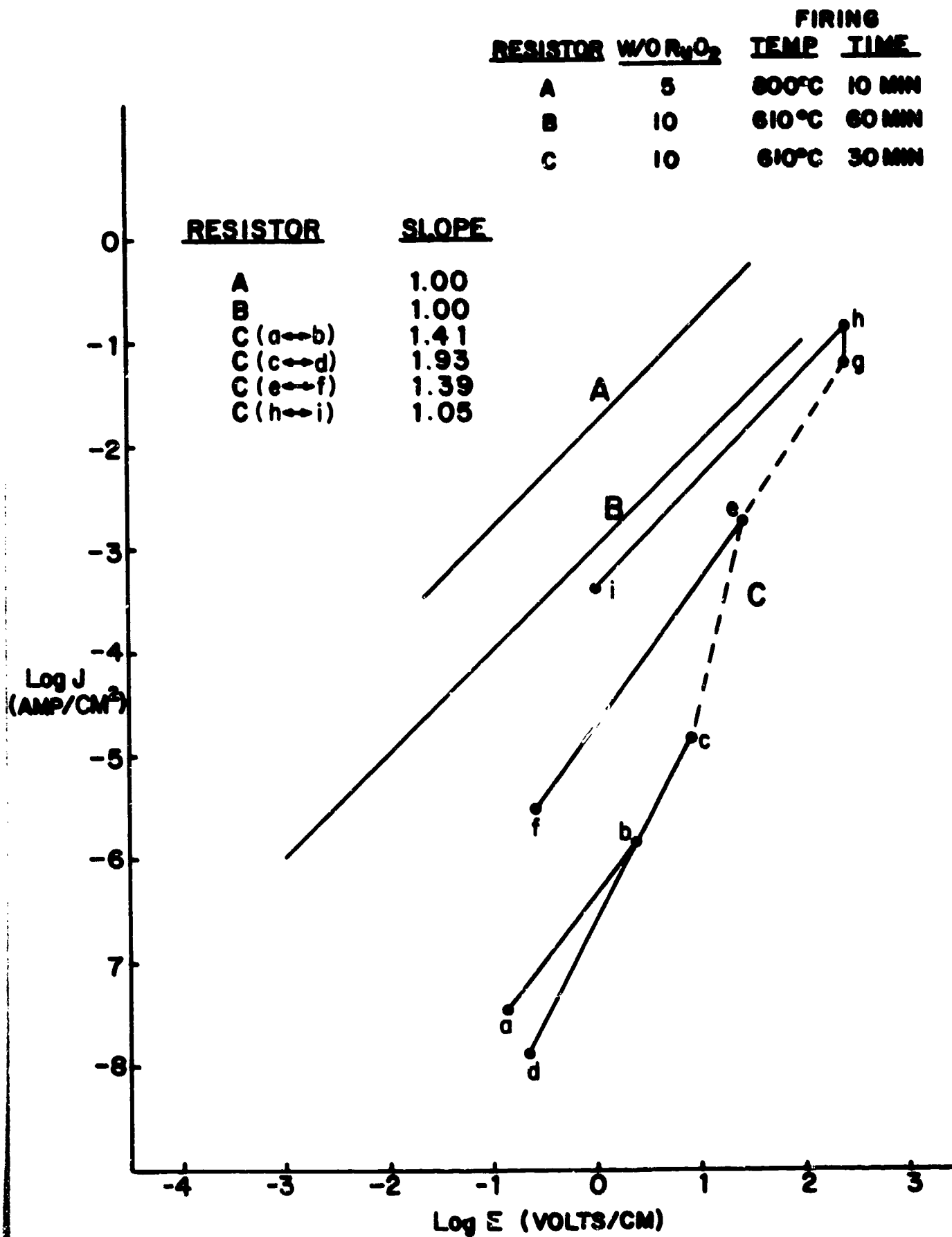
Figure 4.95   Current-voltage Characteristics of RuO$_2$ Resistors

For the resistor fired 60 minutes at 610°C the behaviour was completely reproducible over the entire range of fields studied, and the slope on the log current density, log electric field plot (resistor B in Fig. 4.95) was 1.00. The resistor fired 30 minutes at 610°C, however, showed considerably different behaviour. Four different, reproducible, segments were observed at increasing fields. Referring to the lines for resistor C in Fig. 4.95, the initial segment from a to b was reproducible and had a slope of 1.41 Upon increasing the field from point b to point c subsequent lowering of the field produced points along the segment cd which were reproducible over several cycles and had a slope of 1.93. Further increases of the field from point c to point e with subsequent reductions resulted in the reproducible segment ef with a slope 1.39. Upon increasing the field from point e to point g, the current density was observed to be time dependent. Maintaining the field at point g for 1 day the current density was observed to increase to point h and did not change after three additional days at this same field strength. Subsequent reductions in the field produced the reproducible segment hi having a slope of 1.05.

SECTION 5
Discussion of Results

5.1   Microstructure Development

5.1.1   Discussion of Processes

The blending curve (Fig. 4.83) showing sheet resistance as a function of volume fraction of RuO_2 to glass gives some insight into the type of microstructure which must be present in thick film resistors. This will be discussed more thoroughly in Section 5.2, but the inescapable conclusion is that a considerable degree of ordering of the RuO_2 particles into networks must occur. Evidence of this ordering on a macro scale can be observed in the sequence of optical photomicrographs shown in Fig. 4.34, and in the elapsed time pictures from the video hot-stage (Fig. 4.35). Some details of these macronetworks can be observed in Fig. 4.37, and it is clear from the scanning electron micrographs (Fig. 4.38) that ordering of

the RuO_2 occurs down to the ultimate particle size. A microstructure development model therefore, must explain the development of micronetworks between individual particles or particle agglomerates, the incorporation of these micronetworks into macronetworks, and the subsequent interconnection of the macronetworks into the final highly ordered microstructure. The model developed in this section describes the development of the micro-networks and the macronetworks in terms of six physical processes: glass sintering; glass spreading; microrearrangement; glass densification; conductive sintering; and conductive ripening. The physics and chemistry of these processes will be discussed in the following sections and the predicted kinetics for each combined to generate the microstructure development model.

5.1.2   Glass Sintering

The glass sintering studies (Sec. 4.1.2.5) showed that Newtonian viscous flow is the predominant mechanism for the sintering of the lead borosilicate glass particles, and the kinetics for the initial stages of sintering are described by Eq. 2.12 or 2.13. Figure 4.10 indicates that it takes about 26 minutes for the completion of initial stage sintering ($x/r = 0.3$) between 188 μm glass spheres at 486°C. In a typical RuO_2-glass formulation used for the fabrication of RuO_2-glass thick film resistors, the average size of the glass particles is about 1-10 μm. The time required for the completion of initial stage sintering between 5 μm particles at 486°C can be computed to be about 42 seconds. This indicates that most of the glass sintering during RuO_2-glass thick film resistor fabrication should be completed by the time the sample reaches about 500°C.

From the experimental results, Eq. 2.12 can be written as

$$(\frac{x}{r})^2 = 3.40 \times 10^{25} \ r^{-1} \ t \ exp \ (\frac{-5.61 \times 10^4}{T}) \qquad (5.1)$$

and the time and temperature required to achieve any degree of relative neck growth for any particle size can be computed.

5.1.3 Glass Spreading

In order for the microstructure development to proceed, the glass must spread and wet the RuO_2 particles. The results presented in Section 4.2.3 demonstrated that while the equilibrium contact angle between the lead borosilicate glass and RuO_2 is zero, finite angles might be expected during time-temperature relationships important in thick film technology. Theoretical equations to describe the kinetics of spreading have been developed from several different models. Yin [83] considered the kinetics of spreading of a spherical liquid droplet on a flat, rigid, solid surface, and assumed that spreading is impelled by the horizontal components of the surface tensions at the three phase boundary and retarded by the viscous flow of the droplet. This model of a liquid droplet on a flat surface is a poor approximation for a thick film resistor system, because the solid surface is presented by RuO_2 particles which are orders of magnitude smaller than the starting liquid droplet size (glass particles).

A model which more closely approximates the situation in thick film resistors is that proposed by Newman [84] by means of which he develops a formalism for the rate of penetration of liquids into microirregularities (capillaries and slits) in the solid surface. The driving force is that of capillary pressure as defined by Eq. 2.1. Applying Newman's model to our system, the process of interest is that depicted in Fig. 5.1 where two RuO_2 particles, having radii $\bar{r}$ (0) are separated by a distance $2R$ on the surface of a viscous liquid (glass). The glass penetrates between the two particles and rises to a distance L. Newman's formalism predicts that

$$\frac{dL}{dt} = \frac{R\gamma_{1v}\cos\theta}{4\eta L} \tag{5.2}$$

Integration of Eq. 2.5 gives

$$L^2 = \frac{R\gamma_{1v}\cos\theta}{2\eta} \; t \tag{5.3}$$

Newman suggests describing the time dependence of the contact angle by a function of the type

$$\cos\theta = (\cos\theta_\infty)(1 - ae^{-ct}) \tag{5.4}$$
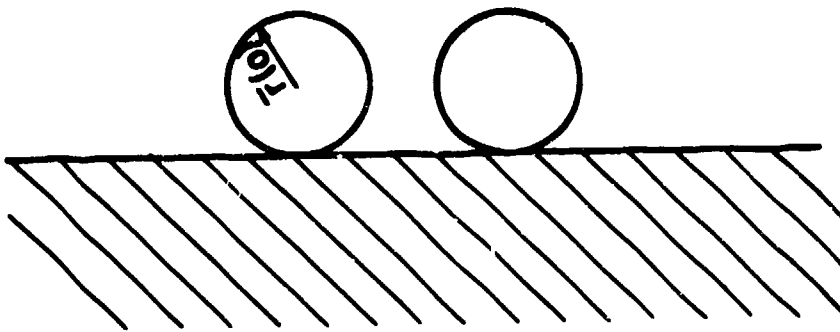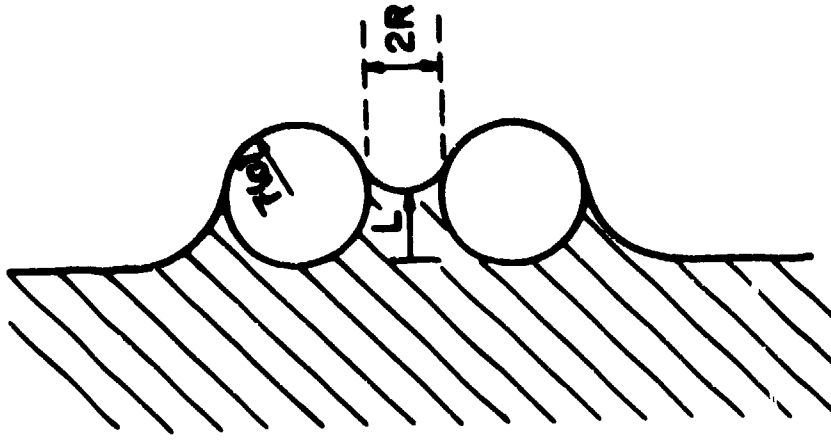
Figure 5.1 Glass Spreading Model

Where Θ_∞ is the equilibrium contact angle and a and c are empirical constants. This relation has the correct boundary conditions and has been shown [84] to adequately describe the rate of wetting of polyethelyene vinyl acetate on aluminum at temperatures where the magnitude of the viscosity of the polymer melt was comparable to the lead borosilicate glass in the early stage of resistor formation. Substituting Eq. 5.4 into Eq. 5.2 gives

$$\frac{dL}{dt} = \frac{R\gamma_{1v}(\text{Cos } \Theta_\infty)(1-ae^{-ct})}{4\eta L} \tag{5.5}$$

Integrating Eq. 5.5 under the boundary condition $L = 0$ at $t = 0$ gives

$$L^2 = \frac{R\gamma_{1v}\text{Cos}\Theta_\infty}{2\eta}\left[(t - \frac{a}{c}) + \frac{ae}{c}^{-ct}\right] \tag{5.6}$$

If we assume that $L = \bar{r}(0)$ (i.e. the case where the thickness of the glass bridge between particles is equal to the particle radius), and also assume that $R = \alpha \bar{r}(0)$ where α is some constant, then Eqs. 5.3 and 5.6 reduce to

$$\frac{2\bar{r}(0)}{\alpha\text{Cos}\Theta} = (\frac{\gamma_{1v}}{\eta}) t \tag{5.7}$$

and

$$\frac{2\bar{r}(0)}{\alpha\text{Cos}\Theta_\infty} = (\frac{\gamma_{1v}}{\eta})\left[(t - \frac{a}{c}) + \frac{ae}{c}^{-ct}\right] \tag{5.8}$$

The surface tension and viscosity of the glass have each been directly measured as a function of temperature (Sections 4.1.2.3 and 4.1.2.4), or, alternatively, the temperature dependence of the surface tension to viscosity ratio can be calculated from the time dependence of the initial stage sintering of the glass at different temperatures (Section 4.1.2.5). Since the temperature range of interest for glass spreading is comparable to that employed in the sintering studies but appreciably below the temperatures were surface tension and viscosity measurements were carried out, it is preferable to use the sintering results for the reasons discussed in Section 4.1.2.5. Knowing γ_{1v}/η as a function of temperature, Eq. 5.7 can be solved for the time required at any temperature for the penetration to reach a distance equal to a particle radius. Carrying out

this calculation with $\bar{r}$ (0) = 30 Å (see Section 4.1.4.1), α = 1, and Θ = 0, the curve labeled Θ = 0 in Fig. 5.2 was obtained. This curve represents a lower limit of spreading time for any temperature, because, in general, the equilibrium contact angle will not be realized.

In order to plot a similar curve for Eq. 5.8 numerical values of a and c must be obtained. Since the driving force for spreading is capillary action the contact angle must be less than 90° for spreading to occur. This gives the boundary condition that Θ = 90° at t = 0, and imposing this condition on Eq. 5.4 requires that a = 1. The contact angle of the lead borosilicate glass on RuO_2 compacts after 3 minutes at 800°C is approximately 30° (see Fig. 4.41), which requires that c = 1.1x 10^{-2} $(sec)^{-1}$. From data on the rate of wetting of polyethelyene vinyl acetate on aluminum [84] it was found that c varied from 2.7 x 10^{-3} to 16.4 x 10^{-3} $(sec)^{-1}$ over the temperature range of the experiments (135° - 190°C). The temperature dependence of c arises through its relation to viscosity, but this dependence cannot be explicitly defined because c is an empirical constant. Choosing c = 10^{-3} $(sec)^{-1}$ as an order of magnitude approximation for our temperature range of interest, and taking a = 1, Eq. 5.8 was solved for time and temperature, and the results of this calculation are also shown on Fig. 5.2. These two lines should represent reasonable upper and lower bounds for the spreading rate in the system of interest.

5.1.4   Microrearrangement

The force acting between two particles separated by a liquid bridge (see Fig. 2.2) was described in Section 2.1.1. This force as a function of particle separation (2R) has been shown [17] to be rather insensitive to contact angle (Θ) for values of θ between 0° and 25°, but changes drastically as Θ approaches 90°. For example, at Θ = 85° the force is negative, i.e. repulsive, at small separation, passes through zero as the interparticle distance increases and becomes attractive for large distances. For contact angles below 25° and ratios of glass volume to particle volume (V/V_o) greater than 0.05, the force given by Eq. 2.8 is almost a linear function of R [17]. For V/V_o = 0.1, Eq. 2.6 can be approximated by

$$F = 54 - 8000R \qquad (5.9)$$
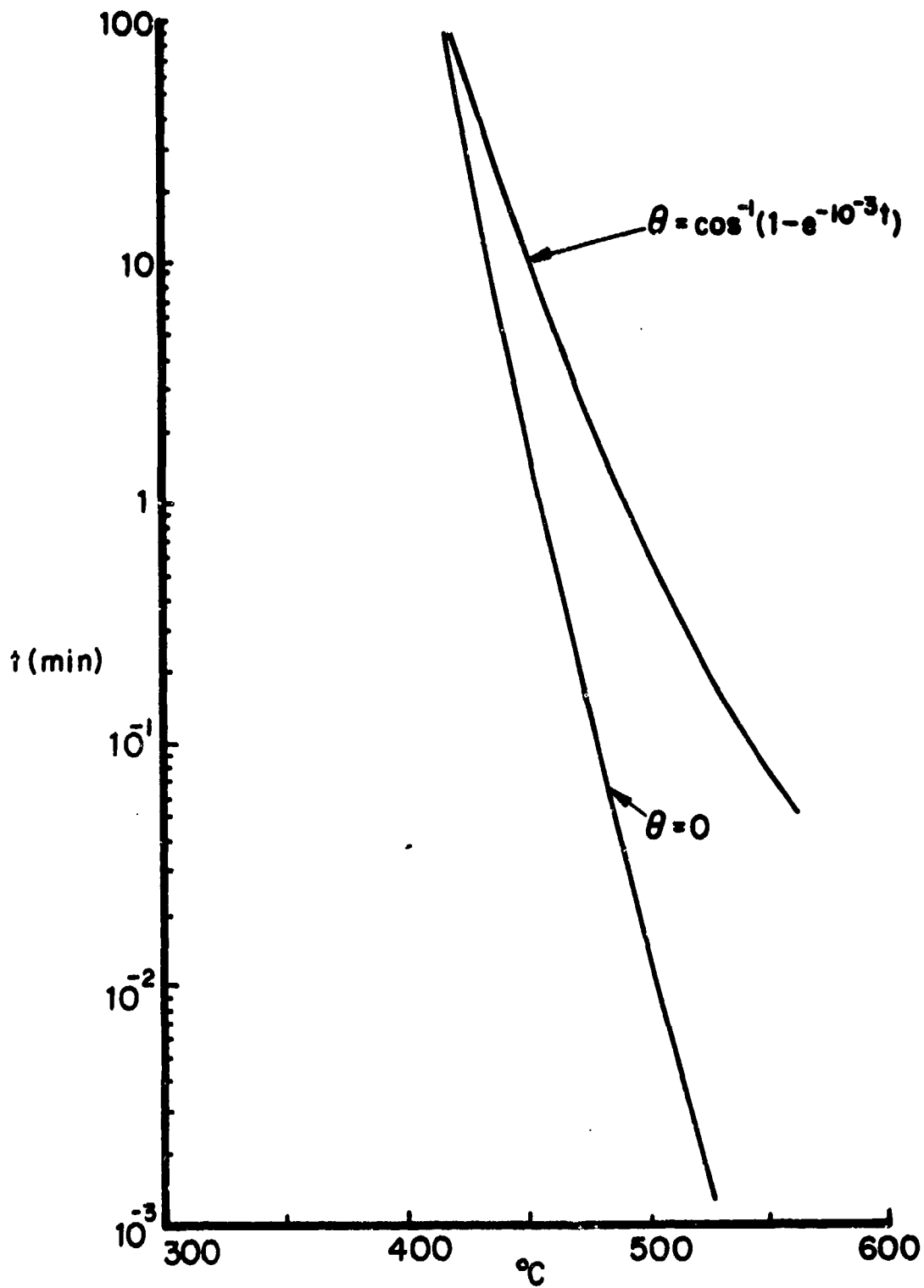
Figure 5.2   Glass Spreading Kinetics

where F is the force in dynes and R is half the particle separation in centimeters. Stoke's law relates the force on a particle of radius r in a liquid to its velocity v:

$$F = 6 \pi r \eta v \qquad (5.10)$$

Considering the velocity to be the rate of approach of two particles connected by a liquid bridge [i.e. $v = d (2R)/dt$], taking $2R = \bar{r}(0) = 30 \overset{o}{A}$ and combining Eqs. 5.9 and 5.10 gives

$$\frac{d (2R)}{dt} \approx \frac{9.55 \times 10^6}{\eta} \qquad (5.11)$$

It is more appropriate to use the viscosity calculated from sintering measurements rather than the viscosity obtained from extrapolation of the direct measurements at higher temperatures for the reasons discussed in Section 4.1.2.3. Using this value of the viscosity, Eq. 5.11 reduces to

$$\frac{d (2R)}{dt} = 2.1 \times 10^{33} \exp(-63,000/T) \qquad (5.12)$$

A plot of Eq. 5.12 is shown in Fig. 5.3. Equation 5.12 can also be integrated to give the time required for the particles to approach each other to any distance for a given temperature.

5.1.5   Glass Densification

The movement of the macronetworks as seen in Figs. 4.34 and 4.35 must be the result of forces acting on the resistor after the glass has completely flowed and the microrearrangement process as described in the preceeding section has been completed. One possible driving force for this process is the negative pressure existing inside of the closed pores as described by Eq. 2.9. This negative pressure inside of the pores leads to an effective hydrostatic compressive force on the outside of the system and the densification rate due to this process can be described by [85]

$$\frac{d\phi}{dt} = \frac{3\gamma_{1v}}{2r_o \eta} \; (1-\phi) \qquad 5.13)$$
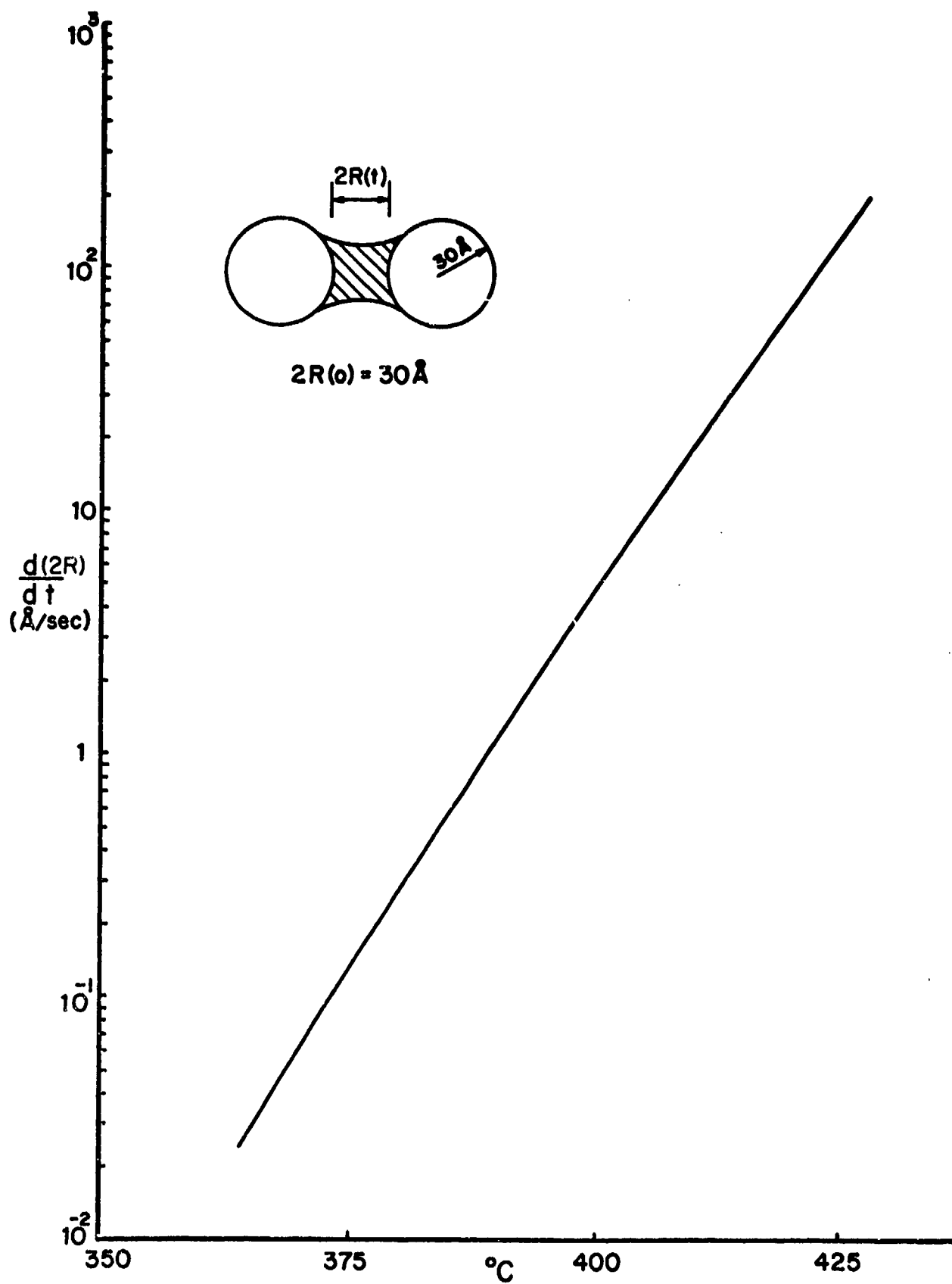
Figure 5.3   Microrearrangement Kinetics

where ϕ is the relative density (the density at time t divided by the theoretical density) and r_o is the initial pore size of the glass. Integration of Eq. 5.13 gives

$$\ln(1-\phi) = \frac{3\gamma_{1v}}{2r_o\eta} \ t \tag{5.14}$$

For $\phi = 0.99$ (99% density achieved) Eq. 5.14 can be rearranged to give

$$t = 3 \ r_o \ (\frac{\eta}{\gamma_{1v}}) \tag{5.15}$$

Taking $r_o = 1 \ \mu m$ which is consistent with the smallest particle size of glass used, and knowing the surface tension to viscosity ratio as a function of temperature, the time to reach 99% density by this process can be calculated as a function of temperature from Eq. 5.15. The result of this calculation is labled "pore collapse" on Fig. 5.4.

From observations on the hot stage microscope it is known that all trapped pores do not collapse, as evidenced by the escaping bubbles seen in Fig. 4.32. In fact, the resistor was observed to be in a dynamic state of agitation due to escape of gas bubbles throughout a considerable portion of the firing cycle. The origin of the bubbles is not known; they could be due to the escape of residual screening agents, oxidation of RuO_2 to gaseous RuO_3 and RuO_4, partial decomposition of the glass, or some other unknown effect, but the most probable source is air entrapment in the glass when the pores initially closed. The surface tension values at temperatures above 700°C are quite low (see Fig. 4.6), and this might be a significant factor during the glass densification because the driving forces for the pore elimination are the capillary forces of surface tension. The pore elimination takes place only if the capillary pressure is more than the gas pressure inside the closed pore. Equation 2.9 describes the pressure in a pore only for the case where there is vacuum (no gas) in the pore, or for the case where the closed pore is filled with a gas that is soluble in the liquid (glass). If this is not the situation, Eq. 2.9 must be modified to give

$$\Delta P = P_c \ [\frac{(r_p)_c}{r_p}]^3 \ (T - T_c) - \frac{2\gamma_{1v}}{r_p} \tag{5.16}$$
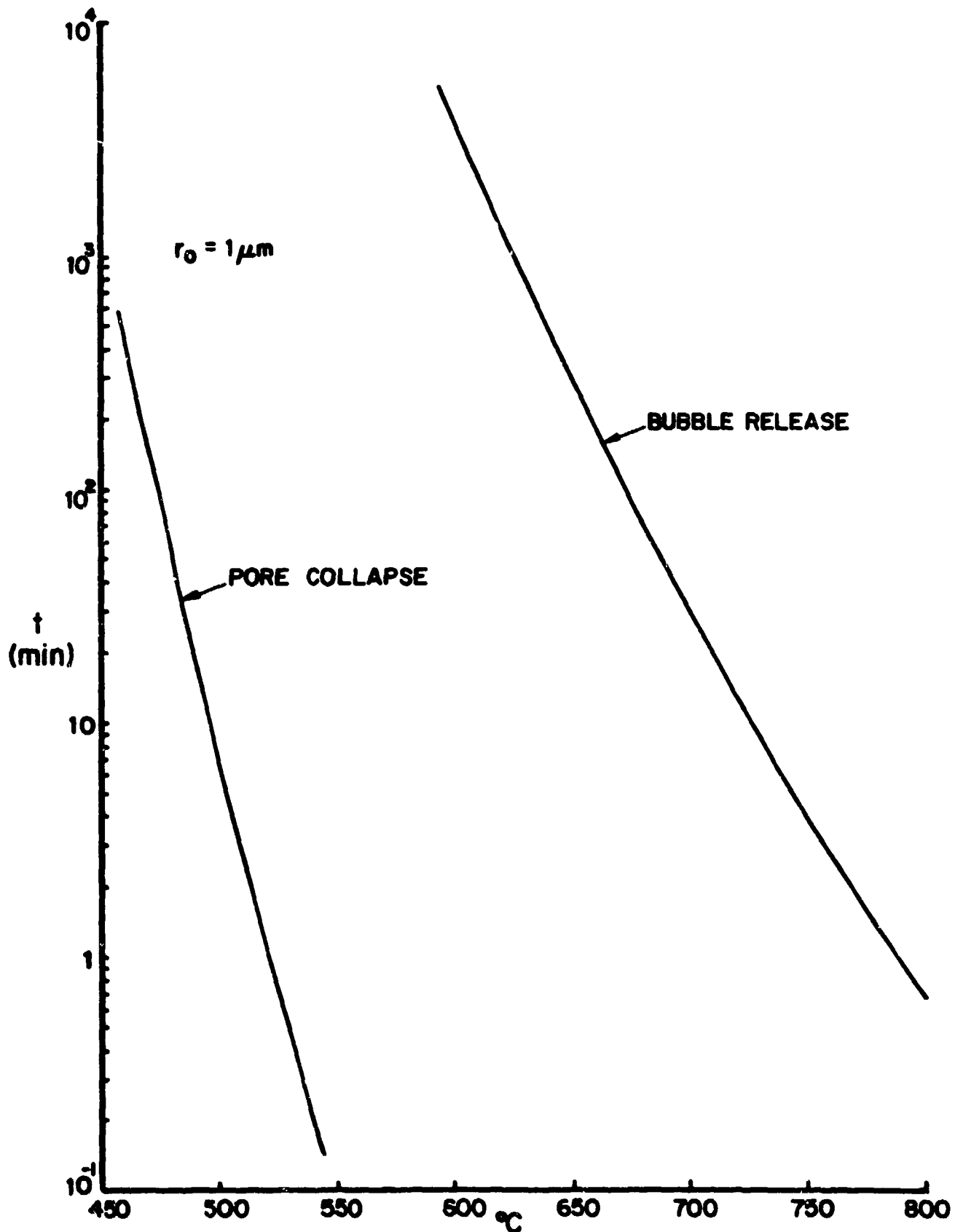
Figure 5.4   Glass Densification Kinetics

where T_c is the temperature of pore closure, $(r_p)_c$ is the pore radius at T_c, and P_c is the ambient pressure at T_c. Once pore closure has occured, a force will be exerted on the bubble due to its buoyancy given by

$$F = V_p \ (\rho_g - \rho_p) \ g \qquad (5.17)$$

where $V_p = 4\pi r_p^3/3$ is the volume of the pore, ρ_g is the density of the glass, ρ_p is the density of the gas in the pore, and g is the gravitational constant. Applying the appropriate values for the case of interest reduces Eq. 5.17 to

$$F = 1.91 \times 10^4 \ r_p^{\ 3} \qquad (5.18)$$

Applying Stoke's law (Eq. 5.10) gives

$$v = 1.02 \times 10^3 \ \frac{r_p^2}{\eta} \qquad (5.19)$$

where v is the velocity of the gas bubble. Equation 5.19 then can be integrated to give the time required for a gas bubble to move any required distance as a function of r_p and η. For example, the time τ, for a bubble to move 1 μm is

$$\tau = \frac{10^{-7}\eta}{r_p} \qquad (5.20)$$

Values for r_p at any temperature can be calculated from Eq. 5.16 if it is assumed that at equilibrium the pressure in the pore is equal to the ambient pressure (i.e. $\Delta P = 0$). Carrying out this calculation with γ_{1v} = 160 dynes/cm, T_c = 500°C, T = 800°C and $(r_p)_c$ = 1 μm, gives r_p = 10 μm. Since the bubble escape occurs at temperatures above the softening point of the glass, the directly measured viscosity as a function of temperature is the most appropriate value to use (see Section 4.1.2.3). Using these values of η and taking r_p = 10 μm, the time-temperature relationship labelled "bubble release" in Fig. 5.4 was calculated using Eq. 20. Bubbles smaller than 10 μm will require an even longer time to move 1 μm at any temperature.

5.1.6   Conductive Sintering and Ripening

Different mechanisms by which sintering and growth of RuO_2 in the

presence of the glass can take place, fall into the following four categories;
(1) viscous or plastic flow; (2) solid state diffusion; (3) evaporation-
condensation; and (4) solution-precipitation. As discussed in Section 2.1.2
contributions to sintering can come from mechanisms in the first three
categories only if the following two requirements are satisfied: (1) the
particles have to come into contact with each other without any liquid
film separating them; and (2) there should be no closed pores inside the
liquid phase.

In the RuO_2-lead borosilicate glass system, the glass completely wets
RuO_2 and penetrates between the particles if the equilibrium contact angle
is approached. This will lead to the presence of a thin layer of glass
separating the particles which probably remains even after they are pulled
together due to capillary forces acting on them. Under these circumstances,
sintering cannot take place by any of the mechanisms in the first three
categories and the most probable mechanism is, therefore, a solution-
precipitaticn process involving solution of particles at areas under com-
pression, transport through the liquid phase, and deposition at the free
surfaces. Supporting evidence for this conclusion comes from the fact that
growth of RuO_2 particles is drastically affected by the presence of the
substrate. Any change in the properties of the liquid phase (to be described
later) can only influence sintering which is dependent on a solution-
precipitation process and not any of the processes in the other three
categories.

In the light of the above considerations it was concluded that
sintering and growth of RuO_2 particles in the lead borosilicate glass occurs
by a solution-precipitation process, and the next step was to establish
whether the rate controlling step for the solution-precipitation process
was diffusion or the phase boundary reaction. The direct method to determine
the rate controlling mechanism is by analyzing the data according to
either Eq. 2.38 or 2.39. If diffusion of the slowest moving species through
the liquid phase is the rate controlling step, then the plot of $\bar{r}(t)^3$ -
$\bar{r}(0)^3$ versus t should be a straight line, whereas, if the phase boundary
reaction leading to dissolution or redeposition is the slower process, then
there is a linear dependence of $\bar{r}(t)^2$ - $\bar{r}(0)^2$ upon t.

In order to check for these two possibilities, a least squares analysis was carried out on the average particle size data obtained from x-ray and surface area measurements (Fig. 4.61). As discussed in Section 4.2.5 there was a discrepancy between x-ray and surface area results at the advanced stages of particle growth due to the presence of a wide distribution of particle sizes; these data were not used in the analysis. The results of the analysis showed the standard deviation for the straight line fit of $\bar{r}(t)^2 - \bar{r}(0)^2$ versus t was smaller by a factor of two or more than that obtained for the fit of $\bar{r}(t)^3 - \bar{r}(0)^3$ versus t using data obtained from either of the measurement techniques at all five different temperatures. Figure 5.5 shows the linear fit obtained for the plots of $\bar{r}(t)^2 - \bar{r}(0)^2$ versus t; all of the lines do not pass through the origin because the abscissa is an arbitrary time scale. This result suggests that the phase boundary reaction was the rate controlling mechanism for the growth of RuO_2 particles in the lead borosilicate glass by a solution-precipitation process.

Phase boundary reaction rate constants (K_T) were determined by substituting the slopes of the plots from Fig. 5.5 in Eq. 2.39. The measured values of solubility (Fig. 4.39) were used, and the value of γ_{sl} was assumed to be 1.5×10^3 ergs/cm^2 for these calculations based on the results reported for similar systems undergoing liquid phase sintering [31]. The K_T values are shown on an Arrhenius plot in Fig. 5.6. As can be seen there is good agreement between the values of K_T obtained from surface area and x-ray results. The activation energy for the growth process was computed from the slope of the plot in Fig. 5.6 to be 100 ± 3 kcal/mol.

The conclusion that the phase boundary reaction was the rate limiting step for the solution-precipitation process was strengthened by comparing the predicted growth behaviour of the particles by a diffusion controlled solution-precipitation process with the observed growth behaviour. The diffusion coefficients plotted in Fig. 5.7 were calculated from the high temperature viscosity data (Fig. 4.4) using the Stokes-Einstein equation (Eq. 2.40). These diffusion coefficients were substituted in Eq. 2.38 to obtain the time required for the average particle size to attain a particular value at the five temperatures where ripening experiments were performed. These values were then compared with the observed times, and
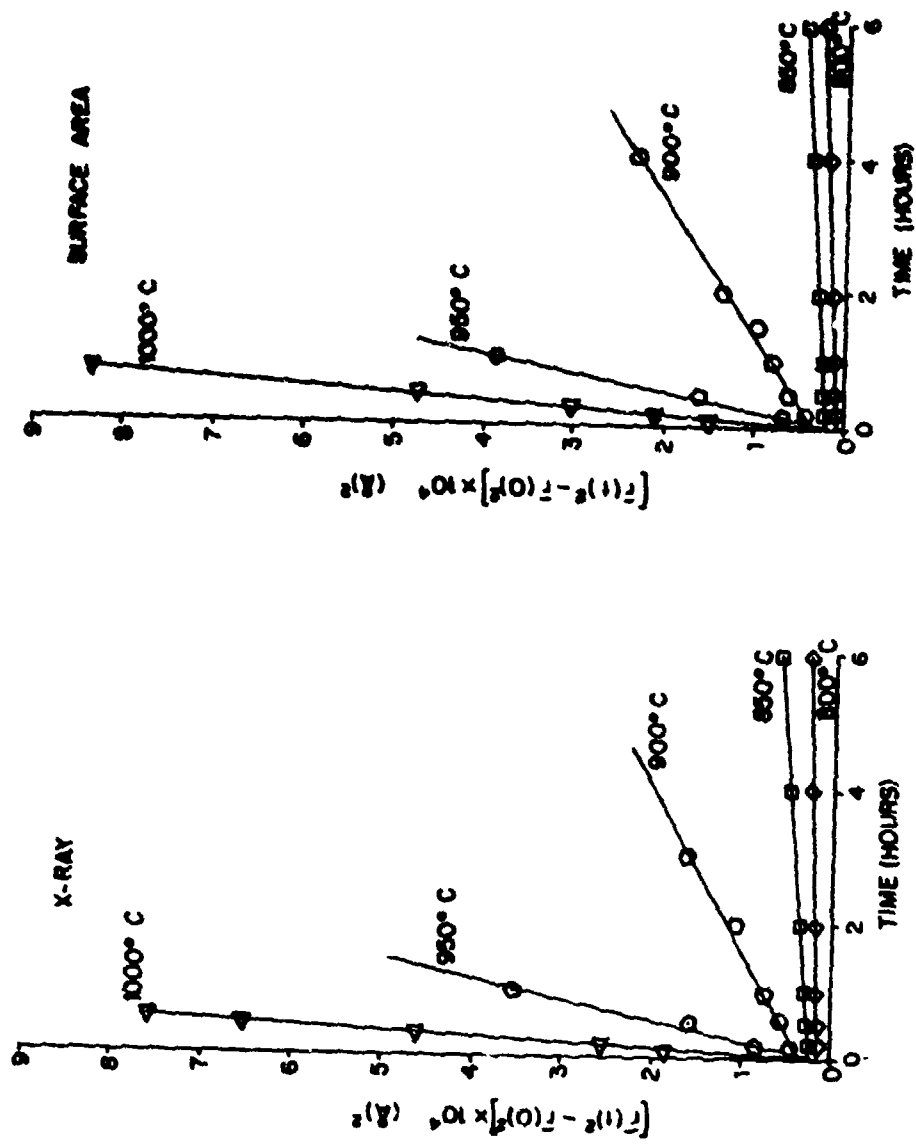
Figure 5.5 Fit to Equation For Phase Boundary Reaction Controlled
Solution-Precipitation Process
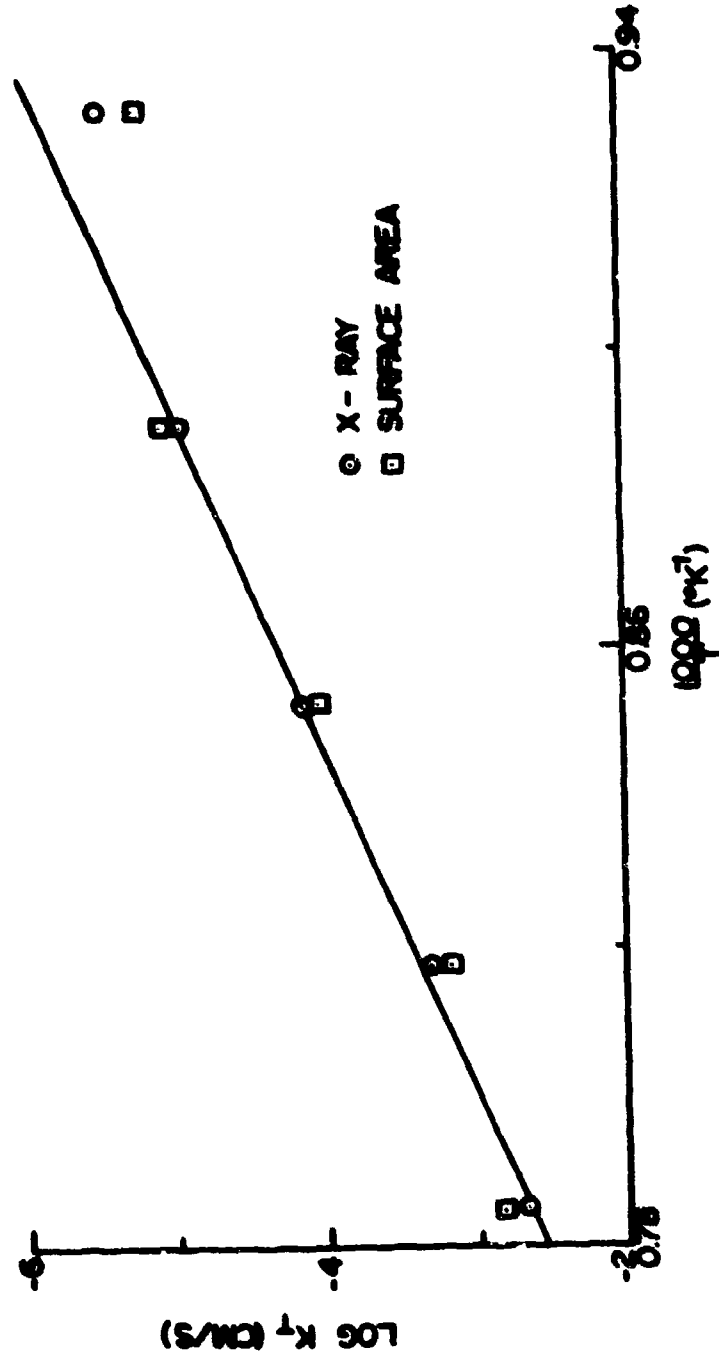
Figure 5.6 Temperature Dependence of Phase Boundary Reaction Rate Constant
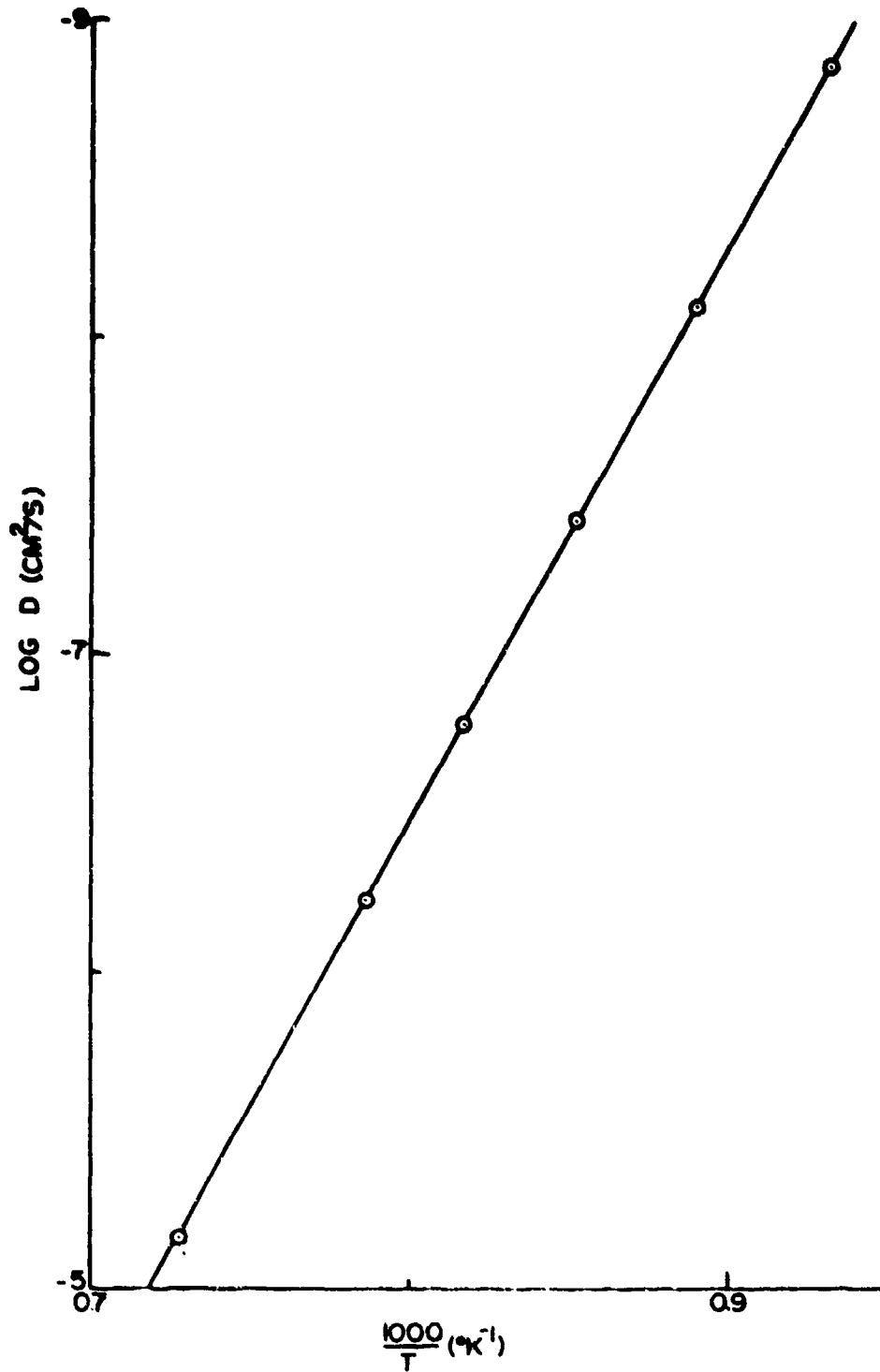
Figure 5.7   Temperature Dependence of Diffusion Coefficient
              Calculated From High Temperature Viscosity Data

the results are shown in Table 5.1. As can be seen, the calculated values are about 100-400 times greater than those observed experimentally suggesting that the diffusional process is much faster than the observed growth behaviour and hence cannot be rate controlling.

Additional support for the conclusion that diffusion cannot be rate controlling comes from the fact that the observed growth behaviour is independent of the amount of the liquid phase. If the predominant mechanism operating is diffusion controlled solution-precipitation, the parameters such as average x-ray crystallite size and surface area should be dependent on the proportion of the glass and RuO_2 in the composite. As the amount of glass increases, the rate of growth of particles should decrease due to an increase in the diffusion length of the dissolved species. The results obtained are contrary to this. For all the different compositions studied (6, 18 and 30 w/o RuO_2), the growth kinetics were the same indicating that the growth of RuO_2 was independent of the amount of glass thus reducing the probability of a diffusional process being rate controlling.

The conclusion drawn from the studies of the influence of the substrate on ripening kinetics (Section 4.2.7) was that the effect was a result of a reduction in the solubility of RuO_2 in the glass. Any reduction in the solubility of RuO_2 in the glass further reduces the rate limiting phase boundary reaction controlled solution-precipitation process and hence the rate of growth of RuO_2 particles. A reduction in solubility of RuO_2 would not be expected to have as great an effect on a diffusion controlled process.

After having established that the growth of RuO_2 particles in the glass occurred by a phase boundary reaction controlled solution-precipitation process, the times required for the completion of initial stage sintering between RuO_2 particles ($\frac{x}{r}$ = 0.3) were computed by substituting the values for the phase boundary reaction rate constant K_T in Eq. 2.21. The constants K_1 and K_2 were assumed to be 1 and 0.5 respectively. The results of these calculations are given in Table 5.2, and the following observations can be made:

1. At 800°C, it takes only about 44 seconds and 174 seconds for the completion of initial stage sintering between 60 and 120 Å particles respectively. Since the average particle size of RuO_2 particles in the resistor formulations lies within this range, it can be concluded that the initial stage sintering of the conductive particles is completed during

Table 5.1 Comparison Between Observed Time and Time Predicted by
Diffusional Process for the Growth of RuO_2 Particles.

Temperature °C	Observed Time / Predicted Time	
	$\bar{r}(t) = 100 \text{ Å}$ $\bar{r}(0) = 30 \text{ Å}$	$\bar{r}(t) = 60 \text{ Å}$ $\bar{r}(0) = 30 \text{ Å}$
1000	193	220
950	240	370
900	345	190
850	379	146
800	—	260

Table 5.2   Predicted Initial Stage Sintering Kinetics

Temperature °C	Time to Reach $\frac{x}{r} = 0.3$			
	$\bar{r}(0) = 30 \overset{\circ}{A}$	$\bar{r}(0) = 60 \overset{\circ}{A}$	$\bar{r}(0) = 1000 \overset{\circ}{A}$	$\bar{r}(0) = 100 \mu m$
800	43.5 seconds	174 seconds	13.45 hours	1.345×10^7 hours
750	26.9 minutes	1.794 hours	- - -	- - -
720	1.908 hours	7.633 hours	- - -	- - -
700	5.3486 hours	21.394 hours	- - -	- - -
680	14.27 hours	57.10 hours	- - -	- - -
650	67.47 hours	269.9 hours	- - -	- - -
600	1118.8 hours	- - -	- - -	- - -

routine firing of RuO_2-lead borosilicate glass thick film resistors for all particles that are adjacent (separated by only a thin glass film) to other particles when the temperature reaches 800°C.

2. The time required for the completion of initial stage sintering at 700°C is more than 400 times greater than the time required at 800°C suggesting a strong temperature sensitivity of the process.

3. As the particle size increases, the rate of growth of the neck radius relative to the particle radius decreases requiring about 1.345×10^7 hours for the completion of initial stage sintering between 200 μm particles. This explains why no sintering was observed during the neck growth study of the particles in this size range using the hot stage microscope.

By utilizing the measured values of solubility (Fig. 4.39), surface tension (Fig. 4.6), and phase boundary reaction rate constant (Fig. 5.6), along with the calculated molar volume and the assumed values of $K_1 = 1$ and $K_2 = 0.5$, the quantity

$$[\frac{8K_1 C_0 \gamma_{1v} V_0 K_T}{K_2 RT}]$$

which appears in Eq. 2.21 was determined as a function of temperature. By this procedure Eq. 2.21 was reduced to

$$x = 31.6T^{-\frac{1}{4}} r^{\frac{1}{2}} t^{\frac{1}{4}} \exp(-1.25 \times 10^4/T) \tag{5.2.}$$

Any one of the four variables (x, r, t, T) in Eq. 5.21 can be determined as a function of one of the others with the remaining two held constant. For example, Fig. 5.8 shows the neck radius that will be formed for any given particle radius when the system is held at 800°C for ten minutes. Equation 5.21 can also be solved explicitly for t as a function of temperature, and the time required to grow a given size neck for a given particle size at any temperature can be calculated.

In addition to providing a vehicle for determining sintering kinetics in thick film resistor systems, the ripening process can also be important in that as it proceeds, with large particles growing at the expense of smaller particles, parts of the conductive network will eventually be destroyed. The important parameter in this regard is the ratio of the number of particles at time t to the number of particles initially present $\frac{N(t)}{N(0)}$. Since the solubility of RuO_2 in the glass is so low, (sec. 4.2.2)
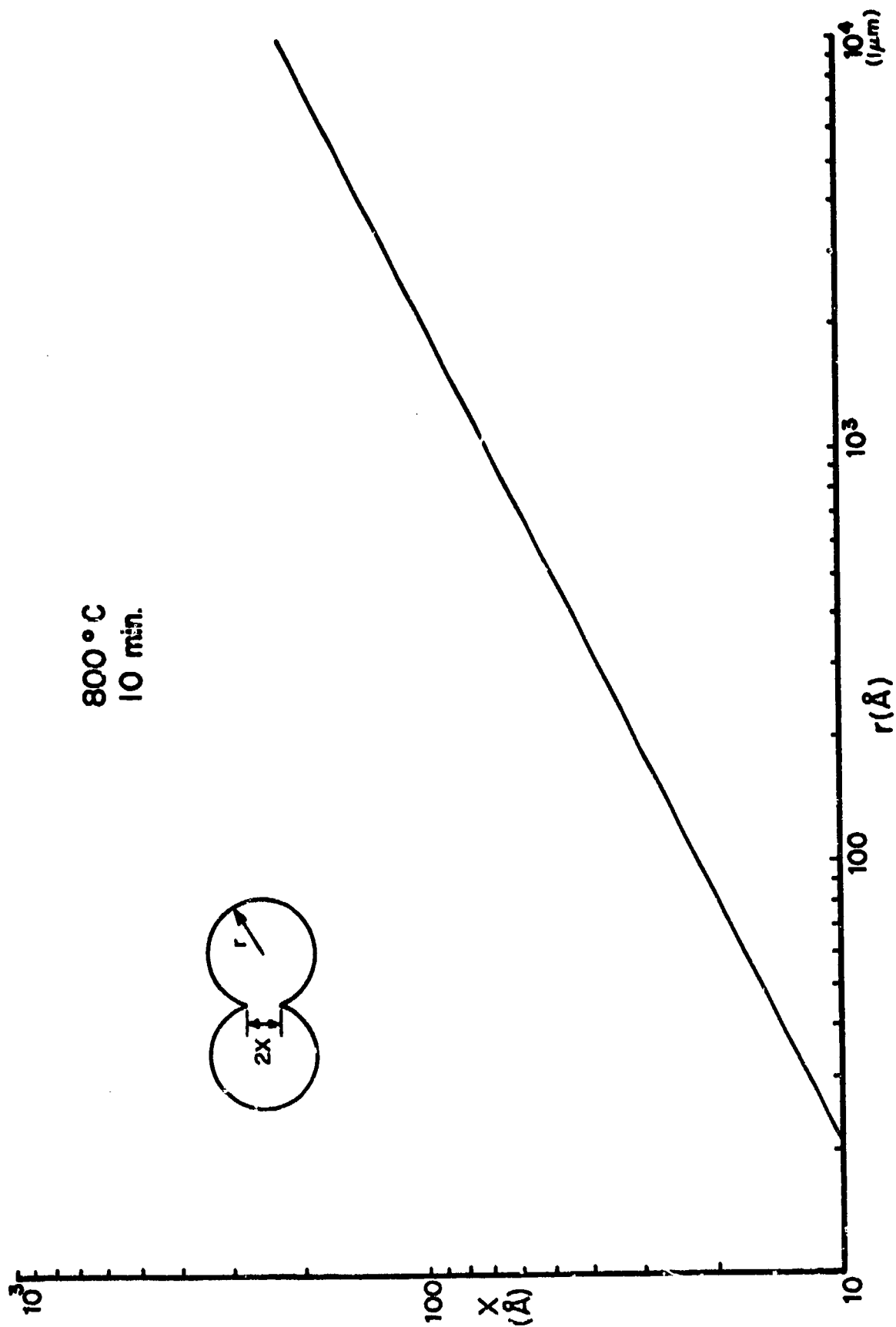
Figure 5.8   Neck Growth of RuO_2 at Constant Time and Temperature

it can be assumed that the total volume of RuO_2 remains constant as a function of time. This assumption leads to the equation

$$N(t) \ [4\pi\bar{r}(t)^3/3] = N(o) \ [4\pi\bar{r}(o)^3/3]\qquad(5.22)$$

which can be reduced to

$$\frac{N(t)}{N(o)} = \frac{\bar{r}(0)^3}{\bar{r}(t)^3}\qquad(5.23)$$

Solving Eq. 2.39 for $\bar{r}(t)$ and substituting the result in Eq. 5.23 gives

$$\frac{N(t)}{N(0)} = \left[\frac{\bar{r}(0)^2}{(\frac{8}{9})^2\dfrac{C_o\gamma_{sl}V_o^2 K_T}{RT}\ t + \bar{r}(0)^2}\right]^{3/2}\qquad(5.24)$$

Equation 5.24 was solved using $\bar{r}(0) = 30$ Å, and Fig. 5.9 shows $N(t)/N(0)$ as a function of temperature for three isochrones. The influence of the ripening process on the conductive networks would not be noticeable until more than half of the initial particles had disappeared, which would correspond to 0.5 of the ordinate of Fig. 5.9.

5.1.7   Model

Experimental results from this project have shown that microstructure development in RuO_2-lead borosilicate glass thick film resistors involves the formation of micronetworks of conductive particles, the coalescence of these micronetworks into macronetworks, the formation of continuous chains of macronetworks throughout the resistor, and finally changes in the macronetworks due to ripening. The micronetworks and macronetworks of conductive in the glass are not a feature unique to the RuO_2-lead borosilicate glass system considered in this study; similar microstructures have been observed [86] for DuPont Birox 1200 Series and Cermalloy 500 Series resistors.
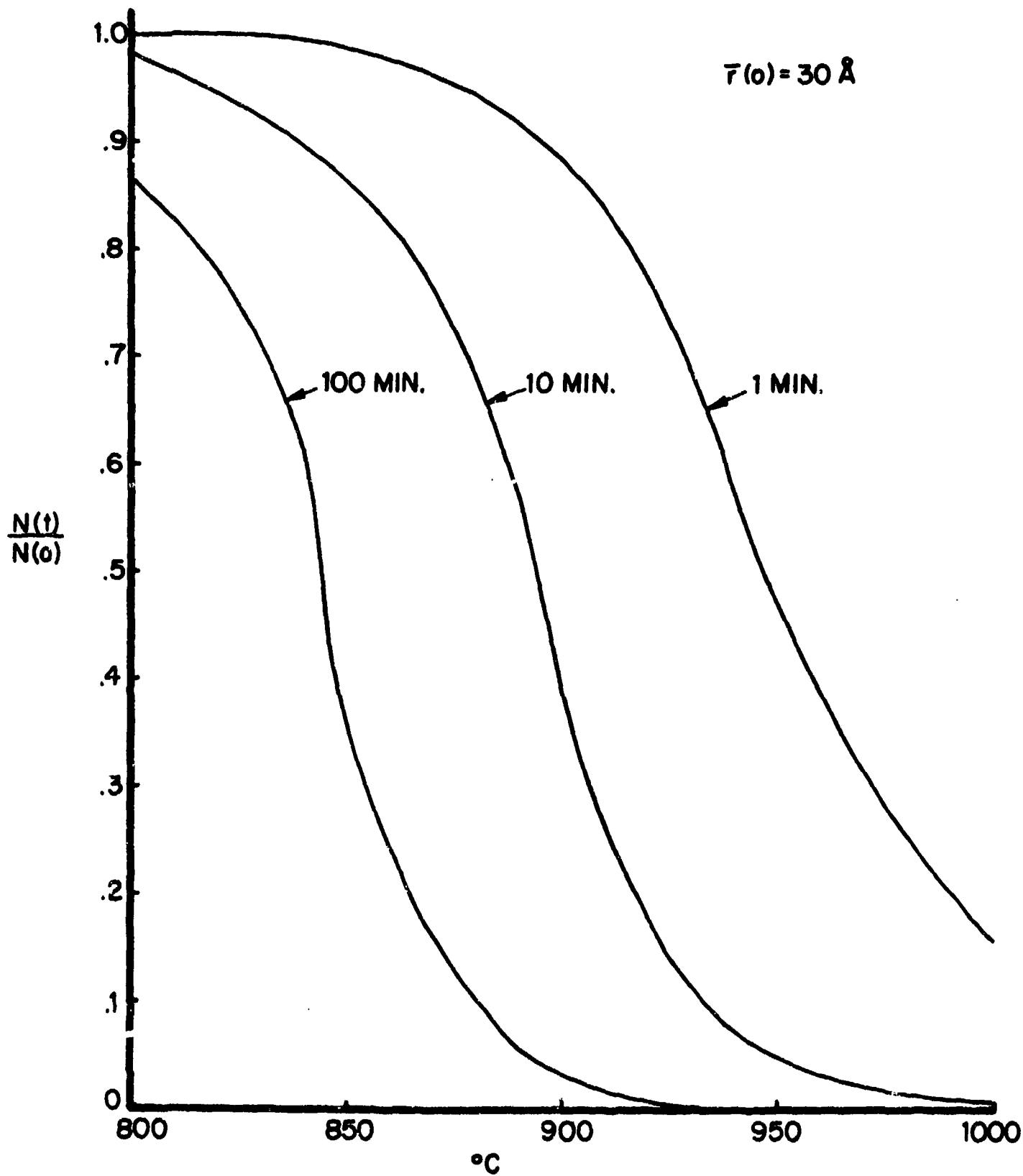
Figure 5.9   Ripening of RuO_2 in Glass

Some studies were performed during the current research program with
DuPont Birox 1200 Series resistors in order to look for differences and
similarities. Observations with the hot stage metallograph during firing
showed behaviour generally similar to the RuO_2-lead borosilicate glass
system, with the most notable difference being the higher viscosity of the
Birox glass at any temperature. The higher viscosity caused the region of
rapid bubble release to move to considerably higher temperatures, but the
motion of the macronetworks was found to be similar. The macronetworks can
be observed in the optical photomicrograph of Fig. 5.10 and are seen to be
similar to those observed with the RuO_2 system. The micronetworks of
bismuth ruthenate particles, shown in Fig. 5.11, are also similar to the
micronetworks of RuO_2. The quality of the SEM photomicrograph (Fig. 5.11)
is not as good as those obtained for the RuO_2 system because no effort was
made to develop the optimum etching technique for the Birox resistors;
however, the sintered chains of conductive showing some loop structures
can be observed.

The kinetics of microstructure development can be described in terms
of six physical processes: sintering of the glass; spreading of the glass;
rearrangement of the conductive particles in the presence of glass;
densification of the glass; sintering of the conductive particles in the
presence of glass; and Ostwald ripening of the conductive in the glass.
Time-temperature regions for these six processes are summarized in Fig. 5.12
for certain assumptions discussed in the next paragraph.

The right hand boundary of the glass sintering region of Fig. 5.12
was obtained by solving Eq. 5.1 using 10 μm for r, which corresponds to
the maximum particle size of glass in the system under study, and assuming
$\frac{x}{r} = 0.3$, which represents the completion of the initial stages of sintering.
The left hand boundary of the glass sintering region was obtained by
solving Eq. 5.1 using 1 μm for r, which corresponds to the minimum particle
size of glass in the system under study, and assuming x = 774 $\overset{\circ}{A}$, which
represents the neck radius after the centers of the particles have moved
30 $\overset{\circ}{A}$, the average radius of an RuO_2 particle. The region for glass spreading
is that shown in Fig. 5.2, and obtained as described in Section 5.1.3. The
left hand boundary of the rearrangement region was obtained by integrating
Eq. 5.12 to obtain the time for two particles, initially separated by a
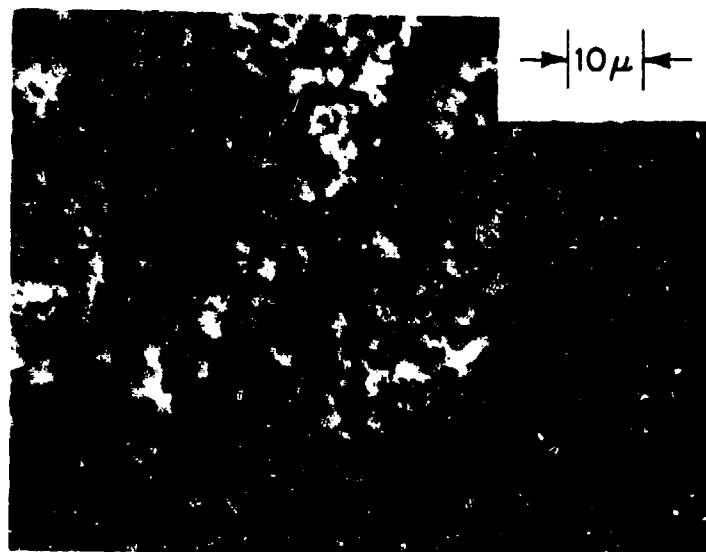
Figure 5.10   Macronetworks of $Bi_2Ru_2O_7$ in DuPont Birox 1200 Series Resistors
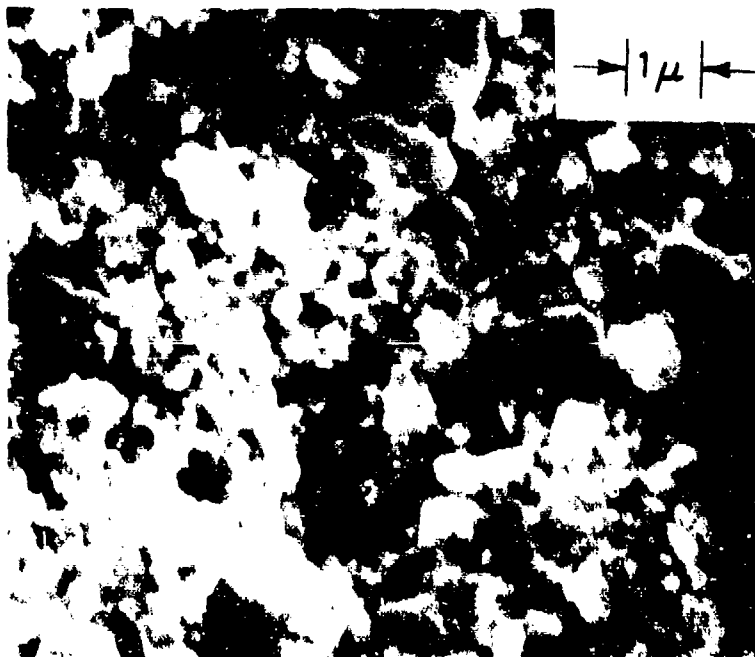
Figure 5.11   Micronetworks of $Bi_2Ru_2O_7$ in DuPont Birox 1200 Series Resistors
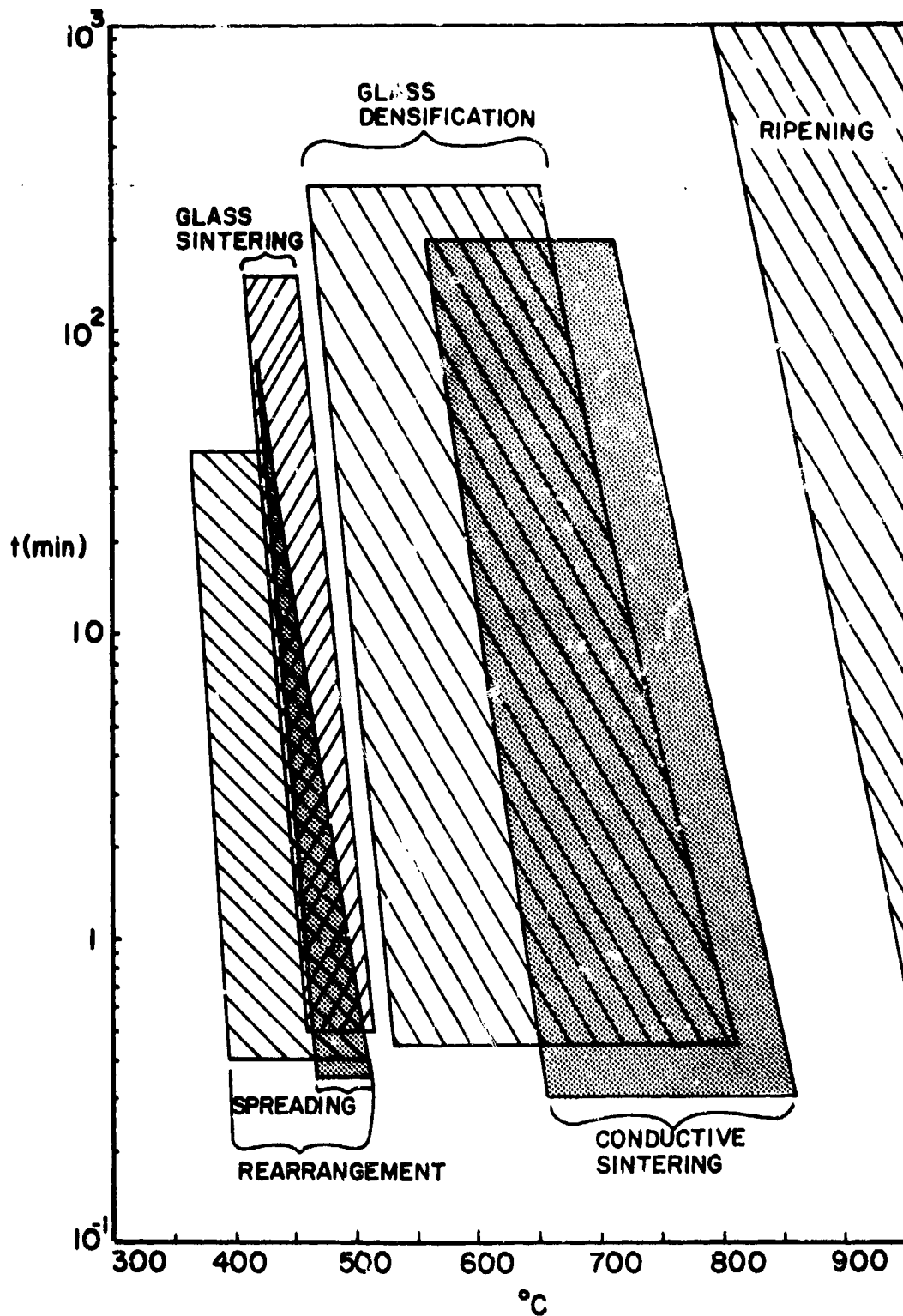
Figure 5.12   Kinetics of Microstructure Development Processes

distance of 60 Å, to come together; however, this boundary is not meaningful because rearrangement cannot occur until a liquid bridge has been produced by the spreading process. The right hand boundary of the rearrangement region was taken to be the same as the glass spreading region, because of the fact that the rearrangement process is fast compared to the spreading process. Boundaries for the glass densification region were taken from Fig. 5.4 obtained as discussed in Section 5.1.5. The bounds for the conductive sintering region were obtained by solving Eq. 5.21 with $\bar{r}(0) = 30$ Å. The left hand boundary was obtained for $x = 1$ Å, which would certainly correspond to a minimum neck, and the right hand boundary was obtained for $x = 10$ Å which corresponds to completion of the initial stages of sintering ($\frac{x}{r} = 0.3$). The left hand boundary for the ripening region was obtained by solving Eq. 5.24 for time as a function of temperature with $\bar{r}(0) = 30$ Å and $N(t)/N(0) = 0.5$. There is no upper bound on the ripening region because this process will continue until only one large particle remains at infinite time.

Of the six processes contributing to microstructure development, the kinetic considerations indicate that ripening and rearrangement are not important for the system under study. For the RuO_2-lead borosilicate glass system utilized in this investigation, the nominal peak firing temperature is 800°C, and at this temperature more than 600 hours would be required to halve the number of RuO_2 particles by the Ostwald ripening process. This does not, however, mean that ripening is, or could not be, important in other thick film systems in which the solubility of the conductive in the glass, the interfacial energy between the conductive and the glass, or the phase boundary reaction rate constant for dissolution of the conductive in the glass are greater. If these terms become sufficiently large the rate limiting process for Ostwald ripening may revert to diffusion, and the diffusion coefficient of the conductive in the glass, which is related to the viscosity of the glass through the Stokes-Einstein equation (Eq. 2.40), would be an important material parameter in addition to solubility and interfacial energy. In addition to ripening, the rearrangement process does not contribute to the overall kinetics of microstructure development for the RuO_2-lead borosilicate glass system. Before rearrangment can occur, a glass bridge must be formed between conductive particles by spreading of

the glass, but as discussed in the preceeding paragraph the rearrangement process is fast at any temperature compared to the spreading process. In practice this means that the particles w ld come together as soon as a glass bridge is formed. Equations 5.2 ... 5.5 would still represent the spreading kinetics for this case, but the integration to obtain Eqs. 5.3 or 5.6 is not valid because R is time dependent. The effect of an R which decreases with time during the spreading process would be to reduce the rate of spreading and to move the region for glass spreading in Fig. 5.12 farther to the right.

The steep temperature dependence of the effective regions for all of the processes depicted in Fig. 5.12 makes it reasonable to describe microstructure development as a sequential process during resistor firing. Essentially all of the organic constituents of the formulation will be gone by the time the temperature reaches 400°C if the heating to this point has been sufficiently slow. As the temperature moves above 400°C, glass particles which are adjacent to RuO_2 particles begin to flow and spread over and between the RuO_2 particles, while glass particles which are adjacent to other glass particles begin to form sintered necks. The glass particles, with RuO_2 particles held on their surfaces by partial wetting, tend to become more spherical in order to minimize their surface area. As the temperature passes 450°C both sintering and spreading processes become more rapid, and any RuO_2 particles which were initially in contact with a glass particle and separated from each other by a distance less than their diameter will be rapidly pulled together by the rearrangement process. Above 500°C the initial stage of glass sintering has been completed, but while the sintering of the glass was proceeding, the centers of adjacent glass particles moved toward one another and individual RuO_2 particles or agglomerates of particles formed by the rearrangment process, which were held on the surfaces of the glass particles, move with them. For example, the center-to-center distance between two glass particles having radius 1 μm will have moved 450 $\overset{\circ}{A}$ by the time the neck radius reaches 0.3 μm, and this distance is large compared to the size of the RuO_2 particles (30 $\overset{\circ}{A}$). When two RuO_2 particles or particle agglomerates come in close proximity due to the motion generated by the glass sintering, they will rapidly be pulled together and held because the kinetics of the rearrangemmet process are very fast at these temperatures.

The rearrangement process acting on particle agglomerates produces marconetworks. As the temperature approaches 550°C, the glass is in the intermediate stage of sintering where closed pores are being formed. In this temperature range, the glass-vapor interfacial area is decreasing very rapidly and with it the driving force for the rearrangment process, which means that the structure of the micronetworks and macronetworks will not change appreciably above 550°C.

The final stage of glass sintering as represented by the glass densification region of Fig. 5.12 begins at temperatures above 550°C and continues for the next two hundred degrees. Over this temperature range (550 to 750°C) the viscosity of the glass is decreasing very rapidly. At the lower temperature part of the region, the compressive stress on the resistor, resulting from the negative pressures in the closed pores as they contract, is the dominant force which leads to motion of the macro-networks, but as the temperature increases, the motion of those pores filled with insoluble gas (bubbles) becomes more and more rapid and this produces a stirring action of the macronetworks. Even after the glass densification has become complete, some stirring action which will lead to motion of the RuO_2 networks would still be expected due to thermal gradients which lead to density gradients. When two RuO_2 particles in adjacent macronetworks, are brought into close proximity by this stirring action, they will remain in contact due to the net compressive force of the collapsing pores, and sintering by a solution-dissolution process will begin. As the temperature passes above 650°C, the sintering between adjacent RuO_2 particles becomes more and more rapid until at 800°C the initial stages of sintering between adjacent RuO_2 particles is completed in less than four minutes. RuO_2 particles which were in contact throughout the high temperature phase of the firing (greater than 700°C) will progress to the intermediate stages of sintering, whereas RuO_2 particles which came into contact with one another very late in the firing sequence will only develop minimal neck diameters, or no neck at all. Because the motion of macronetworks con-tinues throughout the resistor firing there will be a spectrum of neck diameters between RuO_2 particles varying from necks which approach the size of the initial RuO_2 particles to those in which no neck formation has occurred and a glass film still separates the particles.

5.2   Charge Transport

5.2.1   Discussion of Processes

The two electrical characteristics of thick film resistors which
have baffled scientists and engineers are the blending curve and the
temperature dependence of resistivity. A theoretical description of a
blending curve, such as that shown in Fig. 4.83, has not been accomplished
because most of the previous theoretical studies worked from models which
do not apply to thick film resistors. The difficulties encountered in
describing the TCR have arisen because of one of the most desirable
characteristics of thick film resistors, the very low TCR.

Thick film formulations contain a conducting powder and an insulating
powder, and the processing is carried out at temperatures where a continuous
matrix of the insulating phase is formed. The system of conducting particles
dispersed in an insulating medium was first considered by Maxwell in 1881.
His model has been extended and refined by numerous workers since that time,
and has been the subject of several review articles [87-89]. None of these
theoretical approaches predict a decrease from the resistivity of the
insulating phase by more than a factor of ten over the volume fraction range
of interest in thick film resistors (0 - 40%), whereas a decrease of many
orders of magnitude is observed. Percolation theory [90-92] is a more recent
approach to describing the resistivity of a system consisting of a conducting
phase dispersed in an insulating phase. Depending upon the statistical model
chosen, a percolation threshold within the volume fraction range of interest
can be calculated, but in all cases the decrease from the resistivity near
that of the insulating phase to one near that of the conducting phase occurs
over a very narrow volume fraction range and cannot come close to describing
the observed blending curves.

The reason for the failure of these theoretical approaches is obvious
when one considers the microstructure of thick film resistors. The conduct-
ing particles are arranged into micronetworks and macronetworks throughout
the insulating phase, so a successful theoretical approach must predict the
formation of continuous chains of conducting particles as a function of

volume fraction of conductive. A statistical approach has been developed
[93-94] to calculate the probability of forming a chain of given length
consisting of particles of a given size for a given volume fraction.
However, this model of single chains between electrodes is almost as
unrealistic as the random distribution of conducting particles, because the
structures observed for the micronetworks (Fig. 4.38) and the macronetworks
(Fig. 4.37) show that multiple contacts between chains exist and many
conducting paths are formed between electrodes. The approach which seems
most realistic, and the one which will be developed in Section 5.2.5, was
developed by Scarisbrick [95]. He takes a model in which the basic volume
elements are considered to be distributed at random so that there is no
long range order, and the properties on a micro scale are dependent upon
nearest neighbor effects. Bulk properties can then be predicted based on
a statistical average of individual situations.

The TCR of thick film resistors is typically less than $\pm$ 100 ppm/°C,
whereas the conducting phase in bulk form invariably has a large positive
TCR (>5,000 ppm/°C for RuO_2) and the glass has an even larger negative TCR
with its resistivity showing an expotential temperature dependence
(activation energy of 1.58 ev for 63-25-12 lead borosilicate glass). The
concept of varying contact resistance between adjacent conducting particles
due to thermal stress has been introduced to explain the TCR as discussed
in Section 1.2.

The stress (S) between RuO_2 particles in a glassy matrix due to the
mismatch in thermal expansion is given by

$$S = - 3K_R V_g \Delta T [\alpha_\ell (glass) - \alpha_\ell (RuO_2 0] \qquad (5.25)$$

where K_R = bulk modulus of RuO_2

    α_ℓ (glass) = linear coefficient of thermal expansion of the glass

    α_ℓ (RuO_2) = linear coefficient of thermal expansion of RuO_2

    ΔT = temperature change from the zero stress condition

    V_g = volume fraction of glass

The sign was chosen such that a positive stress represents compression, and
a negative stress represents tension. Equation 5.25 predicts the simple
result that the stress between RuO_2 particles is directly proportional to

the difference in coefficients of linear thermal expansion. It has been shown [96] that the electrical resistance (R_c) of the contact between elastic bodies is given by

$$R_c = A \ P^{-1/3} \tag{5.26}$$

where A is a proportionality constant and P is the pressure between contacting members. If the only force acting in the system is that due to the mismatch in thermal expansions, Eq. 5.25 can be substituted for P in Eq. 5.26 to calculate the contact resistance. This approach is valid, however, only for cases where $\alpha_\ell(RuO_2) > \alpha_\ell(glass)$; the opposite case would predict a negative contact resistance. A comparison of the α_ℓ values for

the glasses given in Table 4.12 with the α_ℓ of RuO_2 (6 ppm/°C) reveals that the inequality holds for the first three glasses but is violated for the last five. Since no drastic differences were observed between the electrical properties of composites made from the first three glasses and those made from the last five, (see Table 4.12 and Fig. 4.79) it must be concluded that either other factors are influencing the pressure on the contacts, or contact resistance is not a significant factor. As discussed in Section 2.1.1, a compressive force on the contact between conducting particles is expected from both capillary forces and from pore collapse during micro- structure development. If this force is p, then Eq. 5.26 becomes

$$R_c = A \ (p + S)^{-1/3} \tag{5.27}$$

If p is sufficiently large then the contact resistance model is possible even for an unfavorable inequality in expansion coefficients. The hot temperature coefficient of contact resistance from 25° to 125°C is given by

$$TCR_c = \frac{R_c(125°) - R_c(25°)}{100 \ R_c(25°)} = \frac{R_c(125°)}{100 \ R_c(25°)} - .01 \tag{5.28}$$

Since p depends on surface tension, and the surface tension varies only slowly with temperature it can be assumed that p is constant. Combining Eqs. 5.27 and 5.28 gives

$$100 \ TCR_c = \left[\frac{P - S(25°)}{p - S(125°)} \right]^{1/3} - 1 \tag{5.29}$$

Equations 5.25 and 5.29 predict that TCR_c will be a monotonic function of the difference in expansion coefficients, but the data in Table 4.12 do not show the predicted monotonic increase of TCR with α_ℓ of the glass. Only at the most extreme mismatch in expansion does there appear to be a noticeable effect. It can be concluded from this study that other factors are more important in determining the TCR of a thick film resistor than any differences in coefficient of thermal expansion between the glass and the conductive which would be expected in practice.

Considerations of the microstructure reveal that the conducting chains in thick film resistors would not be expected to have the same electrical properties as the conducting phase in the bulk, and the fact that the TCR's are different should not be surprising. The microstructure development model predicts that there will be a spectrum of neck diameters between RuO_2 particles, varying from sintered necks which approach the size of the initial RuO_2 particles to those in which no sintering has occurred and a glass film still separates the particles. These two extreme cases will be called sintered and non-sintered contacts and the geometry pertaining to each is shown in Fig. 5.13. The transport properties of these two cases are fundamentally different and will be considered separately in Sections 5.2.2 and 5.2.3. The combination of these two types of contacts into single chains and into the overall micronetworks and macronetworks will be discussed in Sections 5.2.4 and 5.2.5 respectively, and a model developed which is consistent with both the microstructure development model and the observed TCR's of thick film resistors.

5.2.2   Sintered Contacts

The geometry chosen for the sintered contact (Fig. 5.13a) contains a volume of conductive $(4\pi r^3/3)$ equal to 1 particle. The task is to calculate the resistivity of this type of contact as a function of the bulk resistivity of the conductive and the ratio of neck radius to particle radius (x/r). For charge transport along the y direction, two terms must be considered: 1) the resistance of the two half particles on each side of the grain boundary (R_p); and 2) the resistance of the grain boundary region (R_b). Since these resistances will appear in series for transport normal to the grain boundary,
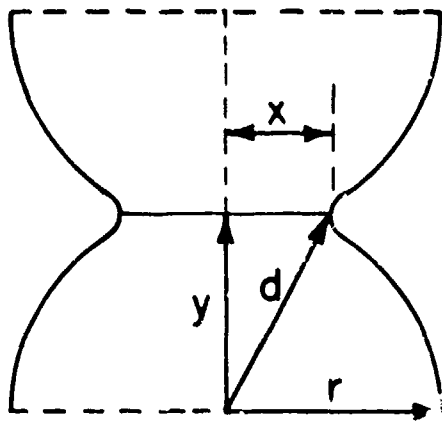
a. Sintered
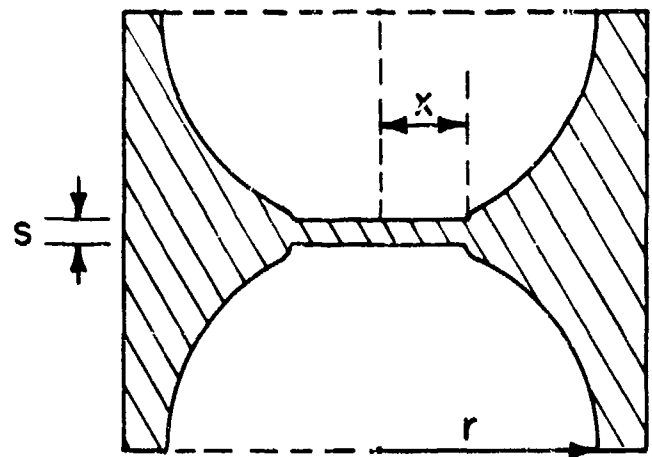
b. Non-sintered

Figure 5.13 Types of Contacts

the resistance of the sintered contact can be written as $R_a = R_p + R_b$. A recent study by Ramanan and Chaklader [97] developed equations for the electrical resistivity of compacts as a function of the resistivity of the particles and x/r ratio. This problem is similar to ours, but differs in that they were interested in the apparent resistivity of the compact, whereas we are interested in the apparent resistivity of a chain or a single contact.

A maximum value for R_p can be obtained by assuming straight flux lines, i.e. that all current is carried by a cylinder of radius x and length 2 y. For this case

$$R_p = \frac{2\, y\rho_p}{\pi x^2} \tag{5.30}$$

where ρ_p is the resistivity of the particle.

A minimum value for R_p can be obtained by assuming that the flux is uniform across each differential area along the y axis. For this case

$$R_p = 2\, \rho_p \int_0^y \frac{dy}{A(y)} \tag{5.31}$$

If it is assumed that the particles are always spherical, $A(y) = \pi(r^2 - y^2)$, and

$$R_p = \frac{2\rho_p}{\pi} \int_0^y \frac{dy}{r^2 - y^2} = \frac{\rho_p}{\pi r} \ln\; [\frac{r + y}{r - y}] \tag{5.32}$$

The assumption of spherical shape will be good at small values of x/r, but become progressively worse as x/r increases. At x = r the entire volume is conducting and the sintered contact has the geometry of a right circular cylinder.

At sufficiently small values of x/r the entire resistance of the sintered contact will be due to constriction resistance in the neck region. For this case it has been shown [98] that

$$R_p = \frac{\rho_p}{2x} \tag{5.33}$$

An approximation valid at large values of x/r can be obtained by the flux tube approach. One half of the sintered contact can be approximated by the geometry shown in Fig. 5.14. If Θ is the angle of rotation out of the
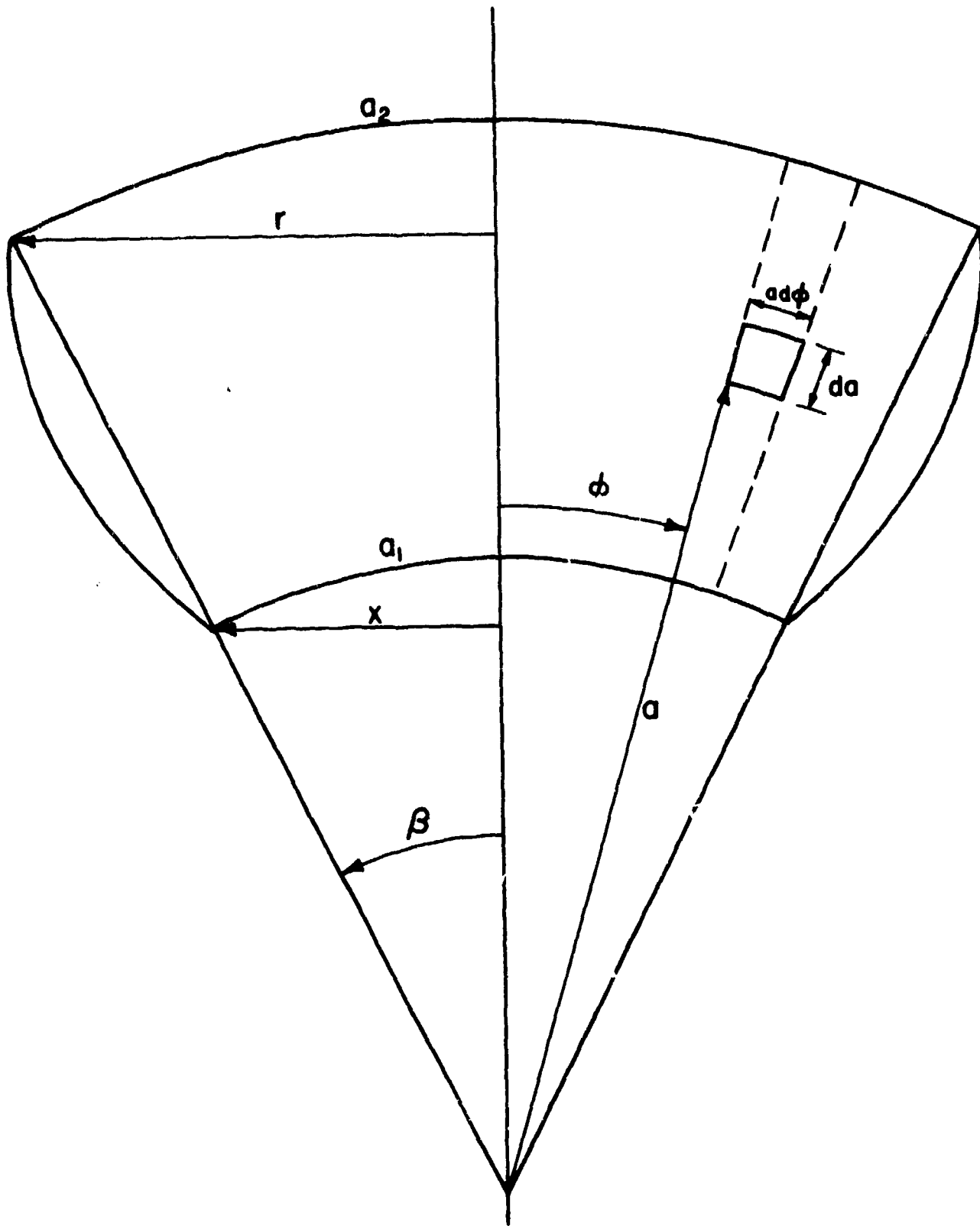
Figure 5.14 Flux Tube Approximation

plane of the paper, the volume element in the differential flux tube will
have a dimension $r \sin \phi \, d\Theta$ in the Θ direction, and the resistance of the
differential flux tube, R_f, can be obtained from

$$R_f = \int_{a_1}^{a_2} \frac{\rho_p \, da}{(rd\phi)(r \sin \phi d\theta)}$$

$$R_f = \frac{\rho_p (a_2 - a_1)}{a_1 a_2 d\theta \sin \phi d\phi} \tag{5.34}$$

Since all of the differential flux tubes will be electrically in
parallel, the resistance of the two half particles in series can be written
as

$$\frac{1}{R_p} = \iint_{\theta \; \phi} \frac{1}{2R_f} = \frac{a_1 a_2}{\rho_p (a_2 - a_1)} \int_0^{2\pi} d\Theta \int_0^{\beta} \sin\phi d\phi \tag{5.35}$$

which can be solved to give

$$R_p = \frac{\rho \, (a_2 - a_1)}{\pi a_1 a_2 (1 - \cos\beta)} \tag{5.36}$$

From Fig. 5.14 it can be easily shown that

$$a_1 = \frac{x \left[(r-x)^2 + y^2 \right]^{\frac{1}{2}}}{r-x}$$

$$a_2 = \frac{r \left[(r-x)^2 + y^2 \right]^{\frac{1}{2}}}{r-x}$$

$$\beta = \frac{r-x}{\left[(r-x)^2 + y^2 \right]^{\frac{1}{2}}}$$

We are ultimately interested in relating the resistivity of a thick
film resistor to the volume fraction of conductive, and we must take into
account the fact that some parts of the conductive are carrying less current

than other parts. This can be accomplished by writing the effective
resistivity of the conductive (ρ_c) as

$$\rho_c = \frac{R_p V}{(2y)^2} \qquad (5.38)$$

Since the volume of conductive in the sintered contact is constant and
equal to $4\pi r^3/3$, Eq. 5.38 can be reduced to

$$\rho_c = \frac{r^3 R_p}{3y^2} \qquad (5.39)$$

At values of $x/r < 0.3$ it has been shown [23] that $y = r (1 - x^2/4r^2)$
is a good approximation. At the limiting value of $x/r = 1$ the geometry is
a cylinder, and if the volume is constant, $2 y \pi x^2 = 4\pi r^3/3$, or $y = 2 r/3$.
An approximation which will satisfy this boundary condition and still give
reasonable agreement at low values of x/r is

$$y = r (1 - x^2) /3r^2 \qquad (5.40)$$

Combining Eqs. 5.30, 5.32, 5.33, 5.36, 5.37, 5.39 and 5.40 gives

Upper Boundary (straight flux lines)

$$\rho_c = \frac{2 \rho_p}{3(x/r)^2 (1 - x^2/3r^2)} \qquad (5.41)$$

Lower Boundary (uniform flux)

$$\rho_c = \frac{\rho_p}{3 (1 - x^2/3r)^2} \ln \left| \frac{6 - x^2/r^2}{x^2/r^2} \right| \qquad (5.42)$$

Constriction

$$\rho_c = \frac{\pi \rho_p}{2 (x/r) (1 - x^2/3r^2)^2} \qquad (5.43)$$

Flux Tube

$$\rho_c = \frac{(1 - x/r)^2 \rho_p}{3 (x/r) (1 - x^2/3r^2)^2 D[1 - \cos (\frac{1 - x/r}{D})]} \qquad (5.44)$$

where $D = [(1 - x/r)^2 + (1 - x^2/3r^2)^2] ^{1/2}$

Examination of Eqs. 5.41 - 5.44 reveals that the relative resistivity, ρ_c/ρ_p, is a function of only x/r for all four cases, and this functional dependence is shown in Fig. 5.15 for the four equations. The curve labeled "best" value was drawn to have a smooth transition between agreement with the constriction curve, which should be exact at sufficiently low x/r, and agreement with the flux tube curve, which should be exact at sufficiently high x/r.

The remaining problem in determining the effective resistivity is to establish a value and a temperature dependence for ρ_p in terms of the bulk values. The various electron scattering processes for RuO_2 discussed in Section 4.1.4.4 were those applicable to an infinite crystal lattice. When the dimensions of the sample approach the mean free path of the electrons, scattering at the surface must be considered. The theory of electron scattering in metals allows us to write the mean free path in infinite crystal lattice (λ_∞) as

$$\lambda_\infty = \frac{h}{2} \left(\frac{3\sigma\mu^2}{\pi e^4}\right)^{1/3} \tag{5.45}$$

where h is Plank's constant, σ is the conductivity, μ is the mobility and e is the electronic charge. The measured Hall mobility for RuO_2 is 3 cm^2/v-sec [63], and from Fig. 4.21 the defect free resistivity of RuO_2 at room temperature is 3.3 x 10^{-5} ohm cm which gives a conductivity of 3 x $10^4 (ohm\ cm)^{-1}$. Using these values in Eq. 5.45 gives a mean free path for electrons in RuO_2 of 22 Å. For our case of interest the particle radius in Fig. 5.13a is 30 Å which means that the neck diameter (2x) will be less than the electron mean free path for x/r values less than 0.37. Since many necks are expected to be below this value the effect of electron scattering at the surface must be considered. Sondheimer [99] developed a theory for diffuse scattering at the surface of a thin film. For $\frac{2x}{\lambda_\infty} > 0.1$ (i.e. x > 1 Å) Sondheimer's integral equation can be approximated [100] as

$$\frac{\rho_p}{\rho_\infty} = 1 + 3\lambda_\infty/16x = 1 + 4.13/x \tag{5.46}$$

where ρ_∞ is the bulk resistivity. Therefore, the resistivity of the material in the particles forming sintered contacts will be greater than the bulk resistivity by a factor varying from 5.13 at a neck radius of 1 Å to a factor of 1.14 and a neck radius of 30 Å. If a particle radius of 30 Å is assumed, Eq. 5.46 can be rewritten as
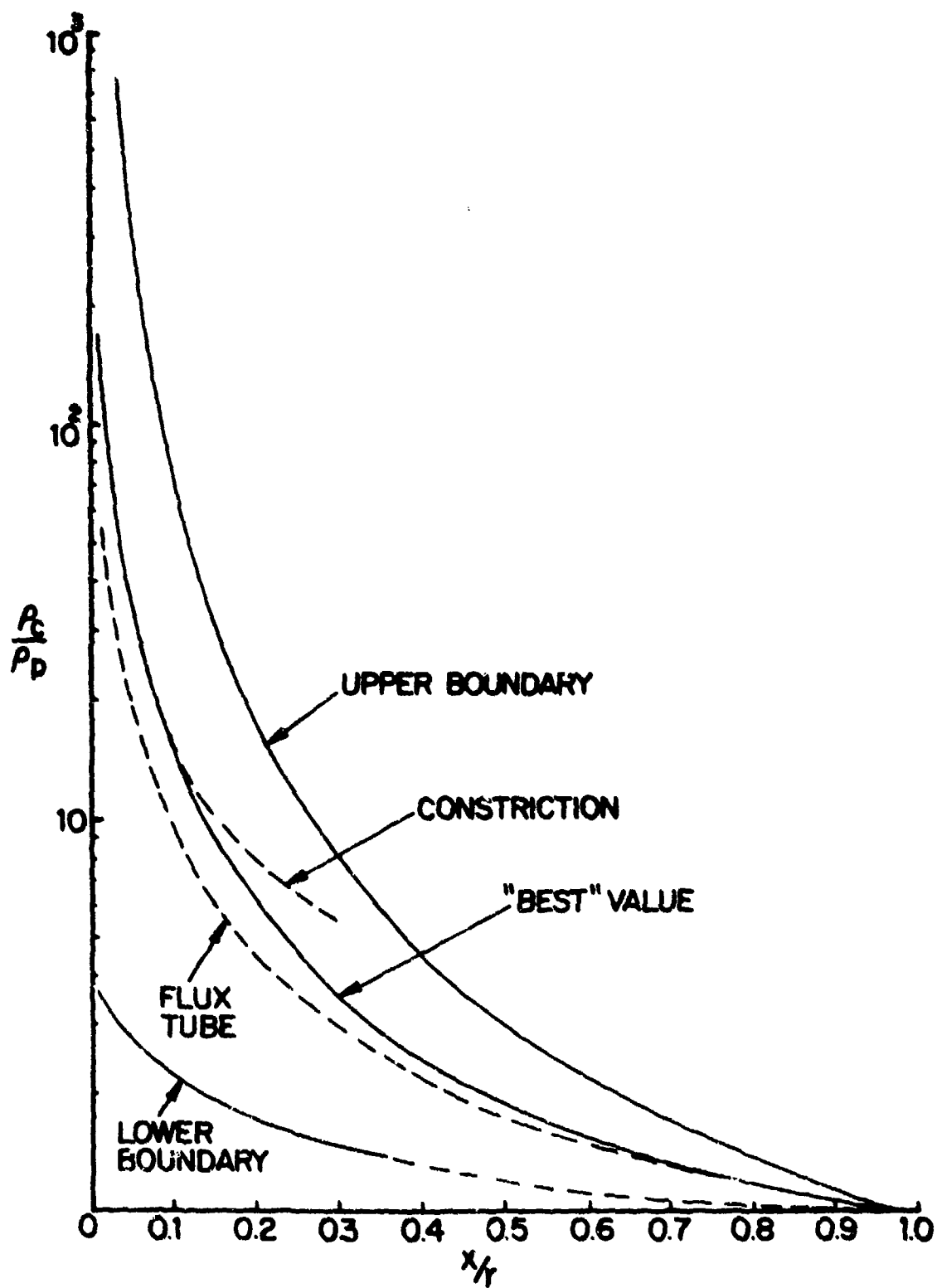
Figure 5.15 Effective Resistivity From Four Models

$$\frac{\rho_p}{\rho_\infty} = \frac{x/r + 0.138}{x/r} \tag{5.47}$$

Finally, applying Eq. 5.47 to the "best" value curve of Fig. 5.15 gives Fig. 5.16.

The temperature coefficient of resistivity ($\alpha = \frac{1}{\rho} \frac{d\rho}{dT}$) is also a function of thickness, and for $\frac{2x}{\lambda_\infty} > 0.4$ it can be approximated [101] as

$$\alpha = \alpha_\infty \left(\frac{1}{1 + 3\lambda_\infty/16x}\right) = \alpha_\infty \left(\frac{1}{1 + 4.13/x}\right) \tag{5.48}$$

Solving Eq. 5.48 at $x = 4$ Å gives $\alpha/\alpha_\infty = 0.49$, and at $x = 30$ Å, $\alpha/\alpha_\infty = 0.88$. The approximation required to derive Eq. 5.48 is not valid at $x = 1$ Å. but using the complete Sondheimer relation [99] it is found that α/α_∞ is approximately 0.3 at $x = 1$ Å. In the neighborhood of room temperature the resistivity of single crystal RuO_2 is a linear function of temperature (see Fig. 4.22) with α_∞ equal to 5670 ppm/°C. Thus ρ_c can be written as

$$\rho_c = \rho_c^\circ (1 + \alpha\Theta) \tag{5.49}$$

where ρ_c° is ρ_c at 25°C, Θ is the temperature in °C minus 25 and α is obtained from Eq. 5.48.

If it is assumed that Matthiessen's rule holds, then the resistivity of the sintered contact can be written as $\rho_a = \rho_c + \rho_b$, and the problem remaining is to assign a value to ρ_b. Typically, the room temperature resistivity of a polycrystalline metal sample is two to five times greater than that of a pure, high quality single crystal. In our case there will be a grain boundary every 50 Å along the conducting path, and the impurity content of the grain boundary will be high because a glass film was present during the early stage of sintering; therefore, the magnitude of the grain boundary resistance relative to the crystal resistance would be expected to be higher than for a typical polycrystalline metal. For calculation purposes we will assume a value of the temperature independent grain boundary resistivity, ρ_b, equal to ten times the crystal resistance at room temperature.

The ratio of effective particle resistivity to single crystal resistivity as a function of x/r is plotted in Fig. 5.16. For example, at $x/r = .15$, $\rho_c = 17 \rho_\infty$. Adding to this $\rho_b = 10 \rho_\infty$ gives $\rho_a = 27 \rho_\infty = 9 \times 10^{-4}$ ohm cm at room temperature.
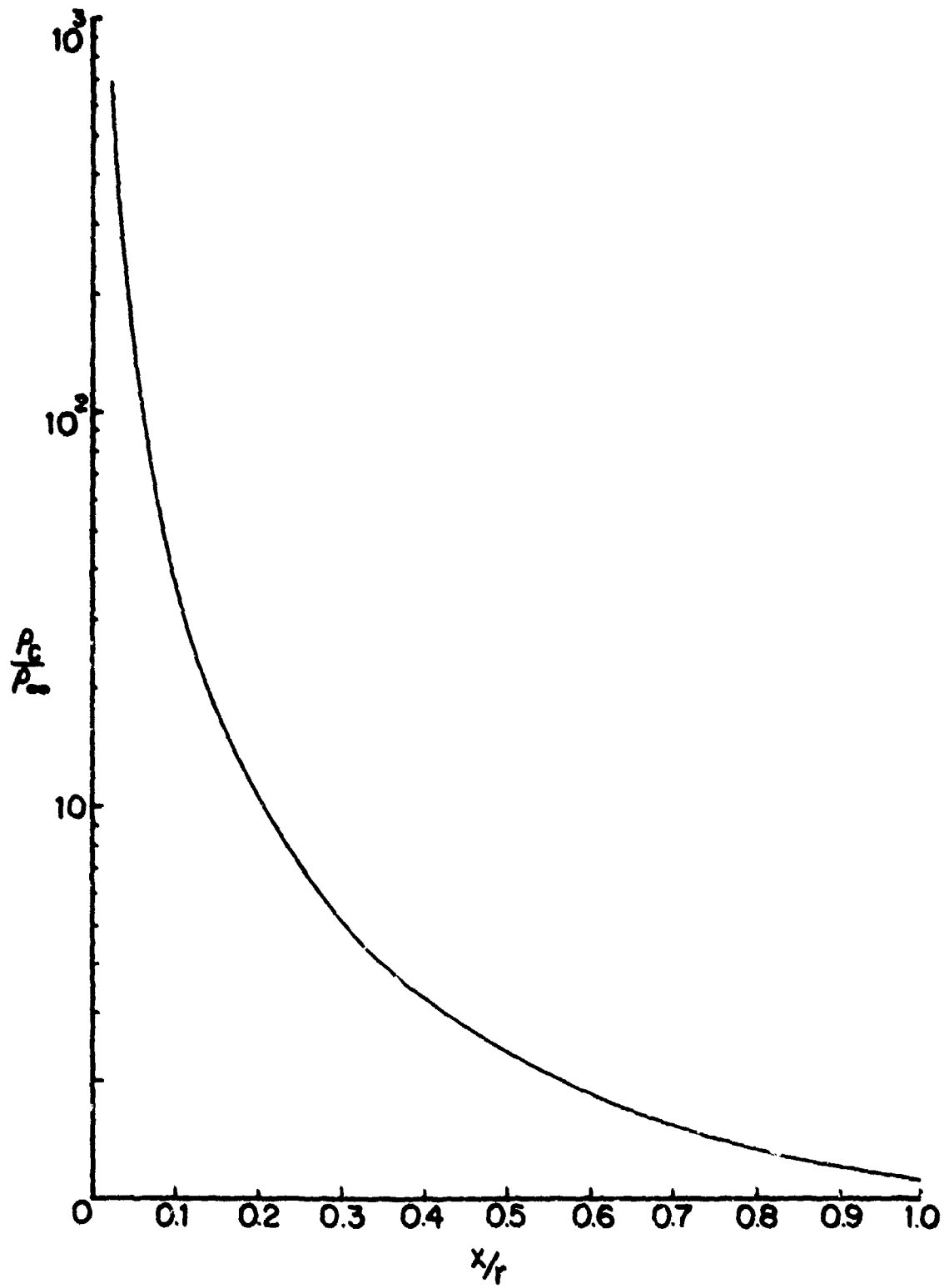
Figure 5.16   Effective Resistivity of Sintered Contacts

To calculate the temperature dependence of the resistance of the
sintered contact, the resistance of the grain can be written as

$$R_p = F (x,r) \rho_c^{\bullet} (1 + \alpha\theta) \qquad (5.50)$$

where $F (x,r)$ is some function of x and r. If the grain boundary resistance
is 10 times the particle resistance at 25°C then $R_b = 10 R_p$, and the total
resistance of the sintered contact can be written as

$$R_a = F (x,r) \rho_c^{\bullet} (1 + \alpha\theta) + 10 F (x,r) \rho_c^{\bullet} \qquad (5.51)$$

Substituting Eq. 5.51 into Eq. 5.38 for hot TCR gives

$$TCR = \frac{F(x,r)\rho_c^{\bullet} (100\alpha)}{11F (x,r)\rho_c^{\bullet} (100)} = \frac{\alpha}{11} \qquad (5.52)$$

Taking a value of $x/r = 0.15$, the temperature coefficient of resistivity
α will equal approximately 0.39 α_{∞}[101]. The temperature coefficient of
resistivity of single crystal RuO_2 (α_{∞}) is 5.67 x 10^{-3}, which gives a value
of $\alpha = 2.2$ x 10^{-3}. Using this value in Eq. 5.52 gives a TCR of 2 x 10^{-4} or
200 ppm/°C. Therefore, small, positive TCR's are predicted for the sintered
contacts alone, the two primary causes being enhanced scattering at surfaces
and grain boundaries.

The crossed crystal results (see Section 4.3.2) can be interpreted in
terms of forming a single, sintered contact. The large decrease in resistance
accompanied by the elimination of contact noise which occurred during the
first firing cycle (Fig. 4.71) is consistant with the formation of a sintered
neck between the single crystal rods. None of the crossed crystal experiments
were conducted at constant temperature so it is impossible to predict a neck
size from the known sintering kinetics. However, reasonable time-temperature
combinations are obtained from Eq. 5.21 using the known crystal diameters
and an x value calculated from Eq. 5.33 using the known resistance.

In terms of the number of conducting contacts, the large particle
resistors (see Section 4.3.4) are between the single contact crossed crystal
samples and more typical resistors. In terms of microstructure development
that depends on developing sintered necks, however, the samples should be
most similar to the crossed crystal samples. The resistance values (Fig. 4.81)

and the range of TCR's obtained with these large particle resistors is consistent with this prediction.

5.2.3   Non-Sintered Contacts

In a thick film resistor the number of non-sintered contacts of the type shown schematically in Fig. 5.13b will decrease with increasing firing time or temperature, but because of the dynamic nature of microstructure development there will always be some of these non-sintered contacts. The possible conduction mechanisms for charge transport across a non-sintered contact can be considered in five different categories [102]: 1) ionic conduction; 2) impurity conduction; 3) space charge limited flow; 4) Schottky and Frenkel-Poole emission; and 5) tunneling and internal field emission.

1. Ionic conduction

Ionic conduction occurs due to the drift of charged atoms under the influence of an applied electric field. This is the dominant mechanism of charge transport in bulk glasses, and was determined for the 63-25-12 lead-borosilicate glass as discussed in Section 4.3.1. Electrodes reversible to the mobile ions are required for steady state ionic transport at DC, which limits the possibilities in the system of interest to ruthenium ions or oxygen ions. At room temperature the electrode reactions, whereby ruthenium or oxygen ions are exchanged between the glass and the crystalline RuO_2, would be very slow and a polarization or electric double layer would be expected. These electrode processes lead to a frequency dependent conductivity in the audio frequency range, but this is not observed in thick film resistors. Therefore, ionic conduction is not expected to provide an important contribution to transport across the non-sintered contacts.

2. Impurity conduction

An electron occupying an isolated donor level in an impure insulator has a wave function that is localized near the impurity, but there is always a small overlap with the wave function of electrons on neighboring donor sites. A conduction process is possible in which the electron moves from one center into the conduction band. If both donor and acceptor sites are present, an electron can move from an occupied donor to an acceptor by a tunneling process, or by a hopping or small poloron process. When the interaction between centers is very large (e.g. with a very high concentration of impurities) then overlap of the electron wave functions throughout the insulator is sufficiently large that a metallic conductivity occurs.

3. Space charge limited flow

Space charge limited current results from carriers injected into the insulator where there is no compensating charge present. This mechanism can be very important at room temperature and below because insulators normally have a low density of free carriers and charge unbalance can be easily produced by an applied voltage. The character and magnitude of space charge limited effects are determined largely by the presence of localized states which can trap and store charge in equilibrium with the free charge. This leads to several possible varieties of space charge limited flow, depending on the types and concentration of traps and recombination centers that are present. Defect states in the insulator will have a considerable influence on the current because the electron lifetime will be changed and also because the current will vary with injection level if traps and recombination centers are present.

4. Schottky and Frenkel-Poole emission

As a result of the high field across thin insulating films, Schottky emission of electrons may occur from the metal contact at a negative potential into the conduction band of the insulator. This mechanism corresponds to thermal activation of electrons over the metal-insulator interface barrier with the added effect that the applied field reduces the height of this barrier. The Frenkel-Poole emission is based on the same lowering of a barrier height by an applied electric field, but is due to field enhanced thermal excitation of trapped electrons into the conduction band.

5. Tunneling and internal field emission

The various electron transitions which have been postulated for tunneling and internal field emission processes are: 1) from the valence to the conduction band; 2) to the conduction band from localized impurity levels (i.e. field ionization); 3) electron tunneling from the cathode in a similar manner to field emission into vacuum; and 4) from the valence band to the anode. Tunneling resistance can be very dependent on voltage and temperature, and in fact, at least one type of cermet film has been prepared in which voltage dependent tunneling was observed [103]. However, it is also possible to have a tunneling that is almost independent of temperature and voltage [104-106], depending only on the barrier material, and the magnitude of the potential. The resistance tends to be independent of temperature when the

potential across the barrier is small compared to the height of the barrier, and independent of applied voltage for thin barriers. If the potential is sufficiently small (<100mv), the resistance is independent of applied voltage for any barrier thickness.

The voltage (V), temperature (T), and insulator thickness (s) dependences of the current density of these basic conduction processes are summarized in Table 5.3. Ionic conduction, impurity conduction, and tunneling at very low voltage are the only mechanisms which predict ohmic behaviour, whereas the other mechanisms predict a stronger dependence of the current on the applied voltage. Frenkel-Poole emission and space charge limited flow near the trap filled limit may exhibit approximately ohmic characteristics depending on the magnitude of the exponential terms. Space charge limited flow with shallow traps and tunneling predict temperature independent currents, however, the tunnel current shows a small temperature dependence if traps are present.

TABLE 5.3

Conduction Processes in Insulating Films

Mechanism	Current Density
Ionic Conduction	$J \propto (V/sT) \exp(-Q_1/T)$
Impurity Conduction	
Tunneling or Hopping	$J \propto (V/s) \exp(-Q_2/T)$
Metallic	$J \propto (V/s) [1/(a + bT)]$
Space Charge Limited	
Shallow Traps	$J \propto V^2/s^3$
Trap Filled Limit	$J \propto (V/s^2) \exp(-Q_3 V/sT)$
Schottky Emission	$J \propto T^2 \exp[(Q_4 V^{1/2}/s^{1/2}T) - (Q_5/T)]$
Frenkel-Poole Emission	$J \propto (V/s) \exp[(2 Q_4 V^{1/2}/s^{1/2}T) - (Q_5/T)]$
Tunneling	
Very Low Voltage	$J \propto (V/s) \exp(-Q_6 s)$
Very High Voltage	$J \propto (V^2/s^2) \exp(-Q_7 s/V)$

It is important to note that most of the processes which are temperature
dependent predict an increasing current with increasing temperature at a
fixed voltage (a negative TCR). Therefore, the contribution of the
non-sintered contacts to the overall charge transport may be significant
when a negative TCR is observed in a thick film resistor. For example, the
data shown in Fig. 4.93 can be interpreted in terms of a relatively large
number of non-sintered contacts present after short firing times with the
number, relative to the number of sintered contacts, decreasing with increasing
firing time. The plateau reached at a TCR of +120 is approaching a value
consistent with only sintered contacts as calculated in the previous section.
The current-voltage curves shown in Fig. 4.95 are also consistent with more
non-sintered contacts contributing to charge transport in resistors fired
for shorter times. Resistor C, which had been fired for 30 minutes at 610°C,
shows non-ohmic behaviour and much higher resistance at low fields than
does resistor B which was the same composition but fired for 60 minutes at 610°C.
The dependence of current on voltage at low voltages suggests a contribution
from emission, tunneling, or space charge limited flow. As the field was
increased, the voltage dependence became less and the resistivity decreased
until the behaviour was almost ohmic and the resistivity was within a factor
of 2 of resistor B. One possible explanation for this behaviour is simply
dielectric breakdown; although the electric field applied across the resistor
is always relatively small, the field across a 100 Å gap could be 10^6 v/cm or
larger. Another possible explanation of the observed behaviour is an increase
in impurity conduction or impurity assisted tunneling across the insulating
gap due to a field assisted transport of ions from the RuO_2 into the gap region.

A combination of the possible transport mechanisms is almost certainly
required to explain the data shown in Fig. 4.95. Since the microstructure
development model predicts a spectrum of film thicknesses, a combination of
mechanisms throughout the resistor would always be anticipated, but a tunneling
mechanism with or without traps would be expected to dominate at longer firing
times and higher temperatures, because this mechanism shows the strongest
dependence on film thickness.

5.2.4   Linear Chains

A single chain of conducting particles in the glassy matrix could

contain both sintered and non-sintered contacts, and the resistance R of a linear chain is the sum of the resistance of all the contacts. As discussed in the preceeding section there are a variety of transport mechanisms which may be operative for the non-sintered contacts, but for considerations involving the temperature dependence of the resistance we can distinguish two basic types of contacts: those which have an exponential temperature dependence and those which are temperature independent (see Table 5.1). We will designate these as types G1 and G2, and the resistance of the linear chain can be written as

$$R = N_a R_a + N_{G1} R_{G1} + N_{G2} R_{G2} \tag{5.53}$$

where N_i is the number of contacts of type i in the chain each having resistance R_i. Following the discussion in Section 5.2.5, the resistance of the sintered contact can be written as

$$R_a = R_p^\circ \; (1 + \alpha\Theta) + R_b \tag{5.54}$$

Assuming that $R_b = 10 \; R_p^\circ$ as before, Eq. 5.54 becomes

$$R_a = R_p^\circ \; (11 + \alpha\Theta) \tag{5.55}$$

If G2 is a tunneling contact, we can approximate its value because tunneling resistivities of approximately 0.1 ohm-cm have been observed [106] for film thicknesses the order of 10 Å. If we take s = 10 Å and x = 5 Å (x/r = 0.2) the resistance of the tunneling contact R_{B2} is approximately 10^6 ohms.

The resistance of contact type G1 can be written as

$$R_{G1} = A \; \exp \; (Q/RT) \tag{5.56}$$

In studies of transport through thin insulating films it is not uncommon to observe [107] that the current due to the temperature independent tunneling effect and that due to the activated effects are of comparable magnitude in the neighborhood of room temperature. To calculate the temperature dependence of resistance for a single chain, therefore, we will assume that $R_{G1} = R_{G2} = 10^6$ ohms at 25°C. Activation energies the order of one electron volt are commonly observed [108] for the temperature dependent processes. Using this value and the room temperature resistance, Eq. 5.56 becomes

$$R_{G1} = 1.74 \times 10^{-11} \exp (11,500/T) \tag{5.57}$$

The resistance of the particle part of the sintered contact (R_p) at room temperature will vary from 3.34×10^4 to 56.4 ohms as x varies from 1 to 30 Å if r = 30 Å (see Eq. 5.39 and Fig. 5.16). For computational purposes we will assume a value of $R_p = 10^3$ ohms at 25°C (x/r = 0.2) which means that $R_{G1} = R_{G2} = 10^3 R_p^\circ$. Using this value and combining Eqs. 5.53, 5.55 and 5.57 gives

$$R = N_a R_p^\circ (11 + \alpha\theta) + 1.74 \times 10^{-14} N_{G1} R_p^\circ \exp (11,500/\%) + 10^3 N_{G2} R_p^\circ$$

Calculating the hot TCR (25° - 125°C) by Eq. 5.28 (using $\alpha = 2.2 \times 10^{-3}$ as discussed in Section 5.2.2) gives

$$TCR = \frac{2.2 \times 10^3 m - 10^7}{11m + 10^3 q + 10^3} \quad (ppm/°C) \tag{5.58}$$

where m is the ratio of sintered contacts to activated contacts (N_a/N_{G1}) and q is the ratio of tunneling contacts to activated contacts (N_{G2}/N_{G1}). An examination of Eq. 5.58 shows that the TCR will have a maximum value of 200 ppm at $m = \infty$ and a minimum value of $-10^4/(1 + q)$ at m = 0. The dependence of the hot TCR on m at various values of q is shown in Fig. 5.17. At the early stage of chain development q will be relatively small and the TCR will be large and negative. As the firing proceeds q will increase as the distance, s, between the non-sintered contact decreases, and the TCR will become less negative. With increasing time at temperature m will begin to increase as more and more non-sintered contacts are converted into sintered contacts. Whether or not q will decrease during this phase of microstructure development depends upon the rate of sintering relative to the rate of decrease of s. Regardless of these relative kinetics, when m becomes greater than 4.55×10^3 the TCR will become positive for all values of q. Beyond this point the only influence of q is to determine the rate at which the TCR approaches its limiting value of +200 ppm. Therefore, a single chain can never have a large positive TCR provided the particle size of the conductive is sufficiently small, but a large negative TCR is possible regardless of particle size.

5.2.5 Model

A consideration of the complexity of the micronetworks and macronetworks

$m = N_a / N_{GI}$

$q = N_{G2} / N_{GI}$
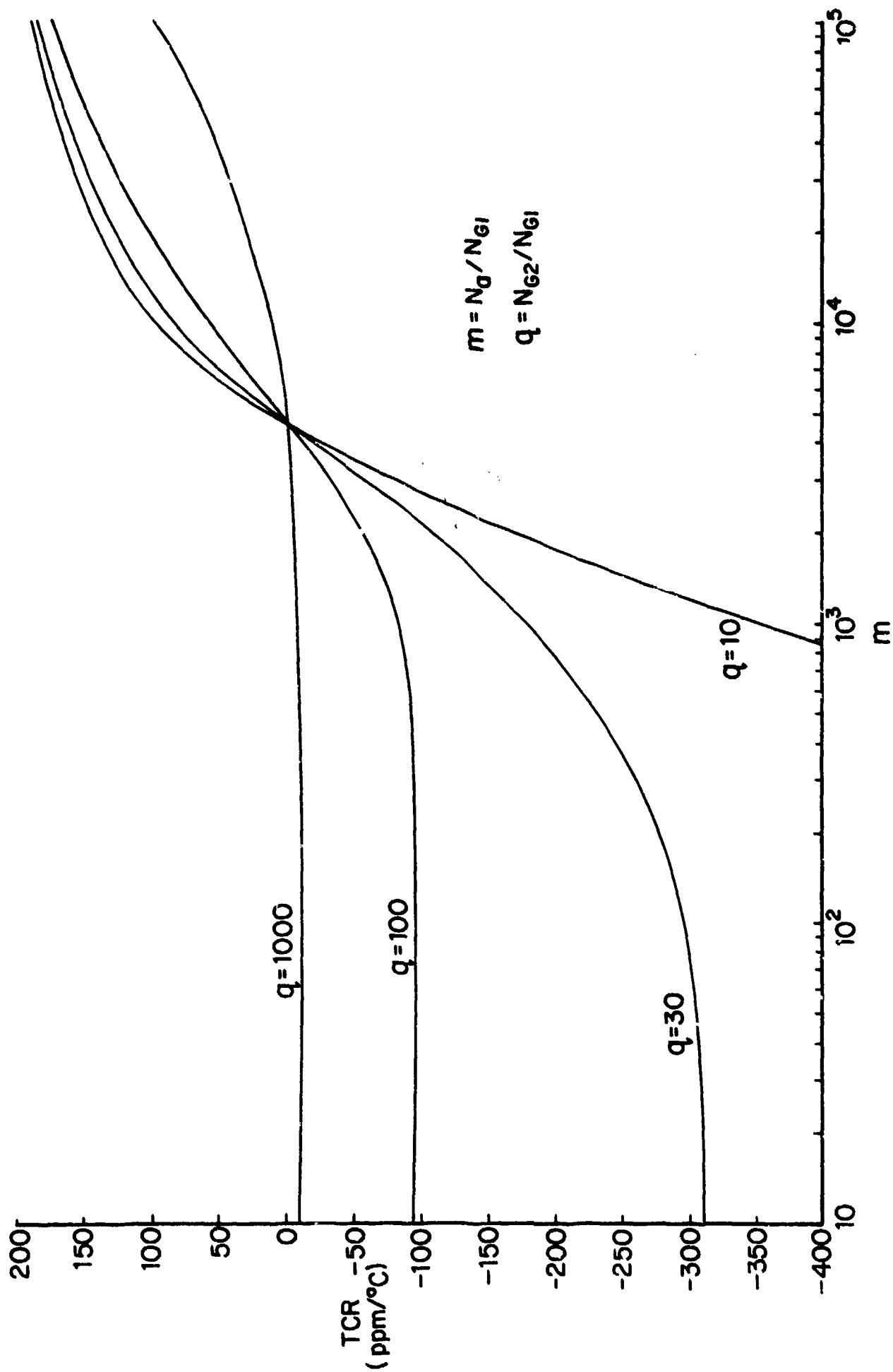
Figure 5.17   TCR For A Linear Chain

present in thick film resistors (see Figs. 4.37 and 4.38) leads to the realization that it is impossible to adequately model in terms of an equivalent circuit involving a parallel combination of linear chains. The actual chains are highly branched and interwoven on both a microscopic and macroscopic scale. However, the general considerations discussed in the preceeding section for the temperature dependence of a single chain apply in general to the resistor as a whole. The TCR data as a function of firing time shown in Fig. 4.92 indicate that fewer and fewer contacts of type Gl are contributing to the overall conductivity as the firing time increases. If one considers the resistivity over a wider temperature range, (see Fig. 4.94) it must be concluded that most of the conducting paths between electrodes do not contain any contacts of type Gl. Even though the resistance change shown in Fig. 4.94 from room temperature to very low temperatures for the two resistors fired for the shortest times is very large by thick film resistor standards, it is very small compared to that expected for a type Gl contact. For an activation energy of 1 ev the ratio of the resistance of a type Gl contact at 4.2°K to that at 25°C is greater than 10^{1000}. Therefore, the only interpretation for data such as those shown in Fig. 4.94 is that even at very short firing times, continuous networks of sintered contacts with perhaps some type G2 contacts are present throughout the body of the resistor. Some segments of these networks may contain loop structures having type Gl contacts which are electrically inactive at low temperatures because of their extremely high resistance. As the temperature increases, these loops shunt out sections of the network thereby lowering the overall resistance.

Many of the continuous networks of sintered and type Gl contacts may not be initially present in the resistor immediately after firing. The type Gl contacts would be expected to lead to a slope greater than 1 (the value expected for sintered contacts) on a plot of log J versus log E. The data shown in Fig. 4.55 and discussed in Section 5.2.3 show that the normal fired resistor (resistor A) and the resistor fired 60 minutes at 610°C (resistor B) have linear slopes within experimental error, and resistor C has a slope of only 1.05 after being exposed to the high fields. The current-voltage results for resistors fired for short times, indicate that many of the type Gl contacts are destroyed or converted into other types of contacts by the initial application of an electric field. For example, consider a 1000 ohm resistor

with a chain extending from one electrode to the other and containing a single contact of type G1 such as that shown schematically in Fig. 5.18(a). If 10 volts is applied to this resistor the entire 10 volts will appear across the G1 contact because its resistance is approximately 10^6 ohms. If $s = 100$ Å the electric field across the G1 contact will be 10^7 volts per cm, which may be sufficient to cause breakdown. Even if breakdown does not occur, the field may be sufficient to drive ruthenium ions into the film which would produce impurity enhanced tunneling [109] and convert the contact to a type G2. However, if the type G1 contact is part of a loop in series with many other structures in the network, such as shown schematically in Fig. 5.18(b), the voltage across the contact will be the IR drop across the sintered contacts carrying current in the loop, and may be only a few millivolts per cm. Based on this interpretation, type G1 contacts in a loop configuration are the only ones which can survive the initial application of the electric field.

As the temperature is raised however, the resistance of the type G1 contact in the loop configuration will decrease until it is carrying more current and the effective resistance of the network has been decreased slightly. It becomes a trivial problem to select values of m_1, m_2 and m_3, for the equivalent circuit of Fig. 5.18(b) to reproduce any set of temperature dependent data, for example, those shown in Fig. 4.94.

As discussed in general terms in Section 5.2.1 the best model for describing resistivity of a thick film resistor as a function of volume fraction of the conducting phase is one which introduces the concept of chains of conducting particles, such as that developed by Scarisbrick [95]. This model represents the conductivity of the system (σ) in terms of the conductivity of the conducting component (σ_c) as

$$\sigma/\sigma_c = P_1 P_2 G \qquad (5.59)$$

or in terms of sheet resistance (R_s) of a thick film resistor

$$R_s = \frac{\rho_c}{P_1 P_2 \, Gt} \qquad (5.60)$$

where P_1 is the probability that any given element in a chain is conducting, P_2 is the probability that a chain is continuous from electrode to electrode, G is a geometry factor relating the measured resistivity of the composite system to the resistivity of the conducting chains, and t is the film thickness.
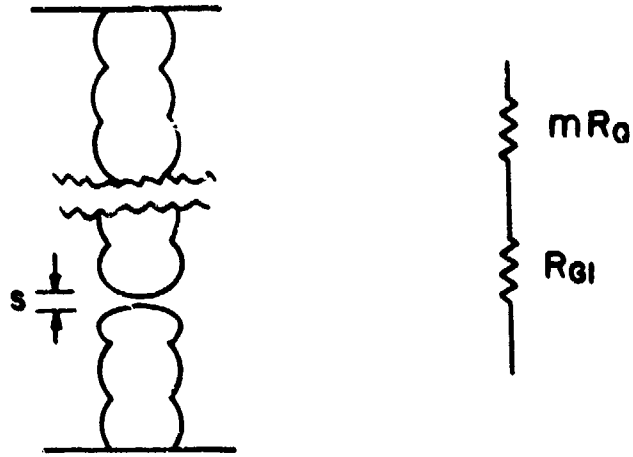
(a) LINEAR CONFIGURATION
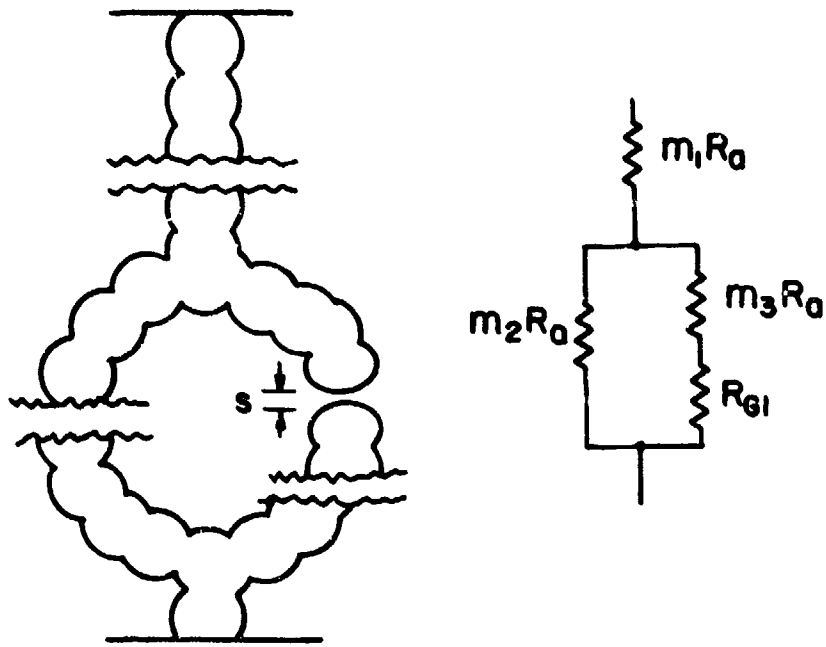
(b) LOOP CONFIGURATION

Figure 5.18 Geometry of Sintered and Activated Contacts

Th geometry factor, G, can be d termined [95] as a function of volume fraction of conductive (V_c) by a method analagous to the kinetic theory of gases, and the relation $V_c = 3 G - 2 G^{3/2}$ results. In order to avoid solving a cubic equation, it is most convenient to make a plot of V_c vs G; G can then be read off for any experimental value of V_c. Scarisbrick [95] assumes that $P_1 = V_c$, that is, that the fraction of elements in the chain which are conducting is equal to the volume fraction of the conductive. From statistical theory, the probability of obtaining a chain of n conducting elements is given by $(V_c)^n$. Thus,

$$P_2 = (V_c)^n \tag{5.61}$$

and the remaining problem is to establish a value for n as a function of V_c. Scarisbrick determined n for two limiting cases: random and ordered. For the random case he considered the conducting elements as spherical with a mean diameter d, and with the associated volume of the insulating phase also spherical and of mean diameter, D. With these qualifications the diameters are related by

$$D/d = 1/(V_c)^{1/3} \tag{5.62}$$

He then applied random walk theory, taking the diameter D as the mean distance between ends of a chain of n links each of length d, to give

$$D = d(n)^{1/2} \tag{5.63}$$

Combining Eqs. 5.62 and 5.63 gives

$$n = (V_c)^{-2/3} \tag{5.64}$$

and therefore

$$P_2 \text{ (random)} = (V_c)^{(V_c)^{-2/3}} \tag{5.65}$$

This is the value of P_2 expected if one assumes a random distribution of the conducting phase initially, which is a poor approximation if the driving forces for formation of the chains are very strong. If all of the conducting particles are part of chains then the probability term P_2 approaches 1. Therefore,

$$P_2 \text{ (ordered)} \approx 1 \tag{5.66}$$

If ρ_c is considered to be the resistivity of bulk RuO_2 (3.5×10^{-5} ohm-cm at 25°C) the sheet resistance of a thick film resistor as a function of volume fraction can be calculated from Eq. 5.60 at either of the extremes. The results of these calculations using Eq. 5.65 and Eq. 5.66 are shown in Fig. 5.19. At high volume fractions the slope approaches that of the ordered model while at low volume fractions the slope approaches that of the random model, but the magnitudes are in disagreement throughout the entire range. Similar results were obtained when this approach was applied to Ag-Pd-PdO and $Bi_2Ru_2O_7$ resistors by Kusy [110]. While the agreement between theory and experiment as shown in Fig. 5.19 is by no means precise, it is considerably better than that obtained with other theoretical approaches (e.g. percolation theory).

Two of the assumptions which led to the theoretical curves of Fig. 5.19 are particularly questionable for a thick film resistor system: the values chosen for ρ_c and P_2. The resistivity of the conducting chain is not equal to the resistivity of RuO_2 for the reasons given in Section 5.2.2. If the chains consist of only sintered contacts, Fig. 5.16 should be used to determine the resistivity of the particles and then the resistivity of the grain boundary should be added to this to obtain the resistivity of the conductive chains. A more reasonable value for ρ_c would be 9×10^{-4} ohm-cm as discussed in Section 5.2.2

Neither the assumption of a completely random initial state nor a final state in which all conducting particles are parts of chains stretching from face to face are reasonable for a thick film resistor. A model between these two extremes can be achieved by starting with Eq. 5.61 to calculate P_2, but assuming that some initial ordering of the conductive particles exists. For ease of computation we will take the geometry shown in Fig. 5.20 where the initial chain is a right square cylinder having dimensions x, y and z, in the center of a cube of the insulating phase having side D. The root-mean-square diameter of the conducting phase is given by

$$d = \left[\frac{x^2 + y^2 + z^2}{3}\right]^{1/2} \tag{5.65}$$

If $y = z$ and $x = bz$, Eq. 5.65 becomes

$$d = z\left[\frac{2 + b^2}{3}\right]^{1/2} \tag{5.66}$$
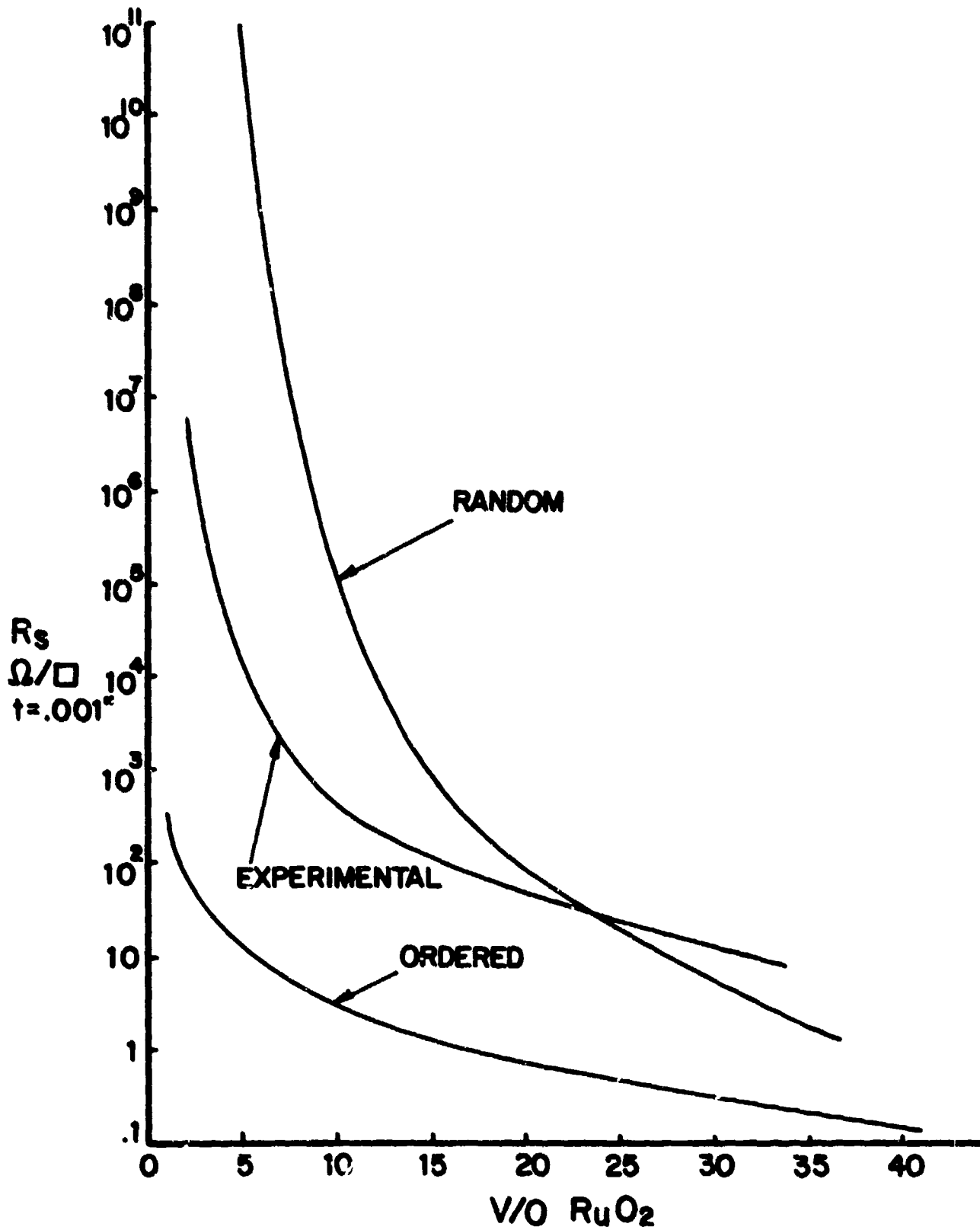
Figure 5.19 Blending Curve According to Scarisbrick's Models
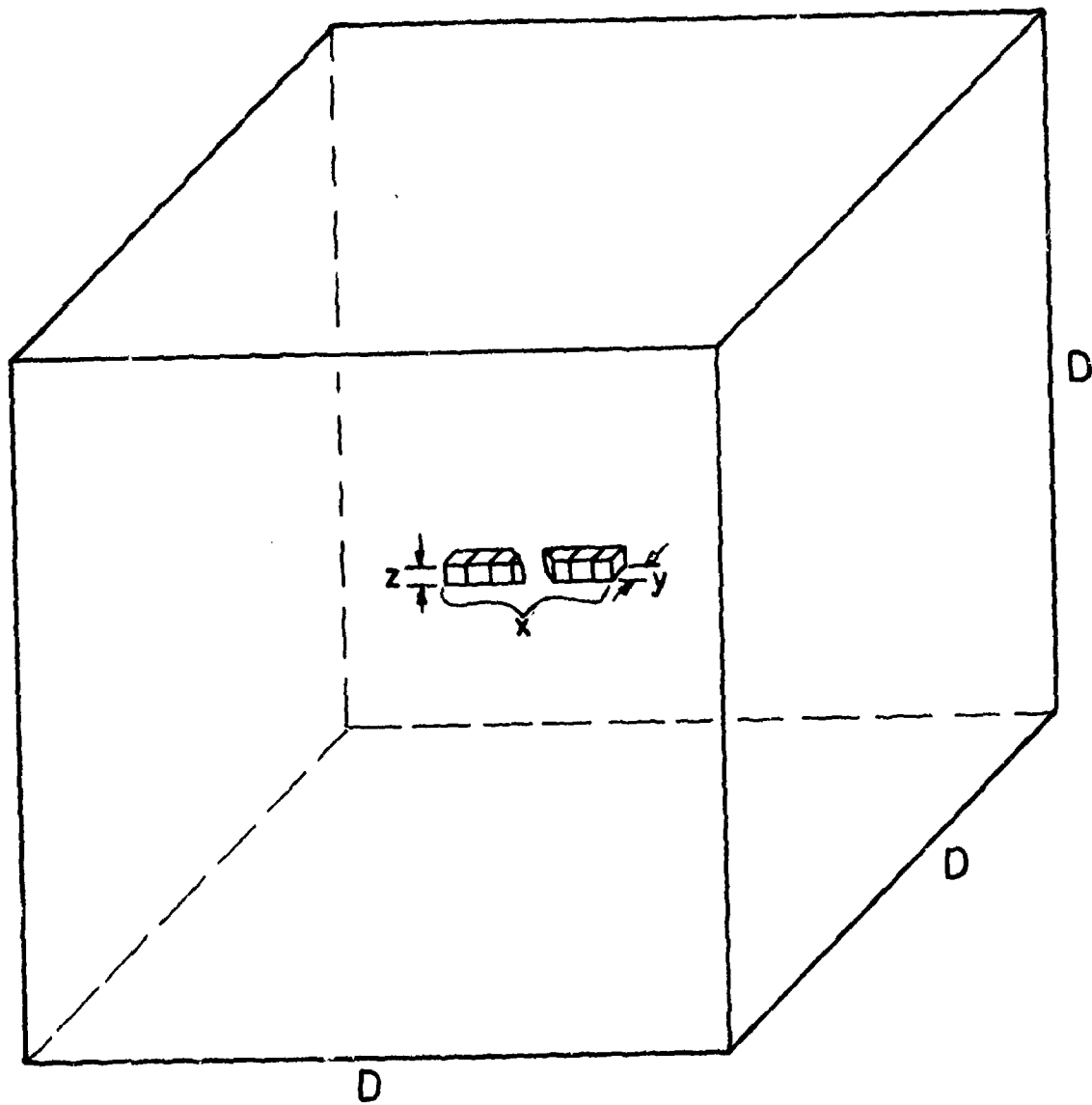
Figure 5.20 Geometry of Initial Chains

The volume fraction of the conductive phase can be written as

$$V_c = \frac{x\,y\,z}{D^3} = \frac{bz^3}{D^3} \qquad (5.67)$$

or

$$D = z\,(b/V_c)^{1/3} \qquad (5.68)$$

Combining Eqs. 5.63, 5.66 and 5.68, and solving for n gives

$$n = \frac{3b^{2/3}\,V_c^{-2/3}}{2 + b^2} \qquad (5.69)$$

Equation 5.69 gives Scarisbrick's random case for b = 1 and his ordered case for b = ∞.

The complete relation for sheet resistance as a function of volume fraction can then be written as

$$R_s = \rho_c/GtV_c(V_c)^{3b^{2/3}(V_c)^{-2/3}/(2 + b^2)} \qquad (5.70)$$

With $\rho_c = 9 \times 10^{-4}$ ohm-cm, it was found that the best fit between Eq. 5.70 and the experimental blending curve (Fig. 4.83) was obtained with b = 9; this fit is shown in Fig. 5.21.

The agreement between theory and experiment over six orders of magnitude change in sheet resistance is truly remarkable. This agreement was achieved by selecting two parameters, ρ_c and b. There is justification for the ρ_c value selected, as discussed in Section 5.2.2, but changing ρ_c would only displace the theoretical curve vertically without changing its shape. The choice of b = 9 was purely arbitrary, but it is a reasonable value; micro-networks made up of units with a 9 to 1 length to thickness ratio are consistant with observed microstructure (see Fig. 4.38).

As discussed in Section 5.1, the final stage of microstructure development in thick film resistors should be ripening of the conductive, a process which will eventually destroy the continuous networks of conductive particles. There-fore the resistance should increase as the ripening proceeds, and the rise in
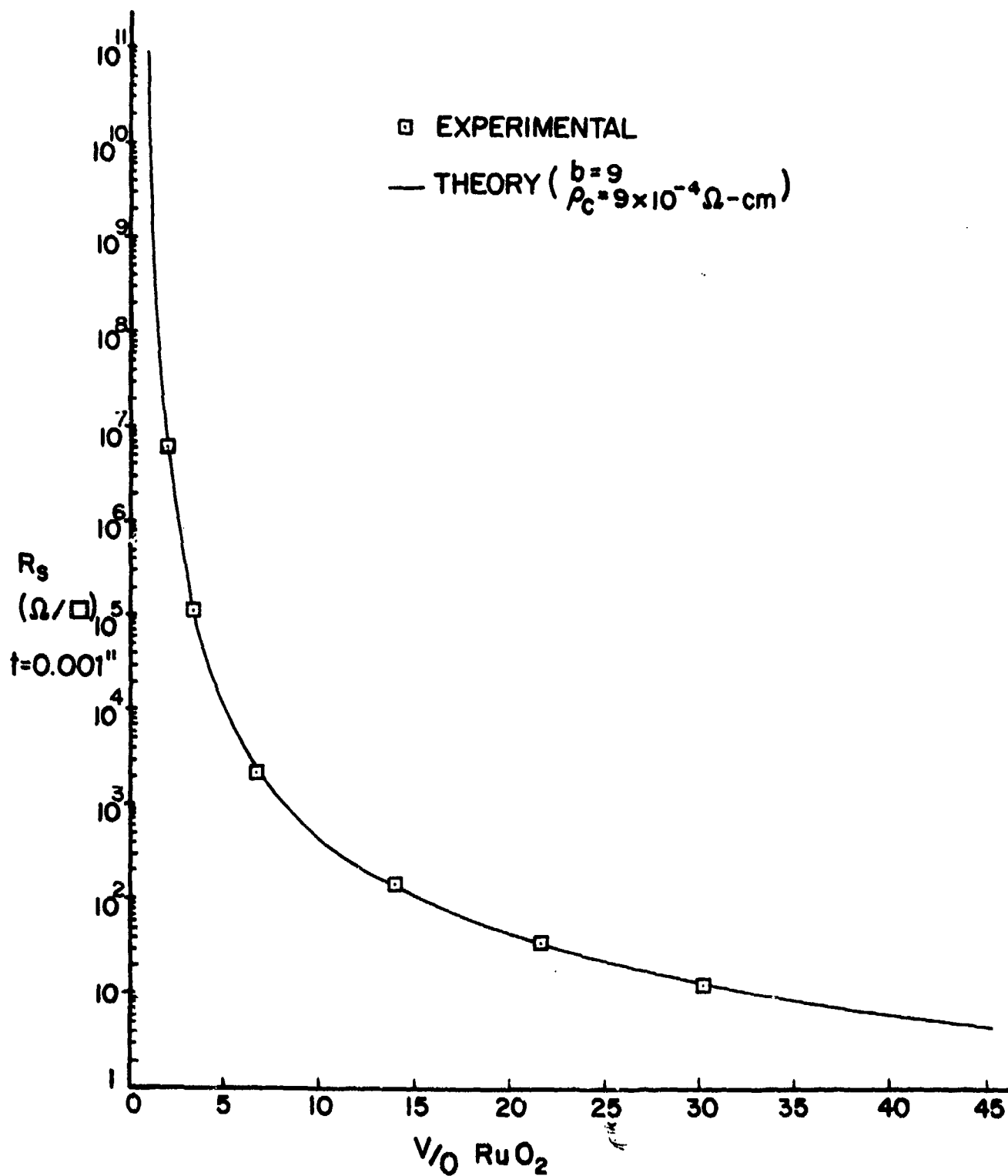
Figure 5.21   Theoretical Fit to Experimental Blending Curve

resistance as a function of time (see Fig. 4.84) can be interpreted as indicating the onset of ripening. At 800°C the observed time for the resistance increase was 25 minutes whereas the initial stage sintering will be completed in 43.5 seconds (see Table 5.2). This again confirms that ripening is not an important factor for the thick film system considered in this study, but it could be important in other thick film systems.

SECTION 6

Summary

A thick film resistor is a very complex, non-equilibrium system!
No one who has done research in the field would argue against the truth of
that statement, but it has several implications that should be discussed.
It means that the TCR and sheet resistance cannot possibly be predicted
from one or two physical properties of the ingredient materials. It means
that a simple model which may correlate some of the properties of a certain
resistor probably will not show any correlation with the properties of a
different resistor system, and may not even apply to the same resistor
system at a different point on the blending curve. Perhaps most importantly,
it means that there will always be some inherent uncertainty in resistor
properties predicted by any model because it is a non-equilibrium system.
The models developed during this study are complex models which cannot be
reduced to single equations, but they do allow us to determine the prop-
erties of the ingredient materials that are important and the degree to
which they should be controlled in order to achieve reproducible results.
They also tell us which properties of the ingredient materials to vary in
order to change certain properties of the resistors. However, all of the
materials properties and resistor properties are inter-related to such an
extent that a certain level of understanding of these inter-relations is
necessary in order to fully utilize the results of this study in technology.

The electrical properties of a thick film resistor are intimately
related to the microstructure and therefore to the processes responsible
for microstructure development. We have identified eight microstructure
development and conductive network development processes which contribute
to the final electrical properties, and these are listed in Table 6.1.
There are ten properties of the ingredient materials which contribute to
the kinetics of these eight processes and the property affecting each of
the processes is checked. Kinetic equations for each of the processes as
a function of the pertinent properties were developed in Section 5. While
the microstructure development processes depend on from three to five materials
properties, the network resistivity depends on nine and the network TCR depends
on all ten. A thick film resistor is a very complex, non-equilibrium system!

Table 6.1   Dependence of Electrical Properties on Materials Properties

Process	Material Property									
	η	d	R_g	γ_{lv}	γ_{sl}	γ_{sv}	C_o	R_c	ρ	α
Microstructure Development										
Glass Sintering	x		x	x	x	x		x		
Glass Spreading	x			x	x	x		x		
Microrearrangement	x	x	x	x						
Glass Densification				x						
Conductive Sintering							x	x		
Conductive Ripening					x		x	x		
Conductive Network Development										
Network Resistivity	x	x	x	x	x	x	x	x	x	
Network TCR	x	x	x	x	x	x	x	x	x	x

η = viscosity of the glass

d = density of the glass

R_g = particle size of the glass

γ_{lv} = surface tension of the glass

γ_{sl} = interfacial energy between glass and conductive

γ_{sv} = surface energy of the conductive

C_o = solubility of the conductive in the glass

R_c = particle size of the conductive

ρ = resistivity of the conductive

α = TCR of the conductive

SECTION 7

References

1. D.P. Burks, B. Greenstein and J. Maher, IEEE Electronic Components Conference, 217, (1967).

2. L.J. Brady, IEEE Electronic Components Conference, 238 (1967).

3. C.J. Pukaite and G. Goodman, Bull. Am. Cer. Soc., 48, 428 (1969) (Abstract) Presented at the Annual Meeting, Am. Cer. Soc. May 1969.

4. F.M. Collins, Bull.Am. Cer. Soc., 48, 805 (1969) (Abstract) Presented at the Fall Meeting of the Elec. Div. of the Am. Cer. Soc. Sept. 1969.

5. P.R. Van Loan, Insulation/Circuits, p. 35, June 1972.

6. L.C. Hoffman, Bull. Am. Cer. Soc., 42, 490 (1963).

7. E.H. Melan and A.H. Mones, IEEE Electronics Components Conference, p.76 (1964).

8. G.J. Kahan, IBM J. Res. Develop., p. 313, July, 1971.

9. A.B. Usowski and A.J. Van Zeeland, Proc. Electronic Components Conf., Washington, D.C., May 1973, p. 2-A-2-1.

10. G.S. Iles, IERE Conference Proceedings 11, 29 (1968), ibid, Platinum Metal Reviews, 11, 126 (1967).

11. C.C. Sartain, W.D. Ryden and A.W. Lawson, J. Non-Cryst. Solids, 5, 55 (1970).

12. D.A. Cash, M.P. Ansell and R.M. Hill, "Conduction Mechanisms in Thick Films", Third Annual Report, Ministry of Defense Contract No. Ru 7-41, Chelsea College, London, November, 1974.

13. J.W.M. Biesterbos, J. Appl. Phys., 45, 153 (1974).

14. C.H. Seager and G.C. Pike "Electrical Properties of DuPont Birox and Cermalloy Thick Film Resistors I", Report No. SAND 75-0019, Sandia Laboratories, Albuquerque, New Mexico, January, 1975.

15. H.C. Angus and P.E. Gainsbury, Elec. Comp., 84 (1968).

16. J.W. Gibbs, Scientific Papers. Volume One, Dover, New York, p. 229 (1961).

17. W.J. Huppmann and H. Riegger, Acta Met, 23, 965 (1975).

18. B. Derjaguin, "On the Repulsive Forces Between Charged Colloid Particles and On the Theory of Slow Coagulation and Stability of Lyophobe Sols.," Trans. Faraday Soc., 36, 203 (1940).

Referencea (Con't)

19. W.D. Kingery, "Densification During Sintering in the Presence of a Liquid Phase. I. Theory", J. Appl. Phys., 30, 301 (1959).

20. J. Frenkel, "Viscous Flow of Crystalline Bodies under the Action of Surface Tension", J. Phys. (U.S.S.R.), 9, 385 (1945).

21. G.C. Kuczynski, B. Neuville, and H.P. Toner, "Study of Sintering of Poly (methyl Methacrylate)", J. Appl. Polymer Sci., 14, 2069 (1970).

22. G.C. Kuczynski, "Study of the Sintering of Glass", J. Appl. Phys., 20, 1160 (1949).

23. W.D. Kingery and M. Berg, "Study of the Initial Stages of Sintering Solids by Viscous Flow, Evaporation-Condensation, and Self Diffusion", J. Appl. Phys., 21, 301 (1950).

24. G.C. Kuczynski, "Self-diffusion in Sintering of Metallic Particles", J. Metals, 1, 169 (1949).

25. D.L. Johnson and I.B. Cutler, "Diffusion Sintering: I, Initial Stage Sintering Models and Their Application to Shrinkage of Powder Compacts", J. Amer. Cer. Soc., 46, 541 (1963).

26. M.F. Burr, V. Lenel, and G.S. Ansell, "Influence of Pressure Upon the Sintering Kinetics of Silver", Trans. AIME, 239, 557 (1967).

27. D.L. Johnson, "New Method of Obtaining Volume, Grain-Boundary, and Surface Diffusion Coefficients from Sintering Data", J. Appl. Phys., 40, 192 (1969).

28. R.L. Coble, "Effects of Particle-Size Distribution in Initial-Stage Sintering", J. Amer. Cer. Soc., 56, 461 (1973).

29. G.H.S. Price, C.J. Smithells, and S.V. Williams, "Sintered Alloys. Part 1.-Copper-Nickel-Tungsten Alloys Sintered with a Liquid Phase Present", J. Inst. Metals, 62, 9 (1938).

30. G.W. Greenwood, "The Growth of Dispersed Precipitates in Solutions", Acta Met., 4, 243 (1956).

31. H. Fischmeister and G. Grimvall, "Ostwald Ripening – A Survey", Mater. Sci. Res., 6, 119 (1973).

32. I.M. Lifshitz and V.V. Slyozov, "The Kinetics of Precipitation from Supersaturated Solid Solutions", J. Phys. Chem. Solids, 19, 35 (1961).

33. C. Wagner, "Theorie der Alterung von Niederschlägen durch Umlosen (Ostwald-Reifung)", Z. Electrochemie, 65, 581 (1961).

34. I.A. Aksay, C.E. Hoge, and J.A. Pask, "Wetting under Chemical Equilibrium and Nonequilibrium Conditions", J.Phys. Chem., 78, 1178 (1974).

35. C. Herring, "Effect of Change of Scale on Sintering Phenomena", J. Appl. Phys., 21, 301 (1950).

References (con't)

36. J.B. Cutler, J. Amer. Ceram. Soc., 52, 14 (1969).

37. W.S. Young, S.T. Rosmussen, and I.B. Cutler in "Ultrafine Ceramics", J.J. Burke, N.L. Reed, and V. Weiss, eds., p. 185, Syracuse Univ. Press, Syracuse, NY (1970).

38. W.S. Young and I.B. Cutler, J. Amer. Ceram. Soc., 53, 659 (1970).

39. D.L. Johnson, Phys. Sintering, 1, B1 (1969).

40. D.A. Venkatu and D.L. Johnson, J. Amer. Ceram. Soc., 54, 641 (1971).

41. R.W. Berry, P.M. Hall, and M.T. Harris, "Thin Film Technology", p. 491, Van Nostrand Reinhold Co., New York (1968).

42. L.F. Miller, Solid State Tech., p. 46, June, 1969.

43. B.M. Austin, Solid State Tech., p. 53, June, 1969.

44. D.R. Kobs and D.R. Voigt, Solid State Tech., p. 34, February, 1971.

45. R.W. Atkinson, Solid State Tech., p. 51, May, 1971.

46. L. Shartsis and S. Spinner, "Viscosity and Density of Molten Optical Glasses", J. Res. Natl, Bur. Std., 46, 176 (1951).

47. L. Shartsis and A.W. Smock, "Surface Tensions of Some Optical Glasses", J. Amer. Cer. Soc., 30, 130 (1947).

48. L. Shartsis, S. Spinner, and A.W. Smock, "Surface Tension of Compositions in the Systems $PbO-B_2O_3$ and $PbO-SiO_2$," J. Amer. Cer. Soc., 31, 23 (1948).

49. E.M. Daver and W.J. Ullrich, "Hot Stage Microscopy of Study of Liquid Phase Sintering", Perspectives in Powder Met., 5, 189 (1970).

50. S.M. Kaufman, T.J. Whalen, L.R. Sefton and E. Eichen, "The Utilization of Electron Microscopy in the Study of Powder Metallurgical Phenomena I. Neck Growth Measurements for Submicron Copper and Silver Spheres", Perspectives in Powder Met., 5, 25 (1970).

51. C.B. Shumaker and R.M. Fulrath, "Initial Stages of Sintering of Copper and Nickel", Mater. Sci. Res., 6, 191 (1973).

52. J.M. Fletcher, W.E. Gardner, B.F. Greenfield, M.J. Holdoway, and M.H. Rand, J. Chem. Soc. (A) p. 653 (1968).

53. F.A. Cotton and J.T. Mague, Inorg. Chem., 5, 317 (1966).

54. D.B. Rogers, R.D. Shannon, A.W. Sleight, and J.L. Gillson, Inorg. Chem., 8, 841 (1969).

55. K.V.K. Rao and L. Iyengar, Acta, Cryst., A25, 302 (1969).

56. C. Boman, Acta, Chem. Scand., 24, 116 (1970).

References (con't)

57. W.E. Bell and M. Tagami, J. Phys. Chem., 67, 2532 (1963).

58. S. Schukarev and A. Ryabov, Russ. J. Inorg. Chem., 5, 941 (1960).

59. H. Schafer, G. Schneidereit, and W. Gehardt, Z. Anorg. allgem. Chem., 319, 327 (1963).

60. S. Pizzini and L. Rossi, J. Electrochem. Soc., 117, 244C (1970) (Abstract) Presented at Fall 1970 Meeting of the Electrochem. Soc.

61. W. Latimer, J. Am. Chem. Soc., 73, 1480 (1951).

62. D. Chatterji and R.W. Vest, J. Am. Cer. Soc., 54, 73 (1971).

63. W.D. Ryden, A.W. Lawson, and C.C. Sartain, Phys. Lett., 26A, 209 (1968) ibid, Phys. Rev., 131, 1494 (1970).

64. B.C. Passenheim and D.C. McCollum, J. Chem. Phys., 51, 320 (1969).

65. S.M. Marcus and S.R. Butler, Phys. Lett., 26A, 518 (1968).

66. C. Osburn, EE 696 Reports, Sch. of Elec. Eng., Purdue University, Jan. 1968, May 1968.

67. R.T. Slivaka and D.N. Langenberg, Phys. Lett., 28A, 169 (1968).

68. R.E. Trease and R.L. Dietz, Solid State Tech., 15, 39 (1972).

69. J. Mukerji and S.R. Biswas, "Solubility of Ruthenium in Soda-Silica Glasses", Cent. Glass Cer. Res. Inst., Bull., 14, 30 (1967).

70. K.K. Dhargupta and J. Mukerji, "Solubility Dependance of Ruthenium Volatilization from Glass", Trans. Ind. Cer. Soc., 27, 123 (1968).

71. R.H. Hallse and R.L. Cook, "Volatility Studies of Lead Silicate Melts", J. Amer. Cer. Soc., 41, 331 (1958).

72. J. White, "Microstructure and Grain Growth in Ceramics in the Presence of a Liquid Phase", Mater. Sci. Res., 6, 81 (1973).

73. N.C. Kothari and J. Waring, "Sintering Kinetics in Iron-Copper Alloys with and without a Liquid Phase", Powder Met., 7, 13 (1964).

74. R. Warren, "Microstructural Development During the Liquid-Phase Sintering of Two-Phase Alloys, with Special Reference to the NbC/Co System", J. Mater. Sci., 3, 471 (1968).

75. S. Sarian and H.W. Weart, "Kinetics of Coarsening of Spherical Particles in a Liquid Matrix", J. Appl. Phys., 37, 1675 (1966).

76. H.E. Exner, "Analysis of Grain-and Particle-Size Distribution in Metallic Materials", Int. Met. Rev., 17, 25 (1972).

References (con't)

77. M.G. Bolinger, Jr., "Electron Microscope Studies of Beryllium Oxide Powders", Fourteenth A.E.C. Metallography Group Meeting, Nuclear Metals, Inc., Boston, April 5-6, 1960.

78. R.C. Rau, "Routine Crystallite Size Determination by X-Ray Diffraction Line Broadening", Advances in X-ray Analysis, 5, 104 (1962).

79. S.F. Bartram, "Crystallite-Size Determination from Line Broadening and Spotty Patterns", Chapter 17 in Handbook of X-Rays, ed. E.F. Kaelble, McGraw-Hill, New York, (1967).

80. R.I. Garrod, J.F. Brett, and J.A. MacDonald, "X-Ray Line Broadening and Pure Diffraction Contours," Australian J. Phys., 7, 77 (1954).

81. F.W. Jones, "The Measurement of Particle Size by the X-Ray Method", Proc. Roy. Soc., 166A, 16 (1938).

82. R.F. Geller, E.N. Bunting, and A.S. Creamer, J. Res. NBS, 20, 57 (1938).

83. T.P. Yin, J. Phys. Chem., 73, 2413 (1969).

84. S. Newman, J. Colloid Interfac. Sci., 26, 209 (1968).

85. J.K. Mackenzie and R. Shuttleworth, Proc. Phys. Soc. (London), B62, 833 (1949).

86. C.H. Saeger and G.C. Pike, Sandia Laboratories, Albuquerque, New Mexico, private communication.

87. R.E. Meridith and C.W. Tobias, in Advances in Electrochemistry and Electrochemical Engineering, P. Delahay and C.W. Tobias, eds., Vol. 2, p. 15, Interscience, New York (1962).

88. L.K.H. Van Beek, in Progress in Dielectrics, Vol. 7, p. 69, Heywood, London (1965).

89. J.C. Wimmer, H.C. Graham and N.M. Tallan, in Electrical Conductivity in Ceramics and Glass, N.M. Tallan, ed., Part B, p. 619, Marcel Dekker, New York (1974).

90. V. Ambegaokar, S. Cochran and J. Kurkijarvi, Phys. Rev., B8, 3682 (1973).

91. P.A. Lightsey, Phys. Rev., B8, 3586 (1973)

92. I. Webman and J. Jortner, Phys. Rev., B11, 2885 (1975).

93. R.B. Grekila and T.Y. Tien, J. Amer. Ceram. Soc., 48, 22 (1965).

94. J.W. Cahn, Acta Met., 14, 477 (1966).

95. R.M. Scarisbrick, J. Phys. D: Appl. Phys., 6, 2098 (1973).

96. R. Holm and E. Holm, "Electric Contacts", p. 43, Springer-Verlag, New York (1967).

References (con't)

97. T. Ramanan and A.C.D. Chaklader, J. Amer. Ceram. Soc., 58, 476 (1975).

98. See reference 96, p. 16.

99. E.H. Sondheimer, Advances in Physics, 1, 1 (1952).

100. R.W. Berry, P.M. Hall and M.T. Harris, "Thin Film Technology", p. 312, Van Nostrand Reinhold, New York (1968).

101. ibid, p. 315

102. D.R. Lamb, "Electrical Conduction Mechanisms in Thin Insulating Films", Methuen, London (1967).

103. N.C. Miller and G.A. Shirn, Solid State Tech., 10, 28 (1967).

104. see reference 96, p. 123

105. J.G. Simmons, J. Appl. Phys., 35, 2655 (1964).

106. ibid, 34, 1793 (1963).

107. S.M. Sze, J. Appl. Phys., 38, 2951 (1967).

108. L.M. Levinson and H.R. Phillipp, Appl. Phys. Lett., 24, 75 (1974).

109. F.W. Schmidlin, J. Appl. Phys., 37, 2823 (1966).

110. A. Kusy, "On the Structure and Conduction Mechanism of Thick Resistive Films", submitted to Thin Solid Films.

7. DISTRIBUTION LIST

Bassett, William J   (1)
Sel-Rex Company
1302 East St Gertrude Place
Santa Ana California 92705

Beer , Mr. Henri B   (1)
Scientific Research Society N V
Postbaan, 69
2190 Essen, Belgium

Bharat Electronics Ltd   (1)
A P Raju, Manager
Components Divisions
Jalahalli, Bangalore 560013
India

Bower , Mariya A E   (1)
Research Library
Engelhard Minerals & Chemicals Corp
Menlo Park, Edison, New Jersey 08817

Brady, Dr Lynn (1)
CTS Corporation
905 N West Blvd
Elkhart, Indiana 46514

Bratschun, Dr W R   (1)
Zenith Radio Corporation
1851 Arthur Avenue
Elk Grove Village, Illinois 60007

Bube, Kenneth R   (1)
RCA Corporation
David Sarnoff Research Center
Princeton, New Jersey 08540

Burdick, Dr. Glenn A (1)
College of Engineering
University of South Florida
Tampa, Florida 33620

Buzan, Frank E Vice President (1)
BALA Electronics Corporation
14 Fayette Street
Conshohocken, Pennsylvania 19428

Cahill, Joseph A (1)
Matthey Bishop Inc.
4 Malin Road
Prazer, Pennsylvania 19355

Carcia, Dr Peter F   (1)
E.I. DuPont DeNemours
Electronic Materials Div
Buffalo Avenue
Niagara Falls, New York 14302

Carkner, Mrs J   (1)
Dept 8E20 Technical
Information Centre
Bell-Northern Research
Box 3511, Station C
Ottawa, Canada K1Y 4H7

Carson, Mr Robert D (1)
Motorola Inc/Govn Electronics Div
8201 E McDowell Road
Scottsdaye, Arizona 85252

Cheng, H L   (1)
Engelhard Industries
1 West Central Avenue
East Newark, New Jersey 08824

Chornik, Leonardo Felix EE   (1)
Instituto De Investigaciones Cientificas Y
Techicas De Las Fuertas Armadas-Microelectronica
ZuFria Tegui y Varela Villa Martelli
Provincia De Buenos Aires
Republica Argentina

Colglazier, Mr J   (1)
CTS Microelectronics, Inc
1201 Cumberland Avenue
West Lafayette, Indiana 47906

Cowart, Mr Michael   (1)
U.S. Naval Avionics Facility
21st Street and Arlington Avenue
Indianapolis, Indiana 46218

Dahlquist, John 201-2E   (1)
3 M Company
P O Box 33221
St Paul, Minnesota 55133

Defense Documentation Center   (20)
Cameron Station
Alexandria, Virginia 22314

Distribution List (con't)

Director, Prog Management   (1)
Advanced Research Projects Agency
1400 Wilson Blvd
Arlington, Virginia   22209

Economos, Dr George   (1)
Sprague Electric Company
6th Ave & Beech St
Grafton, Wisconsin 53024

Fine, Professor Morris (1)
Department of Materials Science
Northwestern University
Evanston, Illinois 60201

Floyd, L J   (1)
Micro Consulting
6332 El Risco Drive
El Paso, Texas 79912

Forlani, Dr Franco (1)
Divisione Elettronica Fivre
27100 Pavia - Via Filzi, 1
9 Miliardi Interamente Vergato-
C.C.I.A.A. 72271
U.R.I. Milano 13977, Italy

Fritz, Dr L Supervisor   (1)
Hybrid Microelectronics
Electronic Systems Group
Western Division
GTE Sylvania, Box 205
Mountain View, California 94040

Georgek, Mr Stanley (1)
CTS Microelectronics, Inc
1201 Cumberland Avenue
West Lafayette, Indiana 47906

Gaudio, J (1)
Zenith Radio Corporation
1851 Arthur
Elk Grove Village, Illinois 60007

Grissom, J T Supervisor (1)
Hybrid Microcircuit Tech Div
Sandia Laboratories
Albuquerque, New Mexico 87115

Guydt, L M (1)
LTT
P O Box 5
78702 Conflans, France

Hailes, L   (1)
Standard Telecommunications Labs LTD
London Road
Harlow, Essex
United Kingdom

Hamer, Don   (1)
State of the Art, Inc
1315 S Allen
State College, Pennsylvania 16801

Herbst, Darwyn   (1)
Grinnell Inc
316 East Sixth Street
Tucson, Arizona 85705

Hoffman, Dr Lewis C   (1)
Electrochemicals Dept
E.I. DuPont de Nemours & Co
Wilmington, Delaware 19898

Hollinger, W   (1)
CTS of Berne, Inc
406 Parr Road
Berne, Indiana 46711

Holmes, Mr Curt   (1)
CTS Corp
905 N West Blvd
Elkhart, Indiana 46514

Hossenlopp, Mr A M (2)
Delco Electronics Division
General Motors Corp
Research & Engineering Bldg
P O Box 1104
Kokomo, Indiana 46901

Isles, Mr G S (1)
Johnson, Matthey & Co Ltd
Group Research Laboratories
Exhibition Grounds, South Way
Wembley, HA 9 OHW
United Kingdom

Jancar, Edward W Project Engineer (1)
Allen Bradley Company
1201 South 2nd Street
Milwaukee, Wisconsin 53204

Jarvis, Dr N L   (3)
Naval Research Laboratory
Code 6170
Washington, D C 20375

Distribution List (Con't)

Jones, Dr W Kinzy (1)
C S Draper Lab MS 62
68 Albany Street
Cambridge, Massachusetts 02139

Kordatsky, Robert W   (1)
Amphenol Connector Division
120 S Main Street
Jamesville, Wisconsin 53545

Koved, Fred   (1)
ITT AECE Group
500 Washington Avenue
Nutley, New Jersey 07110

Kuo, Dr. C Y (1)
Engelhard Ind
1 West Central Avenue
E Newark, New Jersey 07029

Lane, G (1)
Electro Material Corp of America
605 Center Avenue
Mamaroneck, New York 10543

Layer, Edwin (1)
CTS Microelectronics
1201 Cumberland Avenue
West Lafayette, Indiana 47906

Liederbach, W H (1)
Plessey Inc
320 Long Island Expressway So
Melville, New York 11746

Lonborg, James (1)
Jet Propulsion Laboratory
4800 Oak Grove Drive
Pasadena, California 91103

Maddison, Eric A Proj Manager (1)
Allen-Bradley Electronics Ltd
Pilgrims Way, Bede Trading Estate
Jarrow, Tyne & Wear, NE 32 3 EN
England

Maher, John P
Sprague Electric Co
Marshall Street
N Adams, Massachusetts 01220

Merti, Francis (1)
Penn State University
259 MRL
University Park, Pennsylvania 16802

Miller, L F Senior Engineer (1)
IBM, East Fishkill Facility
Dept 13P, Bldg 300-101
Hopewell Junction, New York 12533

McCullough, R R (1)
Westinghouse Electric Corp
P O Box 1693, Mailstop 1204
Baltimore, Maryland 21203

McElroy, James D   (1)
Bell Telephone Labs
555 Union Blvd Rm 2D-011
Allentown, Pennsylvania 18103

Pike, Dr Gordon   (1)
Sandia Laboratories
Division 5155
Albuquerque, New Mexico 87115

Pogue, Ann   (1)
Materials Consultant
258 Barbara Avenue
Solana Beach, California 92075

Polinski, Paul Wm (1)
Allen Bradley Company
1201 S Second Street
Milwaukee, Wisconsin 53204

Postlethwaite, Alan W (1)
Technical Director, Metals Division
Norton Company
45 Industrial Place,
Newton, Massachusetts 02164

Powers, Dr Dana A (1)
Sandia Labs, Div 5831
Kirtland AFT-East
Albuquerque, New Mexico 87115

Prudenziata, Dr Maria (1)
Universita di Modena Phys Dept
Laboratoria di Elettronics, via
Vivaldi 70, 41100 Modena
Italy

Distribution List (Con't)

RCA Corporation (1)
Engineering Library
Meadow Lands, Pennsylvania 15347

Renn, D J (1)
Beckman Instruments, Inc
2500 N Harbor Blvd
Fullerton, California 92634

Rice, Agnes G Librarian (1)
Allen Bradley Company
1201 S Second Street
Milwaukee, Wisconsin 53204

Ridgewell, P (1)
Mullard Research Labs
Redhill, Surrey
England RH1-5HA

Ridgley, Dr Dana (1)
Hooker Research Center
Niagara Falls, New York 14302

Sayer, M Professor of Physics (1)
Dept of Physics Stirling Hall
Queen's University
Kingston, Canada K7L 3N6

Siuta, Dr V (1)
Engelhard Industries
Menlo Park
Edison, New Jersey 08817

Stackpole Carbon Co (1)
Marcella Mullaney Library Supervisor
St Marys, Pennsylvania 15857

Standard Elektrik Lorenz AG (1)
Dr W Poth Abt 642   ITT
Unternehmensgruppe Bauelemente
D-8500 Nurnberg
Postfach 2340 - Platenstrabe 66
Germany

Stein, Dr S J (1)
Electro-Schience Laboratories, Inc
1601 Sherman Avenue
Pennsauken, New Jersey 08110

Stevens, Dr E H (1)
University of Idaho
Dept of Elec Engr, Buchanan Engr Lab
University of Idaho
Moscow, Idaho 83843

Tadiran, R Shalev Librarian (1)
Israel Electronics Industries Ltd
3 Hashalom Road/POB 648
Tel Aviv 61000 Israel

Tallan, Dr Norman N   (1)
Air Force Materials Laboratory
Bldg 450
Wright Patterson AFB, Ohio 45433

Technique & Documentation (1)
c/o Milton Snedeker Corporation
175-11, 148th Avenue
Jamaica, New York 11430

Thome, John R (1)
Motorola, Inc Dommunications Div
1301 E Algonquin Rd Room 1809
Schaumburg, Illinois 60172

Tischler, Oscar Mgr R & D (1)
KDI Pyrofilm Corporation
60 S Jefferson Road
Whippany, New Jersey 07981

Turnbaugh, Jerry 50-397 (1)
Tektronix, Inc
P O Box 500
Beaverton, Oregon 97077

Turner, Basil S (1)
Basil S Turner Foundation
2705 Greenleaf Blvd
Elkhart, Indiana 46514

US Army Electronics Tech & Devices Lab (1)
AMSEL TL-DT
Fort Monmouth, New Jersey 07703

Verma, Kewal (1)
Sel Rex
1302 East Gertrude Place
Santa Ana, California 92705

Walton, Brian (1)
ERA Ltd
Leatherhead
Surrey
England KT 22 7SA

Distribution List (Con't)

Weintraub, Mr William   (1)
US Army Electronics Tech & Devices Lab
ATTN: AMSEL-TL-IT
Fort Monmouth, New Jersey 07703

Willis, James   (1)
Naval Air Systems Command
Code Air 310B
Washington, D. C.   20360

Weldon, Dr Norman R   (1)
CTS Corporation
905 Northwest Blvd
Elkhart, Indiana 46514

Winkler, Dr E R   (1)
Corning Glass
Corning, New York 14830

Wirtz, Gerald P   (1)
University of Illinois
Dept Ceramic Engr
Urbana, Illinois 61801

Wong, Dr J   (1)
General Elec R & D Center
1 River Rd
Schenectady, New York 12345

Young, Margaret M Librarian (1)
TRW, Eastern Research Labs
401 N Broad St
Philadelphia, Pennsylvania 19108

Zarnow, David D/813
Naval Avionic Facility
6000 E 21st St
Indianapolis, Indiana 46205